Dissertation

Search for charged Higgs bosons decaying via $H^{\pm} \to \tau^{\pm}\nu$ in fully hadronic final states with the ATLAS detector at the LHC

Anna Kopp

Fakultät für Mathematik und Physik
Albert-Ludwigs-Universität Freiburg

Search for charged Higgs bosons decaying via $H^{\pm} \to \tau^{\pm}\nu$ in fully hadronic final states with the ATLAS detector at the LHC

Dissertation

zur Erlangung des Doktorgrades der
Fakultät für Mathematik und Physik der

Albert-Ludwigs-Universität
Freiburg im Breisgau

vorgelegt von
Anna Kopp

September 2015

Dekan:	Prof. Dr. Dietmar Kröner
Betreuer der Arbeit:	Prof. Dr. Markus Schumacher
Zweitgutachter:	Prof. Dr. Karl Jakobs
Prüfer:	Prof. Dr. Gregor Herten
	JProf. Dr. Harald Ita
	Prof. Dr. Markus Schumacher
Datum der mündlichen Prüfung:	23. November 2015

Contents

1 Introduction

The Standard Model of particle physics, developed in the 1960s and 70s, describes matter and its interactions via the electromagnetic, weak and strong forces at the fundamental level, based on local gauge symmetries. Throughout the past decades, many predictions of the Standard Model have been confirmed in numerous experiments and almost all observed particle physics phenomena are described by the Standard Model. With the discovery of a Higgs boson by the ATLAS and CMS collaborations at the LHC at CERN in 2012, the last missing piece of the Standard Model may have been found. Properties of the new boson have been and still are being investigated and so far no contradictions to Standard Model predictions have been observed.
However, the discovered particle could also be a Higgs boson of an extended theory. Despite its success, the Standard Model describes only about 5% of the total energy content of the universe and cannot account for such phenomena as dark matter or the matter-antimatter asymmetry observed in the universe. Hence it cannot be a final theory. Many extensions of the Standard Model could account for another 25% of the energy content of the universe, since they provide candidates for dark matter. They often introduce many more elementary particles in addition to those of the Standard Model, including additional Higgs bosons. Two-Higgs-doublet models predict 5 Higgs bosons: three electrically neutral and two electrically charged ones, H^+ and H^-. Since the Standard Model does not include any electrically charged scalar particle, the discovery of a charged Higgs boson would be a clear indicator for new physics.
The Higgs sector of the minimal supersymmetric extension of the Standard Model is a two-Higgs-doublet model. In many scenarios of the minimal supersymmetric Standard Model, the decay of charged Higgs bosons into τ leptons and neutrinos is dominant or relevant over wide $H^\pm$ mass ranges and large regions of the parameter space. The final state with hadronically decaying τ leptons is especially promising for a discovery due to the large branching ratio of hadronic decays of τ leptons. Currently, the LHC provides the unique possibility worldwide for direct charged Higgs boson searches.
In this thesis, searches for charged Higgs bosons in final states with hadronically decaying τ leptons and jets are presented. They are based on $4.6\,\text{fb}^{-1}$ and $19.5\,\text{fb}^{-1}$ of data taken with the ATLAS detector at center-of-mass energies $\sqrt{s} = 7\,\text{TeV}$ and $8\,\text{TeV}$ in 2011 and 2012, respectively. A mass range for charged Higgs bosons between $80\,\text{GeV}$ and $1000\,\text{GeV}$ is probed. It is split up into searches for low-mass and high-mass charged Higgs bosons, depending on whether the charged Higgs boson is lighter or heavier than the top quark. Charged Higgs bosons are then produced either in top quark decays or in association with top a quark. The main focus of this thesis is on the data-driven estimation of the major background to these searches using a so-called embedding technique. The dominant irreducible background consists of $W \to \tau\nu$ decays, mostly originating from $t\bar{t}$ production but also from single top quark and W+jets events. Estimating this

background contribution based on simulation implies large systematic uncertainties. To avoid these uncertainties, a data-driven technique, the embedding method, is developed, validated and deployed instead.
A brief overview of the Standard Model and a non-exhaustive list of its limitations and possible extensions is given in chapter 2. The Higgs sectors of the Standard Model and minimal extension of the Standard Model are described in some detail in this chapter, along with descriptions of the signal processes. The LHC and ATLAS detector are introduced in chapter 3. Information about the data and simulation samples used in the searches presented in this thesis is given in chapter 4, including an overview of relevant background processes. The reconstruction and identification of final state objects is described in chapter 5. In chapter 6, the final states of the searches presented in this thesis and the search strategies are detailed. Chapters 7 and 8 are dedicated to the description of the background estimation methods. In chapter 7, the data-driven estimation of the dominant background contribution of events with true hadronically decaying τ leptons, the main topic of this thesis, is described. In chapter 8, the methods to estimate all other background contributions are summarized and systematic uncertainties of the signal processes are discussed. The statistical methods used to assess the agreement of the data with the background estimates are described in chapter 9. The final results of the searches for low-mass and high-mass charged Higgs bosons are presented in chapter 10. This thesis concludes with a summary given in chapter 11.
The results presented in this thesis have been published in references [1] and [2].

2 Theory Overview

2.1. The Standard Model of Particle Physics

The Standard Model (SM) of particle physics describes the electroweak and strong interactions between all known elementary fermions. It conjoins quantum chromodynamics (QCD) [3, 4], which describes strong interactions, with quantum electrodynamics (QED) [5–11] and the theory of weak interactions [12–14] and provides a consistent description of particle masses via the Brout-Englert-Higgs mechanism (BEH-mechanism) [15–18]. In 2012, a Higgs boson was discovered by the ATLAS and CMS collaborations [19, 20]. This could either turn out to be the last missing piece of the SM, in case all properties of the discovered particle agree with SM predictions or a new particle not described by the SM, in case predicted and observed properties do not agree.

In the first part of this chapter a brief introduction to the Standard Model of particle physics is given. It is based on textbooks and a review article [21–23], where more thorough descriptions may be found. The limitations of the SM are then discussed, followed by a short overview of supersymmetric extensions based on references [24–26]. Finally, the signal processes of the searches presented in this thesis are described.

2.1.1. Elementary Particles

The elementary particles described by the Standard Model are divided into two main classes, depending on whether they follow Fermi-Dirac or Bose-Einstein statistics. Fermions follow Fermi-Dirac statistics, thus they have half-integer spin and bosons are described by Bose-Einstein statistics, thus they have integer spin. Matter consists of fermions with spin $s = 1/2$ and bosons with spin $s = 1$ are responsible for interactions between them.
Fermions are further sub-divided into two main groups, quarks and leptons. An overview is shown in table 2.1. Anti-particles, with identical mass but opposite quantum numbers, exist for every type of particle shown. Additionally, quarks exist in three different color states. Both quarks and leptons appear in 3 generations, indicated in the table by the three columns. Ordinary matter consists basically of particles from the first generation. The three generations show identical quantum numbers except for flavor quantum numbers and differ in masses. The masses range from a few MeV[1] to more than 100 GeV for quarks. Since quarks cannot exist as free particles, their masses are difficult to determine, especially for the lighter quarks. For charged leptons, masses range from

[1] In this thesis, natural units with $\hbar = c = 1$ are assumed, thus all masses are given in units of energy.

Quarks			Electric charge [e]	Leptons			Electric charge [e]
u	c	t	$2/3$	ν_e	ν_μ	ν_τ	0
d	s	b	$-1/3$	e	μ	τ	1

Table 2.1. List of elementary fermions in the SM: the three quark generations on the left and three lepton generations on the right with their electric charges, respectively.

a few hundred keV to less than 2 GeV. Neutrinos are assumed to be massless in the SM. However, with the observation of neutrino oscillations [27, 28] it is clear nowadays that at least 2 of the 3 neutrinos do have masses which are less than 1 eV. This gives a clear hint for physics beyond the Standard Model. The masses can be added to the SM relatively easily, but the exact structure is still unclear.

There are 12 gauge bosons described by the SM: the photon, mediating electromagnetic

Particle	Electric charge [e]	Mass [GeV]	Interactions
Z	0	91.2	weak
W^+	$+1$	80.4	weak
W^-	-1	80.4	weak
γ	0	0	electromagnetic
g	0	0	strong

Table 2.2. Gauge bosons described by the Standard Model. Masses are taken from ref. [29].

interactions and massless, the bosons of the weak interaction, $W^\pm$ and Z, with masses of around 80 and 90 GeV and 8 gluons with different color charges, which are also massless and mediate the strong interaction. All gauge bosons have spin 1.

The Higgs boson, described in more detail in chapter 2.1.3, is the only fundamental scalar, i.e. spin $s = 0$, particle described by the SM.

2.1.2. Fundamental Interactions

Quantum Electrodynamics

Quantum electrodynamics, formulated in the 1940s, is the quantum field theory of electromagnetic interactions. It describes interactions between particles carrying electromagnetic charge via the exchange of photons in a quantized, relativistically invariant way. The symmetry group of QED is $U(1)$.

The Lagrangian of a free fermion with mass m is given by

$$\mathcal{L}_{\text{free}} = \bar{\psi}(i\gamma^\mu \partial_\mu - m)\psi, \tag{2.1}$$

which is not invariant under local gauge transformations,

$$\psi \to e^{ie\alpha(x)}\psi. \tag{2.2}$$

To ensure local gauge invariance, the covariant derivative D_μ and the vector field A_μ need to be introduced: $D_\mu = \partial_\mu - ieA_\mu$, where A_μ transforms as $A_\mu \to A_\mu + \frac{1}{e}\partial_\mu\alpha$. If ∂_μ in equation 2.1 is then replaced with D_μ, local gauge invariance under $U(1)$ symmetry is achieved:

$$\begin{aligned}\mathcal{L} &= \bar{\psi}(i\gamma^\mu D_\mu - m)\psi \\ &= \bar{\psi}(i\gamma^\mu\partial_\mu - m)\psi + e\bar{\psi}\gamma^\mu A_\mu\psi \end{aligned} \tag{2.3}$$

The vector field A_μ may be interpreted as the photon field which couples to fermions with charge $-e$ by adding an additional term corresponding to the kinetic energy of the photon. To retain local gauge invariance, this term needs to be invariant under the same local phase transformation as A_μ. The final Lagrangian of QED is then given by

$$\mathcal{L}_{\text{QED}} = \bar{\psi}(i\gamma^\mu\partial_\mu - m)\psi + e\bar{\psi}\gamma^\mu A_\mu\psi - \frac{1}{4}F_{\mu\nu}F^{\mu\nu} \tag{2.4}$$

with $F_{\mu\nu} = \partial_\mu A_\nu - \partial_\nu A_\mu$. An additional mass term of the form $\frac{m^2}{2}A_\mu A^\mu$ is prohibited in order to keep local gauge invariance; hence the photon must remain massless. The coupling strength α of QED increases with the energy scale of a given process. It is given by $\alpha_{\text{QED}} = e^2/(4\pi)$.

Quantum Chromodynamics

The strong interaction between quarks and gluons is described by quantum chromodynamics. Analogous to QED, the free Lagrangian in this case is given by

$$\mathcal{L}_{\text{free}} = \bar{q}(i\gamma^\mu\partial_\mu - m)q, \tag{2.5}$$

Here,

$$q = \begin{pmatrix} q_r \\ q_b \\ q_g \end{pmatrix}, \tag{2.6}$$

is the quark color field and q_r, q_b and q_g are the three color fields carrying color charges r = red, b = blue and g = green. The symmetry group of QCD is $SU(3)$, hence a local phase transformation transforms the quark color field q as

$$q(x) \to e^{i\alpha_a(x)T_a}q(x) \tag{2.7}$$

with 8 traceless, linearly independent 3×3 matrices T_a. In analogy to QED again, the covariant derivative is given by $D_\mu = \partial_\mu + igT_aG^a_\mu$, where the 8 gauge fields G^a_μ transform as $G^a_\mu \to G^a_\mu - \frac{1}{g}\partial_\mu\alpha_a - f_{abc}\alpha_b G^c_\mu$. The additional term compared to the QED analog with the real structure constants f_{abc} is necessary due to the non-abelian structure of QCD and leads to self-interaction among gluons. The structure of $SU(3)$ is also the reason why not all of the T_a commute. The commutation relation is given by $[T_a, T_b] = if_{abc}T_c$. A possible choice for the T_a are the Gell-Mann matrices $\lambda_a/2$. The

Leptons			Hypercharge Y	Isospin T^3
$\begin{pmatrix} \nu_e \\ e^- \end{pmatrix}_L$	$\begin{pmatrix} \nu_\mu \\ \mu^- \end{pmatrix}_L$	$\begin{pmatrix} \nu_\tau \\ \tau^- \end{pmatrix}_L$	-1 -1	$1/2$ $-1/2$
e^-_R	μ^-_R	τ^-_R	-2	0
Quarks			**Hypercharge Y**	**Isospin T^3**
$\begin{pmatrix} u \\ d' \end{pmatrix}_L$	$\begin{pmatrix} c \\ s' \end{pmatrix}_L$	$\begin{pmatrix} t \\ b' \end{pmatrix}_L$	$1/3$ $1/3$	$1/2$ $-1/2$
u_R	c_R	t_R	$4/3$	0
d'_R	s'_R	b'_R	$-2/3$	0

Table 2.3. Doublets of left-handed and singlets of right-handed fermions and their respective values for hypercharge Y and isospin T^3.

resulting Lagrangian is then given by

$$\mathcal{L}_{\text{QCD}} = \bar{q}(i\gamma^\mu \partial_\mu - m)q - g(\bar{q}\gamma^\mu T_a q)G^a_\mu - \frac{1}{4}G^a_{\mu\nu}G^{\mu\nu}_a, \tag{2.8}$$

where $G^a_{\mu\nu} = \partial_\mu G^a_\nu - \partial_\nu G^a_\mu - g f_{abc} G^b_\mu G^c_\nu$. In analogy to QED, gluons have to be massless to keep local gauge invariance. Mass terms for quarks are allowed if the different color states have the same masses, i.e. $m_r = m_g = m_b$. Contrary to QED, the coupling strength of QCD increases with decreasing energy scale of a process. Thus at high energies, i.e. small spatial distances, quarks and gluons are asymptotically free. On the other hand, at very low energies and hence large spatial distances, the coupling becomes very strong and thus quarks or gluons cannot exist as individual particles but only in bound states. This confinement leads to the effect that only hadrons, i.e. bound states of quarks but not single quarks are observed in experiments. A typical scale to evaluate the strong coupling strength in high energy physics experiments is at $q^2 = m_Z^2$.

Weak Interactions and Electroweak Unification

Electromagnetic and weak interactions are combined and described in a common model, electroweak interactions, proposed by Glashow, Salam and Weinberg [12–14] and thus referred to as the GSW-model. The combined gauge group is $SU(2)_L \times U(1)_Y$ with the weak hypercharge Y, which is connected to electric charge Q and the 3rd component of weak isospin T: $Y = 2Q - 2T^3$. The subscript L implies that in terms of chirality only left-handed fermions couple to the weak isospin current. All left-handed fermions are arranged in isospin doublets. For right-handed fermions only the charged ones are described by the SM in singlets. This arrangement of fermions is shown in table 2.3. Quarks are notated in their rotated eigenstates of the electroweak interaction [30, 31] given by the CKM-matrix.

Charged weak interactions are mediated by $W^\pm$ bosons and neutral weak interactions by Z bosons. In the GSW-model, an isotriplet of vector fields W^i_μ couples to the weak isospin with coupling strength g and an isosinglet vector field B_μ couples to the weak

hypercharge with a coupling strength $g'/2$. While the W_μ^i respect the $SU(2)_L$ symmetry, i.e. they only transform left-handed fermions, B_μ couples to left- as well as right-handed fermions. The fields of the massive charged $W^\pm$ bosons are given by

$$W_\mu^\pm = \sqrt{1/2}(W_\mu^1 \mp iW_\mu^2) \tag{2.9}$$

The fields of the photon, A_μ, and Z boson, Z_μ, are constructed from W_μ^3 and B_μ and given by

$$A_\mu = B_\mu \cos\theta_W + W_\mu^3 \sin\theta_W \tag{2.10}$$

$$Z_\mu = -B_\mu \sin\theta_W + W_\mu^3 \cos\theta_W \tag{2.11}$$

with the weak mixing angle θ_W. Thus charged weak currents are maximally parity violating but neutral weak currents are only partially parity violating. The couplings g and g' are related via

$$g' \cos\theta_W = g \sin\theta_W = e. \tag{2.12}$$

2.1.3. Electroweak Symmetry Breaking

Both photons and gluons are massless and the Lagrangians of QED and QCD do not contain any mass terms. However, W and Z bosons have masses m_W and m_Z, respectively, of the order of 100 GeV and electrically charged fermions are massive as well. Introducing mass terms of the form $m_W^2 W_\mu W^\mu$ and $\frac{1}{2}m_Z^2 Z_\mu Z^\mu$ or $-m\overline{\psi}\psi$ into the electroweak Lagrangian by hand breaks local gauge invariance. In this case, the theory is no longer renormalizable, preventing it from giving sensible predictions. The introduction of so-called spontaneous symmetry breaking, i.e. the BEH-mechanism, allows the addition of mass terms without breaking local gauge invariance. The BEH-mechanism introduces a complex doublet of scalar fields, resulting in an additional scalar particle, the Higgs boson. A scalar particle is also needed to maintain renormalizability of the theory. Without the scalar particle the cross section of processes like WW boson scattering diverges and thus breaks renormalizability.

The gauge group for electroweak interactions is $SU(2) \times U(1)$. The additional isospin doublet with weak hypercharge $Y = 1$ is given by

$$\phi = \begin{pmatrix} \phi^+ \\ \phi^0 \end{pmatrix}, \tag{2.13}$$

with $\phi^+ = (\phi_1 + i\phi_2)/\sqrt{2}$, which is electrically charged and $\phi^0 = (\phi_3 + i\phi_4)/\sqrt{2}$, which is electrically neutral. A Lagrangian invariant under local gauge transformations is given by

$$\mathcal{L} = (D_\mu\phi)^\dagger(D^\mu\phi) - \underbrace{(\mu^2\phi^\dagger\phi + \lambda(\phi^\dagger\phi)^2)}_{=V(\phi)}, \tag{2.14}$$

with the covariant derivative $D_\mu = i\partial_\mu - g\sigma_i W_\mu^i - \frac{g'}{2}YB_\mu$ and $\mu^2 < 0$ and $\lambda > 0$. The potential $V(\phi)$ has a minimum at $\phi^\dagger\phi = -\mu^2/2\lambda$. By choosing one specific point from

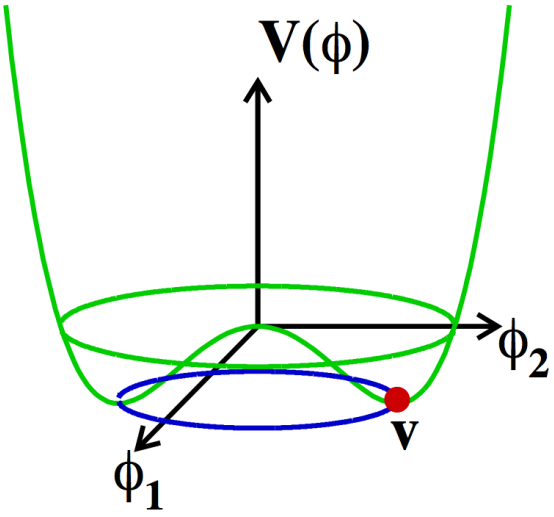

Figure 2.1. The Higgs potential [32].

all minima, e.g. $\phi_1 = \phi_2 = \phi_4 = 0$ and $\phi_3^2 = -\mu^2/\lambda = v^2$, where

$$v = \sqrt{\frac{1}{\sqrt{2}\mathrm{G_F}}} \approx 246\,\mathrm{GeV}, \tag{2.15}$$

is the so-called vacuum expectation value, the $SU(2)_L \times U(1)_Y$ symmetry is effectively broken to $U(1)Q$. It depends on the Fermi constant $\mathrm{G_F} = 1.166 \cdot 10^{-5}/\mathrm{GeV}^2$. With this choice of a minimum the ground state is electrically neutral since $\phi^+ = 0$ as desired. Expanding the potential around its minimum, the isospin doublet can be written as

$$\phi(x) = \frac{1}{\sqrt{2}} \begin{pmatrix} 0 \\ v + h(x) \end{pmatrix} \tag{2.16}$$

where $h(x)$ is the Higgs field. Only one of the original four fields in the isospin doublet ϕ remains, the other 3 give an additional longitudinal degree of freedom and thus mass to the W and Z bosons. The remaining field manifests itself in an additional scalar, the Higgs boson, with mass

$$m_h = \sqrt{-2\mu^2} \tag{2.17}$$

at tree level. However, the $U(1)_\mathrm{Q}$ symmetry remains unbroken and thus the photon remains massless.

The resulting Lagrangian, given in eq. 2.24, contains kinetic energies and self-interaction terms for the gauge bosons, kinetic energies of quarks and leptons and their interactions with the gauge bosons, mass terms for W, Z and Higgs bosons and their coupling as well as mass terms for quarks and leptons and their couplings to the Higgs boson. None of the masses are predicted, however; they are all input parameters to the theory and the mass of the Higgs boson is the last free parameter of the SM. But given a certain mass of the Higgs boson, all other properties of it are fixed. The mass of the W bosons is given by

$$m_W = \frac{1}{2} g v \tag{2.18}$$

and that of the Z boson is given by

$$m_Z = \frac{1}{2} v \sqrt{g^2 + g'^2}. \tag{2.19}$$

Thus m_W and m_Z are related via

$$\frac{m_W}{m_Z} = \cos\theta_W \tag{2.20}$$

The same doublet is used for generating masses of charged leptons. Constructing a doublet ϕ_c of conjugated fields,

$$\phi_c = -i\sigma_2 \phi^* = \begin{pmatrix} -\overline{\phi}^0 \\ \phi^- \end{pmatrix} \tag{2.21}$$

in addition to eq. 2.13 generates masses of quarks. In analogy to ϕ, a specific ground state is chosen, breaking the $SU(2)_L$ symmetry and ϕ_c is expanded around this state

$$\phi_c = \frac{1}{\sqrt{2}} \begin{pmatrix} v + h(x) \\ 0 \end{pmatrix}. \tag{2.22}$$

The conjugated doublet transforms in the same way as the original one but has opposite weak hypercharge, i.e. $Y = -1$. The masses of the fermions depend on arbitrary couplings and cannot be predicted from the theory. The couplings of fermions to the Higgs boson is given by so-called Yukawa couplings. In the SM this coupling λ_f is strictly proportional to the fermion masses m_f,

$$\lambda_f = \frac{\sqrt{2} m_f}{v}. \tag{2.23}$$

The coupling between fermions and the SM Higgs boson is purely scalar and given in the last term of eq. 2.24.

The Final Electroweak Lagrangian

The final electroweak Lagrangian is given by

$$\begin{aligned}\mathcal{L} = & \underbrace{-\frac{1}{4}\left(\mathbf{W}_{\mu\nu}\mathbf{W}^{\mu\nu} + B_{\mu\nu}B^{\mu\nu}\right)}_{\substack{\mathrm{W}^{\pm},\, Z,\, \gamma \text{ self-interactions} \\ \text{and kinetic energies}}} \\ & + \underbrace{\overline{L}\gamma^{\mu}\left(i\partial_{\mu} - g\tau\mathbf{W}_{\mu} - g'\frac{Y}{2}B_{\mu}\right)L}_{\substack{\text{kinetic energies and interactions with} \\ \mathrm{W}^{\pm},\, Z,\, \gamma \text{ of left-handed fermion doublets}}} + \underbrace{\overline{R}\gamma^{\mu}\left(i\partial_{\mu} - g'\frac{Y}{2}B_{\mu}\right)R}_{\substack{\text{kinetic energies and interactions with} \\ Z,\, \gamma \text{ of right-handed fermion singlet}}} \\ & + \underbrace{\left|\left(i\partial_{\mu} - g\tau\mathbf{W}_{\mu} - g'\frac{Y}{2}B_{\mu}\right)\phi\right|^2 - V(\phi)}_{\mathrm{W}^{\pm},\, Z,\, \gamma,\, \text{Higgs boson masses and couplings}} - \underbrace{\left(G_f\overline{L}\phi R + G_{f'}\overline{L}\phi_c R + h.c.\right)}_{\substack{\text{lepton, quark masses and} \\ \text{coupling to Higgs boson}}}, \end{aligned} \tag{2.24}$$

where all coupling strengths g, g' and G need to be determined experimentally. Left-handed doublets L and right-handed singlets R are defined as in table 2.3.

The Higgs Boson

The BEH-mechanism introduces a scalar particle, the Higgs boson. Given a certain mass, all other parameters pertaining to it, e.g. branching ratios or cross sections for specific production mechanisms, are fixed. At the LHC, Higgs bosons are produced without additional particles in the final state or in association with light or heavy quarks or W/Z bosons. In figure 2.2, the cross sections and branching ratios for an SM Higgs boson are shown over a wide mass range. The Higgs boson can decay into a multitude of different

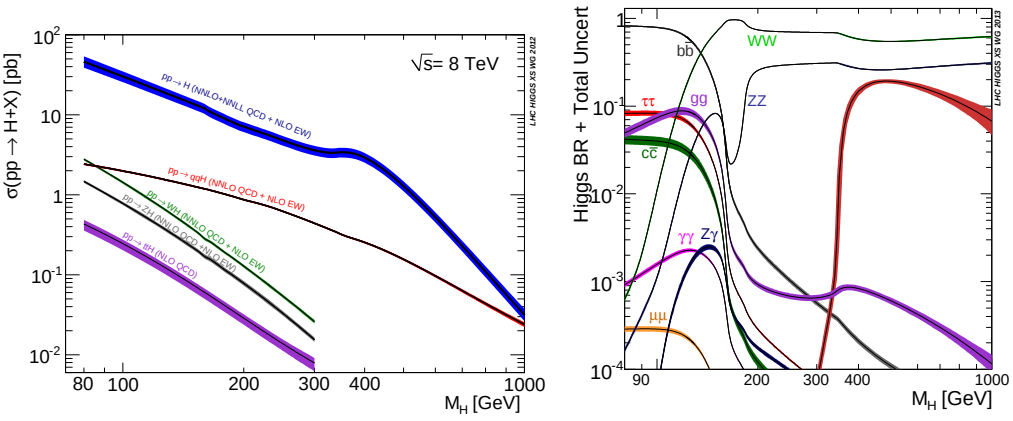

(a) SM Higgs boson production cross section

(b) SM Higgs boson branching ratios

Figure 2.2. Higgs boson (a) cross sections and (b) branching ratios over a mass range of $80\,\mathrm{GeV} < m_H < 1000\,\mathrm{GeV}$ [33].

final states over a wide mass range.

In July 2012, almost 50 years after the BEH-mechanism had been suggested, a Higgs boson was discovered by the ATLAS and CMS collaborations at the LHC [19, 20]. The new particle was found to have a mass around 125 GeV; the combination of the ATLAS and CMS measurements in the $\gamma\gamma$ and ZZ decay channels using the full dataset taken at $\sqrt{s} = 7$ and 8 TeV results in a mass of 125.09 ± 0.24 GeV [34]. Both the ATLAS and CMS collaborations observed or found evidence for the new particle in decays to $\gamma\gamma$, ZZ, WW [35–38], $\tau\tau$ [39, 40] and searched for the decay $H \to bb$ [41, 42]. Current measurements of the spin and parity quantum numbers of the new particle favor SM properties, i.e. spin $s = 0$ and $J^P = 0^+$ over alternative hypotheses [43, 44]. The coupling strength μ measured in ATLAS in different decay channels, with $m_H = 125.36$ GeV, is shown in figure 2.3. A value of $\mu = 1$ corresponds to the SM expectation. The current combination of the measured signal strengths in ATLAS results in a value of $\mu = 1.18^{+0.15}_{-0.14}$. The deviation from $\mu = 1$ could be due to statistical fluctuations or a hint for new physics beyond the SM. The newly discovered boson can also be interpreted as one of the Higgs bosons in a supersymmetric extension of the SM; this is discussed in some detail in chapter 2.3.

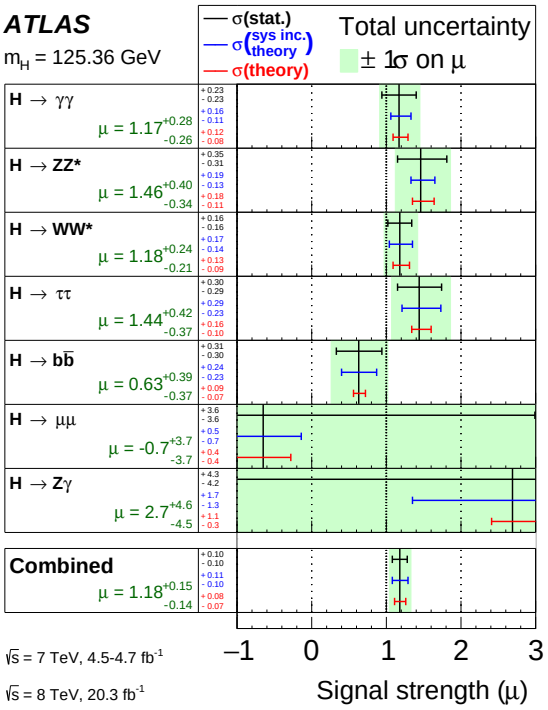

Figure 2.3. Signal strength μ in 5 different decay channels measured in ATLAS and their combined best fit value [45].

2.2. Limitations of the Standard Model

During the last decades, predictions of the SM have been tested successfully to great accuracy. Despite the agreement of experimental observations and theoretical calculations,

however, there are several phenomena and open questions left that cannot be addressed within the framework of the SM. They include the observation of neutrino oscillations, for which neutrino masses are required, the presence of dark matter [46] and dark energy [47, 48] in the universe, for which no candidates or explanations are given in the SM, the asymmetry between matter and anti-matter, the missing unification of forces and the hierarchy problem. A few of these, which could be remedied in extended theories such as supersymmetric models, are discussed in some detail below. More information about supersymmetric extensions of the SM is given in chapter 2.3.1.

Dark Matter

Data from rotation curves of galaxies suggest that luminous, baryonic matter comprises only a small fraction of the actual mass of galaxies. While for the seen mass distribution it is expected that the tangential velocity of observed matter decreases for mass far away from the core of the galaxy, it is observed that the velocity keeps increasing independently of the distance to the center. Since the additional matter is not radiating, i.e. it is interacting gravitationally but not electromagnetically or through the strong interaction. it is called dark matter (DM). From the rotation curves it is deduced that most of this DM forms a halo around the galactic center. The unexpected behavior of these rotation curves is not the only example that can be explained by dark matter. Gravitational lensing effects [49] give additional hints for the existence of DM. About 20% of the total energy content of the universe is expected to be non-baryonic dark matter, but only 5% is expected to be ordinary baryonic matter. Thus neither ordinary cold, baryonic matter nor neutrinos or any other particles of the SM can account for this abundance of non-radiating matter. Neutrinos, which are abundant in the universe, follow Fermi-Dirac statistics and thus there is a maximum phase-space density for them. However, some types of dwarf galaxies indicate that dark matter densities that are much higher than the maximum density allowed for neutrinos. One kind of dark matter candidate particles are so-called WIMPs, weakly interacting massive particles, occurring in many extensions of the SM. However, no particle that satisfies all criteria while explaining the abundance of DM has been found so far.

Unification of Forces

In the SM, electromagnetic, weak and strong interactions are well described. Electromagnetic and weak forces are combined to the electroweak force at an energy of about 100 GeV. It is desirable to include the strong interactions as well and truly unify all 3 fundamental forces described by the SM into one single gauge group based on a single coupling strength. This unification should occur at an energy scale lower than the Planck scale ($\mathcal{O} \approx 10^{19}$ GeV). Otherwise, gravitational effects between elementary particles must be considered, too, since the gravitational coupling strength then becomes of the same order of magnitude as those of other interactions. The running coupling strengths of electromagnetic, weak and strong forces are shown in figure 2.4 for the SM on the left and an extended minimal supersymmetric extension (see chapter 2.3.1) on the right hand side. In this figure, α_1 corresponds to the coupling strength of the $U(1)_Y$ group, α_2 to

that of $SU(2)_L$ and α_3 to the one of $SU(3)_C$. As can be seen, no unification of forces is possible in the SM. In the supersymmetric extension, a unification is achieved. Due to the introduction of new particles in extended theories, such as supersymmetric models, compared to the SM, the behavior of the coupling strengths is changed such that they are unified at a certain energy.

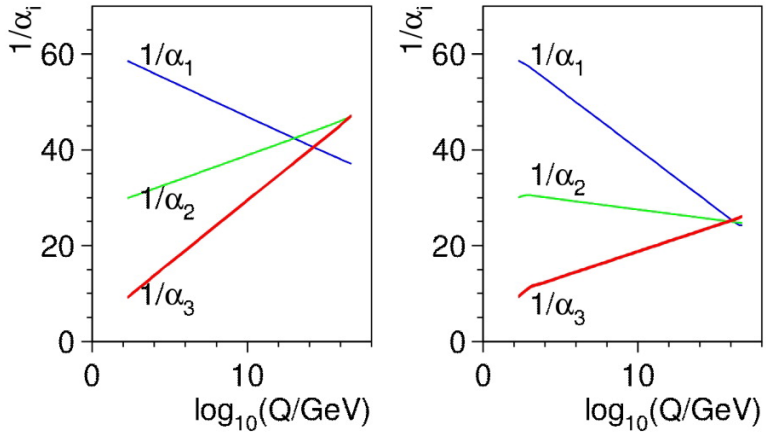

Figure 2.4. Comparison of running coupling strengths in the SM (left) and minimal supersymmetric extension MSSM (right). α_1 corresponds to the coupling strength of the $U(1)_Y$ group, α_2 to that of $SU(2)_L$ and α_3 to the one of $SU(3)_C$, all shown here over a wide range of energies Q. While in the SM no unification of coupling strengths is possible, this can be achieved in the MSSM [50].

Hierarchy Problem

When including higher order loop corrections to the Higgs boson mass squared, a cut-off scale Λ needs to be introduced to avoid divergences. Renormalizability of the SM is maintained in these calculations by adding counterterms. If the cut-off scale Λ, however, is interpreted as a physical scale at which the SM ceases to be valid, the bare Higgs boson mass at tree level will be about Λ, too. Choosing e.g. the Planck scale as the cut-off scale requires fine-tuning of the counterterm to the order of $\mathcal{O}(10^{30})$ GeV, which seems highly unnatural. In supersymmetric extensions of the SM the hierarchy problem does not appear since loop corrections due to scalars (fermions) are automatically canceled by supersymmetric loop corrections due to fermions (scalars).

2.3. Beyond the Standard Model

The simplest way of extending the SM is by adding scalar singlets and multiplets. Two-Higgs-doublet models are extensions of the SM with an additional Higgs doublet. They are relevant for many theories, in particular supersymmetric extensions of the SM. Below, a brief introduction to supersymmetry, two-Higgs-doublet models and the Higgs sector of the minimal supersymmetric Standard Model is given.

2.3.1. Supersymmetric Extensions of the Standard Model

Supersymmetry (SUSY) [51–53] adds a new symmetry to the SM which relates bosons to fermions and vice versa. Assuming there is one supersymmetric generator Q, an anti-commuting spinor, and applying it to fermions and bosons, respectively, yields

$$Q|\text{fermion}\rangle = |\text{boson}\rangle$$
$$Q|\text{boson}\rangle = |\text{fermion}\rangle.$$

More specific, the supersymmetric partners of SM fermions have spin $s = 0$ and those of SM bosons have spin $s = \frac{1}{2}$. All SM particles and their supersymmetric partners are arranged in so-called supermultiplets, which contain both fermions and bosons with equal masses. The generator Q and its hermitian conjugate commute with the generators of SM gauge transformations. Thus supersymmetric particles have the same quantum numbers, except for spin, as their SM counterparts under $SU(3)_C \times SU(2)_L \times U(1)_Y$ transformations. Since no supersymmetric particles have been discovered so far, the exact symmetry between SM particles and their supersymmetric partners, except for spin, must be broken with regard to mass. Supersymmetric partners of SM fermions are usually referred to with the SM name with an additional 's' for scalar as prefix, i.e. squarks and sleptons and e.g. a stau is the supersymmetric partner of an SM τ. Left- and right-handed SM particles are assigned separate left-and right-handed SUSY partners, although of course handedness is not defined for scalar particles. The partners of SM bosons are usually referred to with an '-ino' added as suffix to their SM name. The SUSY partners of gauge bosons are generally referred to as gauginos. Partners of the SM $W^{\pm}$, W^0, (Winos) B (Bino) and Higgs (Higgsino) bosons mix to electrically neutral neutralinos and electrically charged charginos. Gluinos, the partners of SM gluons, do not mix.
At least two Higgs doublets are required in supersymmetric extensions to maintain renormalizability and give masses to the different fermions. In the SM, anomalies theoretically caused by triangular fermion loops would spoil renormalizability of the theory. However, these anomalies disappear since the sum of all hypercharges of all 15 chiral fermions is 0. If there were only 1 Higgs doublet in SUSY, there would be one additional charged fermion, i.e. the particle corresponding to the SUSY partner of the charged component of the scalar field, which would spoil cancelation of the anomaly. With 2 Higgs doublets with opposite hypercharges, however, the cancelation and thus renormalizability are kept. A Higgs doublet with weak hypercharge $Y = 1$ and one with $Y = -1$ is required to give mass to both up-type as well as down-type quarks and charged leptons.

The Minimal Supersymmetric Standard Model

The minimal supersymmetric Standard Model (MSSM) [54] is the minimal possible extension of the SM in terms of particles and interactions: in addition to the SM particles, it contains supersymmetric partners to left- and right-handed up- and down-type quarks, charged leptons and left-handed neutrinos but no additional gauge interactions. Fermions and bosons are organized in supermultiplets. Since the SUSY potential should not contain

2HDM type	isospin up-type fermions	isospin down-type fermions	charged leptons
type I	H_2	H_2	H_2
type II	H_2	H_1	H_1
lepton-specific	H_2	H_2	H_1
flipped	H_2	H_1	H_2

Table 2.4. Overview of couplings between fermions and Higgs doublets in the different types of 2HDMs that do not allow flavor changing neutral currents at tree level [56].

any conjugated fields, a second Higgs doublet compared to the SM is needed to account for fermion masses. Left- and right-handed sfermions mix to new states and their mixing is proportional to the masses of their SM partners. Consequently this is expected to be relevant especially for particles of the third generation.
If CP is conserved, the two Higgs doublets yield 5 physical Higgs bosons: 2 CP-neutral ones, h and H, a CP-odd one, A and two mass-degenerate charged Higgs bosons[2], H^+ and H^-. R-parity is required, where R is a multiplicative quantum number defined as

$$R = (-1)^{2s+3B+L}, \tag{2.25}$$

where s is the spin and B and L are the baryon and lepton quantum numbers, respectively. SM particles are assigned $R = 1$ and their supersymmetric partners are assigned $R = -1$. A consequence of imposing R-parity conservation is that supersymmetric particles are always produced in pairs. Furthermore, there is always an odd number of supersymmetric particles in the decay of a SUSY particle and the lightest supersymmetric particle (LSP) is stable. Explicit mass terms are added to break SUSY and account for mass differences between SM particles and their supersymmetric partners. This breaking can be 'soft', i.e. happen such that quadratic divergences to m_h^2 are not reintroduced. The terms that need to be introduced into the Lagrangian for this soft SUSY breaking to occur are mass terms for gauginos, sfermions and Higgs bosons, bilinear terms for the Higgs bosons as well as trilinear couplings between the Higgs bosons and sfermions.
In addition to the 19 free parameters of the SM, the MSSM in this form introduces more than 100 free parameters.

2.3.2. Two-Higgs-doublet models

General two-Higgs-doublet models (2HDMs) [55] contain two Higgs doublets, one more than the SM, with opposite hypercharge. Requiring that up- and down-type quarks and charged leptons couple to only one of the doublets H_1 or H_2 suppresses flavor changing neutral currents which may otherwise occur, but are not observed. The two doublets allow different combinations of which fermions couple to which doublet. This is summarized in table 2.4. The Higgs sector of the MSSM is a type II 2HDM and discussed in some detail below.

[2]For the remainder of this thesis, charged Higgs bosons are denoted by H^+ and the charge conjugate is always implied.

2.3.3. The Higgs Sector of the MSSM

The Higgs sector of the MSSM [57–61] contains two Higgs doublets:

$$H_1 = \begin{pmatrix} H_1^0 \\ H_1^- \end{pmatrix} \quad \text{and} \quad H_2 = \begin{pmatrix} H_2^+ \\ H_2^0 \end{pmatrix} \tag{2.26}$$

with opposite hypercharge, i.e. $Y_{H_1} = -1$ and $Y_{H_2} = +1$. The vacuum expectation values of the neutral fields are given by

$$\langle H_1^0 \rangle = \frac{v_1}{\sqrt{2}} \quad \text{and} \quad \langle H_2^0 \rangle = \frac{v_2}{\sqrt{2}} \tag{2.27}$$

where v_1 and v_2 are the vacuum expectation values of the two doublets and $(v_1+v_2)^2 = v^2$ with $v \approx 246\,\text{GeV}$. The ratio of these defines the parameter $\tan\beta$:

$$\tan\beta = \frac{v_2}{v_1}. \tag{2.28}$$

Developing the Higgs fields around the vacuum into imaginary and real parts leads to the physical fields and the Higgs bosons:

$$H_1 = (H_1^0, H_1^-) = \frac{1}{\sqrt{2}}(v_1 + H_1^0 + iP_1^0, H_1^-) \tag{2.29}$$

$$H_2 = (H_2^+, H_2^0) = \frac{1}{\sqrt{2}}(H_2^+, v_2 + H_2^0 + iP_2) \tag{2.30}$$

Here, the real parts correspond to the CP-even Higgs bosons while the imaginary parts correspond to the CP-odd Higgs boson and Goldstone bosons.
The relations between the physical neutral CP-even Higgs bosons and the neutral parts of the Higgs doublets are given by

$$\begin{pmatrix} H \\ h \end{pmatrix} = \begin{pmatrix} \cos\alpha & \sin\alpha \\ -\sin\alpha & \cos\alpha \end{pmatrix} \begin{pmatrix} H_1^0 \\ H_2^0 \end{pmatrix} \tag{2.31}$$

The mixing angle α is given by

$$\alpha = \frac{1}{2}\arctan\left(\tan 2\beta \frac{m_A^2 + m_Z^2}{m_A^2 - m_Z^2}\right) \tag{2.32}$$

at lowest order perturbation theory and $-\pi/2 \leq \alpha \leq 0$.
The fields of the CP-odd Higgs boson and the neutral Goldstone bosons are given by

$$\begin{pmatrix} G^0 \\ A \end{pmatrix} = \begin{pmatrix} \cos\beta & \sin\beta \\ -\sin\beta & \cos\beta \end{pmatrix} \begin{pmatrix} P_1^0 \\ P_2^0 \end{pmatrix}. \tag{2.33}$$

Analogously, one obtains

$$\begin{pmatrix} G^\pm \\ H^\pm \end{pmatrix} = \begin{pmatrix} \cos\beta & \sin\beta \\ -\sin\beta & \cos\beta \end{pmatrix} \begin{pmatrix} H_1^\pm \\ H_2^\pm \end{pmatrix}, \tag{2.34}$$

where the charged Goldstone bosons $G^{\pm}$ are massless and the masses of the charged Higgs bosons are given by

$$m_{H^+}^2 = m_A^2 + m_W^2 \tag{2.35}$$

at lowest order perturbation theory. The masses of the CP-even Higgs bosons, h and H are given by

$$m_{h,H}^2 = \frac{1}{2}\Big(m_A^2 + m_Z^2 \mp \sqrt{(m_A^2 + m_Z^2)^2 - 4m_A^2 m_Z^2 \cos^2(2\beta)}\Big) \tag{2.36}$$

Only 2 parameters are free at tree level. These can be taken to be $\tan\beta$ and m_{H^+}. The hierarchy and constraints imposed on the Higgs boson masses at tree level are

- $m_H > \max(m_A, m_Z)$
- $m_{H^+} > m_W$
- $m_h \leq \min(\mathrm{m_A}, \mathrm{m_Z}) \cdot |\cos 2\beta| \leq m_Z$

At higher order perturbation theory, however, these constraints do not hold necessarily. The mass of the h, e.g., is then increased by radiative corrections to $> 100\,\mathrm{GeV}$.
The couplings of the charged Higgs bosons to fermions are given by

$$g_{H^+\bar{u}d} = \frac{-i}{\sqrt{2}v} V_{ud}^* (m_d \tan\beta(1+\gamma_5) + m_u \cot\beta(1-\gamma_5)) \tag{2.37}$$

$$g_{H^-\bar{d}u} = \frac{-i}{\sqrt{2}v} V_{ud} (m_d \tan\beta(1-\gamma_5) + m_u \cot\beta(1+\gamma_5)) \tag{2.38}$$

$$g_{H^+\tau^-\bar{\nu}_\tau} = \frac{-i}{\sqrt{2}v} (m_\tau \tan\beta(1+\gamma_5)) \tag{2.39}$$

$$g_{H^-\tau^+\nu_\tau} = \frac{-i}{\sqrt{2}v} (m_\tau \tan\beta(1-\gamma_5)) \tag{2.40}$$

with the CKM matrix element V_{ud}, which is present in the case of quarks. For $\tan\beta > 1$, the couplings of charged Higgs bosons to fermions with down-type isospin are enhanced. The full scalar potential is given by

$$\begin{aligned} V_H =& (|\mu|^2 + m_{H_1}^2)|H_1|^2 + (|\mu|^2 + m_{H_2}^2)|H_2|^2 - \mu B \epsilon_{ij}(H_1^i H_2^j + h.c.) \\ &+ \frac{g_1^2 + g_2^2}{8}(|H_1|^2 - |H_2|^2)^2 + \frac{g_2^2}{2}|H_1^\dagger H_2|^2 \end{aligned} \tag{2.41}$$

Here, B is the soft SUSY-breaking bilinear Higgs term and μ is the higgsino mass parameter.

Benchmark Scenarios for MSSM Higgs Boson Searches

Given the large number of free parameters in the MSSM, a scan of the whole parameter space is too complex. Thus different benchmark scenarios have been defined, where some parameters, apart from $\tan\beta$ and m_{H^+}, are fixed to certain values. These different scenarios show the phenomenology of different regions of the parameter space. Model-independent limits on e.g. cross sections can then be interpreted in the $\tan\beta - m_{H^+}$

plane in a specific scenario.
The benchmark scenarios presented here have been defined specifically for MSSM Higgs boson searches at hadron colliders and are explained in full detail in ref. [62] and references therein.
The following parameters are used in the scenarios:

- m_{top}: mass of the top quark, always set to 173.2 GeV
- $M_{SUSY} = m_{\tilde{t}_L} = m_{\tilde{t}_R} = m_{\tilde{b}_L} = m_{\tilde{b}_R}$: mass of the left- and right-handed top and bottom squarks, i.e. stop and sbottom
- μ: higgsino mass parameter
- M_2: $SU(2)$ gaugino mass parameter
- X_t^{OS}: $X_t = A_t - \mu/\tan\beta$, where A_t is the trilinear Higgs-top squark coupling and OS refers to evaluation of X_t in a feynman-diagrammatical approach in the on-shell scheme
- A_b: trilinear Higgs-bottom squark coupling
- A_t: trilinear Higgs-top squark coupling
- A_τ: trilinear Higgs-τ slepton coupling
- $m_{\tilde{g}}$: gluino mass
- $M_{\tilde{l}_3}$: third generation slepton masses

The values chosen for these parameters in the specific scenarios are summarized in table 2.5. The trilinear couplings with first and second generation fermions have a negligible impact and are thus set to 0.

The $m_{\mathrm{h}}^{\mathrm{max}}$ scenario The $m_{\mathrm{h}}^{\mathrm{max}}$ scenario was originally defined for Higgs boson searches at LEP and has been modified since. The values of the parameters specified above were chosen to give conservative bounds on $\tan\beta$. The h mass in this scenario is maximized, such that $m_h > 130\,\mathrm{GeV}$ for $\tan\beta > 10$. Thus the observed Higgs boson can only be interpreted as the h in a very small parameter space with low values of $\tan\beta$.

The $m_{\mathrm{h}}^{\mathrm{mod+}}$ and $m_{\mathrm{h}}^{\mathrm{mod-}}$ scenarios The $m_{\mathrm{h}}^{\mathrm{mod+}}$ and $m_{\mathrm{h}}^{\mathrm{mod-}}$ scenarios were defined after the discovery of a Higgs boson to allow this boson to be interpreted as the h in a wider parameter space compared to the $m_{\mathrm{h}}^{\mathrm{max}}$ scenario. It is not required that m_h be maximal in this scenario. This is done by reducing the amount of mixing in the top squark sector, i.e. by reducing the ratio of $|X_t/M_{SUSY}|$ and thus reducing radiative corrections to m_h. This can be done for positive and negative values of X_t/M_{SUSY}, hence the $m_{\mathrm{h}}^{\mathrm{mod+}}$ and $m_{\mathrm{h}}^{\mathrm{mod-}}$ scenarios.

Scenario	M_{SUSY} [GeV]	μ [GeV]	M_2 [GeV]	X_t^{OS}	A_b	$m_{\tilde{g}}$ [GeV]	$M_{\tilde{l}_3}$ [GeV]
$m_{\text{h}}^{\text{max}}$	1000	200	200	$2M_{\text{SUSY}}$	$= A_\tau = A_t$	1500	1000
$m_{\text{h}}^{\text{mod+}}$	1000	200	200	$1.5M_{\text{SUSY}}$	$= A_\tau = A_t$	1500	1000
$m_{\text{h}}^{\text{mod-}}$	1000	200	200	$-1.9M_{\text{SUSY}}$	$= A_\tau = A_t$	1500	1000
light stop	500	350	350	$2.0M_{\text{SUSY}}$	$= A_\tau = A_t$	1500	1000
light stau	1000	500	200	$1.6M_{\text{SUSY}}$	$= A_t$, $A_\tau = 0$	1500	245
τ-phobic	1500	2000	200	$2.45M_{\text{SUSY}}$	$= A_\tau = A_t$	1500	500

Table 2.5. Values of different parameters defining MSSM benchmark scenarios [62].

The light stop scenario Relatively large radiative contributions are needed from the top-stop sector to account for the mass of the discovered Higgs boson. This can be achieved with a large value of $|X_t|$ and rather low value of M_{SUSY}, which results in a relatively light stop quark. The rate of Higgs boson production by gluon-gluon fusion is decreased in this scenario compared to the SM expectation.

The light stau scenario The currently measured value of the Higgs boson coupling to photons is somewhat larger than expected in the SM as shown in figure 2.3. This can be achieved in the theory with light staus and large mixing in the stau sector, which occurs automatically for large values of $\tan\beta$ such that the mixing parameter $X_\tau = A_\tau - \mu \tan\beta$ is large, too.

The tauphobic scenario In the tauphobic scenario, the couplings between Higgs bosons and down-type fermions are modified compared to the SM if the values of A_τ, A_t, A_b, μ and $\tan\beta$ are chosen to be large. In this scenario, staus are rather light, similar to the light stau scenario. Decays of the heavy CP-even Higgs boson into light stau leptons are relevant for large values of $\tan\beta$ and m_A. The decay of the light CP-even Higgs boson to τ lepton pairs is suppressed compared to the SM over a wide parameter region.

2.3.4. Charged Higgs Boson Production Processes

Charged Higgs boson production in type II 2HDMs, where one Higgs doublet generates the masses of up-type quarks and the other one of down-type quarks and charged leptons, is considered only. At the LHC, charged Higgs bosons are produced predominantly in top quark decays or in association with a top quark, depending on the mass of the H^+, m_{H^+}.
Low-mass charged Higgs bosons, i.e. with $m_{H^+} < m_{\text{top}}$, are dominantly produced in top quark decays as shown in figure 2.5. Top quarks are predominantly produced in

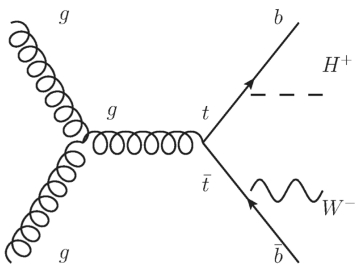

Figure 2.5. Leading-order Feynman diagram for the dominant production mode of low-mass charged Higgs bosons at the LHC

pairs at the LHC; thus the production cross section of H^+ from single top decays is small compared to that from $t\bar{t}$ production and neglected. The cross section for $t\bar{t}$ production with at least one lepton in the final state (90.6 pb at $\sqrt{s} = 7$ TeV and 137.3 pb at $\sqrt{s} = 8$ TeV), relevant for the searches presented here, is significantly larger than that of all single top quark processes with at least one lepton in the final state (38.1 pb at

$\sqrt{s} = 7\,\text{TeV}$ and 52.6 pb at $\sqrt{s} = 8\,\text{TeV}$).
Assuming branching ratios $B(t \to H^+ b) = 5\%$ (0.9%) for the 2011 (2012) data results in cross sections for $t\bar{t} \to H^+ bWb$ of 15.8 pb (4.5 pb) for $B(H^+ \to \tau\nu) = 1$.
For high-mass charged Higgs bosons, i.e. H^+ with masses greater than the top quark mass, the main production mechanism can be approximated in two different ways. The H^+ is produced in association with a top quark and possibly an additional b-quark. The two approximations are shown in figure 2.6. In contrast to the four-flavor

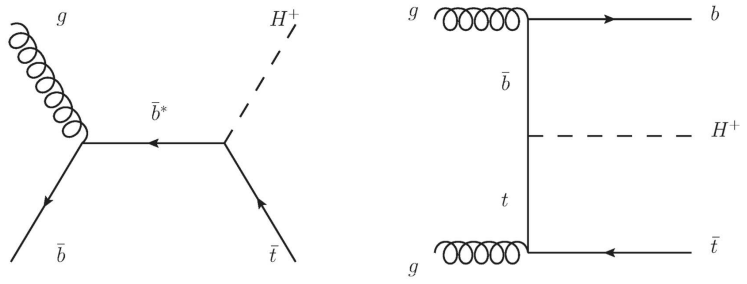

(a) 5FS high-mass H^+ production (b) 4FS high-mass H^+ production

Figure 2.6. Leading-order Feynman diagrams for the dominant production modes of high-mass charged Higgs bosons at the LHC in the (a) five-flavor and (b) four-flavor scheme.

scheme (4FS), the b-quark is considered as an active flavor inside the proton in the five-flavor scheme (5FS). The cross sections calculated in the 4FS and 5FS to all orders in perturbation theory agree. However, any finite order summation yields different results in the 4FS and 5FS due to different ordering of the perturbation expansion. Especially at leading order, the predictions between 5FS and 4FS can vary significantly. To reduce dependence on the chosen approximation and obtain a reliable prediction of the true cross section, cross sections calculated in the 4FS and 5FS approximations are combined and matched according to references [63, 64]. The 4FS and 5FS approaches provide the unique description of the cross section in the asymptotic limits $m_{H^+}/m_b \to 1$ and $m_{H^+}/m_b \to \infty$, respectively. The difference between the two schemes is logarithmic and hence the dependence of the relative weight is controlled by a logarithmic term. The matched cross section is given by

$$\sigma_{\text{matched}} = \frac{\sigma_{4FS} + w\sigma_{5FS}}{1 + w}, \tag{2.42}$$

where the weight w is defined as

$$w = \log \frac{m_{H^+}}{m_b} - 2. \tag{2.43}$$

Here, m_b is the mass of the b-quark. The theoretical uncertainties are combined according to

$$\Delta\sigma_{\text{matched}} = \frac{\Delta\sigma_{\text{4FS}} + w\Delta\sigma_{\text{5FS}}}{1 + w} \tag{2.44}$$

Cross sections matched between the 4FS and 5FS are shown in figure 2.7 for $\tan\beta = 30$ with uncertainties in the 4FS and 5FS as well as combined uncertainties. The cross

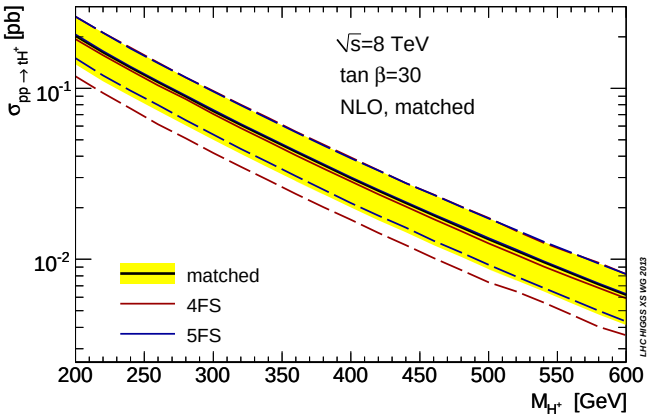

Figure 2.7. Production cross section for high-mass charged Higgs bosons as a function of m_{H^+} for $\tan\beta = 30$ at a center-of-mass energy of $\sqrt{s} = 8\,\text{TeV}$. Values are shown for the 5FS, 4FS and matched according to ref. [63]. The red and blue dashed lines indicate the systematic uncertainties of the 4FS and 5FS, respectively, and the yellow band shows the uncertainty on the matched cross sections [33].

section calculated in the 4FS and 5FS agree mostly within their uncertainties, with discrepancies of at most 10%. The combined uncertainty is in the range of $20 - 30\%$. Cross section predictions for $\sqrt{s} = 14\,\text{TeV}$ for the 4FS, 5FS and the matched prediction are shown in figure 2.8 for $m_{H^+} = 200\,\text{GeV}$ and $m_{H^+} = 600\,\text{GeV}$ as functions of $\tan\beta$. The minimum around $\tan\beta = 8$ is present for $\sqrt{s} = 7\,\text{TeV}$ and $8\,\text{TeV}$ as well.

To convert these general type II 2HDM cross sections into model-specific ones, SUSY-

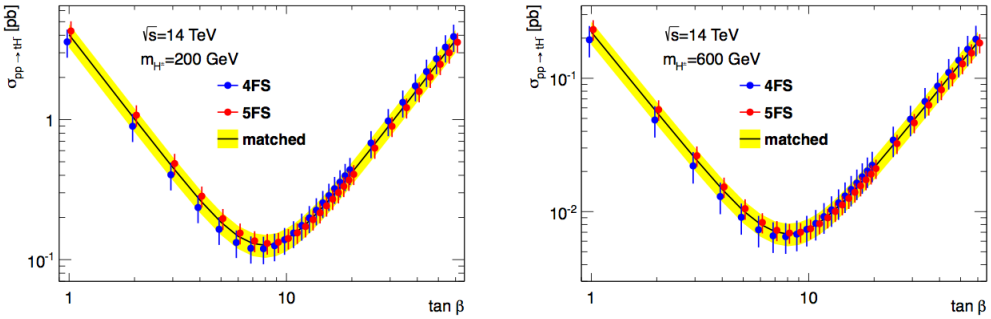

Figure 2.8. Cross sections for $pp \to tH^- + X$ as functions of $\tan\beta$ for $m_{H^+} = 200\,\text{GeV}$ (left) and $m_{H^+} = 600\,\text{GeV}$ (right) at $\sqrt{s} = 14\,\text{TeV}$ [64].

QCD corrections, calculated at next-to-leading order, have to be taken into account. These so-called Δb-corrections depend on $\tan\beta$ and vary from scenario to scenario but are independent of m_{H^+} [65].

The mass range with $m_{H^+} \approx m_{\text{top}}$, $160\,\text{GeV} < m_{\text{top}} < 180\,\text{GeV}$, is not considered in the analyses presented here. In this transition region, low-mass H^+ production from top quark pair decays and high-mass H^+ production in association with a top quark interfere. Neither a calculation at NLO nor an event generator taking this correctly into account is currently available.

2.3.5. Charged Higgs Boson Decays

The decay $H^+ \to \tau\nu$ considered in this thesis is relevant for a large mass range of m_{H^+} in the MSSM. The partial decay width for $H^+ \to \ell^+\nu$, where ℓ denotes any charged lepton with mass m_ℓ, is given by

$$\Gamma(H^+ \to \ell^+\nu) = \frac{G_F m_{H^+}}{4\sqrt{2}\pi} m_\ell^2 \tan^2\beta \left(1 - \frac{m_\ell^2}{m_{H^+}^2}\right)^3 \tag{2.45}$$

The branching ratios $B(H^+ \to \tau\nu)$ as functions of $\tan\beta$ are shown in figure 2.9 for different values of m_{H^+} in all scenarios described before. While the decay $Hp \to \tau\nu$ is dominant for low-mass H^+, the branching ratio $B(H^+ \to \tau\nu)$ decreases for higher values of m_{H^+}.

All branching ratios are shown in figure 2.10 for $\tan\beta = 50$ over a wide range of m_{H^+}

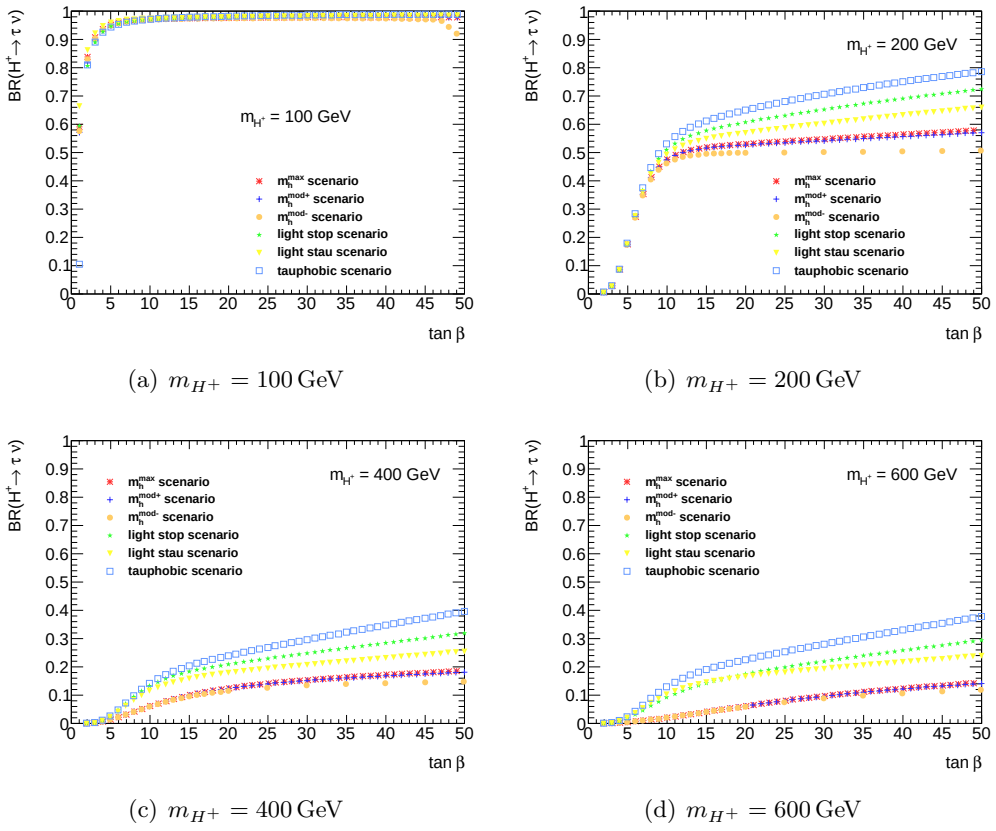

(a) $m_{H^+} = 100\,\text{GeV}$ (b) $m_{H^+} = 200\,\text{GeV}$

(c) $m_{H^+} = 400\,\text{GeV}$ (d) $m_{H^+} = 600\,\text{GeV}$

Figure 2.9. Branching ratios $B(H^+ \to \tau\nu)$ as functions of $\tan\beta$ in the m_h^max, $m_\text{h}^\text{mod+}$, $m_\text{h}^\text{mod-}$, light stau, light stop and tauphobic scenarios for (a) $m_{H^+} = 100\,\text{GeV}$, (b) $m_{H^+} = 200\,\text{GeV}$, (c) $m_{H^+} = 400\,\text{GeV}$ and (d) $m_{H^+} = 600\,\text{GeV}$ [66].

for the 6 different scenarios.

For low-mass charged Higgs bosons, the decay $H^+ \to \tau\nu$ is dominant for $\tan\beta > 2$ and still important for $1 < \tan\beta < 2$. For high-mass H^+, this decay is still significant, especially for large values of $\tan\beta$, but the decay $H^+ \to tb$ is dominant. The different

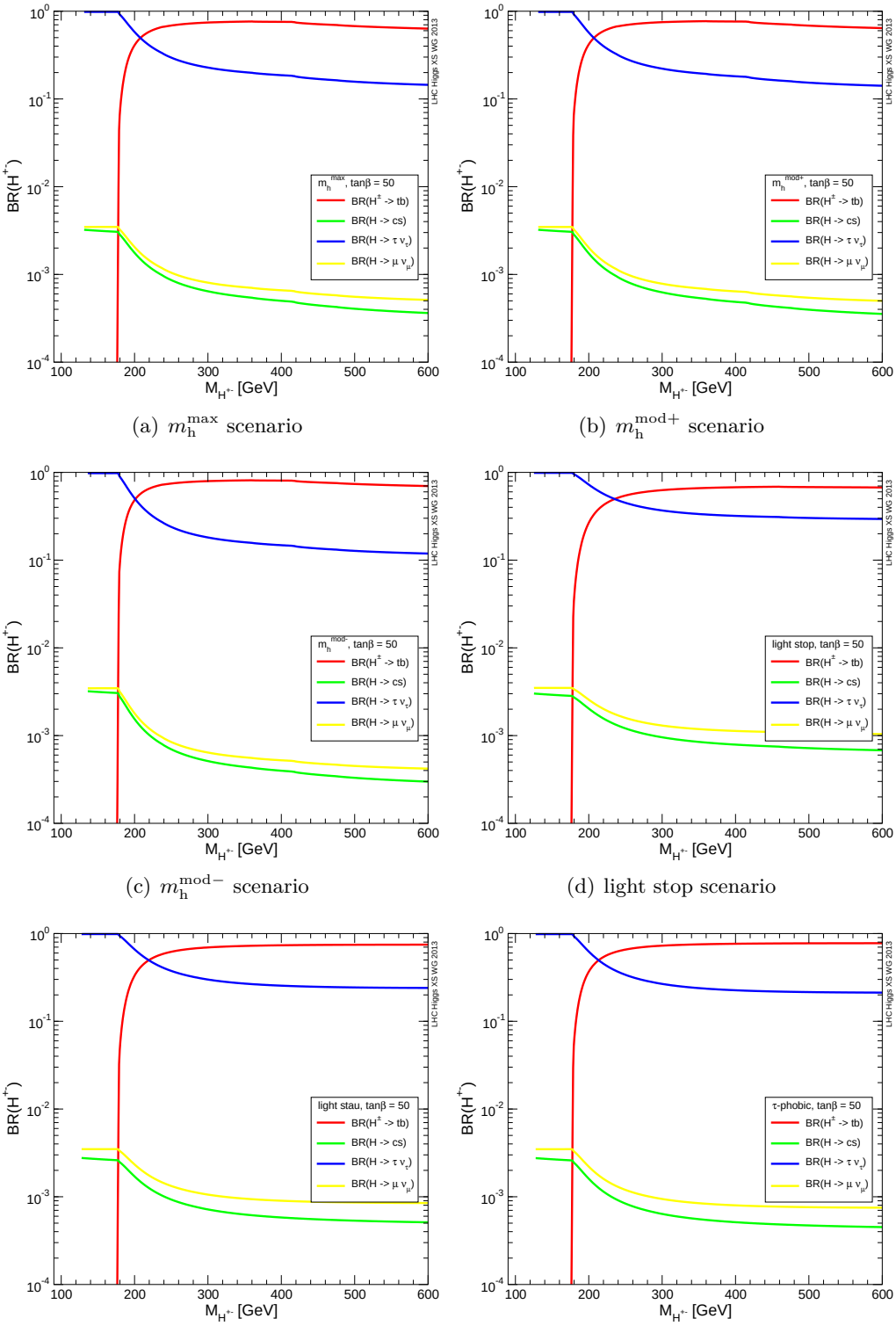

(a) $m_{\mathrm{h}}^{\mathrm{max}}$ scenario

(b) $m_{\mathrm{h}}^{\mathrm{mod+}}$ scenario

(c) $m_{\mathrm{h}}^{\mathrm{mod-}}$ scenario

(d) light stop scenario

(e) light stau scenario

(f) tauphobic scenario

Figure 2.10. Charged Higgs boson branching ratios in the (a) $m_{\mathrm{h}}^{\mathrm{max}}$, (b) $m_{\mathrm{h}}^{\mathrm{mod+}}$, (c) $m_{\mathrm{h}}^{\mathrm{mod-}}$, (d) light stop, (e) light stau and (f) tauphobic benchmark scenarios as defined in reference [62]. Values are shown for $\tan\beta = 50$ [33].

branching ratios are similar in all scenarios.
Different final states are possible depending on the decay of the τ lepton and the W boson from the additional top quark decay. In the analyses presented in this thesis, only final states with a hadronically decaying τ lepton as well as a hadronically decaying W boson are considered ('τ+jets'). In SM $t\bar{t}$ decays, these constitute the major fraction of possible final states with about 44%.

2.3.6. Experimental Constraints

Charged Higgs bosons have been searched for at different previous collider experiments, including the Tevatron experiments CDF and D0 at Fermilab and ALEPH, DELPHI, L3 and OPAL at the Large Electron Positron Collider (LEP) [67] at CERN.
The two collaborations CDF and D0 at Tevatron, a $p\bar{p}$ collider which was operated from 1983 until 2011 at a center-of-mass energy of up to $\sqrt{s} = 1.96\,\text{TeV}$, searched for H^+ in a mass range below the top-quark mass. Decays via $H^+ \to \tau\nu$ and $H^+ \to c\bar{s}$ were considered. Limits on the branching ratio $\text{B}(t \to H^+b)$ and their interpretation in the m_h^max scenario as defined in reference [68] from the D0 collaboration are shown in figure 2.11 [69]. The limits on the branching ratio range between 15% and 20% over a mass range $90\,\text{GeV} \leq m_{H^+} \leq 160\,\text{GeV}$. Interpreted in the m_h^max scenario as defined

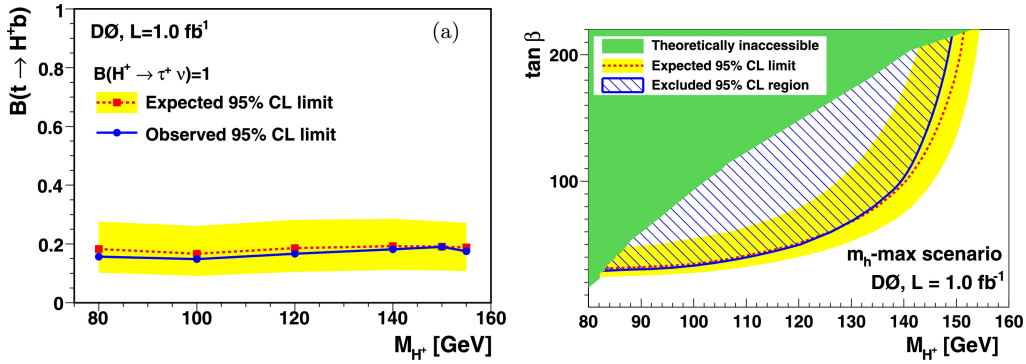

(a) (b)

Figure 2.11. (a) Limits on the branching ratio $\text{B}(t \to H^+b)$ as a function of m_{H^+} and (b) their interpretation in the m_h^max scenario as defined in reference [68] as a function of $\tan\beta$ vs. m_{H^+} [69].

in ref. [68], values of $\tan\beta > 30$ (50) are excluded for $m_{H^+} = 100\,\text{GeV}$ (120 GeV). For higher values of m_{H^+}, only very large $\tan\beta$ values are excluded. No values are excluded for $m_{H^+} \geq 150\,\text{GeV}$.
At LEP, charged Higgs boson production would have been through exchange of a Z/γ^* boson. Thus limits are set not on the branching ratio $\text{B}(t \to H^+b)$ but on the production cross-section σ_{H^+} in a mass range $40\,\text{GeV} < m_{H^+} < 100\,\text{GeV}$. At tree level, the production cross section only depends on m_{H^+}. The combined limits in a type II 2HDM from the LEP experiments are shown in figure 2.12. They are based on a total integrated luminosity of $2.6\,\text{fb}^{-1}$ and only results in the decay channel $H^+ \to \tau\nu$ are shown here. Assuming $B(H^+ \to \tau\nu) = 1$, the combined observed (expected) limit on m_{H^+} is 94

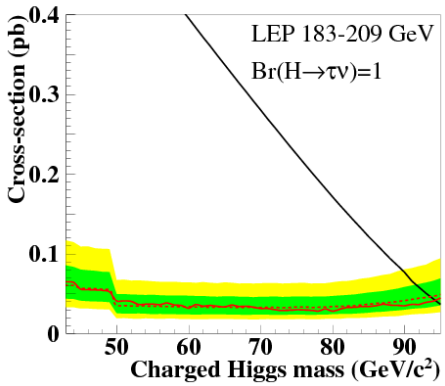

Figure 2.12. Limits on the cross-section for H^+ production in a type II 2HDM depending on the charged Higgs boson mass [70]. The solid (dashed) red line shows the observed (expected) limits. The black line indicates the theoretical H^+ production cross-section at tree-level. The intersection of either red line with the black line shows the observed or expected lower limits at 95%CL on m_{H^+}, respectively.

(93.5) GeV. Without constraints on the decay of the H^+, observed (expected) limits are set at 80 (79.5) GeV. The only additional channel considered by the LEP experiments taken into account for the final results is $H^+ \to c\bar{s}$.

3 The ATLAS Experiment at the LHC

3.1. The Large Hadron Collider

The Large Hadron Collider (LHC) [71] at CERN, the European Organization for Nuclear Research, near Geneva, Switzerland, is the world's largest and most powerful particle accelerator and collider. It is built in a tunnel with a circumference of about 27 km situated between the Jura mountains and Lake Geneva. The tunnel was originally designed and built for the LEP collider, which was operated from 1989 to 2000 at center-of-mass energies of 90 GeV to 209 GeV. Proton or heavy ion (Pb) beams are brought to collisions at 4 interaction points (IPs) where the main experiments are located: ALICE [72], designed to study heavy ion physics, ATLAS [73] and CMS [74], multi-purpose particle detectors and LHCb [75], specialized in studying B meson physics.
The LHC is designed to be operated at a center-of-mass energy of 14 TeV and a peak luminosity of $10^{34}\,\mathrm{cm}^{-2}\mathrm{s}^{-1}$. Until early 2013, when data taking was stopped for upgrades of both the LHC and the experiments, the machine was operated at center-of-mass energies of up to 8 TeV. After a break of more than 2 years, collisions at a center-of-mass energy of 13 TeV started in May 2015.
Since the LHC is a particle-particle collider, two independent rings within the same tunnel are needed for the two beams circulating in opposite directions. Protons are bundled in bunches and passed through various pre-accelerators, shown schematically in figure 3.1. They reach an energy of 450 GeV per beam in the SPS and are injected into the LHC, where they are accelerated to the final energy and brought to collision. With a nominal bunch spacing of 25 ns, up to 2808 bunches are used to fill the LHC. Each bunch consists of about 10^{11} protons. Dipole, quadrupole and higher order superconducting magnets, totaling to about 9600, with magnetic fields exceeding 8 T at temperatures below 2 K are used to keep the beams in their orbit as well as focus and stabilize them. Radio frequency cavities are used for acceleration. Two independent systems are installed to extract the beams from the ring and dump them when the instantaneous luminosity gets too low or in case of emergencies.

3.2. The ATLAS Detector

The ATLAS (A Toroidal LHC ApparatuS) detector [73] is one of the four big experiments at the LHC. The detector measures about 25 m in diameter and 44 m in length. Like CMS (Compact Muon Solenoid) it is designed as a multi-purpose detector. The physics program ranges from precise measurements and tests of the Standard Model to searches

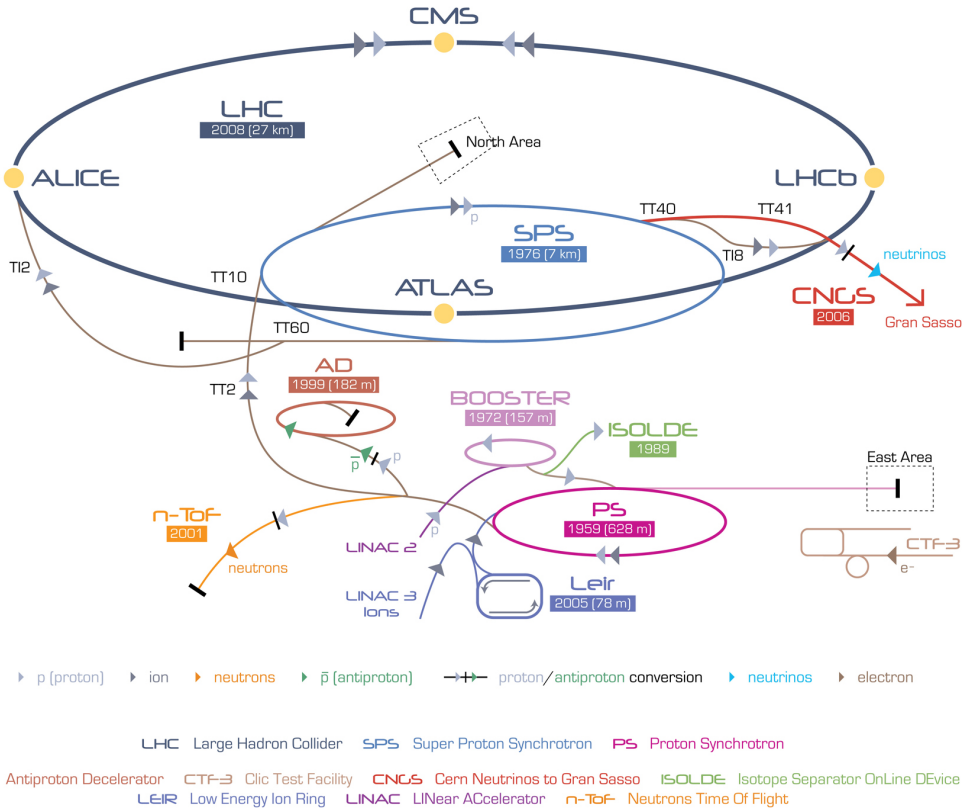

Figure 3.1. Schematic view of the LHC with the 4 experiments ALICE, ATLAS, CMS and LHCb and old accelerators now used as pre-accelerators as well as various other experiments at CERN [76].

for new physics. The high interaction rate and large particle flux necessitate radiation-hard elements with fast readout while the accuracy needed for physics measurements requires very high resolution and efficiencies in the various sub-detectors. The sub-detectors, which make up the barrel and end-caps and consist of a tracking detector, calorimeters and a muon spectrometer all designed to meet these requirements, and the magnet system are shown in figure 3.2 and described in some detail below.

Coordinate System

ATLAS uses a right-handed coordinate system where the beam line is defined as the z-axis. The positive x-axis is defined as pointing from the nominal interaction point to the center of the ring and the positive y-axis as pointing upwards. The azimuthal angle ϕ is measured around the z-axis and the polar angle θ is measured from the beam. The pseudorapidity is given by $\eta = -\ln\tan(\theta/2)$. All transverse variables are measured in the $x-y$-plane. Angular three-dimensional separation is measured in $\Delta R = \sqrt{\Delta\phi^2 + \Delta\eta^2}$.

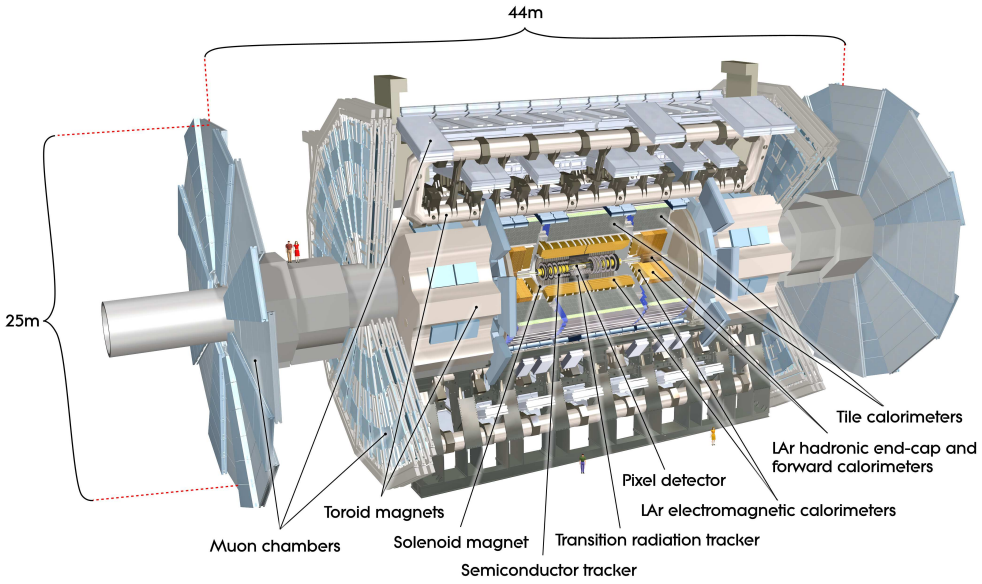

Figure 3.2. Schematic cut-away view of the ATLAS detector showing the different layers of the inner detector, the calorimeters, toroid magnets and muon spectrometer [73].

3.2.1. The Inner Detector

The inner detector (ID) is the innermost part of ATLAS and measures about 6 m in length and 2 m in diameter. It consists of high-resolution pixel and silicon microstrip (SCT) detectors and a transition radiation tracker (TRT). A solenoid surrounding the ID produces a 2 T magnetic field. A detailed view of the different ID parts and layers and their distances to the beam line is shown in figure 3.3. The design resolution for measurements of charged-particle momenta in the ID is $\sigma_{p_T}/p_{\mathrm{T}} = 0.05\%\, p_{\mathrm{T}} \oplus 1\%$.
The pixel and SCT detectors cover a range up to $|\eta| < 2.5$. They are arranged cylindrically around the beam axis in the central barrel part of the detector and perpendicular to the beam axis in the forward regions. Each of the pixel layers is segmented in R, ϕ and z. The cells have a minimum size of $R - \phi \times z$ of $50 \times 400\,\mu\mathrm{m}^2$. Typically 3 pixel layers are crossed by a track and 4 layers in the SCT. In the barrel region, one set of strips in each layer is parallel to the beam axis, while the other one is placed at a small stereo angle. A similar concept is realized for the forward disks where one set of strips is running radially outwards and the other set at a small angle to it. Combined, pixel and SCT detectors allow very precise measurements of tracks and thus vertices. In the pixel detector, the intrinsic accuracy is $10\,\mu$m in the $R - \phi$-plane in the barrel and disks and $115\,\mu$m in the z-direction of the barrel (R in the end-caps). For the SCT it is $17\,\mu$m in the $R - \phi$-plane in the barrel and end-caps and $580\,\mu$m in the z-direction of the barrel (R in the end-caps).

The TRT covers a region up to $|\eta| < 2.0$. Straw tubes filled with a xenon-based gas mixture and with a diameter of 4 mm only segmented in half at about $\eta = 0$ are arranged cylindrically around the beam axis in the barrel part and radially on disks in the forward regions. The TRT thus only provides $R - \phi$ information. A track leaves typically 36 hits in the TRT. The large number of hits in the TRT and larger radii add

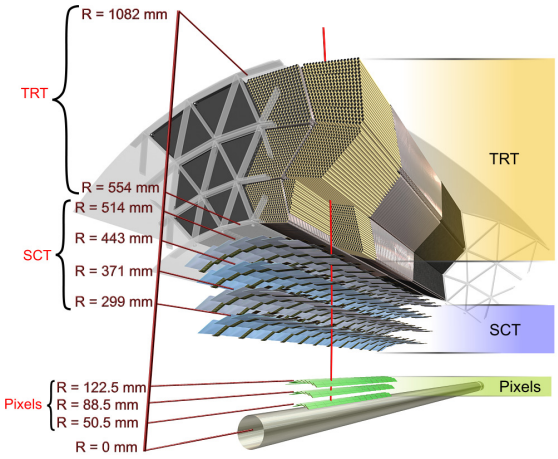

Figure 3.3. Detailed view of the differnt layers of the inner detector and their distances from the beam axis [73].

significantly to a precise measurement of transverse momenta of particles when combined with measurements from the pixel and SCT detectors. The intrinsic accuracy of the tubes is 130 μm per straw in the $R-\phi$-plane.

3.2.2. The Calorimeter System

Different sampling calorimeters are used in ATLAS. They are designed to fully contain electromagnetic and hadronic showers and thus limit punch-through to the muon system. An electromagnetic calorimeter with fine granularity provides high precision measurements of photons and electrons. A hadronic calorimeter with coarser granularity extending to larger pseudorapidities allows measurements of jet energy and missing transverse momentum due to nearly complete coverage of the solid angle. The different calorimeters are explained in some detail below and a sketch of them is shown in figure 3.4.

The Electromagnetic Calorimeter

The electromagnetic (EM) calorimeter consists of a barrel part, which is further divided into two identical half-barrels at $z = 0$, and two end-caps. The thickness of the barrel is > 22 radiation lengths (X_0) and $> 24\,X_0$ in the end-caps. The barrel covers a range $|\eta| < 1.475$. Each of the end-caps is divided into an outer and inner wheel. The outer wheels cover a range $1.375 < |\eta| < 2.5$ and the inner wheels extend further to $|\eta| < 3.2$. A design with accordion-shaped electrodes and lead absorber plates and liquid argon (LAr) as active material was chosen to provide full ϕ coverage. The region up to $|\eta| < 2.5$, i.e. the region that is also covered by the ID, is segmented into 3 layers with very high granularity. A coarser granularity and only 2 layers are chosen for the inner wheels of the end-caps. The design energy resolution of the EM calorimeter is $\sigma_E/E = 10\%/\sqrt{E} \oplus 0.7\%$. An additional active LAr layer, a so-called presampler

detector, is used in the region $|\eta| < 1.8$. It accounts for energy losses of electrons and photons before they reach the calorimeter system.

The Hadronic Calorimeters

A tile calorimeter is used outside the EM calorimeter. It is split up into a barrel, covering $|\eta| < 1.0$ and two extended barrels in the range $0.8 < |\eta| < 1.7$. Scintillating tiles are used as active material, hence the name, and steel plates are used as absorbers. It is segmented radially into 3 layers and azimuthally into 64 modules. The total thickness is 9.7 interaction lengths at $\eta = 0$.
For large pseudorapidities, a LAr calorimeter is used. Two wheels per end-cap cover a region up to $|\eta| < 3.2$. Each wheel is divided into 2 layers in depth and 32 radially arranged modules. Copper plates are used as absorbers. The design energy resolution of the hadronic calorimeters is $\sigma_E/E = 50\%/\sqrt{E} \oplus 3\%$ in the barrel and end-caps.

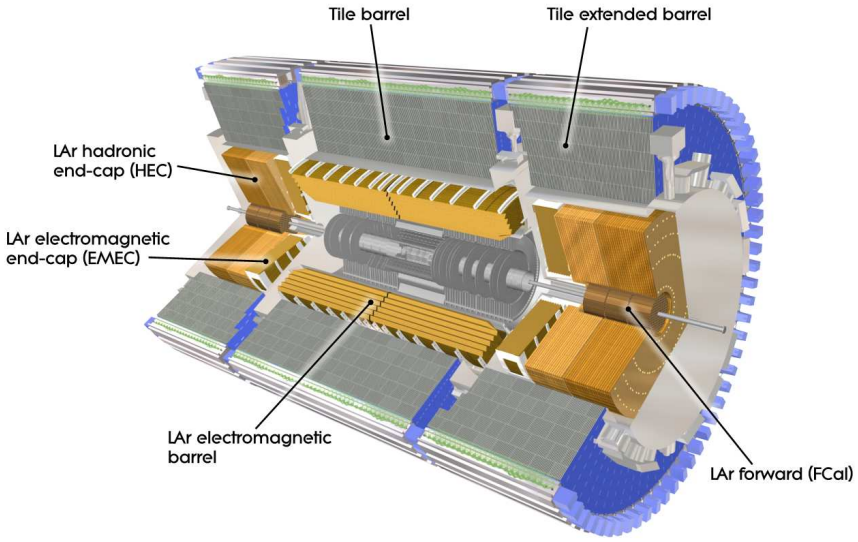

Figure 3.4. Schematic cut-away view of the different parts of the ATLAS calorimeter system [73].

The Forward Calorimeters

The forward calorimeters extend the coverage to $3.1 < |\eta| < 4.9$. They are segmented into 3 layers meeting different physics requirements. The first layer is optimized for electromagnetic measurements. It uses copper as absorber material. The outer two layers are optimized for hadronic interactions and tungsten is used as absorber. In all 3 modules, LAr is used as active material. The forward calorimeters have a design energy resolution of $\sigma_E/E = 100\%/\sqrt{E} \oplus 10\%$.

3.2.3. The Muon Spectrometer

Due to the low interaction rate and long lifetime of muons, the muon spectrometer (MS) is the outermost part of ATLAS. Three toroidal magnets with 8 coils each provide the magnetic field to bend the muon trajectories so their momenta can be measured. The barrel toroid provides a magnetic field of about 1.5 to 5.5 Tm and covers a range $0 < |\eta| < 1.4$. The two end-cap toroids, which are rotated by 22.5° with respect to the barrel, provide coverage in a range $1.6 < |\eta| < 2.7$ with a bending power of 1 to 7.5 Tm. An overview of the different parts of the muon spectrometer, which are described below, is shown in figure 3.5.
The muon spectrometer allows to measure muon momenta from a few GeV up to the TeV range. The MS is also designed to trigger on muons with dedicated trigger chambers. Like other sub-detectors in ATLAS, the MS consists of a barrel and end-caps. In the

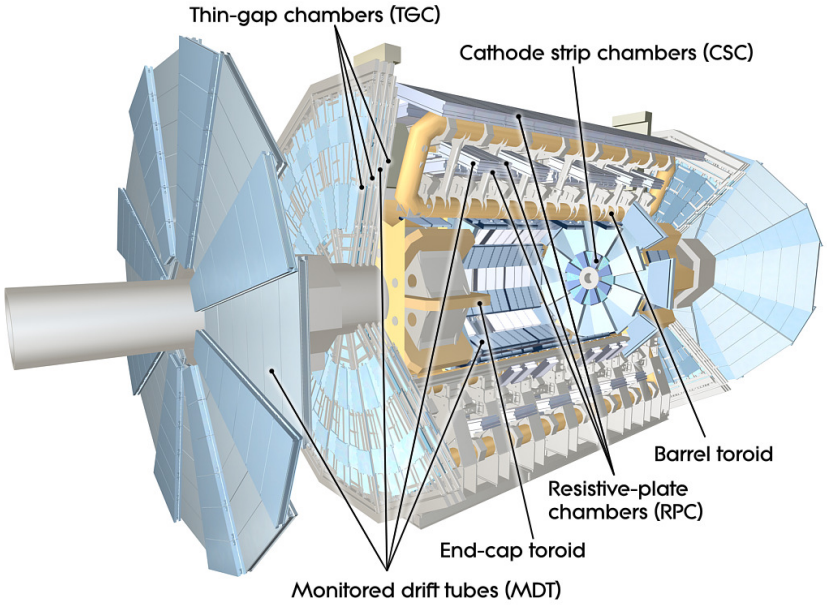

Figure 3.5. Schematic cut-away view of the muon spectrometer [73].

barrel, muon chambers are arranged cylindrically around the beam axis in 3 layers. Four separate wheels with modules form the end-caps. To provide access and space for supporting structure, some gaps are left in the muon spectrometer. Monitored Drift Tubes (MDTs), guaranteeing a robust and reliable operation, provide precision measurements of tracks up to $|\eta| < 2.7$. In the innermost layer of the end-caps, they are replaced by Cathode Strip Chambers (CSCs) in a region $2.0 < |\eta| < 2.7$. These can cope better with the higher particle rates in this region. An optical system monitoring the MDTs ensures the alignment of the chambers needed to achieve the desired momentum resolution. The design momentum resolution for a muon with a transverse momentum of 1 TeV is $\sigma_{p_T}/p_T = 10\%$.
Thin Gap Chambers (TGCs) and Resistive Plate Chambers (RPCs) are used to trigger on muons. RPCs cover a region $|\eta| < 1.05$ and TGCs extend this up to $|\eta| < 2.4$. Information on both η and ϕ is provided by the muon trigger chambers. Furthermore,

they are fast enough to provide reliable information on and tag beam-crossings.
A detailed sketch of the different chamber types of the muon system and which chambers

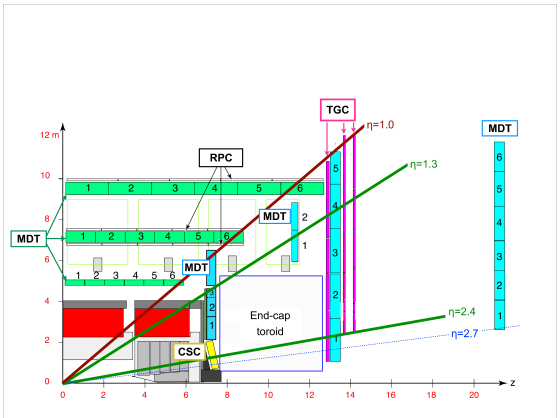

Figure 3.6. Sketch of the different chambers in the muon system [77].

a muon will traverse for different pseudorapidities is shown in figure 3.6.

3.2.4. ALFA and LUCID

Two detectors dedicated to luminosity determination are installed at ±17 m and ±240 m from the nominal interaction point in ATLAS. LUCID (LUminosity measurement using Cerenkov Integrating Detector) measures inelastic proton-proton scattering in the forward direction to determine the relative luminosity and beam conditions online. ALFA (Absolute Luminosity For ATLAS) consists of scintillating-fibre trackers inside of Roman pots. It determines the absolute luminosity by measuring elastic scattering at very small angles.

3.2.5. The Trigger System

The ATLAS trigger system consists of 3 levels: level 1 (L1), level 2 (L2) and event filter (EF). It is needed to reduce the amount of data from the original rate of the proton-proton interactions to something manageable and storable. At each level, trigger decisions from the previous level are refined and possibly new criteria are added. During data taking in 2012, the event rate is reduced to 75 kHz at L1 and less than 1 kHz after EF.
The L1 trigger is hardware-based. Objects like muons, electrons, jets, hadronically decaying τ leptons or photons are reconstructed using coarse detector information. The L1 trigger can also recognize and accept events with large total or missing transverse momentum. The selection is based on calorimeter information except in the case of muons, for which dedicated trigger chambers in the MS are used. One or more regions-of-interest (RoIs) are defined and information about interesting features and criteria passed are saved and handed to the next level. The latency, i.e. the time passing between a bunch crossing and a trigger decision, is about 2 μs at L1. At L2, complete detector

information is used at full precision within the RoIs defined at L1. The latency is increased to about 40 μs on average but can be up to 100 μs for very high instantaneous luminosities. The L2 and EF triggers are software-based. The selections applied at EF are very close to the final offline selections applied for analyses. The latency at EF is approximately 1 s.

4 Data and Simulation Samples

4.1. Data

4.1.1. Data Taking

In early 2013, the first data taking period of the LHC was completed successfully after about 3 years of data taking at center-of-mass energies ranging from $\sqrt{s} = 900\,\text{GeV}$ to $\sqrt{s} = 8\,\text{TeV}$ for proton-proton (pp) collisions.

The total amount of data from proton-proton collisions delivered by the LHC and

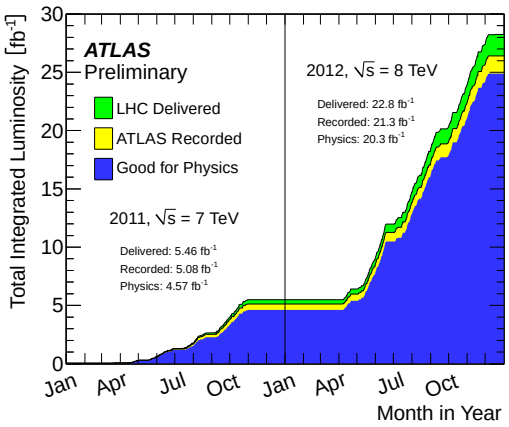

Figure 4.1. Integrated luminosity from proton-proton collisions during 2011 and 2012. The total integrated luminosity delivered by the LHC is shown in green, the amount of data recorded by ATLAS is shown in yellow and the subset that is used for physics analyses is shown in blue [78].

recorded by the ATLAS experiment in 2011 and 2012 at $\sqrt{s} = 7\,\text{TeV}$ and $\sqrt{s} = 8\,\text{TeV}$, respectively, is shown in Fig. 4.1. It is given by the time integral over the instantaneous luminosity $\mathcal{L}$ [79], which is defined by beam and machine parameters,

$$\mathcal{L} = \frac{f n_b N_1 N_2}{2\pi \Sigma_x \Sigma_y}. \tag{4.1}$$

Here, n_b gives the number of colliding bunches in each beam, N_1 and N_2 denote the number of protons in each bunch in beam 1 and 2, respectively, f is the revolution frequency and Σ_x and Σ_y are the horizontal and vertical beam widths at the interaction point assuming gaussian distributed shapes of the beams and head-on collisions. The

product of integrated luminosity and cross section σ yields the number of events N expected for a certain process,

$$N = \sigma \times \int \mathrm{d}t\mathcal{L}. \tag{4.2}$$

It is thus essential to measure the luminosity very precisely. The luminosity can also be

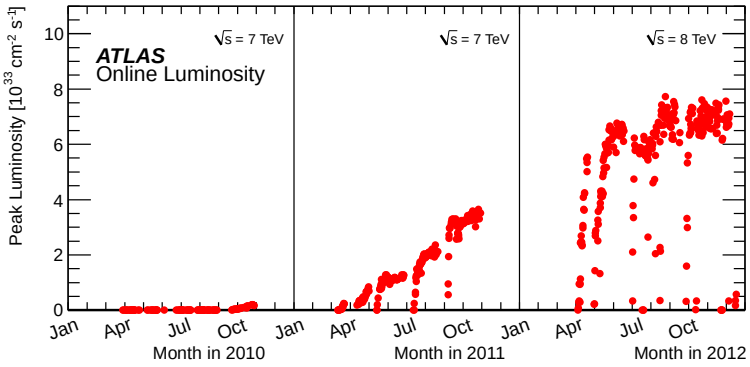

Figure 4.2. Peak instantaneous luminosity delivered to ATLAS per day during proton-proton collisions in 2010-2012 [78].

expressed as

$$\mathcal{L} = \frac{\mu n_b f}{\sigma_{inel}} = \frac{\mu^{vis} n_b f}{\sigma_{vis}} \tag{4.3}$$

with on average μ inelastic interactions per bunch crossing and a pp inelastic cross section of σ_{inel}. The average amount of visible inelastic interactions per bunch crossing is given by $\mu^{vis} = \epsilon\mu$, where ϵ gives the efficiency for an inelastic pp interaction to pass some selection criteria. Thus the luminosity can be determined based on an event counting method. The visible cross section σ_{vis} can then be extracted by comparing μ_{vis} to the peak luminosity during a so-called van der Meer scan: the beams are moved horizontally and vertically across one another and the interaction rate is measured as a function of the beam separation. Combining equations 4.1 and 4.3 yields

$$\sigma_{vis} = \mu_{vis}^{max} \frac{2\pi\Sigma_x\Sigma_y}{N_1 N_2}, \tag{4.4}$$

where μ_{vis}^{max} is the observed visible interaction rate per bunch crossing at the peak of the scan curve.
The ALFA and LUCID detectors, see chapter 3.2.4, measure the luminosity for the ATLAS detector. The uncertainty on the measured luminosity for 2011 is 3.9% [80]. An uncertainty of 2.8% is determined for the integrated luminosity measured in 2012 [81]. The peak instantaneous luminosity delivered to ATLAS in 2011 and 2012 exceeded $3.5 \cdot 10^{33}\,\mathrm{cm}^{-2}\mathrm{s}^{-1}$ and $7.7 \cdot 10^{33}\,\mathrm{cm}^{-2}\mathrm{s}^{-1}$, respectively, and is shown in figure 4.2. Accordingly, the mean number of interactions per bunch crossing, μ, increased over time from on average about 9 in 2011 to almost 21 in 2012. In figure 4.3, the recorded luminosity for a given μ is shown. These multiple interactions per bunch crossing are referred to as pile-up henceforth. There are two kinds of pile-up interactions: in a typical proton-proton bunch

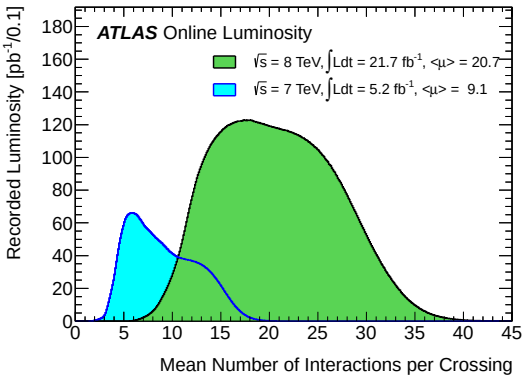

Figure 4.3. Distribution of the recorded luminosity as a function of the mean number of interactions per bunch crossing for proton-proton collision data in 2011 (blue) and 2012 (green) [78].

collision at the LHC, multiple interactions occur simultaneously. This is referred to as in-time pile-up. Additionally, remnants of a previous interaction can still be processed in the detector during another scattering process in the next bunch-crossing taking place, so-called out-of-time pile-up. Due to the additional occupancy from pile-up, object reconstruction and identification can deteriorate. The distribution of peak interactions per day for proton-proton collision data taken in 2010-2012 is shown in figure 4.4.

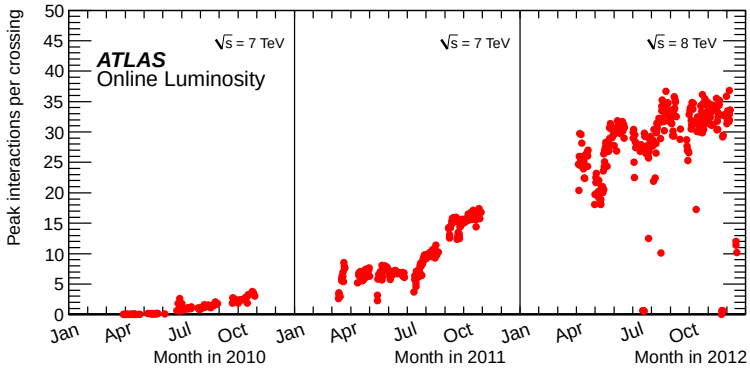

Figure 4.4. Peak interactions per bunch crossing per day in proton-proton collision data recorded by ATLAS in 2010-2012 [78].

4.1.2. Data Quality

Although 5.08 fb^{-1} and 21.3 fb^{-1} were recorded in 2011 and 2012, respectively, only up to 4.6 fb^{-1} and 20.3 fb^{-1} were used for physics analyses, as shown in figure 4.1. The data has to pass several steps and meet certain requirements to be considered for physics analyses. More detail is given in chapter 6. During data taking, data quality is monitored online to spot faulty behavior of (parts of) sub-detectors and thus limit the amount of data loss due to severe detector problems. Data that passes all requirements is collected in so-called Good Run Lists. Only data from these lists is used for physics analyses.

4.2. Simulation

4.2.1. Simulation of Proton-Proton Collisions

Event generators based on Monte Carlo simulation methods are an essential tool for different reasons. They are important in planning and designing experiments by making predictions of what could be achieved in e.g. future colliders. On the other hand, they are widely used to probe the agreement or disagreement of theoretical predictions and the outcome of an experiment when evaluating data.
Although many different generators exist, they often share a common structure of splitting up the full physics process into single steps: the hard interaction based on the matrix element, the parton shower and subsequent hadronization, the underlying event and possible higher-order corrections. Unstable hadronization products are decayed and possible final state radiation is added. These sub-processes are shown schematically in figure 4.5. A brief description of the different steps is given below. More thorough explanations about different generators and the theory behind the simulation may be found e.g. in references [82–84].
At hadron-hadron colliders like the LHC, the fundamental interactions do not take place between the protons but rather between partons constituting the protons. The total cross section of these processes is given by a combination of long- and short-distance behavior of the partons. The different behavior at different scales is described using factorization theorems to allow predictions. The bulk of these interactions are soft scattering processes where only a small amount of momentum is transferred. In case of large momentum transfer in an interaction, i.e. a hard process, the cross section of such an interaction at lowest order is given by

$$\sigma = \sum_{a,b} \int \mathrm{d}x_a \, \mathrm{d}x_b \, f_a^A(x_a, \mu_F^2) \, f_b^B(x_b, \mu_F^2) \, \sigma_{ab\to n}(x_a P, x_b P, \alpha_s, Q^2, \mu_F^2) \tag{4.5}$$

where two partons a and b inside hadrons A and B, respectively, interact. The $f_{a/b}^{A/B}$ denote the parton distribution functions (pdfs), i.e. the momentum distributions of partons a and b. The partons carry momenta x_a and x_b, respectively, which are fractions of the total proton momenta P. The partonic cross sections of a final state n initiated by a and b is given by $\sigma_{ab\to n}$. The factorization scale μ_F is an arbitrary parameter and can be understood as the scale separating short- and long-distance processes. It is usually chosen to be of the same order as the momentum transfer Q^2. The renormalization scale μ_R, the energy scale which is chosen to evaluate integrals properly to avoid divergences, is chosen to be equal to μ_F in equation 4.5.

Parton Distribution Functions

Parton distribution functions have been measured in deep-inelastic scattering experiments such as e.g. those at HERA at DESY. Examples for parton distribution functions as functions of the parton momentum fraction, evaluated at $Q^2 = 10\,\mathrm{GeV}^2$ and $Q^2 = 1000\,\mathrm{GeV}^2$, are shown in figure 4.6. As can be seen in figure 4.6, the pdfs vary depending

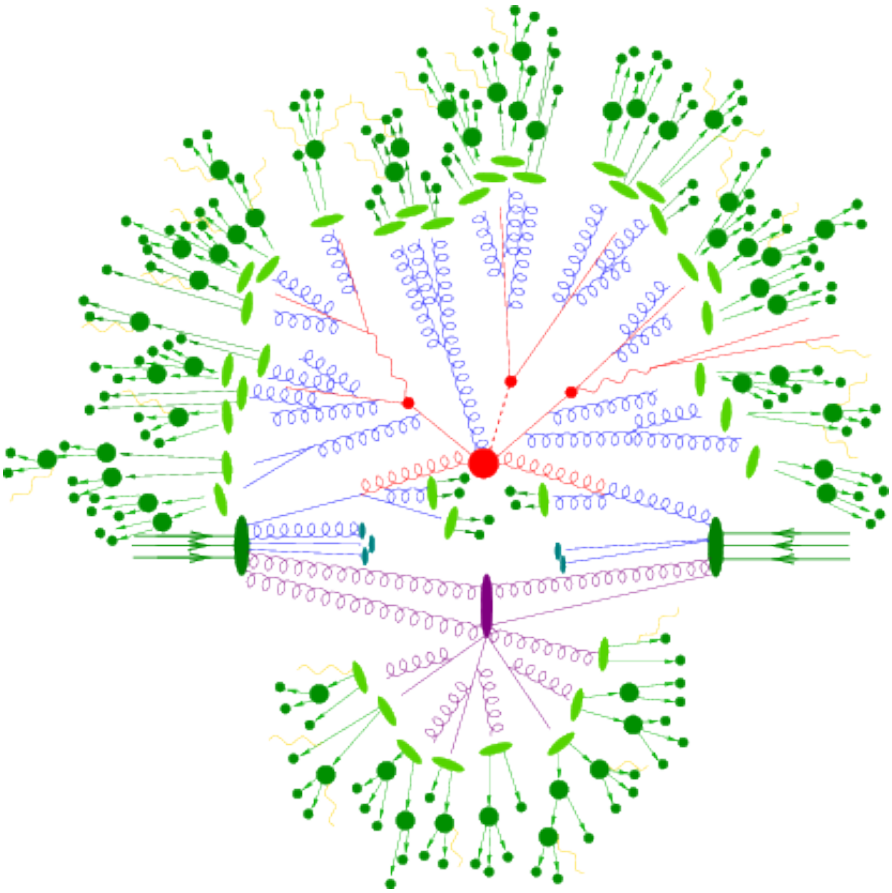

Figure 4.5. Schematic view of a proton-proton collision and the various sub-processes/stages that are simulated. Different colors depict different sub-processes/stages: the hard interaction (red), parton shower (blue), underlying event (purple), hadronization (light green) and decay of unstable hadronization products (dark green) and final state radiation (yellow) [85].

on the Q^2 they are measured at. With the DGLAP equations [87–89], pdfs can be evolved to other values of Q^2, thus permitting combinations of measurements from different experiments. Various different groups provide sets of pdfs, such as the MSTW [86], NNPDF [90] or CTEQ [91] collaborations. Since each group incorporates different sets of measurements and uses different methods to evaluate them, the resulting pdfs are also slightly different.

The Hard Scatter

Quarks and gluons are asymptotically free and thus the cross sections of hard processes are calculated based on perturbation theory. Nowadays not only the leading-order (LO) matrix element is calculated but for many processes also next-to-leading-order (NLO) or next-to-next-to-leading-order (NNLO) corrections, i.e. virtual loops or additional emissions, are available. The integration over the phase space is usually carried out numerically employing Monte Carlo methods due to the complexity of the processes. The renormalization and factorization scales are often chosen to have the same value Q^2,

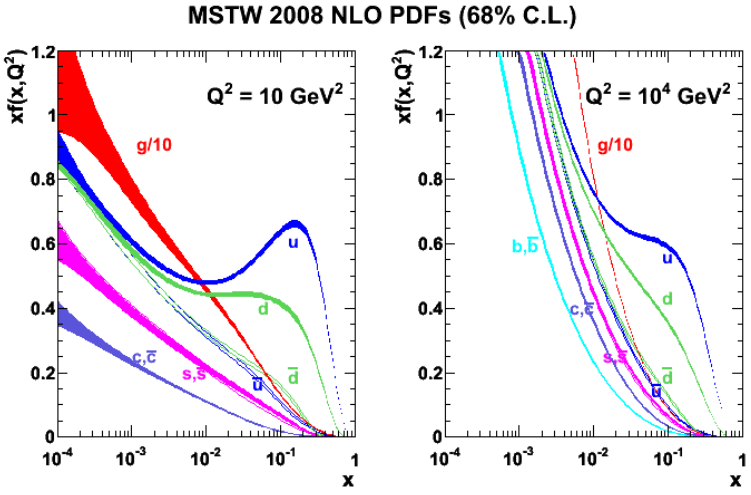

Figure 4.6. Examples of parton distribution functions at different values for Q^2 as a function of the parton momentum fraction x [86].

which is not given by first order principles but rather by choice. The leading-order cross sections for different Standard Model processes span many orders of magnitude and are shown in figure 4.7.

Showering and Hadronization

The cross section of the hard scatter matrix element is often calculated to low orders only, thus it only contains very few final state particles. In experimental analyses, however, these restrictions to a certain fixed order are typically not applied. Instead, fully inclusive final states are analyzed. To describe these processes more realistically, a parton shower can be added to a low order cross section, resulting in a more complex final state with additional final state particles. It evolves the in- and/or out-going partons of the hard scatter to lower momentum scales by adding radiation, i.e. additional quarks and gluons. The evolution is based on the DGLAP equations. The probability for a certain quark or gluon to emit a parton with a certain momentum is evaluated based on Sudakov form factors. The evolution to lower momenta needs to be cut off at a certain scale before α_s gets too large and QCD loses perturbativity. In case the matrix element is calculated at NLO it has be ensured that any overlap between partons from NLO emissions and the parton shower are removed. Such a method is described e.g. in reference [93].
Since quark and gluons are not observed as individual particles, hadrons are formed from the outgoing partons. This process, referred to as hadronization, cannot be calculated and is thus based on phenomenological models. Two models for hadronization are used in most cases, the string [94, 95] and cluster [96–99] models. Since most hadrons emerging from hadronization are unstable, they are then decayed to lighter hadrons until particles stable on the scale of the detector are formed.

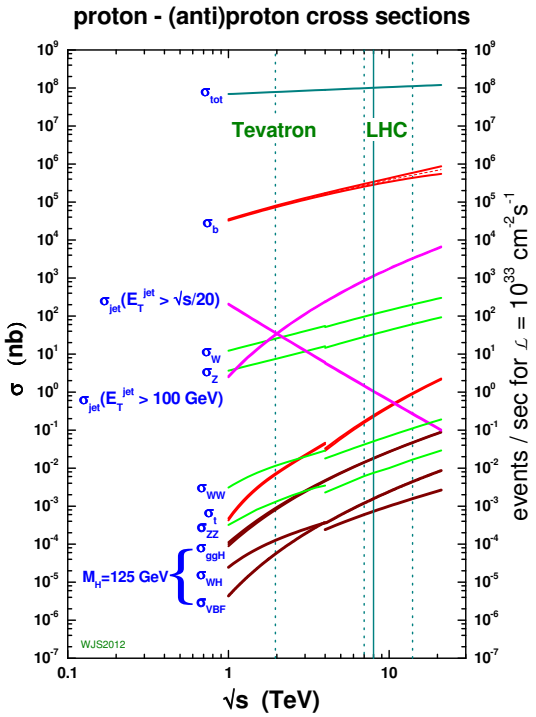

Figure 4.7. Leading-order cross sections for different SM processes at the Tevatron with $\sqrt{s} = 1.96\,\text{TeV}$ and the LHC with $\sqrt{s} = 7$, 8 and 14 TeV [92].

Pile-up and Underlying Event

Both in-time and out-of-time pile-up interactions as defined in chapter 4 are taken into account. This can be done by adding simulated minimum bias events.
In addition to the interesting, hard scattering process, multiple soft interactions may occur in the same pp interaction. This so-called underlying event (UE) cannot be calculated but only described using phenomenological models. It is modeled by multi parton interactions. These additional soft interactions can have a non-negligible impact on the full event.

4.2.2. Background Processes

Due to the similarity of the final states of charged Higgs boson production and decays considered here to SM $t\bar{t}$ decays, the latter are the main background to the searches presented in this thesis. Single top quark production and W+jets production are also relevant background processes. The W bosons from single top quark or W+jets events can decay to a τ lepton and a neutrino with a subsequent hadronic τ decay. This leads to a signature including visible decay products of the τ and missing transverse momentum due to the neutrino, which escapes the detector. With additional jets, these final states can easily mimic the signal process. Additionally, multi-jet production is an important

background process. A jet can be mis-identified as a hadronically decaying τ lepton and missing transverse momentum can result from mis-measurements in the calorimeters, leading to a similar final state as the signal process. Z+jets events and di-boson events (WW, WZ and ZZ production) contribute as minor backgrounds. If e.g. in a $Z \to \tau\tau$ decay the τ leptons decay hadronically but one of them is not identified correctly, the resulting final state may be mistaken as a signal process final state. Since at least 1 jet containing a b-quark is always present in the signal processes, SM processes with b-quarks are more signal-like and thus more likely to pass an event selection and be considered as a possible signal event.

4.2.3. Simulation Samples

The background processes to the searches presented here consist of SM $t\bar{t}$, single top-quark, W+jets, Z/γ^*+jets, multi-jet and diboson production. Simulation samples are used to develop and validate the analyses presented in this thesis. They are processed with the full ATLAS GEANT4 simulation [100, 101] and reconstruction is done using the same algorithms as in data. Additional minimum bias events generated with PYTHIA8 [102] are overlaid to account for pile-up. Simulated events are reweighted to match the average amount of pile-up interactions in data.
All event generators used are tuned to describe ATLAS data. The AUET2B [103] tune is used in samples where PYTHIA6 [104] is interfaced to AcerMC [105] or used alone. For samples generated with HERWIG [106], the AUET2 [107] tune is used. If HERWIG++ is used, the UE-EE3 [108] tune is used instead. Finally, the Perugia 2011 C tune [109] is used for samples where PYTHIA6 is interfaced to POWHEG [110] and the AU2 tune is used for all samples interfaced to PYTHIA8 [111]. Except for samples produced with PYTHIA8, TAUOLA [112] is used for hadronic τ decays. PHOTOS [113] is used for photon radiation from charged leptons in all samples where needed.

Default Background Samples

Standard Model $t\bar{t}$ and single-top quark production in the s-channel as well as in combination with a W boson is modeled with MC@NLO [93, 114]. Single-top quark events in the t-channel are generated using AcerMC. The set of parton distribution functions used is CT10 [115] and the top-quark mass is set to 172.5 GeV. Parton shower and underlying event are added to samples generated with MC@NLO and AcerMC using HERWIG/JIMMY [116] and PYTHIA6, respectively. Approximate NNLO predictions for inclusive cross sections are used for $t\bar{t}$ [117] and single top-quark [118–120] production. Overlaps between SM $t\bar{t}$ and single top-quark production in association with a W boson are removed [114]. W+jets and Z/γ^*+jets events are simulated with up to five additional partons using ALPGEN [121] interfaced to HERWIG and JIMMY. Dedicated samples with matrix elements for the production of additional $b\bar{b}$ and $c\bar{c}$ pairs are simulated using ALPGEN. HERWIG is used to generate WW, ZZ and WZ events. The CTEQ6.1 [91] and CTEQ6L1 [122] parton distribution function sets are used for these samples in the 7 and 8 TeV analysis, respectively. The cross sections are normalized to next-to-leading-order predictions for diboson production [123] and to NNLO calculations for single vector

boson production [124, 125]. An overview of all SM simulation samples used in the 7 and 8 TeV analyses and their cross sections is given in tables 4.1 and 4.2, respectively.

Signal Samples

For the low-mass H^+ search, PYTHIA6 is used to generate signal samples in a mass range $90\,\text{GeV} \leq m_{H^+} \leq 160\,\text{GeV}$ in m_{H^+} steps of 10 GeV. An additional mass point at $m_{H^+} = 80\,\text{GeV}$ is used in the 8 TeV analysis. The signal processes are $t\bar{t} \to b\bar{b}H^+W^-$, $t\bar{t} \to b\bar{b}H^-W^+$ and $t\bar{t} \to b\bar{b}H^+H^-$, where the charged Higgs bosons decay as $H^+ \to \tau\nu$ and W bosons from top quark decays decay to all possible final states. The cross section for these processes only depends on the total $t\bar{t}$ cross section and the branching ratio $\text{B}(t \to H^+b)$.

POWHEG interfaced to PYTHIA8 is used for the simulation of high-mass H^+ samples in a mass range $180\,\text{GeV} \leq m_{H^+} \leq 1000\,\text{GeV}$, where the H^+ is produced in association with a top quark. In the mass range $m_{H^+} \leq 200\,\text{GeV}$, signal samples are produced in m_{H^+} steps of 10 GeV, then in steps of 25 GeV up to $m_{H^+} = 300\,\text{GeV}$. Subsequently samples are produced in m_{H^+} intervals of 50 GeV up to $m_{H^+} = 600\,\text{GeV}$. Two additional samples with $m_{H^+} = 750\,\text{GeV}$ and $m_{H^+} = 1000\,\text{GeV}$ are produced. The samples are generated based on the 5FS at NLO and using the narrow-width approximation for the H^+. The production cross sections are calculated based on a combination of the 4FS and 5FS [64] as described in chapter 2.3.4 and including theoretical uncertainties.
All signal mass points are summarized in table 4.3. A summary of the generators, pdfs and tunes used for signal samples in the 7 and 8 TeV analyses is given in table 4.4.

4.2.4. Event Generation-related Systematic Uncertainties

To estimate systematic uncertainties due to the event generator chosen, background and signal samples are produced with different generators as well as parton shower and hadronization models and compared. Additional samples are evaluated to account for uncertainties on the jet production rate.
For the 2011 analysis, $t\bar{t}$ samples are also produced using POWHEG interfaced to PYTHIA6 using the CTEQ6L1 pdf set to evaluate uncertainties due to the choice of event generator and the parton shower model. Since no alternative generator is available for signal processes, the relative difference in acceptance between $t\bar{t}$ samples produced with MC@NLO interfaced to HERWIG/JIMMY and AcerMC interfaced to PYTHIA6 is taken as systematic uncertainty on the generator and parton shower choice for the signal. The CTEQ6L1 pdf set is used for the sample produced with AcerMC. Since low-mass charged Higgs bosons are expected to be produced in $t\bar{t}$ decays this approach is expected to describe the uncertainty well. To evaluate uncertainties due to initial and final state radiation, which modify the jet production rate, $t\bar{t}$ samples produced with AcerMC interfaced to PYTHIA6, where the jet production parameters are set to a range of values not excluded by experiments, are evaluated. The same uncertainty is used for signal samples, too.
For the 2012 analyses, $t\bar{t}$ samples produced with POWHEG interfaced to PYTHIA6 or JIMMY, using the CTEQ6L1 and CT10 pdf sets, respectively, are evaluated to assess

Process	Matrix Element	Parton Shower & Underlying Event	Tune	PDF Set	Cross section [pb] at $\sqrt{s} = 7\,\text{TeV}$
SM $t\bar{t}$ ($\geq 1\ell$)	MC@NLO	HERWIG/JIMMY	AUET2	CT10	90.6
SM $t\bar{t}$ ($\geq 1\ell$)	POWHEG	PYTHIA6	Perugia 2011 C	CTEQ6L1	90.6
SM $t\bar{t}$ ($\geq 1\ell$)	POWHEG	HERWIG/JIMMY	AUET2	CT10	90.6
SM $t\bar{t}$ ($\geq 1\ell$)	AcerMC	PYTHIA6	AUET2B	CTEQ6L1	90.6
Single top-quark t-channel ($\geq 1\ell$)	AcerMC	PYTHIA6	AUET2B	CT10	20.9
Single top-quark s-channel ($\geq 1\ell$)	MC@NLO	HERWIG/JIMMY	AUET2	CT10	1.5
Single top-quark Wt-channel (inc.)	MC@NLO	HERWIG/JIMMY	AUET2	CT10	15.7
$W \to \ell\nu$+jets	ALPGEN	HERWIG/JIMMY	AUET2	CTEQ6L1	3.1×10^4
$Wb\bar{b}$+jets	ALPGEN	HERWIG/JIMMY	AUET2	CTEQ6L1	1.3×10^2
$Z/\gamma^*(\ell\ell) + \text{jets}$, $m(\ell\ell)$ >10 GeV	ALPGEN	HERWIG/JIMMY	AUET2	CTEQ6L1	1.5×10^4
$Z/\gamma^*(\ell\ell)b\bar{b} + \text{jets}$, $m(\ell\ell)$ >30 GeV	ALPGEN	HERWIG/JIMMY	AUET2	CTEQ6L1	38.7
WW	HERWIG	JIMMY	AUET2	CTEQ6L1	17.0
ZZ	HERWIG	JIMMY	AUET2	CTEQ6L1	1.3
WZ	HERWIG	JIMMY	AUET2	CTEQ6L1	5.5

Table 4.1. All background simulation samples used in the 7 TeV analysis with the generators for matrix element and parton shower, pdfs and tunes and their cross sections. Here, ℓ refers to any charged lepton. For the $t\bar{t}$ samples, the first one is used as nominal sample in the analysis while the others are used to evaluate systematic uncertainties as described in chapter 4.2.4.

Process	Matrix Element	Parton Shower & Underlying Event	Tune	PDF Set	Cross section [pb] at $\sqrt{s} = 8\,\text{TeV}$
SM $t\bar{t}$ ($\geq 1\ell$)	MC@NLO	HERWIG/JIMMY	AUET2	CT10	137.3
SM $t\bar{t}$ ($\geq 1\ell$)	POWHEG	PYTHIA8	Perugia 2011 C	CTEQ6L1	137.3
SM $t\bar{t}$ ($\geq 1\ell$)	POWHEG	JIMMY	AUET2	CT10	137.3
SM $t\bar{t}$ ($\geq 1\ell$)	AcerMC	PYTHIA6	AUET2B	CTEQ6L1	137.3
Single top-quark t-channel ($\geq 1\ell$)	AcerMC	PYTHIA6	AUET2B	CT10	28.4
Single top-quark s-channel ($\geq 1\ell$)	MC@NLO	HERWIG/JIMMY	AUET2	CT10	1.8
Single top-quark Wt-channel (inc.)	MC@NLO	HERWIG/JIMMY	AUET2	CT10	22.4
$W \to \ell\nu$+jets	ALPGEN	HERWIG/JIMMY	AUET2	CTEQ6L1	3.6×10^4
$Wb\bar{b}$+jets	ALPGEN	HERWIG/JIMMY	AUET2	CTEQ6L1	1.6×10^2
$Wc\bar{c}$+jets	ALPGEN	HERWIG/JIMMY	AUET2	CTEQ6L1	4.5×10^2
Wc+jets	ALPGEN	HERWIG/JIMMY	AUET2	CTEQ6L1	1.8×10^3
$Z/\gamma^*(\ell\ell) + \text{jets}$, $m(\ell\ell)$ >10 GeV	ALPGEN	HERWIG/JIMMY	AUET2	CTEQ6L1	1.7×10^4
$Z/\gamma^*(\ell\ell)b\bar{b} + \text{jets}$, $m(\ell\ell)$ >30 GeV	ALPGEN	HERWIG/JIMMY	AUET2	CTEQ6L1	49.2
$Z/\gamma^*(\ell\ell)c\bar{c} + \text{jets}$, $m(\ell\ell)$ >30 GeV	ALPGEN	HERWIG/JIMMY	AUET2	CTEQ6L1	98.1
WW	HERWIG	JIMMY	AUET2	CTEQ6L1	20.9
ZZ	HERWIG	JIMMY	AUET2	CTEQ6L1	1.5
WZ	HERWIG	JIMMY	AUET2	CTEQ6L1	7.0

Table 4.2. All background simulation samples used in the 8 TeV analyses with the generators for matrix element and parton shower, pdfs and tunes and their cross sections. Here, ℓ refers to any charged lepton. For the $t\bar{t}$ samples, the first one is used as nominal sample in the analysis while the others are used to evaluate systematic uncertainties as described in chapter 4.2.4.

low-mass H^+ search									
m_{H^+} [GeV]	(80)	90	100	110	120	130	140	150	160
high-mass H^+ search									
m_{H^+} [GeV]	180	190	200	225	250	285	300	350	400
	450	500	550	600	750	1000			

Table 4.3. Overview of all signal mass points used in the low-mass and high-mass H^+ searches. The mass point at 80 GeV is used only in the 2012 analysis.

Process	Matrix Element	Parton Shower & Underlying Event	Tune	PDF Set
low-mass H^+	PYTHIA6	PYTHIA6	AUET2B	CTEQ6L1
high-mass H^+	POWHEG	PYTHIA8	AU2	CT10
high-mass H^+	MC@NLO	HERWIG++	UE-EE3	CT10
high-mass H^+	MadGraph	PYTHIA8	AU2	CTEQ6L1
high-mass H^+	POWHEG	PYTHIA8	AU2	CT10

Table 4.4. Signal simulation samples used in the 7 and 8 TeV analyses. The first two samples are the default ones while all others are used to evaluate systematic uncertainties. In the low-mass H^+ search, SM $t\bar{t}$ samples are used to evaluate these systematics.

the systematic uncertainty due to the chosen event generator and parton shower for both SM and low-mass H^+ signal processes. Uncertainties due to initial and final state radiation, modifying the jet production rate, are evaluated in $t\bar{t}$ samples and applied to SM and low-mass H^+ signal processes from samples produced with AcerMC interfaced to PYTHIA6, where the parameters are set values not yet excluded by experimental data. The pdf set CTEQ6L1 is used for these samples.
For the high-mass H^+ search in 2012 data, samples produced with MC@NLO and HERWIG++ [126] are used to evaluate the systematic uncertainty due to the chosen event generator and parton shower model. The pdf set CT10 is used. The uncertainty arising from initial and final state radiation is evaluated based on samples produced with POWHEG interfaced to PYTHIA8 and using the CTEQ6L1 pdf set, where the factorization and renormalization scales are varied up and down by a factor of 2 compared to the default samples. A systematic uncertainty due to different acceptances between H^+ production in the 4FS and 5FS is evaluated using dedicated samples produced with MadGraph [127] interfaced to PYTHIA8. The CTEQ6L1 pdf set is used. Uncertainties due to the chosen pdf are evaluated for $t\bar{t}$ and signal samples. They are found to be negligible and thus not included in the statistical analysis.

5 Reconstruction and Identification of Physics Objects

The following descriptions focus on particle reconstruction and identification as used for data taken in 2012. Major differences to algorithms used in 2011 are pointed out. The general procedures for reconstructing and identifying the physics objects, i.e. jets, hadronically decaying τ leptons, muons etc. used in the analyses presented in this thesis are described in this chapter. Specific selections and working points are given in chapter 6 and relevant systematic uncertainties are described in chapter 7.

5.1. Tracks and Vertices

5.1.1. Track Reconstruction

Track reconstruction in the ID is based on a sequence of algorithms [128]. The standard algorithm in ATLAS uses seeds in the silicon detectors and moves outwards from there, thus extending tracks into the TRT [129]. This procedure is designed mostly for tracks from particles with either a lifetime $t > 3 \times 10^{-11}$ s produced in a proton-proton collision or $t < 3 \times 10^{-11}$ s and produced in a subsequent decay or interaction. These are referred to as primaries. A track is required to have a transverse momentum $p_{\mathrm{T}} > 400\,\mathrm{MeV}$. Additionally, track reconstruction can also start from segments in the TRT, moving inwards by adding hits in the silicon layers. This algorithm is implemented mostly for reconstructing particles resulting from interactions of primaries.
Increasing pile-up during data taking in 2011 and 2012 made efficient and reliable track reconstruction more challenging. Higher occupancy of cells results in more fake tracks, i.e. tracks that cannot be matched to any particle. For the data taken in 2011, a track is required to have at least 7 hits in the silicon detector (SCT + pixel detector) and a maximum of 2 holes in the pixel detector. Hits refer to measurement points while holes describe non-existing measurement points where hits are expected. For more robustness against pile-up, these requirements are tightened in 2012 to at least 9 hits in the silicon detector and no holes in the pixel detector. The track reconstruction efficiency, defined as the amount of primaries passing all criteria that are matched to reconstructed tracks, decreases due to these more robust requirements. Since these measures also reduce the fraction of fake tracks, the overall performance improves. In the data taken in 2011, the track reconstruction efficiencies using the default and robust requirements are around at least 80%.

5.1.2. Vertex Reconstruction

Vertex reconstruction is based on results from track reconstruction described in section 5.1.1. The z-position of a reconstructed track is used as a primary vertex seed. The seeds are processed by an iterative vertex-finding algorithm to find primary vertices using also information from close-by tracks [130]. Each track is assigned a weight indicating the compatibility with a found vertex. If a track is too far from a vertex it is used as a seed for a new vertex until no additional vertices are reconstructed. At least two tracks are associated with a vertex during reconstruction. As for tracks, the performance of vertex reconstruction depends on the amount of pile-up. Robust requirements for track reconstruction as described above also lead to a more robust and cleaner vertex reconstruction. The efficiencies for vertex reconstruction and fake vertex reconstruction are shown in figure 5.1 as functions of the average number of interactions per bunch crossing. The same matching between tracks and particles is used as for the track reconstruction efficiency. A vertex is regarded as matched to an interaction when the sum of the weights of the tracks is greater than 50%.

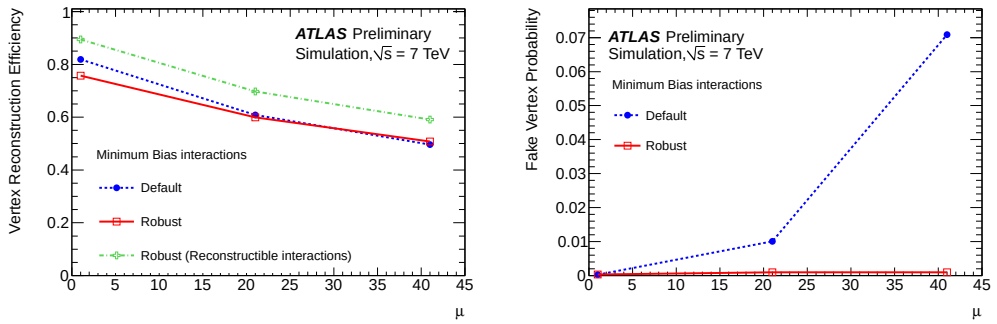

(a) (b)

Figure 5.1. (a) Primary vertex reconstruction efficiency and (b) fake vertex probability with default and robust requirements [129].

5.2. Topological Clusters

Topological Clusters, also referred to as topo-clusters below, are used as seeds for jets, electron, photons and hadronic τ reconstruction [131].
Electrons and hadrons lose their energy in the calorimeters as they traverse them, depositing it in many different calorimeter cells. Algorithms are needed to cluster these cells and calculate the total energy deposited. Topo-clusters are constructed from a seed cell to which neighboring cells are added iteratively. A cell serves as seed if the energy significance, i.e. the signal to noise ratio, is above a certain threshold t_{seed}. A neighboring cell is added if its significance is higher than another, lower threshold t_{cell}. In case the energy significance of the neighboring cell is above an intermediate level $t_{neighbor}$ it can be used as an additional seed. This clustering algorithm leads to three-dimensional clusters containing a variable amount of cells and no fixed form.

5.3. Jets

Jets originate from the hadronization of gluons and quarks. Objects carrying color charge cannot exist in unbound, colored states. This leads to bound objects, i.e. hadrons, in the final states of proton-proton collisions. Jets are produced copiously at hadron colliders. They are important as signatures for measuring known processes as well as searching for new phenomena. In the detector, jets are reconstructed based on energy clusters in the calorimeters. In simulation, jets can also be reconstructed on particle level. The complex final states produced in proton-proton collisions at the LHC require efficient jet reconstruction algorithms. The one used in the analyses presented here is introduced in section 5.3.1. The jet calibration is explained in section 5.3.2. Because of the relatively long lifetime of b mesons, jets containing these are identified with so-called b-tagging algorithms. More information on this is given in section 5.3.3.

5.3.1. Reconstruction

Quarks or gluons produced in collisions hadronize to form collimated cone-like jets of particles. In the analyses presented here, they are reconstructed using the anti-k_t algorithm [132] as implemented in the FASTJET package [133, 134] and based on energy deposits, i.e. topo-clusters, in the calorimeters that have been clustered following the procedure outlined in section 5.2. Compared to some other jet reconstruction algorithms, the anti-k_t algorithm is both collinear and infrared safe.
Two distance parameters are defined,

$$d_{ij} = \min(k_{ti}^{-2}, k_{tj}^{-2}) \frac{\Delta_{ij}^2}{R^2} \tag{5.1}$$

$$d_{iB} = k_{ti}^{-2} \tag{5.2}$$

where $\Delta_{ij} = (y_i - y_j)^2 + (\Phi_i - \Phi_j)^2$ and k_t, y and Φ give the transverse momentum, rapidity and azimuthal angle of the entities i and j and B refers to the beam. For the analyses presented here, a value of 0.4 is chosen for the radius parameter R. The algorithm calculates all distances d_{ij} between two entities i and j and between entities i and the beam B, d_{iB}. The smallest distance is then selected. If it is found between two objects i and j then these are combined. If it is found between an entity i and the beam, i is identified as a jet and cleared from the list of entities. All distances are then recalculated and the algorithm starts from the beginning until no entities but only jets remain. The chosen way of combining different entities leads to cone-like shapes with a radius R for jets with high momenta. Shapes can be more complex for soft jets.
Jets reconstructed in the acceptance region of the inner detector are matched to tracks by so-called ghost association [135]. In this approach, the transverse momenta of tracks are scaled by a very small number such that they are treated as infinitesimally soft. These re-scaled tracks are then added to the input list of the jet reconstruction algorithm. Due to the very low transverse momenta the calorimeter-based reconstruction of jets is not influenced but it is still possible after jet reconstruction to associate a track with a certain jet.
A jet vertex fraction (JVF) [136] is defined for jets, specifying the fraction of the momenta

of tracks associated with the jet originating from the primary vertex compared to any vertex:

$$\mathrm{JVF}(\mathrm{jet}_i, \mathrm{PV}_j) = \frac{\sum_k p_{\mathrm{T}}(\mathrm{track}_k^{\mathrm{jet}_i}), \mathrm{PV}_j}{\sum_n \sum_l p_{\mathrm{T}}(\mathrm{track}_l^{\mathrm{jet}_i}), \mathrm{PV}_n}. \tag{5.3}$$

The JVF of jet_i originating in a vertex PV_j is given by the sum of the transverse momenta of all tracks associated with this jet and originating from the specified vertex divided by the sum of the transverse momenta of all tracks associated with the jet but originating from any vertex. It is used to suppress jets from pile-up interactions. Once the primary vertex of the hard scatter is identified, the JVF of a jet resulting from this PV will tend to be greater than that of any pile-up jet. A schematic picture of the JVF of two jets with regard to two primary vertices is shown in figure 5.2, together with the JVF distribution of jets resulting from the hard-scatter compared to pile-up jets.

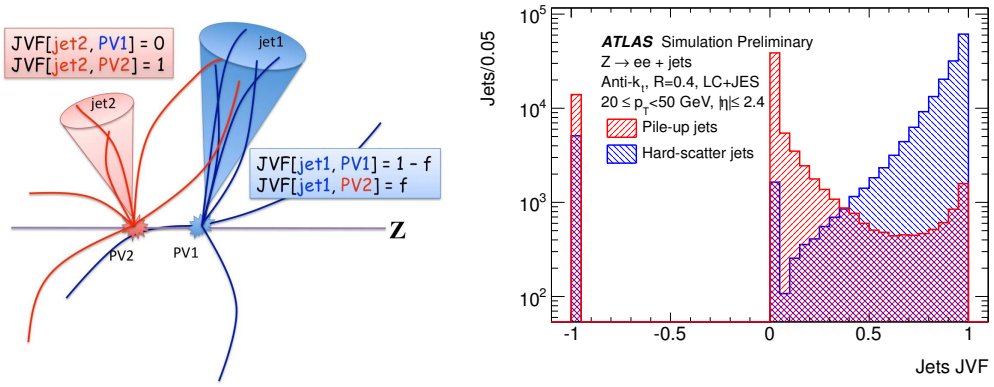

(a) (b)

Figure 5.2. (a) Sketch of the JVF principle and (b) JVF distribution for jets resulting from the hard scatter (blue) or pile-up (red) with $20\,\mathrm{GeV} < p_{\mathrm{T}} < 50\,\mathrm{GeV}$ and $|\eta| < 2.4$ in $Z \to ee$+jets events [136].

5.3.2. Jet Energy Scale and Resolution

Topo-clusters used for jet reconstruction are calibrated either at the electromagnetic (EM) scale or at the hadronic scale using the local cluster (LC) weighting method. For the LC method, topo-clusters are corrected locally in the calorimeters and void of any jet context. In the analyses presented here, both calibrations are used. While topo-clusters used for jet reconstruction in the analysis at $\sqrt{s} = 7\,\mathrm{TeV}$ are calibrated at the electromagnetic scale, those in 2012 are calibrated using the LC method. The latter leads to a better energy resolution compared to the first method [137, 138].
Reconstructed jets undergo further calibration for various effects. Energy deposits due to pile-up interactions are removed. The direction of the jet is then corrected such that it points to the PV instead of the detector center. The jet energy is corrected to the particle level by applying energy- and η-dependent calibration factors. Finally, the

energy is calibrated also taking into account observables like the structure of energy deposits longitudinally in the calorimeter or tracks associated with the jet. The jets are referred to as calibrated at the EM+JES or LC+JES scale, depending on how the original topo-clusters are calibrated.
In di-jet events it is expected that, in leading order QCD, the two jets have equal transverse momenta $p_{\mathrm{T}} = p_{\mathrm{T}}^{avg}$. Assuming a $2 \to 2$ topology, discrepancies between the transverse momenta originate from different responses of the calorimeter in different regions. The calorimeter response $1/c$ relative to a well-calibrated reference region, defined as the ratio of the transverse momenta of a probe and a reference jet, respectively, in di-jet events,

$$\frac{1}{c} = \frac{p_{\mathrm{T}}^{\mathrm{probe}}}{p_{\mathrm{T}}^{\mathrm{ref}}} \tag{5.4}$$

is shown in figure 5.3 for jets calibrated at the LC+JES scale as a function of the pseudorapidity for two different p_{T} bins and comparing data to simulation. Both the jet

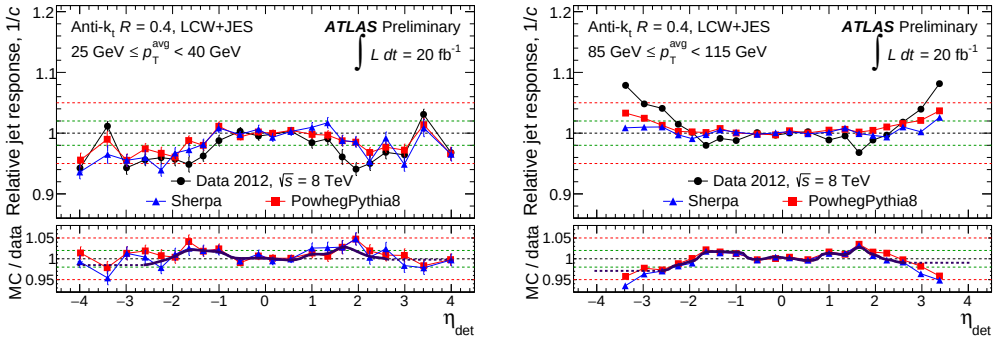

(a) (b)

Figure 5.3. Relative response of jets calibrated at the LC+JES (named LCW+JES in the plot) scale in two different p_{T} bins, (a) $25\,\mathrm{GeV} < p_{\mathrm{T}}^{avg} < 40\,\mathrm{GeV}$ and (b) $85\,\mathrm{GeV} < p_{\mathrm{T}}^{avg} < 115\,\mathrm{GeV}$ [138].

energy scale calibration and jet energy resolution are found to agree very well between data and simulation. The uncertainty on the jet energy scale for jets in the central detector region and with high transverse momenta is less than 1%.

5.3.3. Tagging of jets containing b quarks

Identifying jets containing b quarks with so-called b-tagging algorithms is important for many different physics applications, e.g. top quark or Higgs boson related measurements or searches. Similarly, these algorithms are relevant for processes with only light-flavor jets to veto events containing jets originating from b quarks.

Several different algorithms are available to identify jets containing b quarks. For the b-tagging algorithms applied in the analyses presented here, information about the longitudinal and transverse impact parameters or their significances as well as information about the secondary vertex is used in multivariate methods. The transverse impact parameter, shown schematically in figure 5.4, is defined as the shortest distance of a

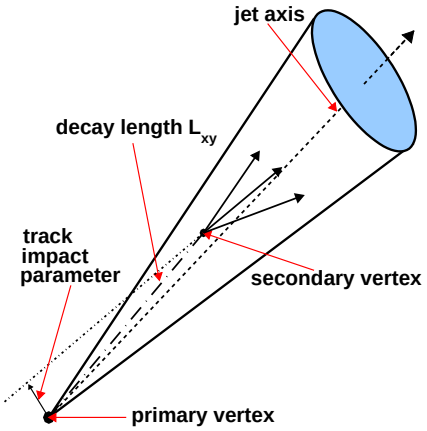

Figure 5.4. Schematic sketch of a b-tagged jet showing the secondary vertex of the subsequent decay and the impact parameter used in b-tagging algorithms [139].

track to the PV in the $r - \phi$ plane [140]. The longitudinal impact parameter is given by the product of the absolute value of the z coordinate of the track at this point and $\sin\theta$. Since all of this information relies on the inner detector, b-tagging can only be applied to jets within $|\eta| < 2.5$. In the analyses presented here, the MV1 tagger [141] combining information about the impact parameter and secondary vertex is used. The performance of a b-tagging algorithm is assessed using measurements of its efficiency, i.e. how often a jet containing a b hadron is tagged, and rejection rates, i.e. the rate of rejecting jets not containing b hadrons, so-called light jets, correctly. The efficiencies and rejection rates in data and simulation are measured in bins of the transverse momenta and pseudorapidities of the jets since they can vary considerably depending on these variables.
The rejection rate for light-flavor jets measured in $t\bar{t}$ simulation is shown in figure 5.5 as a function of the b-tagging efficiency for the MV1 tagger used in the 2012 analyses presented here.

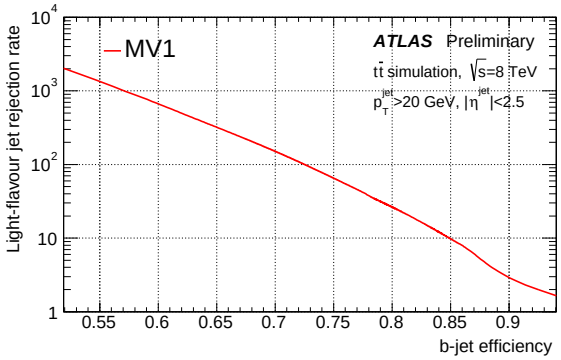

Figure 5.5. Rejection rates for light-flavor jets for the MV1 tagging algorithm as a function of the b-tagging efficiency [142].

5.4. Hadronically Decaying τ Leptons

Tau leptons decay to either an electron or a muon or hadrons, accompanied by the relevant neutrinos which escape the detector. Hadronic decays happen in about 65% of the cases [29] and the reconstruction and identification of these hadronic τ decay products is described below. Leptonic τ decays are not considered in the analyses presented here. Tau leptons have a proper decay length of $87\,\mu$m and decay before reaching any active material in the ATLAS detector. Thus they can only be identified via their decay products. In most cases, the hadronic decay products are either 1 or 3 charged pions or charged Kaons, possibly accompanied by one or more neutral pions. Decays with more than 3 charged particles happen very rarely ($\mathcal{O} < 1\%$) and are not taken into account here.
Hadronically decaying τ leptons (τ_{had}) leave traces in the detector that are similar to those of jets but can be distinguished based on the shape of the shower in the calorimeter, the number of associated tracks and the vertex from the τ lepton decay. The shower profile of hadronic τ decays tends to be narrower than that of quark- or gluon-initiated jets. Additionally, quark- or gluon-initiated jets are often associated with more than 1 or 3 charged-particle tracks. These properties are used in dedicated algorithms to distinguish between τ- and quark- or gluon-initiated jets. Electrons can also mimic the signature of hadronic τ lepton decays. Thus a separate algorithm is needed to differentiate between these. These algorithms are described in some detail in section 5.4.1. Like jets, decay products from hadronic τ decays need also to be calibrated. Information about the τ energy scale and resolution is given in section 5.4.2.

5.4.1. Reconstruction and Identification

Trigger Objects

As described in section 3.2.5, the trigger system used in ATLAS consists of 3 levels. The first level is hardware based and the full information used for identification of the visible products of a hadronic τ decay ($\tau_{\text{had-vis}}$), as presented in the following section, is not available at this stage. Nevertheless, $\tau_{\text{had-vis}}$ identification at trigger level (also called online) is as close as possible to that during event reconstruction (also referred to as offline). At L1, regions of interest (RoIs) are formed based on calorimeter information. Information from these RoIs is further processed by the L2 system, refining the quantities used taking into account more information from all detector sub-systems. Finally at the Event Filter level, the algorithms used to identify $\tau_{\text{had-vis}}$ are based on mostly the same quantities as those used for offline reconstruction. Rates for different triggers at EF level are shown in figure 5.6 as functions of instantaneous luminosity.

Reconstruction

Jets reconstructed with the anti-k$_t$ algorithm using a distance parameter $R = 0.4$ with topo-clusters calibrated using a local hadronic calibration are used as seeds for $\tau_{\text{had-vis}}$ reconstruction [143]. They need to have transverse momenta (p_{T}) of at least 10 GeV

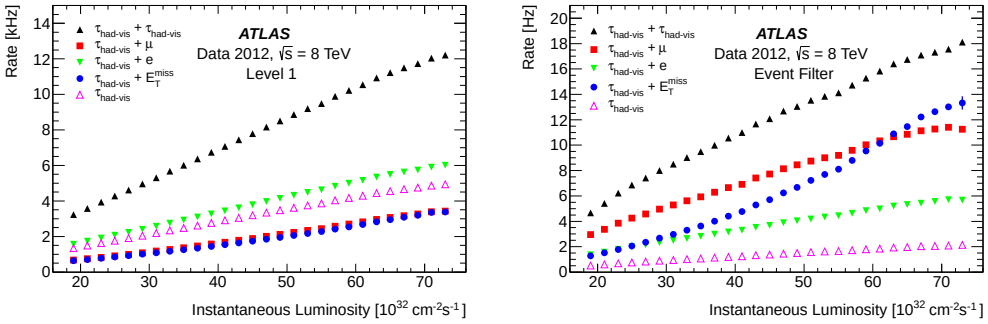

(a) (b)

Figure 5.6. Trigger rates at (a) L1 and (b) Event Filter level for different triggers based on hadronic τ decays including a $\tau_{\text{had-vis}}$+$E_{\text{T}}^{\text{miss}}$ trigger used in the 2012 analysis presented here as a function of the instantaneous luminosity [143].

and be within $|\eta| < 2.5$. A tau vertex is identified separately from the primary vertex. For this, the transverse momenta of all tracks associated with the $\tau_{\text{had-vis}}$ candidate with $p_{\text{T}} > 1\,\text{GeV}$ that satisfy certain quality and hits criteria and are within $\Delta R < 0.2$ of the jet seed direction are added. The primary vertex with the largest sum of these transverse momenta is identified as the τ vertex. The direction of the $\tau_{\text{had-vis}}$ candidate, the number of associated tracks and the coordinate system to calculate identification variables are determined based on this vertex. Tracks have to be within $\Delta R < 0.2$ of the $\tau_{\text{had-vis}}$ candidate's direction to be matched to it. They need to fulfill the following criteria: $p_{\text{T}} > 1\,\text{GeV}$, at least 2 hits in the pixel layers of the ID, at least 7 hits in total in the pixel and SCT layers, the transverse impact parameter with respect to the τ vertex $|d_0| < 1\,\text{mm}$ and the longitudinal impact parameter $|z_0 \sin\theta| < 1.5\,\text{mm}$. Additionally, tracks within an annulus of $0.2 < \Delta R < 0.4$ that fulfill these criteria are used for some identification variables. Dedicated algorithms are applied to reconstruct neutral pions. This information is the only bit not used for identification at the EF level that is used in the discrimination against quark- or gluon-initiated jets.

Discrimination against Jets

After reconstruction, a separate identification algorithm is run to distinguish $\tau_{\text{had-vis}}$ candidates from quark- or gluon-initiated jets. Different algorithms are used in the analysis at $\sqrt{s} = 7\,\text{TeV}$ and $\sqrt{s} = 8\,\text{TeV}$ but they are mostly based on the same input variables. The identification efficiency is defined as the ratio of the number of identified $\tau_{\text{had-vis}}$ candidates with 1 or 3 charged-particle tracks (called 1-prong or 3-prong, respectively, hereafter) matched to a true $\tau_{\text{had-vis}}$ and the number of true $\tau_{\text{had-vis}}$ with 1 or 3 charged-particle tracks. To be matched to a true $\tau_{\text{had-vis}}$, the reconstructed and true particle have to be within $\Delta R < 0.2$ of each other and only true $\tau_{\text{had-vis}}$ with $p_{\text{T}} > 20\,\text{GeV}$ and within $|\eta| < 2.5$ are considered. Simulated $Z \to \tau\tau$, $Z' \to \tau\tau$ and $W \to \tau\nu$ samples are used as signal while data enriched in QCD di-jet events is used as background.
For the 2011 analysis, a likelihood ratio is used to discriminate τ_{had} decays from quark- or gluon-initiated jets, separately for 1-prong and 3-prong $\tau_{\text{had-vis}}$ candidates. Five variables,

with only 2 of them used for both likelihoods, are used as input [144, 145]. Three signal efficiencies are defined corresponding to a loose, medium and tight working point with average efficiencies of 60%, 50% and 30% for 1-prong $\tau_{\text{had-vis}}$ and 65%, 55% and 35% for 3-prong $\tau_{\text{had-vis}}$ candidates, respectively. To reduce dependence on the pile-up conditions, the likelihood functions are binned in number of reconstructed vertices. A flat signal efficiency as a function of the p_{T} of the $\tau_{\text{had-vis}}$ candidate is ensured by determining the thresholds of the likelihoods as a function of the transverse momentum.
For the 2012 analysis, a boosted decision tree (BDT) [146, 147] is used instead with 8 and 9 input variables for the identification of 1-prong and 3-prong τ_{had} decays, respectively, with 6 input variables common to both [143]. As for the identification algorithm used in 2011, the thresholds for the loose, medium and tight working points are calculated as a function of the p_{T} of the $\tau_{\text{had-vis}}$ candidate and correspond to signal efficiencies of about 65, 55 and 30% for 1-prong and 45, 40 and 30% for 3-prong $\tau_{\text{had-vis}}$, respectively. These efficiencies are shown as functions of the number of reconstructed vertices in an event in figure 5.7. In figure 5.8, the inverse background efficiencies are shown as functions of the

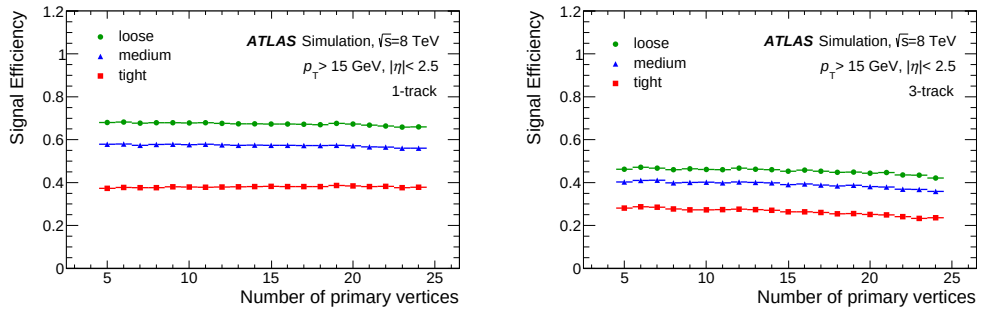

(a) (b)

Figure 5.7. Offline $\tau_{\text{had-vis}}$ identification efficiencies for 3 different working points as functions of the number of vertices in the event for (a) 1-prong and (b) 3-prong τ decays [143].

signal efficiencies, separately for 1-prong and 3-prong $\tau_{\text{had-vis}}$ candidates with high or low transverse momenta. For a signal efficiency of 40%, an inverse background efficiency of 60 is achieved for $\tau_{\text{had-vis}}$ candidates with low momenta.

Discrimination against Electrons

Electrons may be misidentified as $\tau_{\text{had-vis}}$ candidates due to similar signatures. They leave only a single track and deposit energy in the calorimeters. However, several criteria can be used to distinguish electrons from τ_{had} decays, e.g. that electrons are more likely to emit transition radiation than the charged pions and kaons resulting from τ_{had} decays. The fraction of energy deposited in the electromagnetic calorimeter compared to that deposited in both the electromagnetic and hadronic calorimeters is also different for electrons and $\tau_{\text{had-vis}}$ candidates. Several variables are used to train BDTs, separately for 1- and 3-prong $\tau_{\text{had-vis}}$, to specifically reject electrons misidentified as $\tau_{\text{had-vis}}$ candidates. Similar to the discrimination against jets, 3 working points are defined corresponding to

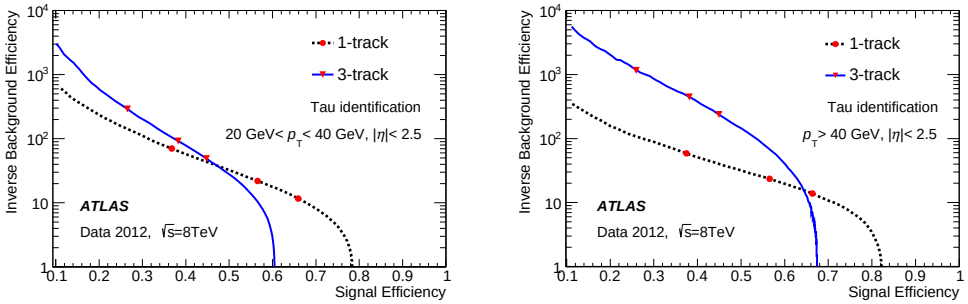

(a) (b)

Figure 5.8. Inverse background efficiencies as functions of signal efficiencies for (a) 20 GeV$<$ $p_{\mathrm{T}}^{\tau} < 40$ GeV and (b) $p_{\mathrm{T}}^{\tau} > 40$ GeV [143].

signal efficiencies. For the 2011 dataset these correspond to about 65%, 57% and 47%. The BDTs are retrained for the 2012 dataset, leading to efficiencies of 95%, 85% and 75%. For both the 2011 and 2012 algorithms, the set of variables may vary depending on the η region. The inverse background efficiencies of the electron veto for different

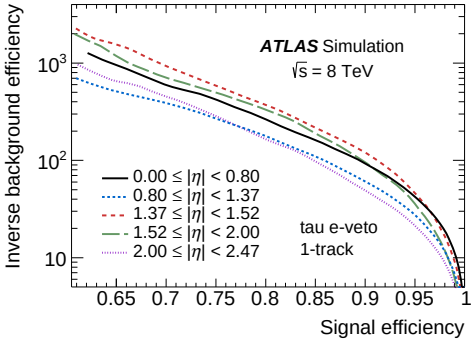

Figure 5.9. Inverse background efficiencies of the electron veto as functions of the signal efficiency for different pseudorapidities for 1-prong $\tau_{\text{had-vis}}$ candidates [143].

pseudorapidity ranges and as a function of the signal efficiency is shown in figure 5.9. The background efficiencies are measured in simulated $Z \to ee$ events.
In the analyses using the 2012 data, a separate veto is used to suppress electrons misidentified as 3-prong $\tau_{\text{had-vis}}$ candidates. They are binned in p_{T} and $|\eta|$ of the track with the highest p_{T}.

Discrimination against Muons

Muons are unlikely to be misidentified as $\tau_{\text{had-vis}}$ candidates and are mostly discarded by standard muon identification algorithms as described in section 5.5. In case a muon does deposit a large amount of energy in the calorimeters and fails muon spectrometer reconstruction, it may be misidentified as a $\tau_{\text{had-vis}}$ candidate. To reduce the amount of contamination due to muon misidentified as $\tau_{\text{had-vis}}$ candidates to a negligible one, a

simple cut-based selection using 4 (2) variables in 2011 (2012) is applied. The signal efficiency results in about 96%, while about 40% of muons misidentified as $\tau_{\text{had-vis}}$ candidates are discarded.

5.4.2. Energy Scale and Resolution

Since the LC calibration for jets used as seeds for $\tau_{\text{had-vis}}$ reconstruction is optimized neither for the mixture of hadrons observed in hadronic τ decays nor for the cone size used to measure the momentum of the $\tau_{\text{had-vis}}$ candidate, additional calibration is necessary to ensure that the $\tau_{\text{had-vis}}$ energy scale (TES) is the same as the true energy scale. This is achieved in several steps. First, calibration factors derived from simulation are applied and bring the TES within a few percent of the true energy scale. They also improve the $\tau_{\text{had-vis}}$ energy resolution (TER) and remove dependencies on η, the energy, pile-up and number of associated tracks. These correction factors are shown in figure 5.10 as functions of the energy of the $\tau_{\text{had-vis}}$ candidate at the LC scale, separately for 1- and 3-prong $\tau_{\text{had-vis}}$ candidates. They are derived from simulated $Z \to \tau\tau$, $W \to \tau\nu$ and $Z' \to \tau\tau$ samples. Afterwards, a minor correction is applied to the pseudorapidity of the

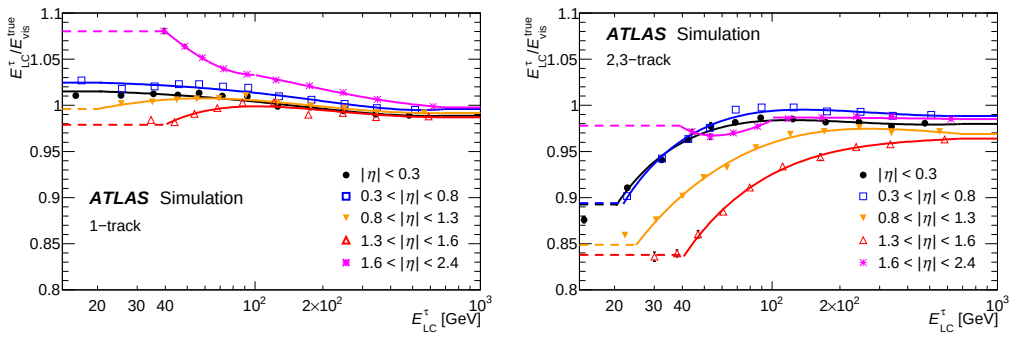

Figure 5.10. Correction factors for calibration of the TES for (a) 1-prong and (b) 3-prong hadronic τ decays, split up into different $|\eta|$ bins for $\sqrt{s} = 8\,\text{TeV}$ [143].

$\tau_{\text{had-vis}}$ candidates. This is necessary because of a bias originating from underestimated cluster energies in detector regions that are poorly instrumented. Finally, a certain amount of energy proportional to the number of vertices in a given event is subtracted to account for energy variations due to pile-up.

The final TER for 1-prong and 3-prong $\tau_{\text{had-vis}}$ candidates is shown in figure 5.11. It varies between about 20% at low energies and 5% at several hundred GeV.

5.5. Muons

Muons interact only very weakly with the detector, leave minimal deposits in the calorimeters and traverse the muon spectrometer (MS). Thus they are easily distinguishable from other particles and a very high and pure reconstruction efficiency can be achieved. In

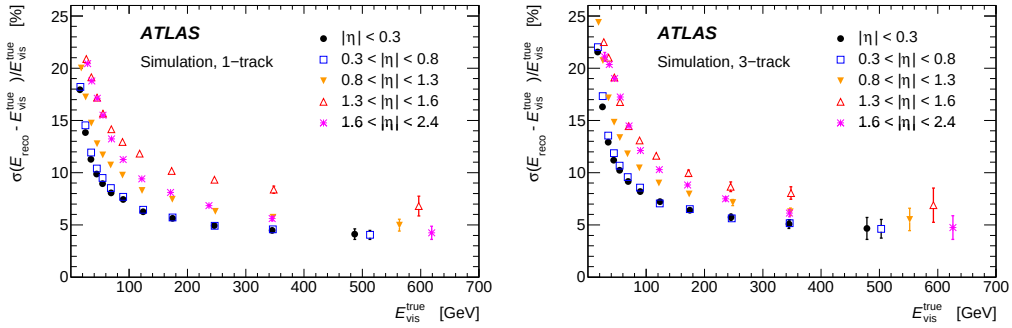

(a) (b)

Figure 5.11. Energy resolution for (a) 1-prong and (b) 3-prong $\tau_{\text{had-vis}}$ candidates for different $|\eta|$ bins [143].

the analyses presented in this thesis, events containing muons are vetoed. However, the background estimation method described in chapter 7 is based on a muon trigger and subsequent muon+jets event selection.

5.5.1. Trigger

Like other triggers in ATLAS the muon trigger is split up into 3 levels [77]. About 99% of the endcap regions but only 80% of the barrel are covered by muon trigger chambers due to the support structure and service shafts. At L1, hits in the RPCs or TGCs pointing to the primary vertex have to coincide both in space and time to be considered for muon reconstruction. Corresponding detector regions are then marked as RoIs and further processed by the L2 and EF triggers. Track construction at L2 is refined by adding information from the MDT chambers. The reconstructed muon at this level is combined with the best-matching inner detector track. Two different procedures are implemented

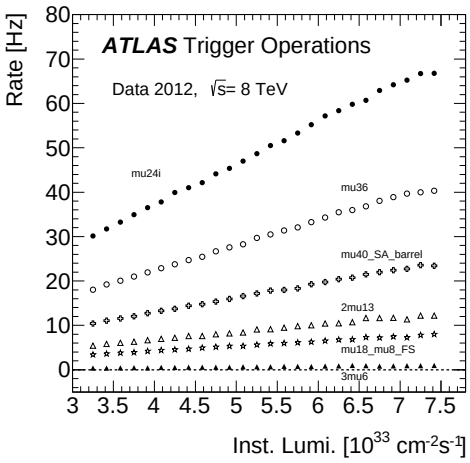

Figure 5.12. Trigger rates at EF for different single- and multi- muon triggers as functions of the instantaneous luminosity as measured in data [77].

at EF to reconstruct muons. One relies on information from the RoI combined with ID tracks while the other method finds additional muons that are not identified at L1. For this, candidates are built first from information in the full muon detectors and then tracks from the ID are searched for. Different criteria on the transverse momenta and isolation are used at different levels and for different triggers. Trigger rates are measured in data and simulation using a tag-and-probe approach. The rates for triggers used in the 2012 analysis presented here are shown in figure 5.12 as functions of the instantaneous luminosity. In figure 5.13 the efficiencies are shown as functions of the

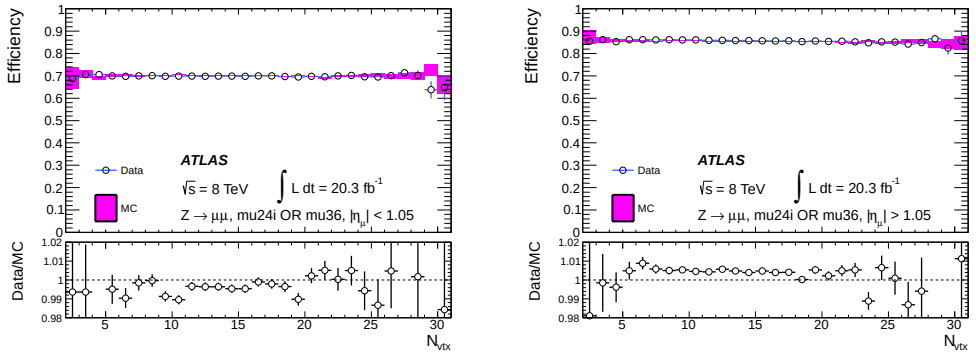

(a) (b)

Figure 5.13. Efficiencies of the muon trigger combination used in the 2012 analysis as functions of the number of reconstructed vertices in an event, separately for the (a) barrel and (b) endcap regions in data and simulation. The error bars indicate statistical uncertainties only [77].

number of reconstructed vertices in one event for the trigger combination used in the 2012 analysis.

5.5.2. Reconstruction

Muons are reconstructed based on information from the MS, inner detector and calorimeter [148]. Depending on what information from which sub-detector is used for reconstruction, different 'types' of muons are available. For the analyses presented here, only so-called combined + segment-tagged muons are used. To qualify as a combined muon, track reconstruction is run separately in the MS and ID and if a combination of these tracks is possible a combined track is formed. A track in the ID has to meet the following criteria to be considered for muon reconstruction in 2012 (2011) data: more than 0 (1) hit(s) in the pixel layer, at least 5 (6) SCT hits, no more than 2 pixel or SCT sensors are crossed but no hit is registered and for $0.1 < |\eta| < 1.9$ at least 9 hits in the TRT have to be registered. Additional criteria on TRT hits and the innermost layer of the pixel detector are used in the 2011 analysis. A requirement on the longitudinal impact parameter is applied to the 2012 data, $|z_0 \sin\theta| < 2\,\text{mm}$. Due to the limited coverage of the ID, muons are only reconstructed within $|\eta| < 2.5$. If a track in the ID is associated with at least one track segment in the MDT or CSC chambers once it is extrapolated to the MS, it qualifies as a segment-tagged muon. Segment-tagged muons increase the

acceptance of muons with low transverse momenta or muons in poorly instrumented detector regions. Reconstruction efficiencies for combined + segment-tagged muons are

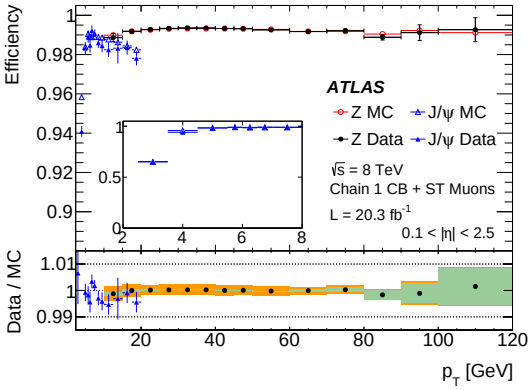

Figure 5.14. Muon reconstruction efficiencies for combined + segment-tagged muons as a function of their transverse momenta [148].

shown in figure 5.14. They are measured in simulation and data using a tag-and-probe method. The efficiency is about 99% for most of the detector regions. Since muons leave signatures in the detector that are easy to distinguish from other physics objects, no separate identification algorithm, as e.g. is the case for τ_{had}, is run.

5.6. Electrons

Electrons are not part of the final state in the analyses presented here and thus only selected to veto events containing them.

5.6.1. Reconstruction and Identification

Reconstruction of electrons with $|\eta| < 2.47$ is based on clustered energy deposits in the electromagnetic calorimeter [149]. These clusters are then matched to reconstructed tracks in the ID. Electrons with larger pseudorapidities are not taken into account in the analyses presented here and their reconstruction and identification is not described. The reconstruction of clusters reaches an efficiency of more than 99% for electrons with transverse energies $E_{\text{T}} > 15\,\text{GeV}$. At least one track satisfying quality criteria has to be matched to a cluster for an electron to be reconstructed. In case there are several tracks that can be matched, the best one is chosen by requiring a hit in the pixel layers and choosing the track with minimal distance to the cluster. The reconstruction algorithm used in 2012 is improved compared to the one used in 2011 to better take into account energy losses due to bremsstrahlung [150]. The total energy of an electron candidate after reconstruction is set by an estimate of the energy deposited before the EM calorimeter is reached, the measured energy of the cluster in the calorimeter and estimates for both longitudinal and lateral leakage, i.e. energy deposited outside the cluster and beyond the EM calorimeter [151].

Similarly to $\tau_{\text{had-vis}}$ candidates, a separate identification algorithm is run after reconstruction to discard other objects such as jets mimicking electrons. Employing information about the transverse and longitudinal shapes of showers in the calorimeter, matching between clusters and tracks and properties of the tracks in the ID, a cut-based identification algorithm is built. Electrons can then be selected at different levels of efficiencies and purities. The selections are binned in the transverse energy and pseudorapidity of the electrons. The selection is optimized in the 2012 data compared to that taken in 2011 to be more robust against pile-up. In addition to identification, electrons are required to pass certain isolation criteria. These are based on the amount of energy deposited in a certain cone around the cluster in the calorimeter or around the track in the ID.
Reconstruction and identification efficiencies are measured using tag-and-probe methods

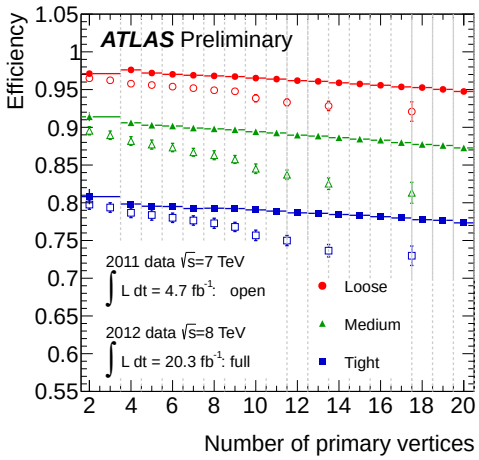

Figure 5.15. Electron identification efficiencies for different working points measured in data at $\sqrt{s} = 7\,\text{TeV}$ and $8\,\text{TeV}$ as functions of the number of reconstructed vertices in an event [149].

in both data and simulation. The efficiencies of the different working points for identification measured in data in 2011 and 2012 are shown in figure 5.15 as functions of the number of reconstructed vertices in an event.

5.6.2. Energy Scale

The energy scale of the electromagnetic calorimeter is calibrated using test-beam data [152]. The precise knowledge of the Z boson mass is employed to improve the electron energy scale and establish a linear response of the calorimeter. The calibration is split up into 3 steps. First, the signal from each cell in the calorimeter is converted into a corresponding energy based on the electronic calibration of the EM calorimeter. Afterwards, a calibration correction retrieved from simulation is applied. The final energy is determined by an additional in-situ calibration based on $Z \to ee$ events.

5.7. Missing Transverse Momentum

In proton-proton collisions, the momenta of incoming partons before scattering are expected to be negligible in the plane transverse to the beam axis. Using momentum conservation in this plane, a momentum imbalance called $\mathbf{E}_T^{\text{miss}}$ in the $x-y$-plane is calculated as the negative sum of the momenta of all detected particles [153]. Its magnitude is called missing transverse momentum henceforth and denoted as $E_{\text{T}}^{\text{miss}}$. Missing transverse momentum may arise due to particles that are not detected, like neutrinos, or mis-measurements in the calorimeters or elsewhere. The $\mathbf{E}_T^{\text{miss}}$ calculation is based on energy deposited in the calorimeters as well as muons from the MS. Fully reconstructed, identified and calibrated objects are used in the following order: electrons, jets, muons. If an energy deposit in a calorimeter is not associated with any of these objects, it is taken into account in a separate term denoted as CellOut which is calibrated at the EM scale. Photons are not taken into account since they are not considered in any of the analyses presented here. Hadronically decaying τ leptons are considered as the jets associated with them. An energy deposit associated with a certain object is not used for any other object. To obtain the $\mathbf{E}_T^{\text{miss}}$, first the x and y components are calculated as

$$E_{x,y}^{\text{miss}} = E_{x,y}^{\text{miss, Electrons}} + E_{x,y}^{\text{miss, Jets}} + E_{x,y}^{\text{miss, SoftJets}} + E_{x,y}^{\text{miss, Muons}} + E_{x,y}^{\text{miss, CellOut}} \quad (5.5)$$

For all objects, the same identification criteria as applied in the object selections are used. For the Jets term, only jets with $p_{\text{T}} > 20\,\text{GeV}$ are used, calibrated either using the EM+JES or LC+JES calibration for data taken in 2011 or 2012, respectively. Jets with 7 (10) GeV$< p_{\text{T}} < 20\,\text{GeV}$ are included in the SoftJets term calibrated at the EM (LC) scale for data taken in 2011 (2012). Photons are not included. Electrons have to satisfy $p_{\text{T}} > 10\,\text{GeV}$ to be considered for $\mathbf{E}_T^{\text{miss}}$ calculation. Muons are considered up to $|\eta| < 2.7$, i.e. in the full range of the MS. For $|\eta| < 2.5$, combined muons as described in section 5.5.2 are used. In the range $2.5 < |\eta| < 2.7$, which is not covered by the ID, muons reconstructed in the MS only are used.
The final $E_{\text{T}}^{\text{miss}}$ is given by

$$E_{\text{T}}^{\text{miss}} = \sqrt{\left(E_{\text{x}}^{\text{miss}}\right)^2 + \left(E_{\text{y}}^{\text{miss}}\right)^2}. \quad (5.6)$$

In figure 5.16, the $E_{\text{T}}^{\text{miss}}$ distributions in $Z \to \mu\mu$ and $W \to e\nu$ events seen in data are compared to simulation. Only $W \to e\nu$ events contain real $E_{\text{T}}^{\text{miss}}$ due to the neutrino in the final state.
The resolution of E_x^{miss} and E_y^{miss} as functions of the total transverse energy in an event, i.e. the sum of the total transverse energy in the calorimeters and p_{T} of muons, in simulated $t\bar{t}$ events is shown in figure 5.17. In the analyses presented in this thesis, the $E_{\text{T}}^{\text{miss}}$ version without pile-up suppression is used. As can be seen, the differences between the different versions are small.

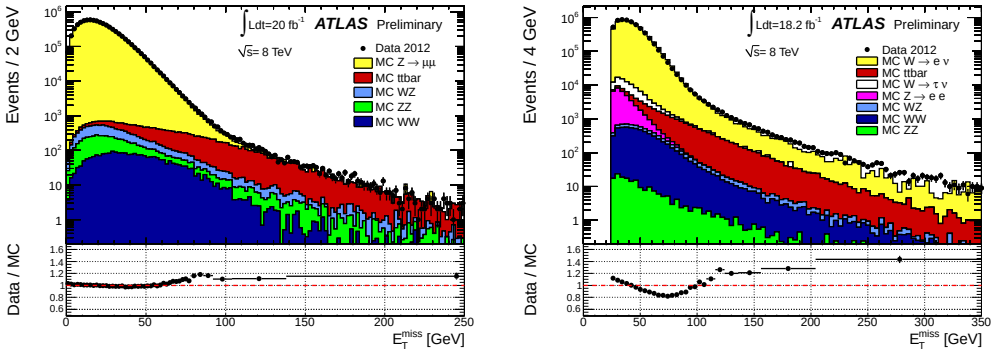

(a) (b)

Figure 5.16. $E_{\mathrm{T}}^{\mathrm{miss}}$ measured in data in (a) $Z \to \mu\mu$ events and (b) $W \to e\nu$ events compared to simulation. The distributions agree well in $Z \to \mu\mu$ events and the discrepancies in $W \to e\nu$ events are likely due to multi-jet background, which is not included in the simulation samples [153].

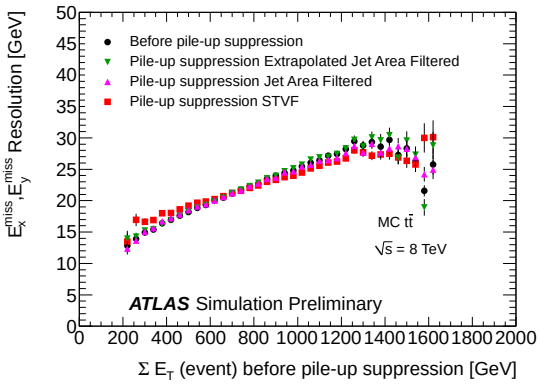

Figure 5.17. E_x^{miss} and $E_{y\_}^{\mathrm{miss}}$ resolution as functions of the total transverse energy in an event shown for simulated $t\bar{t}$ events. The plot contains two entries for each event, one for E_x^{miss} and one for E_y^{miss}. In the analyses presented in this thesis, the version of $E_{\mathrm{T}}^{\mathrm{miss}}$ 'Before pile-up suppression' is used [153].

5.8. Removal of Objects Overlapping Geometrically

Energy deposits can be assigned to more than one object during reconstruction. The procedures for overlapping objects differ between the 2011 and 2012 data. The full object selection requirements mentioned below are explained in more detail in chapter 6.
In the 2011 data, the following procedure is applied in this order before any selected, reconstructed objects are vetoed:

- Muon candidates are removed if they are within $\Delta R < 0.4$ of a jet passing all p_{T}, η and JVF requirements.
- Hadronically decaying τ candidates are removed if they are within $\Delta R < 0.2$ of any selected electron or muon.

- Jets are removed if they are within $\Delta R < 0.2$ of a selected $\tau_{\text{had-vis}}$ candidate.
- Finally, jets are removed if they are within $\Delta R < 0.2$ of a selected electron.

The order and requirements on the objects applied in the 2012 data are slightly different:

- The closest jet within $\Delta R < 0.2$ to each selected electron is removed
- Then, any electron candidate within $\Delta R < 0.4$ of a jet passing all p_{T}, η and JVF requirements is removed.
- Next, muon candidates are removed if they are within $\Delta R < 0.4$ of a jet passing all p_{T}, η and JVF requirements.
- Hadronically decaying τ candidates are rejected if they are within $\Delta R < 0.2$ of any selected electron or muon.
- Finally, jets are removed if they are within $\Delta R < 0.2$ of a selected $\tau_{\text{had-vis}}$ candidate.

6 Analysis Overview

In the analyses presented in this thesis, charged Higgs bosons are searched for in a final state containing a hadronically decaying τ lepton, $E_{\mathrm{T}}^{\mathrm{miss}}$ and jets including at least one b-tagged jet. Thus major background contributions to these searches arise from events with $t\bar{t}$ or single top quark production, multi-jet and W+jets events. Minor background contributions are due to Z+jets and diboson production.
However, in the analyses presented here, background processes are not classified according to their production mode but rather depending on the type of reconstructed object that is identified as the $\tau_{\text{had-vis}}$ candidate. Thus two types of events exist: those with a true τ_{had} and those with another object identified as the $\tau_{\text{had-vis}}$ candidate.
The major background contribution consists of events with a true hadronically decaying τ lepton. Other background contributions are categorized slightly differently in the 7 TeV and 8 TeV analyses. For the 7 TeV analysis, events where a jet is misidentified as the $\tau_{\text{had-vis}}$ candidate are further subdivided into events due to multi-jet production and events from W+jets production. In the 8 TeV analysis no further subcategorization is done, but only one background contribution is assessed for all events where a jet is misidentified as the $\tau_{\text{had-vis}}$ candidate. These contributions, events with a true τ_{had} and events where a jet is misidentified as a $\tau_{\text{had-vis}}$ candidate, dominate the background and are estimated using data-driven methods both in the 7 TeV and 8 TeV analyses. A minor background where light leptons are misidentified as $\tau_{\text{had-vis}}$ candidates is estimated in a data-driven method in the 7 TeV analysis but based on corrected simulation in the 8 TeV analysis.
The event selection for the 7 TeV analysis and the low-mass and high-mass H^+ searches at 8 TeV are optimized separately with the aim of suppressing background events while retaining as many potential signal events as possible. This optimization is mostly based on simulation samples. For the optimization of the 8 TeV analyses, a data-driven approach is used for estimating the background contribution due to multi-jet events. The event selections are optimized based on expected limits as explained in chapter 9.1.
Data quality requirements as mentioned in chapter 4.1.2 are applied in all analyses presented here. Events containing one or more jet(s) with $p_{\mathrm{T}} > 20\,\mathrm{GeV}$ (25 GeV), that is/are likely due to instrumental effects like noise in the EM calorimeter and large noise signals in the hadronic end-cap calorimeters or non-collision background, are discarded in the data taken in 2011 (2012). The primary vertex in the event is required to have at least five associated tracks.
Both in the 2011 and 2012 analyses, the transverse mass of the $\tau_{\text{had-vis}}$ candidate and $E_{\mathrm{T}}^{\mathrm{miss}}$ is used as final discriminating variable after all other event selection requirements specified in sections 6.1 and 6.2 are applied. This is defined as

$$m_{\mathrm{T}} = \sqrt{2p_{\mathrm{T}}^{\tau}E_{\mathrm{T}}^{\mathrm{miss}}(1-\cos\Delta\phi)}, \tag{6.1}$$

where $\Delta\phi$ is the azimuthal angle between the $\tau_{\text{had-vis}}$ candidate and $E_{\text{T}}^{\text{miss}}$. The transverse mass corresponds to the transverse mass of the W boson in SM top quark decays $t \to bW \to b\tau\nu$ and to the transverse mass of the H^+ in the case of signal events.

6.1. Search for Low-mass Charged Higgs Bosons at $\sqrt{s} = 7$ TeV

The event selection is optimized for the following process and final state:

$$t\bar{t} \to (W^-\bar{b})(bH^+) \to (q\bar{q}'\bar{b})(b\tau^+_{\text{had}}\nu)$$

Only data with all sub-systems operational is used. This results in an integrated luminosity of $4.6\,\text{fb}^{-1}$. A combined $\tau_{\text{had-vis}}$+$E_{\text{T}}^{\text{miss}}$ trigger is used, where the threshold is 29 GeV on the $\tau_{\text{had-vis}}$ trigger object and 35 GeV for the $E_{\text{T}}^{\text{miss}}$ trigger. Although the thresholds on the $\tau_{\text{had-vis}}$ trigger object and $E_{\text{T}}^{\text{miss}}$ trigger are the same during the whole year, two slightly different trigger definitions were used for $2.2\,\text{fb}^{-1}$ and $2.4\,\text{fb}^{-1}$ of data, respectively. The following event selection is then applied:

- At least four jets are required with $p_{\text{T}} > 20\,\text{GeV}$, $|\eta| < 2.5$ and $|\text{JVF}| > 0.75$.
- The event contains exactly one $\tau_{\text{had-vis}}$ candidate with $p_{\text{T}} > 40\,\text{GeV}$ and $|\eta| < 2.3$ passing 'tight' likelihood identification criteria and no additional $\tau_{\text{had-vis}}$ candidate with $p_{\text{T}} > 20\,\text{GeV}$ passing these η and identification requirements. The selected $\tau_{\text{had-vis}}$ candidate has to overlap geometrically ($\Delta R < 0.2$) with the $\tau_{\text{had-vis}}$ trigger object.
- If a selected electron and muon share the same ID track, the event is discarded.
- No electron passes 'tight' identification with $E_{\text{T}} > 20\,\text{GeV}$ and $|\eta| < 2.47$ (excluding the transition region between the barrel and end-cap calorimeters, $1.37 < |\eta| < 1.52$) as well as E_{T}- and η-dependent calorimeter- and track-based isolation requirements with cone sizes of $\Delta R < 0.2$ and 0.3, respectively.
- No isolated muon passing 'tight' identification with $p_{\text{T}} > 20\,\text{GeV}$ is found. To pass the isolation requirement, the energy deposited in the calorimeter (the transverse momentum of all ID tracks) has to be less than 4 GeV (2.5 GeV) in a cone of radius $\Delta R < 0.2$ (< 0.3) around the muon but excluding the muon itself.
- The missing transverse momentum satisfies $E_{\text{T}}^{\text{miss}} > 60\,\text{GeV}$.
- The quantity $\frac{E_{\text{T}}^{\text{miss}}}{0.5\cdot\sqrt{\sum p_{\text{T}}^{\text{PVtrk}}}}$ (also referred to as $E_{\text{T}}^{\text{miss}}$ significance) must be greater than $13\,\text{GeV}^{1/2}$. Here, $\sum p_{\text{T}}^{\text{PVtrk}}$ is the sum over the transverse momenta of all tracks with $p_{\text{T}} > 1\,\text{GeV}$, $|z_0| < 1.5\,\text{mm}$, $|d_0| < 1.5\,\text{mm}$, at least 1 hit in the pixel and 6 hits in the SCT detector originating from the primary vertex. This variable is used because of its robustness against pile-up interactions.
- At least one of the selected jets is b-tagged at a 70% efficient working point.

· The mass of the hadronically decaying top quark candidate jjb with the highest p_{T} is required to satisfy $120\,\text{GeV} < m_{jjb} < 240\,\text{GeV}$. Here, b denotes a b-tagged jet and j denotes jets failing the b-tagging requirement but passing all other jet selection requirements.

The requirements on the transverse momentum of the $\tau_{\text{had-vis}}$ candidate and $E_{\text{T}}^{\text{miss}}$ in this offline selection are more stringent than those used in the online selection.
Expected numbers of background events passing this selection, except for multi-jet events, are summarized in table 6.1, where 'Preselection' contains all data quality requirements, the trigger and jet selection. The numbers shown here are based on simulation (see chapter 4.2.3), but data-driven methods are used to estimate the background contributions as described in chapters 7 and 8. The expected signal efficiencies of the full event selection

Selection	$t\bar{t}$	Single top quark	W+jets
Preselection	48806	20859	5662
$\tau_{\text{had-vis}}$ requirement	1202	1084	108
Electron/muon veto	1050	1081	102
$E_{\text{T}}^{\text{miss}}$ requirement	764	755	69
$\frac{E_{\text{T}}^{\text{miss}}}{0.5\cdot\sqrt{\sum p_{\text{T}}^{\text{PVtrk}}}}$ requirement	541	527	49
b-tagged jet requirement	472	70	39
m_{jjb} requirement	269	33	18

Table 6.1. Expected background events not including multi-jet events in $4.6\,\text{fb}^{-1}$ of data at $\sqrt{s} = 7\,\text{TeV}$ passing the event selection. Numbers are based on simulation samples. The $t\bar{t}$ sample contains only decays with at least one lepton in the final state and only $W \to \tau\nu$ decays are considered for the W+jets sample [154].

are shown in table 6.2. They generally tend to increase for higher H^+ masses since the higher the H^+ mass is, the higher the $\tau_{\text{had-vis}}$ candidate's energy. However, the closer the H^+ mass is to m_{top}, the lower the momentum of the b-quark produced in the decay $t \to H^+b$, making it harder to b-tag the corresponding jet.

m_{H^+} [GeV]	Efficiency in %
90	0.17
100	0.19
110	0.23
120	0.27
130	0.30
140	0.31
150	0.33
160	0.33

Table 6.2. Signal efficiencies in % using the 2011 H^+ selection determined from simulation for the different H^+ masses [154].

6.2. Search for Low-mass and High-mass Charged Higgs Bosons at $\sqrt{s} = 8$ TeV

The event selection applied is optimized separately for the search for low-mass and high-mass charged Higgs bosons. Due to the very similar topology, however, some requirements are identical in both searches. The searches target the following final states:

- for the low-mass H^+ search:

$$t\bar{t} \to (W^-\bar{b})(bH^+) \to (q\bar{q}'\bar{b})(b\tau^+_{\text{had}}\nu)$$

- for the high-mass H^+ search:

$$g\bar{b} \to \bar{t}H^+ \to (W^-\bar{b})H^+ \to (q\bar{q}'\bar{b})(\tau^+_{\text{had}}\nu) \text{ in the 5FS and}$$
$$gg \to \bar{t}bH^+ \to (W^-\bar{b})bH^+ \to (q\bar{q}'\bar{b})b(\tau^+_{\text{had}}\nu) \text{ in the 4FS,}$$

  where the only difference is an additional b-quark in the 4FS approximation compared to the 5FS.

The final state in the low-mass H^+ search is identical to that in the 4FS approximation. Only data recorded with all ATLAS sub-systems operational is used, resulting in an integrated luminosity of $19.5\,\text{fb}^{-1}$. Compared to the $20.3\,\text{fb}^{-1}$ labeled as 'Good for Physics' in figure 4.1, $0.8\,\text{fb}^{-1}$ can not be analyzed for the searches presented here due to non-availability of the used triggers. All events are required to pass a combined $\tau_{\text{had-vis}} + E_{\text{T}}^{\text{miss}}$ trigger. The threshold at EF on the transverse momentum of the $\tau_{\text{had-vis}}$ trigger object is 27 GeV or 29 GeV and 40 GeV or 50 GeV for the $E_{\text{T}}^{\text{miss}}$ trigger. The multiple trigger thresholds result from varying trigger definitions throughout the data taking period in 2012. In detail the combinations are:

- $p_{\text{T}} > 29\,\text{GeV}$ for the $\tau_{\text{had-vis}}$ trigger object and $E_{\text{T}}^{\text{miss}} > 40\,\text{GeV}$ used in $1.3\,\text{fb}^{-1}$ of data
- $p_{\text{T}} > 29\,\text{GeV}$ for the $\tau_{\text{had-vis}}$ trigger object and $E_{\text{T}}^{\text{miss}} > 50\,\text{GeV}$ used in $8.5\,\text{fb}^{-1}$ of data
- $p_{\text{T}} > 27\,\text{GeV}$ for the $\tau_{\text{had-vis}}$ trigger object and $E_{\text{T}}^{\text{miss}} > 50\,\text{GeV}$ used in $9.7\,\text{fb}^{-1}$ of data

The following event selection is then applied:

- At least four (three) jets are required with $p_{\text{T}} > 25\,\text{GeV}$ and $|\eta| < 2.5$ for the low-mass (high-mass) signal selection. If a jet satisfies $|\eta| < 2.4$ and $p_{\text{T}} < 50\,\text{GeV}$, then $|\text{JVF}| > 0.5$ is required additionally.
- The event contains exactly one $\tau_{\text{had-vis}}$ candidate with $p_{\text{T}} > 40\,\text{GeV}$ and $|\eta| < 2.3$ passing 'tight' BDT identification criteria. No additional $\tau_{\text{had-vis}}$ candidate with $p_{\text{T}} > 20\,\text{GeV}$ passing these η and identification requirements is allowed. The selected $\tau_{\text{had-vis}}$ candidate must also overlap geometrically ($\Delta R < 0.2$) with the τ trigger object.

- If a selected electron and muon share the same ID track, the event is discarded.
- No electron passes 'tight' identification with $E_{\mathrm{T}} > 25\,\mathrm{GeV}$ and $|\eta| < 2.47$ (excluding the transition region between the barrel and end-cap calorimeters, $1.37 < |\eta| < 1.52$) as well as E_{T}- and η-dependent calorimeter- and track-based isolation requirements with cone sizes of $\Delta R < 0.2$ and 0.3, respectively.
- No isolated muon passing 'tight' identification with $p_{\mathrm{T}} > 25\,\mathrm{GeV}$ is found, where the isolation requirement is based on an algorithm using a cone size that shrinks with increasing momentum of the muon candidate and is of a maximal size $\Delta R = 0.4$. The scalar sum of the transverse momenta of all tracks within this cone, excluding the muon itself, must be less then 5% of the transverse momentum of the muon.
- The missing transverse momentum satisfies $E_{\mathrm{T}}^{\mathrm{miss}} > 65\,\mathrm{GeV}$ ($> 80\,\mathrm{GeV}$) for the low-mass (high-mass) H^+ search.
- The quantity $\frac{E_{\mathrm{T}}^{\mathrm{miss}}}{0.5 \cdot \sqrt{\sum p_{\mathrm{T}}^{\mathrm{PVtrk}}}}$ ($E_{\mathrm{T}}^{\mathrm{miss}}$ significance) must be greater than $13\,\mathrm{GeV}^{1/2}$ ($12\,\mathrm{GeV}^{1/2}$) for the low-mass (high-mass) H^+ search. Here, $\sum p_{\mathrm{T}}^{\mathrm{PVtrk}}$ is the sum over the transverse momenta of all tracks with $p_{\mathrm{T}} > 1\,\mathrm{GeV}$, $|z_0| < 1.5\,\mathrm{mm}$, $|d_0| < 1.5\,\mathrm{mm}$, at least 1 hit in the pixel and 6 hits in the SCT detector originating from the primary vertex.
- At least one of the selected jets is b-tagged at a 70% efficient working point.

Compared to the analysis based on the data taken in 2011, the selection of a hadronically decaying top quark is dropped. In the 2012 data, this requirement would have only reduced the amount of data further but not have improved the ratio of potential signal to background events.
A final cut on the transverse mass is placed at $m_{\mathrm{T}} > 20\,\mathrm{GeV}$ (40 GeV) for the low-mass (high-mass) signal selection. This cut is motivated in chapter 7.4.1.

Expected events due to $t\bar{t}$, W+jets, single top and Z+jets processes passing the

Selection	$t\bar{t}$	Single top	W+jets	Z+jets
Preselection	157976	14651	95313	8301
$\tau_{\text{had-vis}}$ requirement	7637	607	5885	1169
Electron/muon veto	7013	574	5812	1048
$E_{\mathrm{T}}^{\mathrm{miss}}$	4164	356	3456	437
b-tagged jet requirement	3476	268	540	65

Table 6.3. Expected events in $19.5\,\mathrm{fb}^{-1}$ of data at $\sqrt{s} = 8\,\mathrm{TeV}$ passing the low-mass H^+ selection based on simulation. Data quality and trigger requirements are combined with the jet selection into the 'Preselection'. The $E_{\mathrm{T}}^{\mathrm{miss}}$ selection includes both the requirements on $E_{\mathrm{T}}^{\mathrm{miss}}$ and $E_{\mathrm{T}}^{\mathrm{miss}}$ significance [155].

selection criteria except for the one on m_{T} are summarized in tables 6.3 and 6.4 for the low-mass and high-mass H^+ searches, respectively. These numbers are derived from simulation samples (see chapter 4.2.3), but data-driven methods are used to estimate the background contributions as described in chapters 7 and 8. The expected contributions

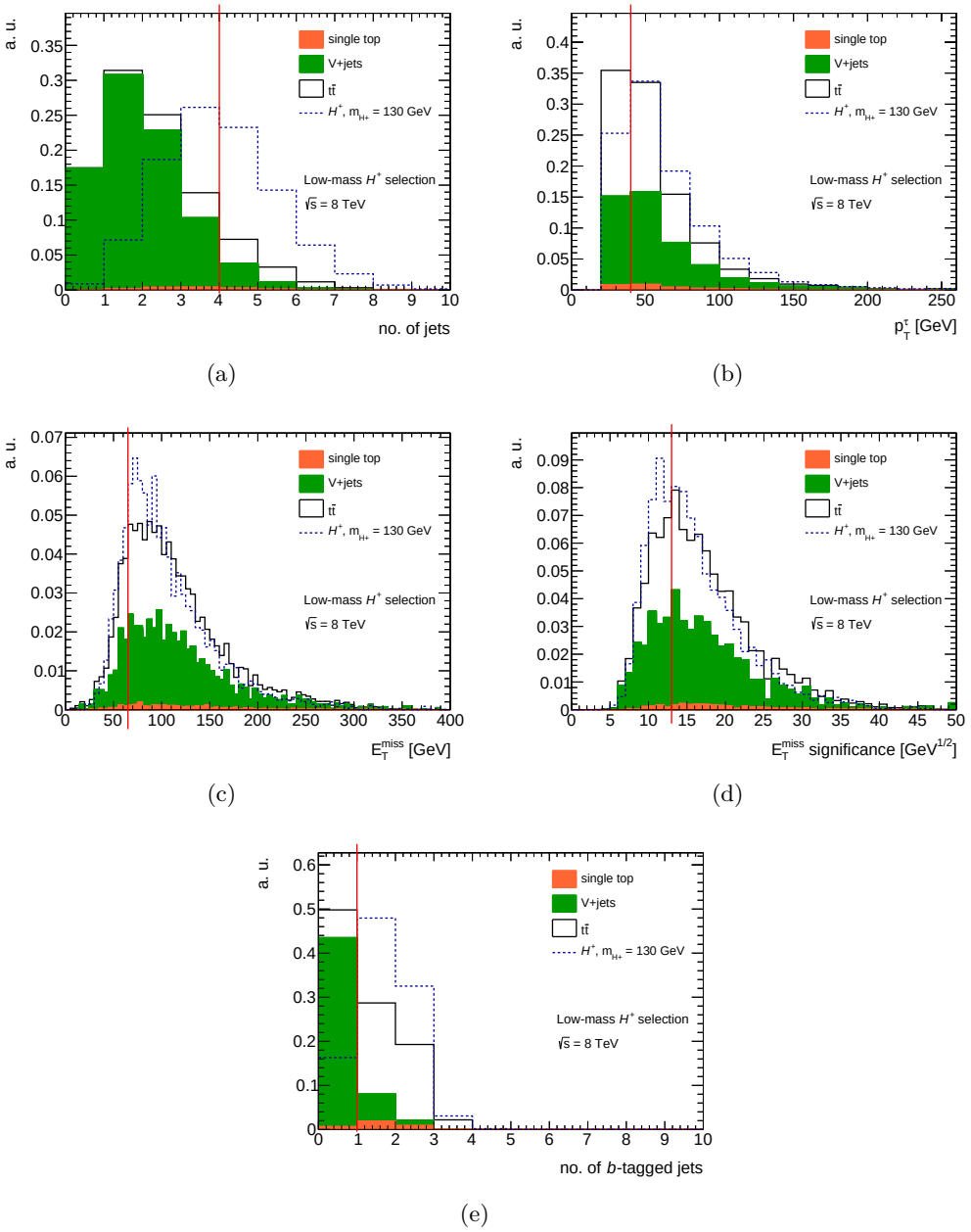

Figure 6.1. Expected contributions from different background processes to the low-mass H^+ search in data taken at $\sqrt{s} = 8\,\text{TeV}$. Contributions from multi-jet processes are not included. The relative contribution of all shown background processes is normalized according to their cross sections but the overall background normalization is arbitrary. Hypothetical signal with $m_{H^+} = 130\,\text{GeV}$ is scaled arbitrarily and overlaid. Each variable is shown just before the requirement indicated by the vertical red line is imposed. Displayed are distributions of (a) no. of jets passing the selection, (b) p_T of the leading $\tau_\text{had-vis}$ candidate with $p_\text{T} > 20\,\text{GeV}$, (c) E_T^miss, (d) E_T^miss significance and (e) no. of b-tagged jets.

from different background processes and hypothetical signal for events with true $\tau_\text{had-vis}$ candidates are also shown in figure 6.1 and 6.2 for the low-mass and high-mass H^+

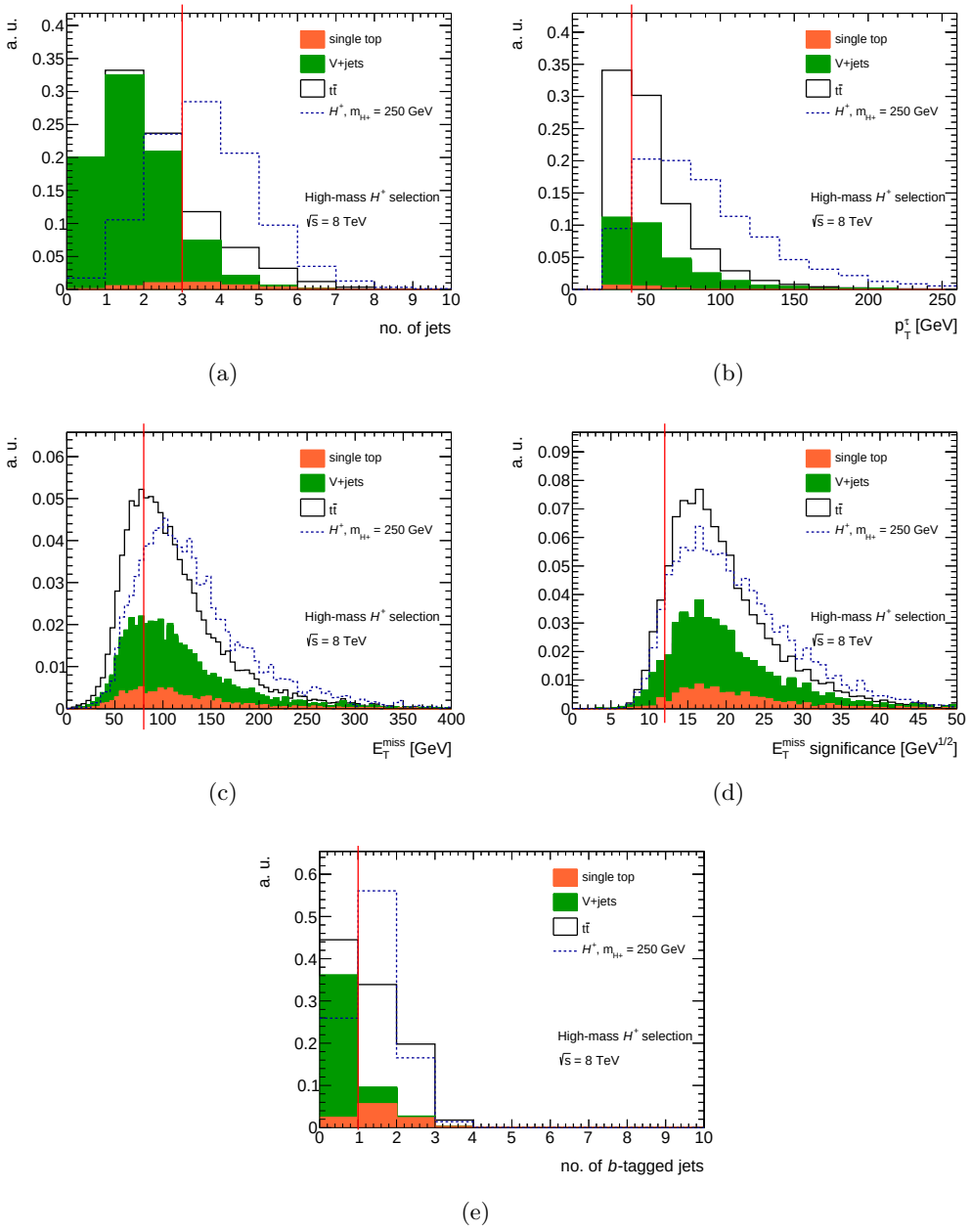

Figure 6.2. Expected contributions from different background processes to the high-mass H^+ search in data taken at $\sqrt{s} = 8\,\text{TeV}$. Contributions from multi-jet processes are not included. The relative contribution of all shown background processes is normalized according to their cross sections but the overall background normalization is arbitrary. Hypothetical signal with $m_{H^+} = 250\,\text{GeV}$ is scaled arbitrarily and overlaid. Each variable is shown just before the requirement indicated by the vertical red line is imposed. Displayed are distributions of (a) no. of jets passing the selection in each event, (b) p_T of the leading $\tau_\text{had-vis}$ candidate with $p_\text{T} > 20\,\text{GeV}$, (c) E_T^miss, (d) E_T^miss significance and (e) no. of b-tagged jets in all events.

searches, respectively. Variables are shown just before a certain requirement as described

Selection	$t\bar{t}$	Single top	W+jets	Z+jets
Preselection	240857	31500	293058	21567
$\tau_{\text{had-vis}}$ requirement	12928	1429	19183	3275
Electron/muon veto	11280	1346	18980	2951
$E_{\text{T}}^{\text{miss}}$	7179	884	12150	1323
b-tagged jet requirement	5791	626	1707	156

Table 6.4. Expected events in 19.5 fb^{-1} of data at $\sqrt{s} = 8$ TeV passing the high-mass H^+ selection based on simulation. Data quality and trigger requirements are combined with the jet selection into the 'Preselection'. The $E_{\text{T}}^{\text{miss}}$ selection includes both the requirements on $E_{\text{T}}^{\text{miss}}$ and $E_{\text{T}}^{\text{miss}}$ significance [155].

above, in each case indicated by the vertical red line, is imposed.

The expectation from SM $t\bar{t}$, single top and W/Z+jets events and different signal

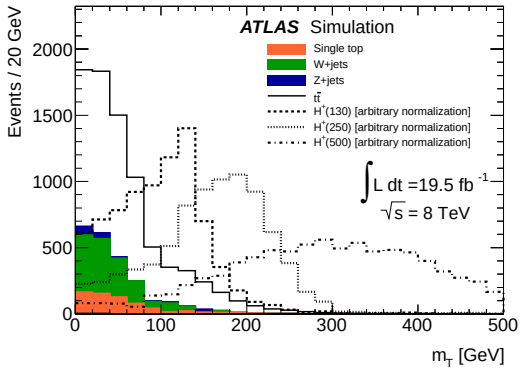

Figure 6.3. The transverse mass distribution shown for events passing the high-mass signal selection but for the full m_{T} range. Simulated background contributions without multi-jet processes are shown stacked and normalized to luminosity while hypothetical signals are overlaid and scaled arbitrarily for shape comparison [156].

hypotheses after applying all requirements except for the m_{T} selection is shown in figure 6.3. The high-mass H^+ selection is applied to all signal samples shown in this plot to illustrate the shift in m_{T} to higher values for higher H^+ masses.

The efficiencies of the signal selection depending on the H^+ mass for the low-mass and the high-mass H^+ searches are given in table 6.5. The final m_{T} requirement is not included in these tables since it is used due to a background estimation method only and not to achieve a better ratio of potential signal and background events passing the full selection. As is shown in chapter 9.4, this additional requirement does not affect the expected limits in a noticeable way. Similar to the 2011 analysis, the efficiencies first increase for higher H^+ masses since the momentum of the $\tau_{\text{had-vis}}$ increases as well. For low-mass H^+ with m_{H^+} close to m_{top}, the efficiencies plateau since it is harder to b-tag a jet if the b quark from the top quark decay is produced almost at rest. For the high-mass H^+ search, the efficiencies increase over the entire investigated mass range. For higher H^+ masses, the momentum of the $\tau_{\text{had-vis}}$ candidate is larger, $E_{\text{T}}^{\text{miss}}$ increases

m_{H^+} [GeV]	Efficiency in %	m_{H^+} [GeV]	Efficiency in %
80	0.60	180	1.78
90	0.72	190	1.88
100	0.76	200	2.00
110	0.85	225	2.31
120	0.92	250	2.75
130	1.02	275	2.93
140	1.19	300	3.15
150	1.19	350	3.60
160	1.18	400	4.05
		450	4.19
		500	4.48
		550	4.78
		600	4.89
		750	5.48
		1000	5.83

Table 6.5. Signal efficiencies in % determined from simulation for the different H^+ masses considered in the (left column) low-mass H^+ and (right column) high-mass H^+ searches. The final m_{T} requirement is not applied [155].

and jets containing b quarks can be b-tagged with high efficiency.

7 Estimation of Background Events with true hadronically decaying τ Leptons

Events with true hadronically decaying τ leptons constitute the major background to the charged Higgs boson searches presented in this thesis. Since it is difficult to define a control region with $\tau_{\text{had-vis}}$+jets events in data to assess this background, μ+jets events are used instead, where the muon is removed and replaced with a τ lepton. The τ lepton is 'embedded' into the event, hence the name embedding method. Compared to $\tau_{\text{had-vis}}$+jets events, μ+jets events feature a very similar topology. Since the branching ratio $H^+ \to \mu\nu$ is negligible in the type II 2HDM assumed, a muon+jets sample is expected to be signal free.

7.1. Embedding Method

The method used to estimate the background contribution of events with a true τ_{had} lepton is referred to as embedding [157]. It relies on the assumptions that lepton universality holds for W boson decays, thus the decay $W \to \mu\nu$ occurs with the same probability as $W \to \tau\nu$ and the topologies of $W \to \mu\nu$ and $W \to \tau\nu$ events are identical except for the presence of a muon and a τ lepton, respectively.
In this method, a muon+jets selection, detailed in section 7.2, is applied. This selection is consistent with the following decay:

$$t\bar{t} \to (W^-\bar{b})(W^+b) \to (q\bar{q}'\bar{b})(\mu^+\nu b),$$

but other events with a muon, jets and $E_{\text{T}}^{\text{miss}}$ in the final state are selected as well e.g. from W+jets or single top quark production. Events from Z+jets as well as diboson production are selected to a far lesser extent. Similar to the signal selections, slightly differing requirements are applied for the low-mass and high-mass H^+ searches. In the events passing the respective selection, the momentum of the muon, $\vec{p}_\mu$ is extracted. It is then rescaled to account for the higher mass of the τ lepton, m_τ:

$$\vec{p}_\tau = \frac{\sqrt{E_\mu^2 - m_\tau^2}}{\sqrt{\vec{p}_\mu \cdot \vec{p}_\mu}} \cdot \vec{p}_\mu, \tag{7.1}$$

where E_μ is the energy of the muon. The particle is subsequently labeled as a τ lepton. To produce the τ decay products, this τ lepton is fed into TAUOLA and additional photon final state radiation is generated using PHOTOS.
In the embedding technique used for the 2011 data, energy depositions in the calorimeter

from the original data event are replaced (added) in a cone with $\Delta R < 0.1$ ($\Delta R < 0.3$) around the muon by (to) those of the τ decay product. The original track and MS segments are removed.
To minimize the removal of energy depositions not caused by the selected muon, a more sophisticated version of this method is used in the 2012 data. The extracted muon momentum is used to simulate another muon and the energy depositions in the calorimeter ascribed to this muon are removed from the original event. The track and MS segments of the original muon are removed as well.
In both the 2011 and 2012 version of the embedding technique, energy deposits in the calorimeters are removed, replaced or added at cell level.
The τ decay products are propagated through ATLAS detector simulation and merged with the original event except for the muon. The hybrid event is then propagated through full ATLAS reconstruction except for the track reconstruction. The full procedure is shown schematically in figure 7.1. Since in the analyses presented here only hadronically

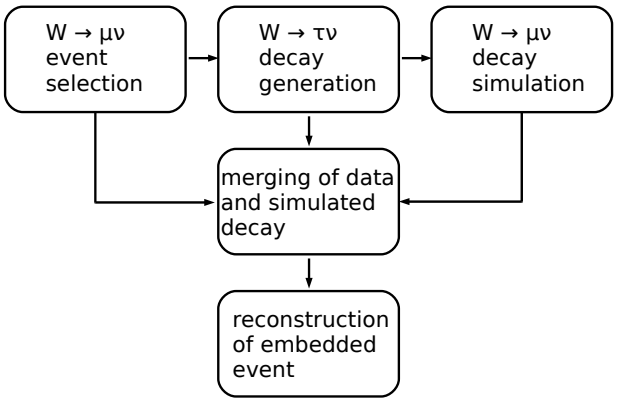

Figure 7.1. Schematic flowchart of the embedding procedure. After selecting $W \to \mu\nu$ events, the momenta of the muons are rescaled to produce $W \to \tau\nu$ decays. To remove the original muons, $W \to \mu\nu$ events are simulated using the original kinematic information. The original events except for the muons are then merged with the τ decay products and the hybrid events are reconstructed.

decaying τ leptons are considered, TAUOLA is forced to decay all τ leptons hadronically. Kinematic information about the original muon is saved in the final event for applying necessary corrections as described below.
In figure 7.2, the embedding procedure is illustrated with a data event: starting from the $W \to \mu\nu$ event, simulating the τ_{had} decay and then finally merging the original event except for the muon with the decay products of the τ lepton.
Compared to simulation, the embedding method has the advantage that everything except for the τ lepton, including the underlying event, pile-up, detector noise, number of jets and $E_{\text{T}}^{\text{miss}}$ except for the neutrinos resulting from the τ decay, is taken directly from data. Only the hadronic decay products of the τ lepton and the neutrinos stemming from this decay are taken from simulation. Additionally, the method does not rely on cross section calculations and their uncertainties for normalization.

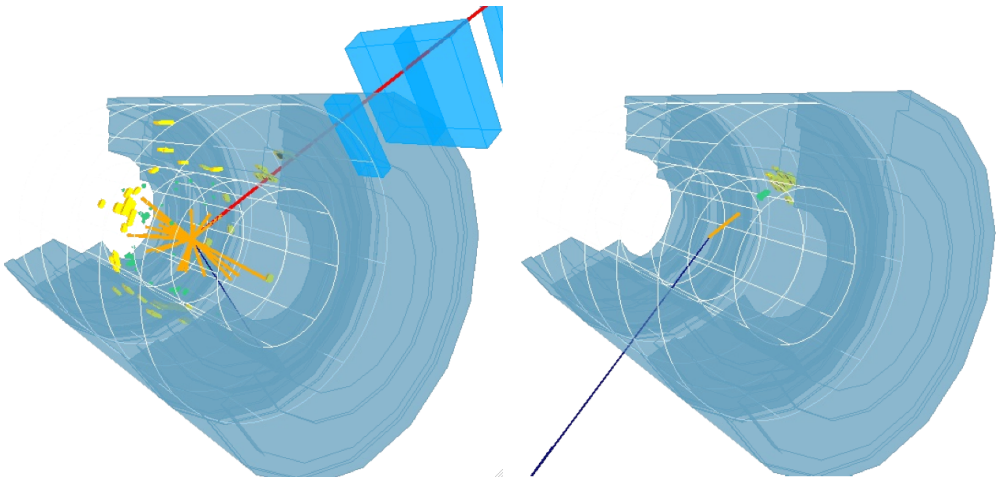

(a) $W \to \mu\nu$ event (b) simulated τ_{had} decay

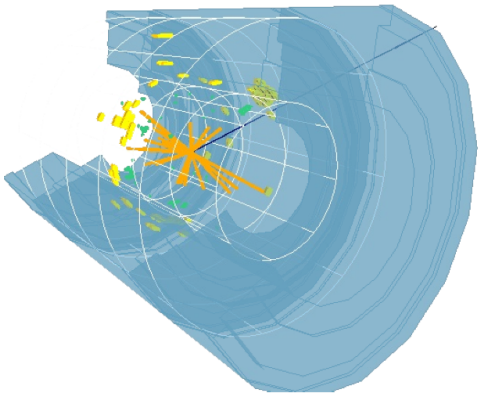

(c) embedded hybrid event

Figure 7.2. Displays of the (a) $W \to \mu\nu$ event, (b) simulated hadronic τ lepton decay and (c) embedded hybrid event in a cut-away view of the ATLAS detector. The muon is shown in red and traverses the muon chambers, $E_{\text{T}}^{\text{miss}}$ is shown in dark blue. The $\tau_{\text{had-vis}}$ candidate can be identified by its track (orange) and deposits in the calorimeters (green and yellow).

7.2. μ+Jets Selection

The muon+jets selections applied are similar to the signal selections except for all τ-related requirements. They are also looser to minimize any bias possibly introduced by the selection. The data quality cuts used in the μ+jets selection are the same as those in the respective signal selections. As for the signal selection, the muon+jets selection applied to 2011 data differs from that applied to 2012 data. For data taken in 2012, separate low-mass and high-mass selections are applied.
Events from $W \to \tau\nu_\tau \to \mu\nu_\mu\nu_\tau\nu_\tau$ that can pass the μ+jets selections and then end up in the embedded sample although undesirably, are corrected for later as described in

chapter 7.4.2. A possible bias due to signal events decaying via $H^+ \to \tau\nu_\tau \to \mu\nu_\mu\nu_\tau\nu_\tau$ is investigated and described in chapter 9.5.

7.2.1. Selection applied to the 2011 data

In the data taken at $\sqrt{s} = 7\,\text{TeV}$, an event has to meet the following requirements to be selected for embedding:

- It is triggered by a single muon trigger with a p_T threshold on the muon trigger object of 18 GeV.
- Exactly one isolated muon passing 'tight' identification with $p_\text{T} > 25\,\text{GeV}$ is found with less than 4 GeV (2.5 GeV) in a calorimeter (tracking) cone around the muon with radius $\Delta R < 0.2$ (0.3).
- No isolated electron, with the same isolation and E_T criteria as described in section 6.1 is found.
- The event contains at least four jets fulfilling the same requirements as detailed in section 6.1.
- At least one of the selected jets must be b-tagged at a 75% efficient working point.
- The missing transverse momentum is $E_\text{T}^\text{miss} > 35\,\text{GeV}$.

After applying this selection to the 2011 dataset, 39139 events are selected.

7.2.2. Selection applied to the 2012 data

In order to be selected for embedding, an event has to fulfill the following requirements:

- It is triggered by a single muon trigger with a p_T threshold on the muon trigger object of 24 GeV or 36 GeV. The trigger with a p_T threshold of 24 GeV requires the selected muon to be isolated.
- Exactly one isolated muon passing 'tight' identification with $p_\text{T} > 25\,\text{GeV}$ is found with less than 4 GeV (2.5 GeV) in a calorimeter (tracking) cone around the muon with radius $\Delta R < 0.2$ (0.3).
- No isolated electron, with the same isolation and p_T criteria as described in section 6.2 is found.
- The event contains at least four (three) jets fulfilling the same requirements as detailed in section 6.2 for the low-mass (high-mass) μ+jets selection.
- At least one of the selected jets is b-tagged at an 80% efficient working point.
- The missing transverse momentum fulfills $E_\text{T}^\text{miss} > 25\,\text{GeV}$ (40 GeV) for the low-mass (high-mass) μ+jets selection.

The 2012 data sample contains 255617 (398505) events after applying the low-mass (high-mass) μ+jets selection.

7.3. $\mu \to \mu$ Embedding

As a closure-check, $\mu \to \mu$ embedding is run on both data and $t\bar{t}$ simulation. Since this option was not available in 2011, it is done only on 2012 data and $t\bar{t}$ simulation. It provides the means to validate the technical procedures of removing the track of the original muon as well as calorimeter cells ascribed to this muon and embedding a simulated muon into the event.
The procedure for selecting and extracting the muon is the same as described above. Instead of rescaling the muon's momentum, however, it is kept and the simulated muon is embedded into the original event instead of a τ lepton.
After embedding, only the muon selection as described in chapters 7.2.1 and 7.2.2 is applied but no further event selection since the original and embedded events are expected to be almost identical. Due to technical reasons, no trigger information is available in the embedded sample. Thus the μ trigger efficiency is not corrected for. Rather it is assumed that the embedded muon is similar enough to the original one so that it would have triggered the event, too, and the trigger efficiency is implicit in the embedded sample.
Below, an overview of necessary corrections applied to the embedded samples is given. The impact of these corrections is shown by comparing embedded simulation (data) with the corrections applied to embedded simulation (data) without the corrections. Finally, the fully corrected $\mu \to \mu$ embedded simulation (data) is compared to the originally selected μ+jets simulation (data) sample. All distributions shown are normalized to unity to allow shape comparisons.

7.3.1. Corrections Applied to Embedded Samples

Correction for the Muon Reconstruction Efficiency As mentioned above, embedded events are reconstructed twice. To account for inefficiencies of the muon reconstruction, the inverse efficiency is applied as a correction factor to each embedded event. The efficiencies depend on p_{T} and η of the embedded muon and are shown in figure 7.3 for simulation. For the momentum range requested ($p_{\mathrm{T}} > 25\,\mathrm{GeV}$) and over the full pseudorapidity range of the muons, the efficiencies are close to 100% except for a gap around $\eta = 0$ due to an access shaft in the detector. To account for differences between efficiencies in simulation and data, an additional scale factor, i.e. the ratio of efficiencies in data and simulation, is applied to embedded data.

Distributions of the muon p_{T}, η, ϕ and $E_{\mathrm{T}}^{\mathrm{miss}}$ in the events comparing $\mu \to \mu$ embedded $t\bar{t}$ simulation before and after applying the muon reconstruction efficiency correction are shown in figure 7.4 after applying the high-mass μ+jets selection. The effect of the muon reconstruction efficiency correction is rather small and can be seen in small shifts in the η^{μ} distributions. The entries in the $E_{\mathrm{T}}^{\mathrm{miss}}$ distributions with $E_{\mathrm{T}}^{\mathrm{miss}} < 40\,\mathrm{GeV}$ arise from slightly differing $E_{\mathrm{T}}^{\mathrm{miss}}$ definitions used in the samples the μ+jets selection is run on and those used for embedding. Since these differences are due to the chosen muon definition, they only appear in $\mu \to \mu$ embedding and do not occur in $\mu \to \tau$ embedding, where events containing muons after embedding are vetoed. Corresponding distributions for data are shown in figure 7.5. There the same effect in the $E_{\mathrm{T}}^{\mathrm{miss}}$ distributions can be observed.

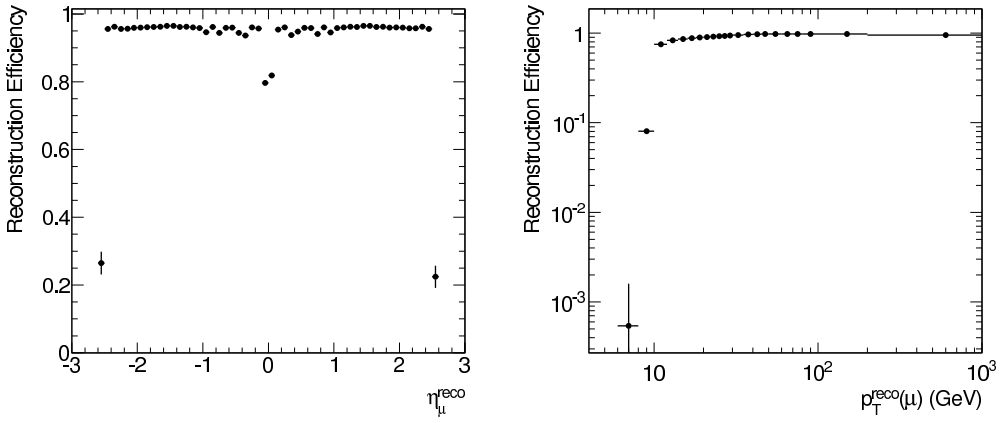

(a) (b)

Figure 7.3. Muon reconstruction efficiencies in simulation as a function of (a) p_{T}^{μ} and (b) η^{μ}. The reciprocal of the efficiency is applied as correction on the embedded muon [158].

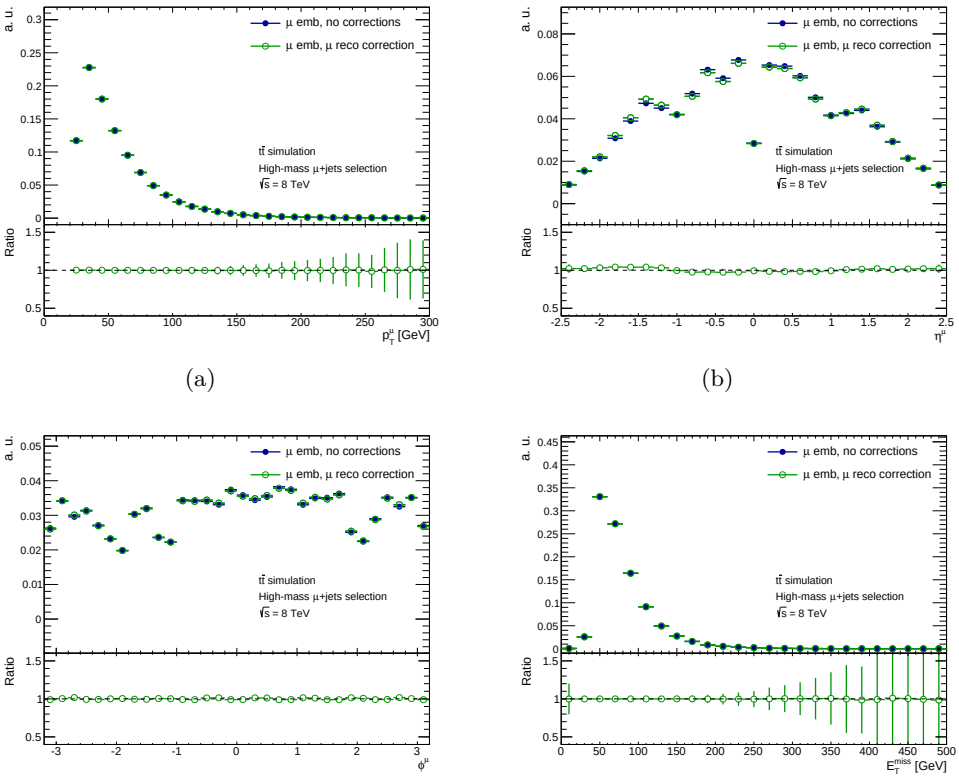

(a) (b)

(c) (d)

Figure 7.4. Comparisons of (a) p_{T}^{μ}, (b) η^{μ}, (c) ϕ^{μ} and (d) $E_{\mathrm{T}}^{\mathrm{miss}}$ of $\mu \to \mu$ embedded $t\bar{t}$ simulation before and after applying the muon reconstruction efficiency correction. The high-mass μ+jets selection is applied.

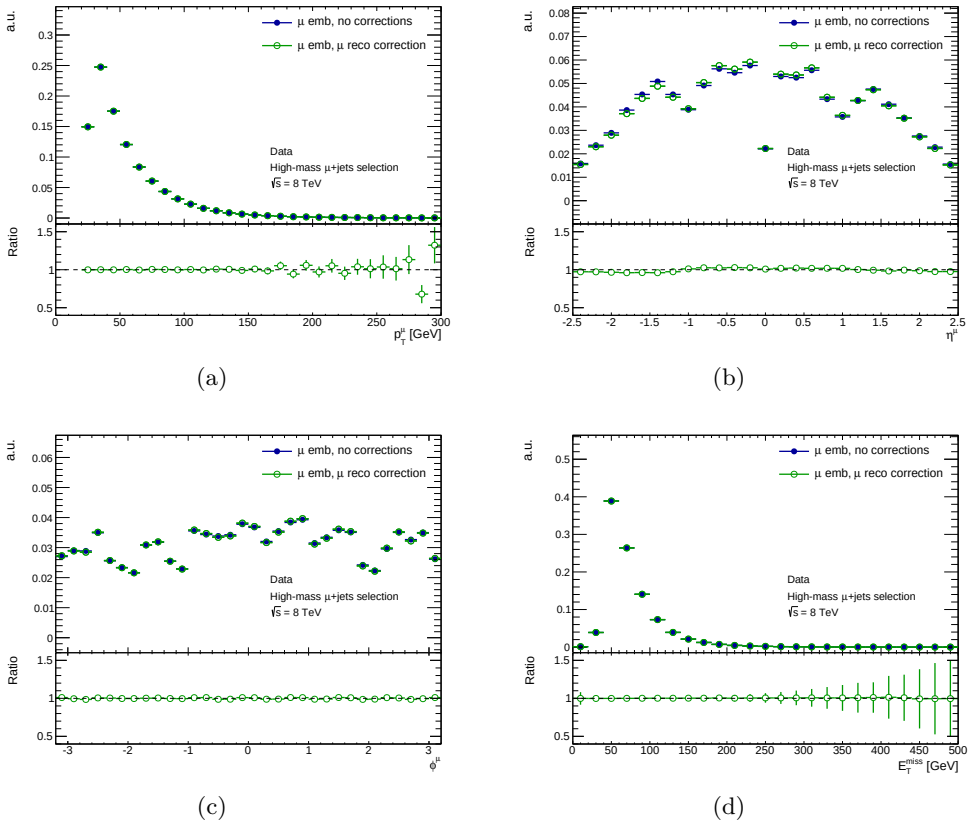

Figure 7.5. Comparisons of (a) p_{T}^{μ}, (b) η^{μ}, (c) ϕ^{μ} and (d) $E_{\mathrm{T}}^{\mathrm{miss}}$ of $\mu \to \mu$ embedded data before and after applying the muon reconstruction efficiency correction. The high-mass μ+jets selection is applied.

***b*-layer Correction** A correction for hits in the innermost ID layer (the so-called *b*-layer) is applied to account for faulty requirements during reconstruction of $\mu \to \mu$ embedded events. In the embedded sample, requirements on the innermost ID layer are applied even if no hit is expected there. This is inconsistent with default simulation and data, where the requirements are only applied if a hit is expected. The inverse of the efficiency in this layer as a function of ϕ and η of the reconstructed muon that is applied to embedded simulation and data is shown in figure 7.6. The *b*-layer correction is optimized to correct the η^{μ} and ϕ^{μ} distributions in data and has negligible effects on the p_{T}^{μ} and $E_{\mathrm{T}}^{\mathrm{miss}}$ distributions. The effect of applying the *b*-layer correction is shown in figures 7.7 and 7.8 for simulation and data, respectively, for the high-mass μ+jets selection. As for the muon reconstruction efficiency correction, entries with $E_{\mathrm{T}}^{\mathrm{miss}} < 40\,\mathrm{GeV}$ appear in the $E_{\mathrm{T}}^{\mathrm{miss}}$ distributions due to a slightly different $E_{\mathrm{T}}^{\mathrm{miss}}$ definition shown here compared to the one when applying the μ+jets selection.

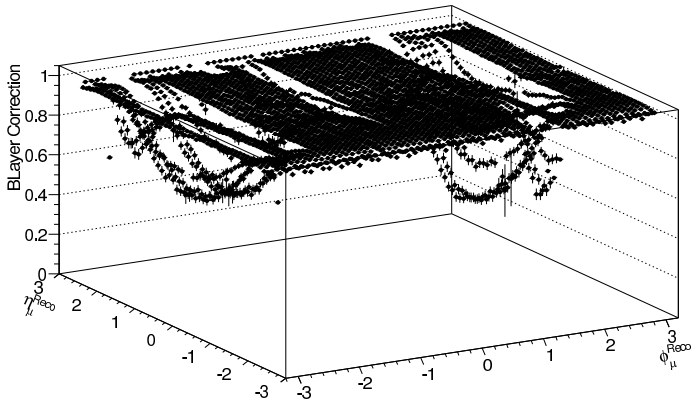

Figure 7.6. *b*-layer efficiency on embedded, reconstructed muons as a function of η^μ and ϕ^μ. To account for the deficiency in the modeling, the inverse of the efficiency is applied as a correction factor to the embedded muon [158].

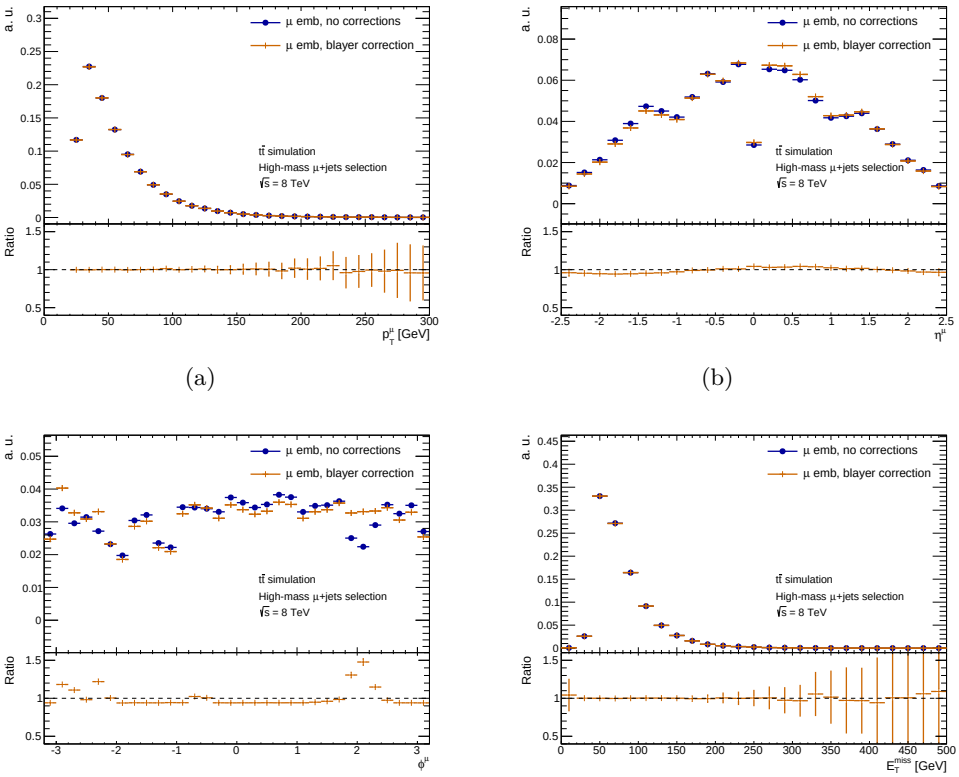

Figure 7.7. Comparisons of (a) p_{T}^{μ}, (b) η^{μ}, (c) ϕ^{μ} and (d) $E_{\mathrm{T}}^{\mathrm{miss}}$ of $\mu \to \mu$ embedded simulation before and after applying the *b*-layer correction. The high-mass μ+jets selection is applied.

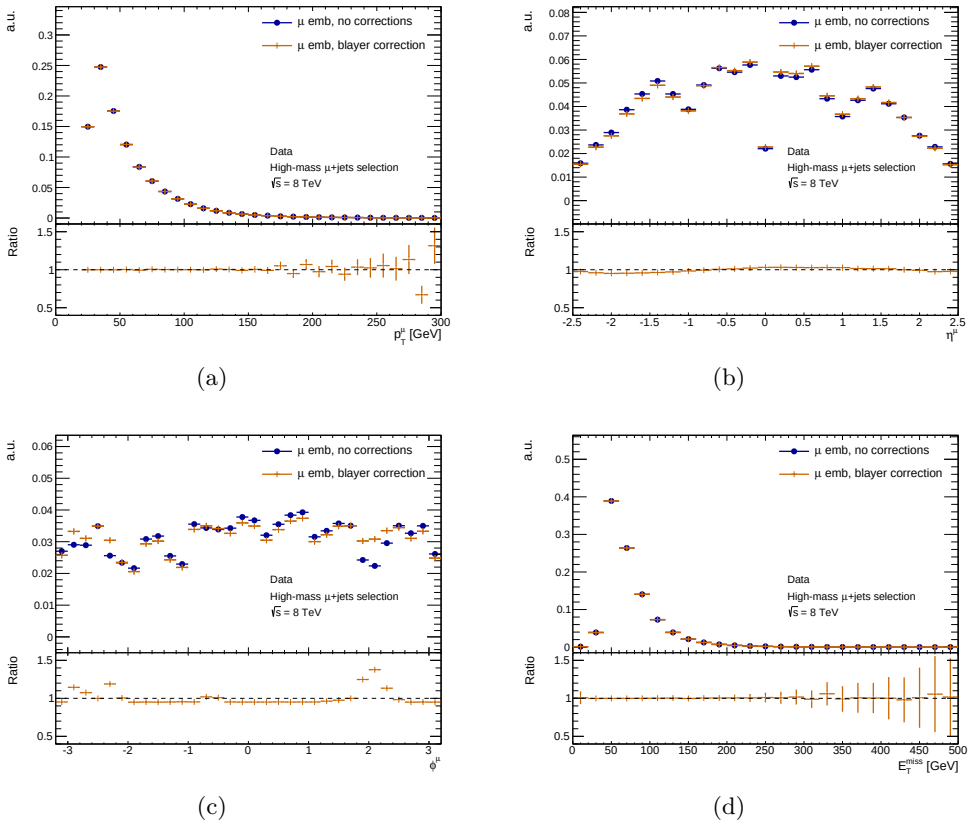

Figure 7.8. Comparisons of (a) p_{T}^{μ}, (b) η^{μ}, (c) ϕ^{μ} and (d) $E_{\mathrm{T}}^{\mathrm{miss}}$ of $\mu \to \mu$ embedded data before and after applying the b-layer correction. The high-mass μ+jets selection is applied.

7.3.2. Embedded Simulation and Data

After applying both the muon reconstruction efficiency and the b-layer correction, default and embedded simulation (data) are expected to agree very well, shown in figure 7.9 (7.10) for different distributions after applying the high-mass μ+jets selection. Only statistical uncertainties are shown.

All muon-related quantities agree well between the original and embedded samples. The small discrepancies in the η^{μ} and ϕ^{μ} distributions are due to the non-perfect b-layer correction. This correction was optimized for data, hence the agreement of embedded and original distributions in data is better than in simulation. The $E_{\mathrm{T}}^{\mathrm{miss}}$ definition used when applying the muon+jets is slightly different than the one shown here, hence there are also entries for $E_{\mathrm{T}}^{\mathrm{miss}} < 40\,\mathrm{GeV}$ even in the original sample. A different muon definition for calculating $E_{\mathrm{T}}^{\mathrm{miss}}$ is used here compared to the one in the muon+jets selection. These mixed $E_{\mathrm{T}}^{\mathrm{miss}}$ definitions are due to technical reasons and do not affect $\mu \to \tau$ embedding, presented in chapter 7.4, since events containing muons after embedding are vetoed. As can be seen from the small shifts for very low p_{T}^{μ} and $E_{\mathrm{T}}^{\mathrm{miss}}$ values, these variables tend to be slightly softer in the embedded samples than in the original one.

Distributions after applying the low-mass μ+jets selection are shown in appendix A.

Despite the small differences between the original and embedded distributions shown in

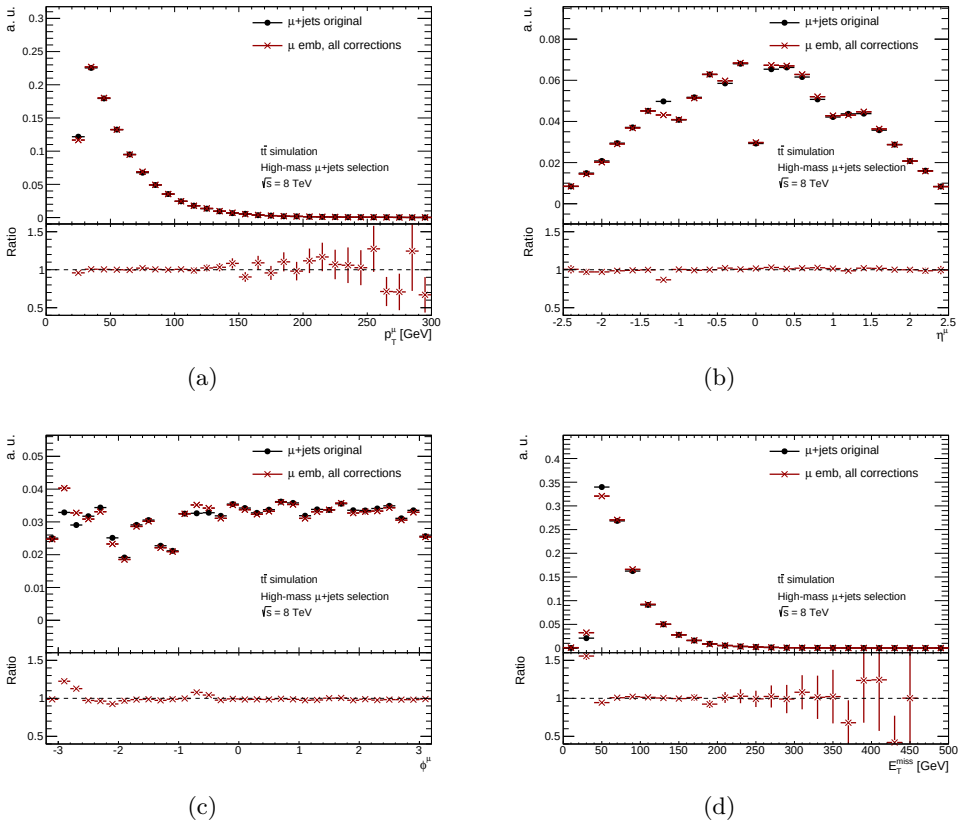

Figure 7.9. Comparisons of (a) p_{T}^{μ}, (b) η^{μ}, (c) ϕ^{μ} and (d) $E_{\mathrm{T}}^{\mathrm{miss}}$ of default and $\mu \to \mu$ embedded $t\bar{t}$ simulation after applying all corrections. Only statistical uncertainties are shown. The high-mass μ+jets selection is applied.

figure 7.9 and 7.10, the technical aspects of removing the original muon and embedding a simulated muon in $\mu \to \mu$ embedding work well both in simulation and data and the closure test is considered successful.

7.4. $\mu \to \tau$ Embedding

Here, the full embedding procedure as described in section 7.1 is applied. Both $t\bar{t}$ simulation and data are embedded. While the embedded data is used for the estimation of background events with true hadronically decaying τ leptons, embedded simulation is used as an additional cross-check. The technical procedure of removing the muon and replacing it with a hadronically decaying τ lepton is validated in this sample by comparing the embedded simulation with default τ+jets events in $t\bar{t}$ simulation.

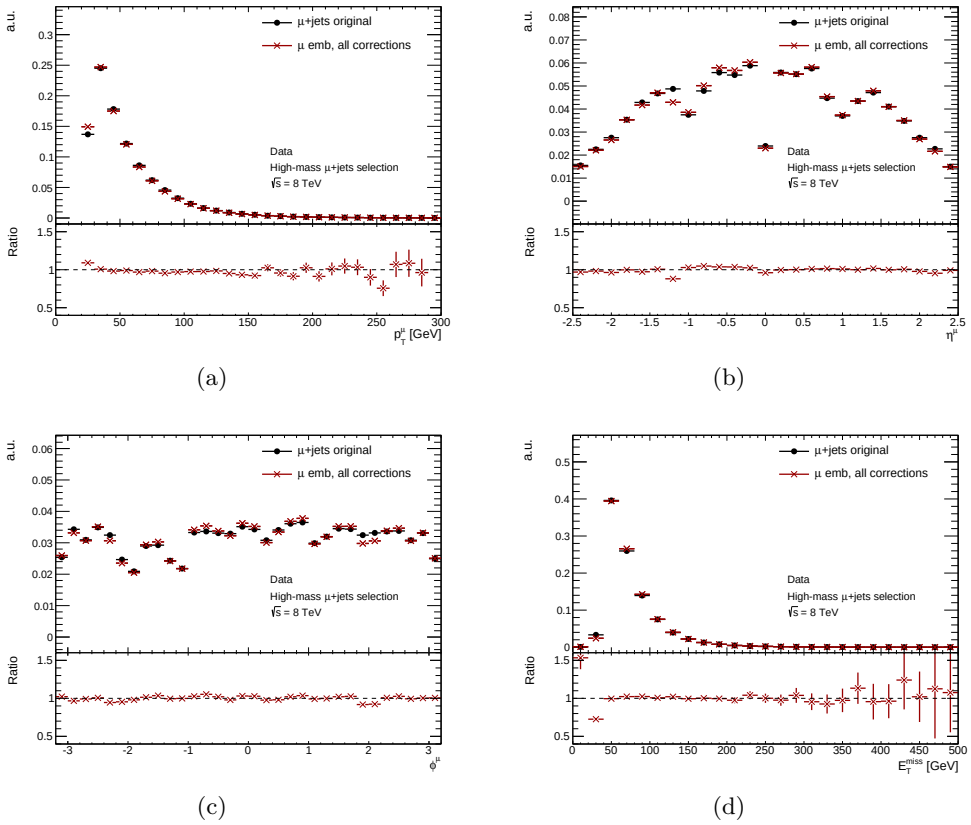

Figure 7.10. Comparisons of (a) p_{T}^{μ}, (b) η^{μ}, (c) ϕ^{μ} and (d) $E_{\mathrm{T}}^{\mathrm{miss}}$ of collision data and $\mu \to \mu$ embedded data after applying all corrections. Only statistical uncertainties are shown. The high-mass μ+jets selection is applied.

7.4.1. Implications of the Additional Neutrino from the τ Decay

The missing transverse momentum has to be greater than 35 GeV in the μ+jets selection applied to 2011 data and greater than 25 GeV (40 GeV) in the low-mass (high-mass) μ+jets selection applied to 2012 data, respectively. The neutrino from the hadronic τ lepton decay in an embedded event contributes to the final $E_{\mathrm{T}}^{\mathrm{miss}}$ of the event. If this contribution is significant, it can occur that the $E_{\mathrm{T}}^{\mathrm{miss}}$ in the original, muon+jets event is too small for the event to pass the muon+jets event selection, but the final $E_{\mathrm{T}}^{\mathrm{miss}}$ in the embedded event would be large enough for the event to pass the τ+jets selection. Events where this applies are thus not included in the embedded sample. However, they are present in any simulation sample the embedded data is compared to and also in normal collision data.
This effect was not noticed in the 2011 data due to the small size of the embedded data sample.

To estimate the effect of these missing events in the 2012 data, a new $E_{\mathrm{T}}^{\mathrm{miss}}$ is calculated in simulation events, where a τ mimicking the original muon is formed from the visible decay products $\tau_{\text{had-vis}}$ and the neutrino coming from the hadronic τ decay. Hence the neutrino of the τ_{had} decay is not taken into account for $E_{\mathrm{T}}^{\mathrm{miss}}$ calculation. Except for the

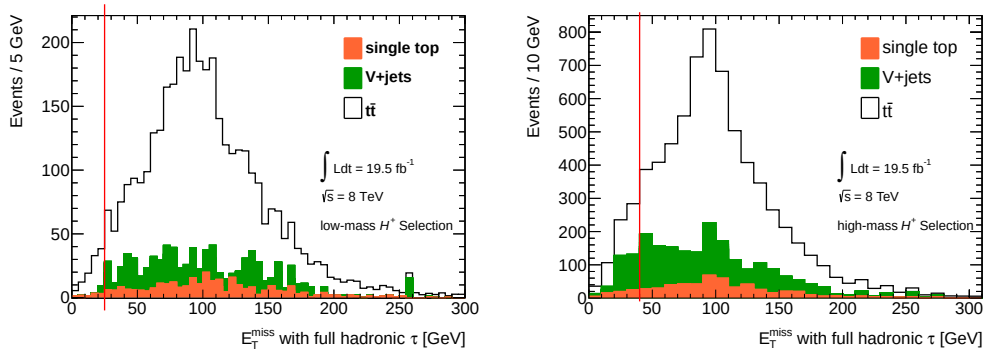

(a) low-mass H^+ selection (b) high-mass H^+ selection

Figure 7.11. $E_{\mathrm{T}}^{\mathrm{miss}}$ of simulated events passing the τ+jets selection. Here, the $\tau_{\text{had-vis}} + \nu_\tau$ leptons are considered as one particle mimicking the original muon for the (a) low-mass and (b) high-mass H^+ search. Except for the differences between the muon and τ lepton mass, this $E_{\mathrm{T}}^{\mathrm{miss}}$ is the same as that of a muon+jets event. Entries below the red line do not pass the muon+jets selection and are thus missing in the embedded sample.

mass difference between muons and τ leptons, this re-calculated $E_{\mathrm{T}}^{\mathrm{miss}}$ is the same as that in the original muon+jets events. The re-calculated $E_{\mathrm{T}}^{\mathrm{miss}}$ is shown in figure 7.11 for simulation events passing the full τ+jets selection for the low-mass and high-mass H^+ selections. The vertical red lines indicate the $E_{\mathrm{T}}^{\mathrm{miss}}$ requirement applied in the respective muon+jets selection. All events with values of this re-calculated $E_{\mathrm{T}}^{\mathrm{miss}}$ below 25 GeV (40 GeV) for the low-mass (high-mass) H^+ search are missing in the embedded samples compared to collision data or default simulation.
The m_{T} distributions of these missing events are shown in figure 7.12. Only events in very low m_{T} bins are missing. A final requirement $m_{\mathrm{T}} > 20$ GeV (40 GeV) is thus added to the signal selection for the low-mass (high-mass) H^+ search in 2012. With this requirement, about 2 (14) events with higher m_{T} values are still missing in the embedded samples. Considering the size of the full embedded samples (more than 250000 events for the low-mass H^+ search and almost 400000 events for the high-mass H^+ search) and that of other systematic uncertainties, discussed below, no additional systematic uncertainty is considered for these few missing events. The expected loss of sensitivity due to the m_{T} requirement is expected to be negligible and shown in figure 9.2 in chapter 9 for both the low-mass and high-mass H^+ searches.

7.4.2. Corrections Applied to Embedded Samples

After embedding, the sample is normalized and various corrections are applied to get the final number of background events with true hadronically decaying τ leptons, N_τ:

$$N_\tau = N_{\text{embedded}} \cdot (1 - c_{\tau\to\mu}) \frac{\varepsilon^{\tau_{\text{had-vis}} + E_{\mathrm{T}}^{\mathrm{miss}} - \text{trigger}}}{\varepsilon^{\mu\text{-reco, trigger}}} \cdot B(\tau \to \text{hadrons } \nu) \qquad (7.2)$$

The N_{embedded} events in the sample are corrected for unavoidably embedded leptonic τ decays with a factor $c_{\tau\to\mu}$, which amounts to 4.4% in the 2011 data and 4% in 2012

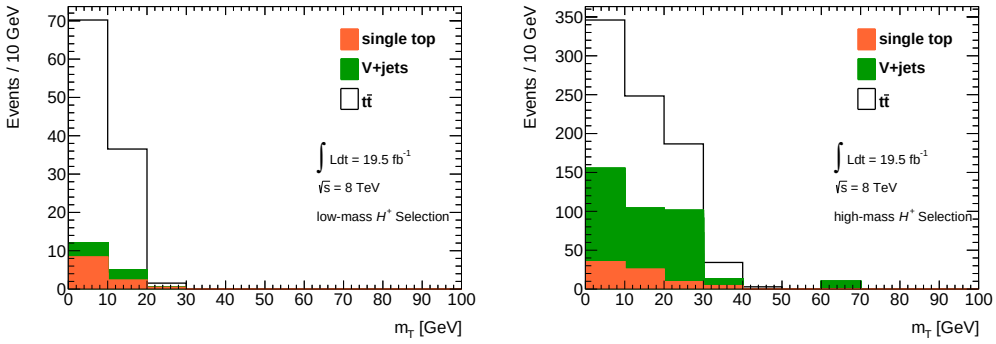

(a) low-mass H^+ selection

(b) high-mass H^+ selection

Figure 7.12. Distribution of the transverse mass, m_T, of events failing the muon+jets selection due to the $E_\mathrm{T}^\mathrm{miss}$ requirement for the (a) low-mass and (b) high-mass H^+ search. These events would however pass the τ+jets selection because the neutrino from the τ decay contributes significantly to the final $E_\mathrm{T}^\mathrm{miss}$.

data. This factor is estimated based on embedded $t\bar{t}$ simulation, where the amount of events, where the original muon came from a τ or W decay, and pass the τ+jets selection after embedding, are compared. Since muons from τ lepton decays tend to have lower transverse momenta than muons from W decays, the former are less likely to pass the τ+jets selection after embedding, where the requirement is $p_\mathrm{T}^\tau > 40\,\mathrm{GeV}$ compared to $p_\mathrm{T}^\mu > 25\,\mathrm{GeV}$ in the muon+jets selection.

The muon trigger and reconstruction efficiencies, $\varepsilon^{\mu\text{-reco, trigger}}$, are corrected for to remove muon-related (in-)efficiencies which would otherwise be present in embedded simulation and data but not in default simulation and collision data compared to. The reconstruction efficiencies depend on p_T^μ and η^μ. The trigger efficiencies depend on the p_T^μ, η^μ, ϕ^μ, E^μ and the data taking period. For both reconstruction and trigger efficiencies, μ refers to the original muon. This correction is described in more detail and the effect on various distributions is shown below.

Due to technical reasons, no trigger information is available in embedded samples. Thus, $\tau_\text{had-vis} + E_\mathrm{T}^\mathrm{miss}$ trigger efficiencies $\varepsilon^{\tau_\text{had-vis}+E_\mathrm{T}^\mathrm{miss}-\text{trigger}}$ are applied to embedded data. They depend on p_T^τ and $E_\mathrm{T}^\mathrm{miss}$ and are applied individually for each event. More detailed information and the effect of this correction on the samples is given and shown below.

Finally, to take into account that only about 65% of all τ leptons decay hadronically, the number of events is multiplied by the branching ratio of τ lepton decays involving hadrons, $B(\tau \to \text{hadrons}\ \nu)$.

In addition to this normalization, correction factors are needed for any $\tau_\text{had-vis}$-related quantities when comparing embedded to collision data. Since the $\tau_\text{had-vis}$ in the embedded data is simulated and $\tau_\text{had-vis}$ identification efficiencies in data and simulation are different, this also needs to be corrected.

Below, embedded samples without any corrections are compared to embedded samples with one correction applied at a time. This is shown only for corrections that affect the normalization as well as the shapes of distributions. For simulation, the distributions are all normalized to unity to allow shape comparisons. For data, all distributions are normalized to luminosity such that both the shape differences as well as normalization

differences introduced by the corrections are visible.

Correction for the Muon Reconstruction and Trigger Efficiencies As mentioned, the muon reconstruction efficiency needs to be corrected for in $\mu \to \tau$ embedded events. This efficiency has an impact on the embedded samples but not on the simulation or collision data they are compared to. To remove this effect, the inverse of the efficiencies shown in figure 7.13 for data taken in 2012 is applied to embedded data as a function of p_{T} and η of the original muon. Correspondingly, efficiencies are applied to the 2011 embedded data and simulation [148].

Additionally, to remove effects of the muon trigger efficiency, its inverse is applied as a

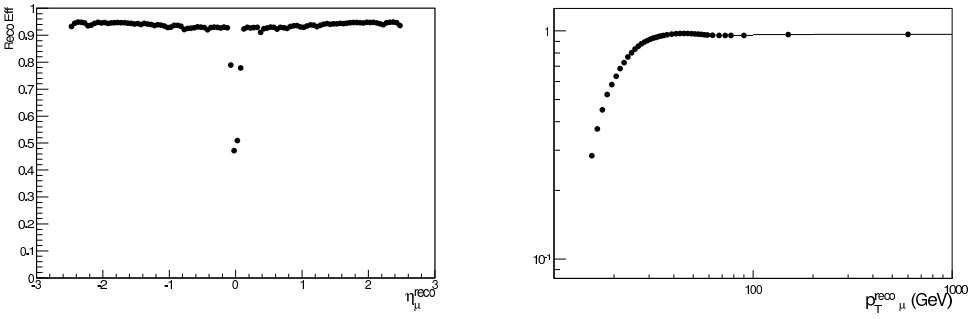

(a) μ reconstruction efficiency vs. η (b) μ reconstruction efficiency vs. p_{T}

Figure 7.13. Muon reconstruction efficiencies in data as a function of (a) p_{T}^{μ} and (b) η^{μ}. The reciprocal of the efficiency is applied as correction depending on the original muon information that is saved in embedded events [158].

correction factor to the embedded samples. The efficiencies as functions of η^{μ} and p_{T}^{μ} determined in a fraction of data corresponding to $6.1\,\mathrm{fb}^{-1}$ of the data taken in 2012 are shown in figure 7.14.

Distributions of p_{T}^{τ}, η^{τ}, $E_{\mathrm{T}}^{\mathrm{miss}}$ and m_{T} of $\mu \to \tau$ embedded $t\bar{t}$ simulation and of data

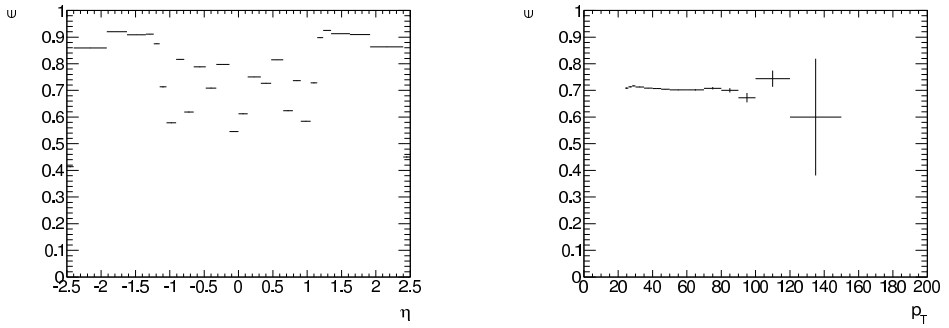

(a) μ trigger efficiency vs. η (b) μ trigger efficiency vs. p_{T}

Figure 7.14. Efficiencies of the muon triggers used in the μ+jets selection in $6.1\,\mathrm{fb}^{-1}$ of data taken in 2012 as a function of (a) η^{μ} and (b) p_{T}^{μ}. The inverse of these efficiencies is applied as a correction factor to the embedded event [158].

before and after applying the muon reconstruction and trigger efficiency corrections are shown in figures 7.15 and 7.16, respectively, after applying the high-mass H^+ selection. More distributions and corresponding figures after applying the low-mass H^+ selection may be found in appendix B. The effect of this correction is about 30% as a function of p_{T}^{τ} and between 10% and 50% as a function of η^{τ} on the normalization of the data sample.

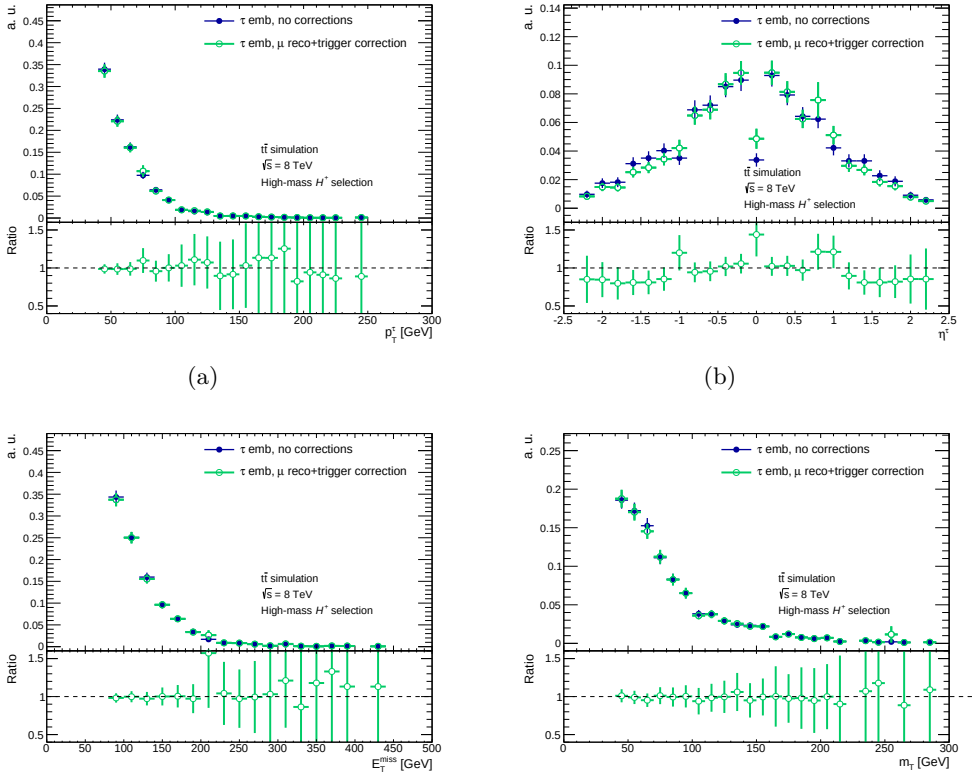

Figure 7.15. Comparisons of (a) p_{T}^{τ}, (b) η^{τ}, (c) $E_{\mathrm{T}}^{\mathrm{miss}}$ and (d) m_{T} of $\mu \to \tau$ embedded $t\bar{t}$ simulation before and after applying the muon reconstruction and muon trigger corrections. The high-mass H^+ selection is applied.

Application of the $\tau_{\text{had-vis}} + E_{\mathrm{T}}^{\mathrm{miss}}$ Trigger Efficiency No trigger information is available in embedded samples due to technical reasons. Thus $\tau_{\text{had-vis}} + E_{\mathrm{T}}^{\mathrm{miss}}$ trigger efficiencies are applied to embedded data and simulation as functions of p_{T}^{τ} and $E_{\mathrm{T}}^{\mathrm{miss}}$. In the 2011 data, $\tau_{\text{had-vis}} + E_{\mathrm{T}}^{\mathrm{miss}}$ trigger efficiencies are determined based on simulation and scale factors derived from a tag-and-probe approach in a $\mu + \tau_{\text{had-vis}}$ data sample are applied additionally. Efficiencies are measured in 5 bins in p_{T}^{τ} and $E_{\mathrm{T}}^{\mathrm{miss}}$ each, shown in tables 7.1 and 7.2. Scale factors are determined in 2 bins in p_{T}^{τ} and $E_{\mathrm{T}}^{\mathrm{miss}}$ each. While the efficiencies are measured separately for data-taking periods with different trigger requirements, no such sub-division is done for the scale factors. The latter are shown in table 7.3 with their statistical uncertainties. If p_{T}^{τ} or $E_{\mathrm{T}}^{\mathrm{miss}} > 500\,\mathrm{GeV}$, the values for

	$40\,\text{GeV} \leq p_\text{T}^\tau < 45\,\text{GeV}$	$45\,\text{GeV} \leq p_\text{T}^\tau < 55\,\text{GeV}$	$55\,\text{GeV} \leq p_\text{T}^\tau < 65\,\text{GeV}$	$65\,\text{GeV} \leq p_\text{T}^\tau < 85\,\text{GeV}$	$85\,\text{GeV} \leq p_\text{T}^\tau$
$65\,\text{GeV} \leq E_\text{T}^\text{miss} < 73\,\text{GeV}$	0.48 ± 0.04	0.62 ± 0.04	0.68 ± 0.04	0.74 ± 0.04	0.70 ± 0.05
$73\,\text{GeV} \leq E_\text{T}^\text{miss} < 85\,\text{GeV}$	0.52 ± 0.03	0.65 ± 0.03	0.73 ± 0.04	0.76 ± 0.03	0.81 ± 0.05
$85\,\text{GeV} \leq E_\text{T}^\text{miss} < 100\,\text{GeV}$	0.56 ± 0.04	0.64 ± 0.04	0.77 ± 0.05	0.79 ± 0.04	0.84 ± 0.06
$100\,\text{GeV} \leq E_\text{T}^\text{miss} < 150\,\text{GeV}$	0.53 ± 0.04	0.66 ± 0.04	0.73 ± 0.04	0.85 ± 0.04	0.83 ± 0.05
$150\,\text{GeV} \leq E_\text{T}^\text{miss}$	0.53 ± 0.05	0.64 ± 0.04	0.75 ± 0.05	0.83 ± 0.04	0.88 ± 0.05

Table 7.1. Trigger efficiencies with statistical uncertainties for the $\tau_\text{had-vis} + E_\text{T}^\text{miss}$ trigger used in $2.2\,\text{fb}^{-1}$ of data taken at $\sqrt{s} = 7\,\text{TeV}$ measured in a $t\bar{t}$ simulation sample.

	$40\,\text{GeV} \leq p_\text{T}^\tau < 45\,\text{GeV}$	$45\,\text{GeV} \leq p_\text{T}^\tau < 55\,\text{GeV}$	$55\,\text{GeV} \leq p_\text{T}^\tau < 65\,\text{GeV}$	$65\,\text{GeV} \leq p_\text{T}^\tau < 85\,\text{GeV}$	$85\,\text{GeV} \leq p_\text{T}^\tau$
$65\,\text{GeV} \leq E_\text{T}^\text{miss} < 73\,\text{GeV}$	0.48 ± 0.03	0.56 ± 0.03	0.58 ± 0.04	0.63 ± 0.03	0.70 ± 0.05
$73\,\text{GeV} \leq E_\text{T}^\text{miss} < 85\,\text{GeV}$	0.50 ± 0.03	0.55 ± 0.03	0.63 ± 0.03	0.69 ± 0.03	0.71 ± 0.04
$85\,\text{GeV} \leq E_\text{T}^\text{miss} < 100\,\text{GeV}$	0.48 ± 0.04	0.62 ± 0.04	0.63 ± 0.04	0.75 ± 0.04	0.76 ± 0.05
$100\,\text{GeV} \leq E_\text{T}^\text{miss} < 150\,\text{GeV}$	0.52 ± 0.04	0.61 ± 0.04	0.74 ± 0.04	0.78 ± 0.03	0.79 ± 0.05
$150\,\text{GeV} \leq E_\text{T}^\text{miss}$	0.50 ± 0.04	0.57 ± 0.04	0.68 ± 0.04	0.80 ± 0.03	0.79 ± 0.05

Table 7.2. Trigger efficiencies with statistical uncertainties for the $\tau_\text{had-vis} + E_\text{T}^\text{miss}$ trigger used in $2.4\,\text{fb}^{-1}$ of data taken at $\sqrt{s} = 7\,\text{TeV}$ measured in a $t\bar{t}$ simulation sample.

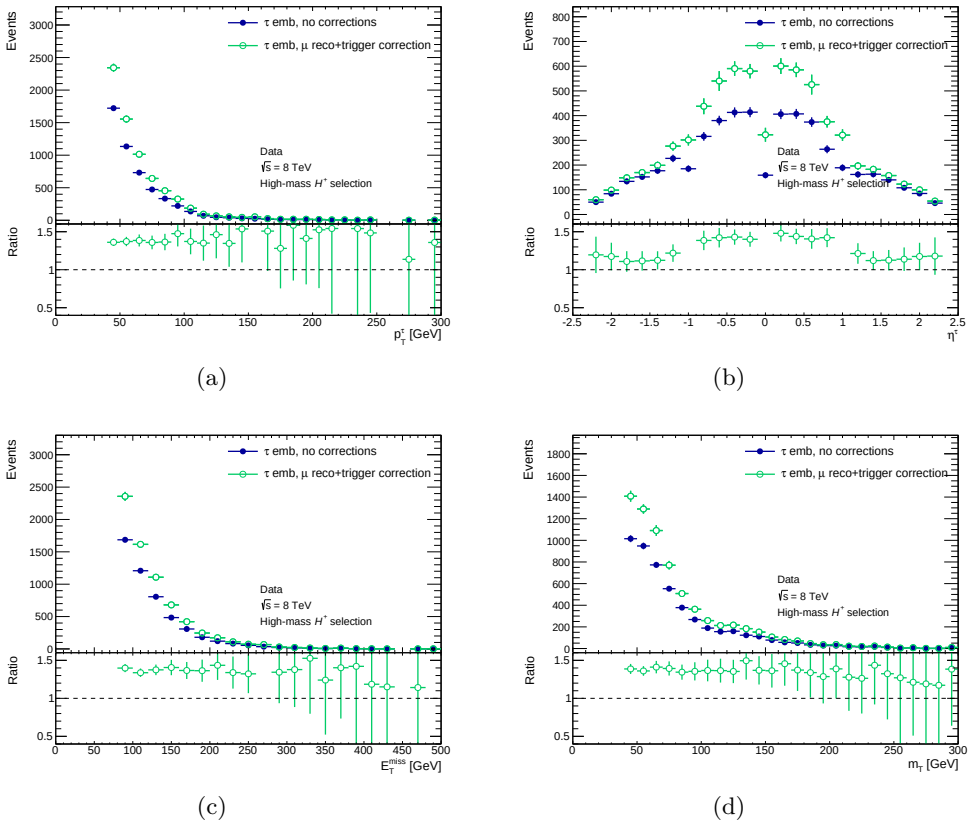

Figure 7.16. Comparisons of (a) p_{T}^{τ}, (b) η^{τ}, (c) $E_{\mathrm{T}}^{\mathrm{miss}}$ and (d) m_{T} of $\mu \to \tau$ embedded data before and after applying the muon reconstruction and muon trigger corrections. The high-mass H^+ selection is applied.

500 GeV are used. The systematic uncertainties related to these trigger efficiencies are summarized and discussed below.

A more complex approach is taken for the 2012 data. To increase the sample size, the

	$40\,\mathrm{GeV} \leq p_{\mathrm{T}}^{\tau} < 70\,\mathrm{GeV}$	$70\,\mathrm{GeV} \leq p_{\mathrm{T}}^{\tau} < 500\,\mathrm{GeV}$
$65\,\mathrm{GeV} \leq E_{\mathrm{T}}^{\mathrm{miss}} < 100\,\mathrm{GeV}$	0.76 ± 0.09	0.86 ± 0.13
$100\,\mathrm{GeV} \leq E_{\mathrm{T}}^{\mathrm{miss}} < 500\,\mathrm{GeV}$	1.10 ± 0.12	0.91 ± 0.14

Table 7.3. Trigger scale factors applied to the embedded 2011 data sample [154].

efficiencies of the $\tau_{\text{had-vis}}$ and $E_{\mathrm{T}}^{\mathrm{miss}}$ legs of the triggers are determined separately. To further increase the sample size, the data is not sub-divided into different periods where different trigger definitions are used.

The trigger efficiencies are determined in data using a tag-and-probe method. A $\mu + \tau_{\text{had-vis}} + E_{\mathrm{T}}^{\mathrm{miss}}$ sample, consistent with $t\bar{t}$ decays in the $\mu + \tau$ final state, is selected, where the muon trigger is used as tag and the $\tau_{\text{had-vis}}$ and $E_{\mathrm{T}}^{\mathrm{miss}}$ triggers as probe. Efficiency points are determined in bins up to 500 GeV in both p_{T}^{τ} and $E_{\mathrm{T}}^{\mathrm{miss}}$ and then fit with an

error function, yielding continuous values. The fits including statistical and systematic uncertainties, discussed below, are shown in figure 7.17. The same is done in simulation samples and scale factors taking into account the different efficiencies are derived. The $E_{\mathrm{T}}^{\mathrm{miss}}$ trigger efficiencies shown in figure 7.17 are applied to the embedded sample.

Since the amount of true $\tau_{\text{had-vis}}$ in the sample used for the tag-and-probe method is only

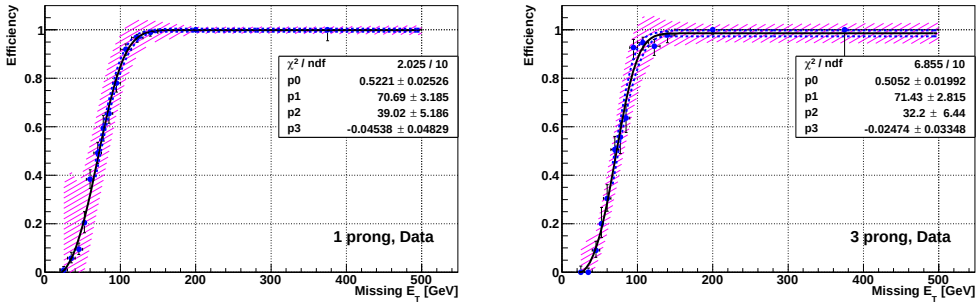

(a) (b)

Figure 7.17. Efficiencies of the $E_{\mathrm{T}}^{\mathrm{miss}}$ leg of the combined $\tau_{\text{had-vis}} + E_{\mathrm{T}}^{\mathrm{miss}}$ triggers used in 2012 data, determined from data with a tag-and-probe method. Efficiencies are shown separately for events with (a) 1-prong and (b) 3-prong $\tau_{\text{had-vis}}$. The efficiency points are fit with an error function. The hatched bands indicate the sum of all statistical and systematic uncertainties in quadrature [155].

around 50% but the embedded samples contain only true $\tau_{\text{had-vis}}$ and efficiencies for true $\tau_{\text{had-vis}}$ candidates are higher than for misidentified $\tau_{\text{had-vis}}$ candidates, the efficiencies for the $\tau_{\text{had-vis}}$ leg of the trigger to be applied to the embedded sample are measured in simulation. To take into account differences to trigger efficiencies in data, additional scale factors are applied to the efficiencies used for the embedded sample. Measured efficiency points and scale factors are fit with error functions, except for the 3-prong $\tau_{\text{had-vis}}$ trigger efficiency in simulation, which is fit with an arctan function. The efficiencies and scale factors with their statistical and systematic uncertainties, discussed below, are shown in figures 7.18 and 7.19, respectively.

In figure 7.20 and 7.21, distributions of the p_{T}^{τ}, η^{τ}, ϕ^{τ} and $E_{\mathrm{T}}^{\mathrm{miss}}$ are compared for embedded $t\bar{t}$ simulation and data, respectively, before and after applying the $\tau + E_{\mathrm{T}}^{\mathrm{miss}}$ trigger efficiencies. More distributions and corresponding distributions after applying the low-mass H^{+} selection may be found in appendix B. The effect on the normalization of the embedded sample ranges between -40% and -10% as a function of p_{T}^{τ} and between -50% and -10% as a function of $E_{\mathrm{T}}^{\mathrm{miss}}$.

$\tau_{\text{had-vis}}$ Identification Scale Factors Since the $\tau_{\text{had-vis}}$ in embedded data are simulated and the identification efficiencies for $\tau_{\text{had-vis}}$ differ between data and simulation, they need to be corrected for in both embedded data and simulation. This is done by applying scale factors. These scale factors for data taken at $\sqrt{s} = 8\,\mathrm{TeV}$ are shown in figure 7.22, separately for 1-prong and 3-prong $\tau_{\text{had-vis}}$ candidates, barrel and end-cap parts of the detector and different levels of $\tau_{\text{had-vis}}$ identification. In the analyses presented here, the

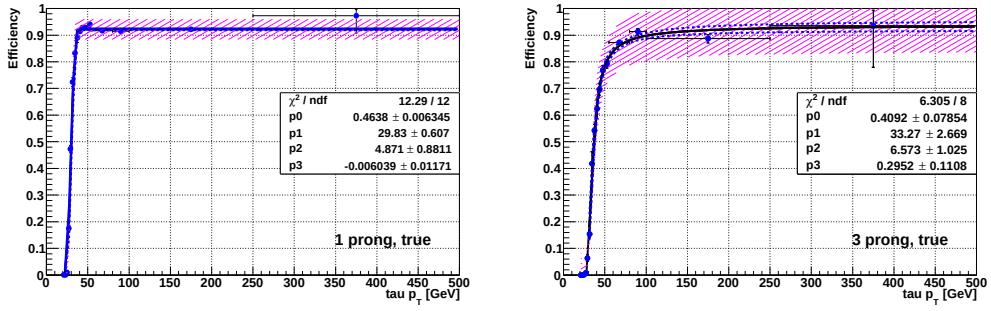

(a) (b)

Figure 7.18. Trigger efficiencies for the $\tau_{\text{had-vis}}$ leg of the used $\tau_{\text{had-vis}} + E_{\text{T}}^{\text{miss}}$ triggers measured in simulation, separately for (a) 1-prong and (b) 3-prong $\tau_{\text{had-vis}}$ [155].

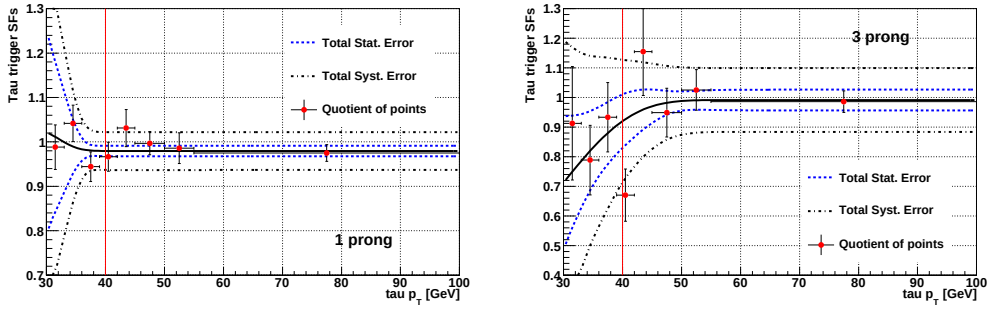

(a) (b)

Figure 7.19. Scale factors to account for differences between $\tau_{\text{had-vis}}$ trigger efficiencies in simulation and data separately for (a) 1-prong and (b) 3-prong $\tau_{\text{had-vis}}$ candidates, applied to the embedded data sample [155].

'tight' identification is used. Correction factors to the 2011 data are consistent with unity [159].

7.4.3. Systematic Uncertainties

Advantages of using embedded data instead of simulation for estimating the background with true hadronically decaying τ leptons are the independence of theoretical cross sections and their uncertainties, the choice of generator model and the jet production rate. Also, since everything except the τ in embedded data is taken directly from collision data, no additional uncertainties related e.g. to the jet energy scale, b-tagging efficiency or pile-up need to be considered. Systematic uncertainties affecting embedded data are discussed below. A normalization uncertainty due to the correction factor for muons from τ decays collected in the μ+jets sample of 2.5% and 2% for 2011 and 2012 data, respectively, is taken into account.

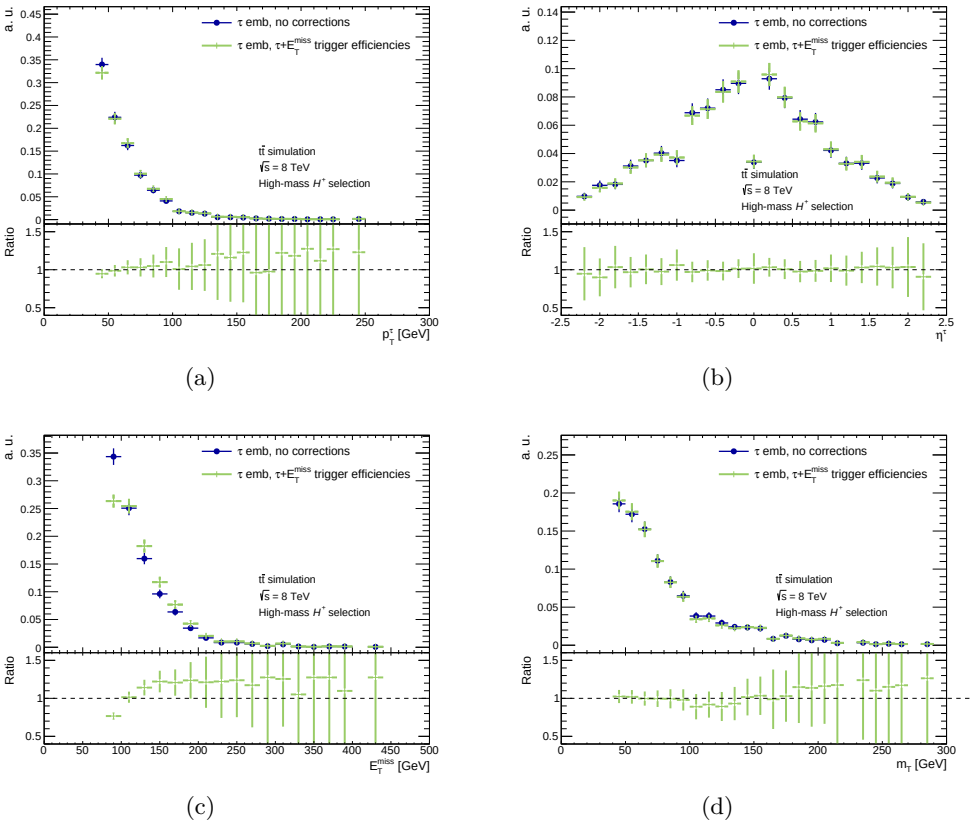

Figure 7.20. Comparisons of (a) p_{T}^{τ}, (b) η^{τ}, (c) $E_{\mathrm{T}}^{\mathrm{miss}}$ and (d) m_{T} of $\mu \to \tau$ embedded $t\bar{t}$ simulation before and after applying the $\tau + E_{\mathrm{T}}^{\mathrm{miss}}$ trigger efficiency correction. The high-mass H^{+} selection is applied.

Muon Trigger- and Reconstruction-Related Uncertainties Uncertainties on the muon trigger and reconstruction efficiencies used for normalizing the embedded samples are accounted for by shifting the efficiencies by one standard deviation and evaluating the effects on the total yields and final distributions. The trigger efficiency uncertainties depend on p_{T}^{μ}, η^{μ}, ϕ^{μ}, as well as on the charge of the muon and the data taking period. The uncertainties on the reconstruction efficiency depend on the same variables except for the data taking period.

Muon Isolation-Related Uncertainties The muon isolation requirements used in the μ+jets selection are loosened to evaluate the effect of contamination from multi-jet background events. The requirements are varied from 4 GeV (2.5 GeV) to 10 GeV (7 GeV) in calorimeter (tracking) cones with $R < 0.2$ ($R < 0.3$) around the muon. This uncertainty is symmetrized during the statistical analysis presented in chapter 9 to also take into account the effect of fewer multi-jet events.

$\tau_{\text{had-vis}} + E_{\mathrm{T}}^{\mathrm{miss}}$ Trigger-Related Uncertainties In the 2011 data, systematic uncertainties on the $\tau_{\text{had-vis}} + E_{\mathrm{T}}^{\mathrm{miss}}$ trigger scale factors are estimated by varying the muon

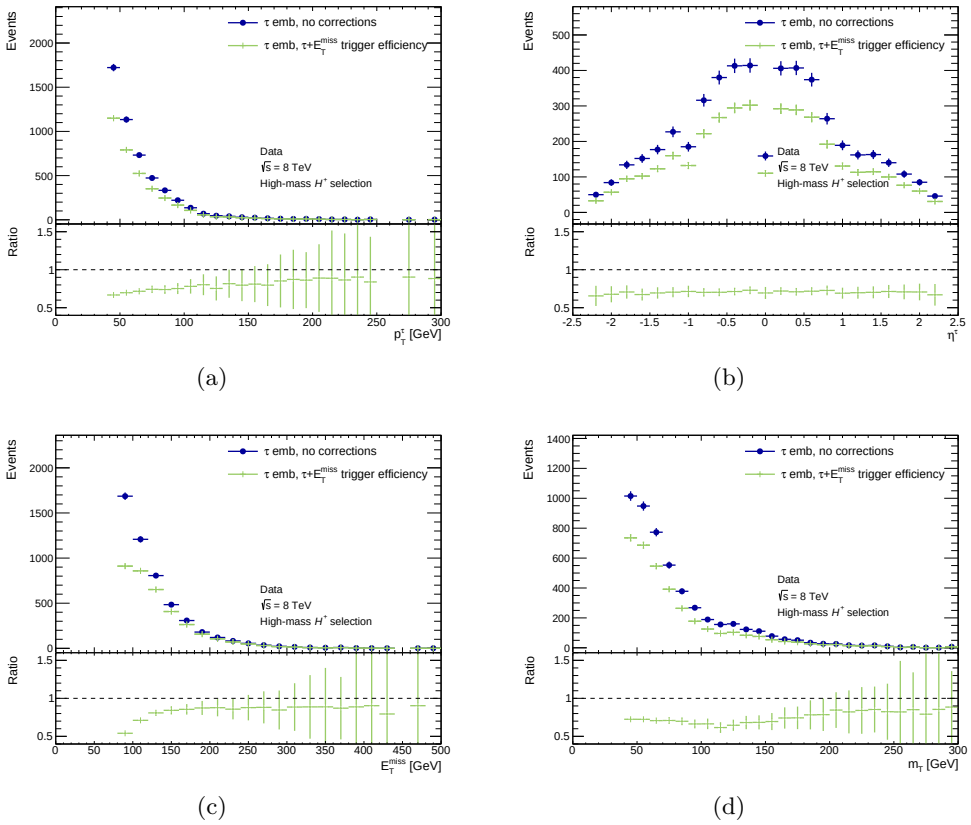

Figure 7.21. Comparisons of (a) p_{T}^{τ}, (b) η^{τ}, (c) $E_{\mathrm{T}}^{\mathrm{miss}}$ and (d) m_{T} of $\mu \to \tau$ embedded data before and after applying the $\tau + E_{\mathrm{T}}^{\mathrm{miss}}$ trigger efficiency correction. The high-mass H^+ selection is applied.

isolation requirements used for the tag-and-probe method. Multi-jet events are the only background contribution not included in simulation samples when calculating scale factors. By loosening the muon isolation requirement the data sample gets enriched in multi-jet events and the uncertainty due to this contribution is estimated. The resulting systematic uncertainties are shown in table 7.4.

The estimation of $\tau_{\text{had-vis}} + E_{\mathrm{T}}^{\mathrm{miss}}$ trigger-related systematic uncertainties in the 2012 data sample is more complex [155]. Different sources of systematic uncertainties are evaluated separately and for each uncertainty a new fit of the efficiencies is performed.

- The fit itself may lead to a bias. This is evaluated by using an arctan function instead of an error function for fitting, except for the efficiency of events with true 3-prong $\tau_{\text{had-vis}}$ candidates, where an error function is used instead of an arctan function. The maximum effect observed in the plateau is for the $E_{\mathrm{T}}^{\mathrm{miss}}$ trigger and events with 3-prong $\tau_{\text{had-vis}}$ candidates and of the order of 1%.

- The requirement on the transverse momentum of the muon in the $\mu + \tau_{\text{had-vis}}$ sample is tightened to vary the composition of the sample and evaluate its effect on the efficiencies. The maximum effect is observed for events with 3-prong $\tau_{\text{had-vis}}$ candidates in the $E_{\mathrm{T}}^{\mathrm{miss}}$ trigger leg and of the order of 1% in the plateau.

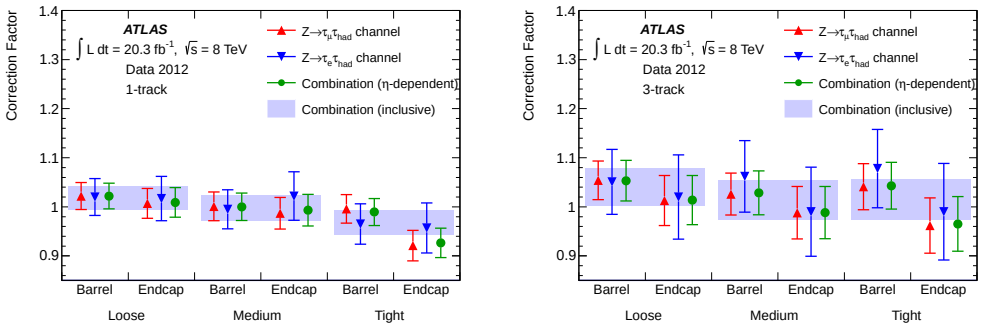

(a) Correction factors for 1-prong $\tau_{\text{had-vis}}$ (b) Correction factor for 3-prong $\tau_{\text{had-vis}}$

Figure 7.22. Scale factors to account for different $\tau_{\text{had-vis}}$ identification efficiencies between data and simulation [143]. These are applied to simulation and embedded data taken in 2012.

	$40\,\text{GeV} \leq p_{\text{T}}^{\tau} < 70\,\text{GeV}$	$70\,\text{GeV} \leq p_{\text{T}}^{\tau} < 500\,\text{GeV}$
$65\,\text{GeV} \leq E_{\text{T}}^{\text{miss}} < 100\,\text{GeV}$	$+7\%, -13\%$	$+7\%, -0\%$
$100\,\text{GeV} \leq E_{\text{T}}^{\text{miss}} < 500\,\text{GeV}$	$\pm 0\%$	$+0\%, -3\%$

Table 7.4. Systematic uncertainties on the trigger scale factors measured in 2011 data. Numbers give the percent variation from the nominal scale factors [154].

- The fact that no sub-division is done for the different triggers used throughout the data taking period may lead to a bias. This is evaluated by measuring the efficiencies of each trigger used separately. The maximum effect in the plateau is about 4‰, observed in the $E_{\text{T}}^{\text{miss}}$ trigger for events with 3-prong $\tau_{\text{had-vis}}$ candidates.

- The impact of misidentified $\tau_{\text{had-vis}}$ in the $\mu + \tau_{\text{had-vis}}$ sample used for the tag-and-probe method is evaluated by removing all events with non-true $\tau_{\text{had-vis}}$ candidates based on simulation and symmetrizing this effect. This effect is 4% (10%) for events with 1-prong (3-prong) $\tau_{\text{had-vis}}$ candidates in the plateau.

- The impact of the $\tau_{\text{had-vis}}$ energy scale uncertainty on the trigger efficiency is evaluated. This effect ranges between the permille level and about 1% for events with 1-prong and 3-prong $\tau_{\text{had-vis}}$ candidates in the plateau, respectively.

- A systematic uncertainty due to the difference between the combination of the individual $\tau_{\text{had-vis}}$ and $E_{\text{T}}^{\text{miss}}$ legs of the triggers and the combined $\tau_{\text{had-vis}} + E_{\text{T}}^{\text{miss}}$ triggers, referred to as residual correlation below, is evaluated by comparing the product of the efficiencies measured separately for the $\tau_{\text{had-vis}}$ and $E_{\text{T}}^{\text{miss}}$ triggers to the efficiencies of the combined triggers. While for background samples this correlation is small and only relevant for low $E_{\text{T}}^{\text{miss}}$ values it gets more important the higher the H^{+} mass. The residual correlations for different signal mass ranges and $t\bar{t}$ background are shown in figure 7.23.

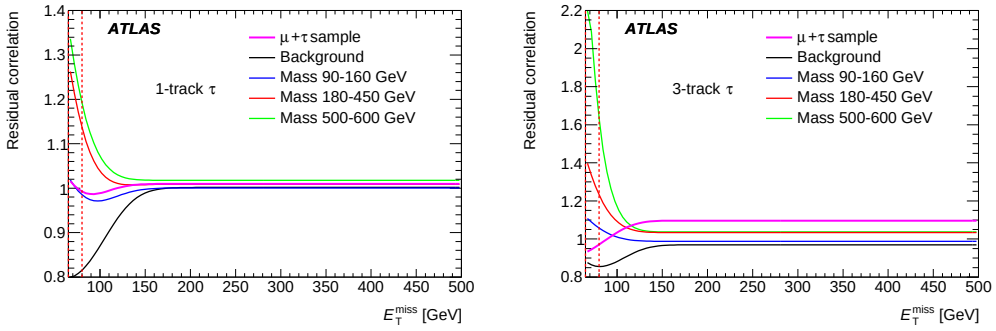

(a) Events with 1-prong $\tau_{\text{had-vis}}$ candidates (b) Events with 3-prong $\tau_{\text{had-vis}}$ candidates

Figure 7.23. Residual correlation between the $E_{\text{T}}^{\text{miss}}$ and $\tau_{\text{had-vis}}$ legs of the trigger used in 2012 data for (a) 1-prong and (b) 3-prong $\tau_{\text{had-vis}}$ candidates. For the embedded sample, only the black 'Background' curve is relevant [156].

- The impact of multi-jet events in the $\mu + \tau_{\text{had-vis}}$ sample is evaluated and found to be at the permille level in the plateau.

$\tau_{\text{had-vis}}$-Related Uncertainties Since the $\tau_{\text{had-vis}}$ in the embedded samples is simulated, uncertainties on the $\tau_{\text{had-vis}}$ identification correction factors and energy scale need to be considered. They are evaluated by shifting the particular parameter by one standard deviation and checking the effect on the final distributions and yields.
The uncertainty on the $\tau_{\text{had-vis}}$ identification in 2011 data is 4% for 1-prong and 7% for 3-prong $\tau_{\text{had-vis}}$ candidates. The energy scale uncertainties are binned in p_{T}^{τ} and $|\eta^{\tau}|$ and range from 2.5% to 3.5% for 1-prong and 3-prong $\tau_{\text{had-vis}}$ candidates in 2011 data [159]. The uncertainty on the $\tau_{\text{had-vis}}$ identification for 2012 data is 2.80% for 1-prong and 4.56% for 3-prong $\tau_{\text{had-vis}}$ passing 'tight BDT' identification with $p_{\text{T}} > 20\,\text{GeV}$ and $|\eta| < 1.37$. For $1.37 \leq |\eta| < 2.5$, these uncertainties increase to 3.25% and 5.76% for 1-prong and 3-prong $\tau_{\text{had-vis}}$, respectively. The uncertainty on the energy scale is binned in η and p_{T}, separately for 1-prong and 3-prong $\tau_{\text{had-vis}}$ candidates. It varies between 2% and 3% for 1-prong and 2.5% to 4% for 3-prong $\tau_{\text{had-vis}}$ candidates passing 'tight' BDT identification, respectively [160].

Embedding-Related Uncertainties The embedding method itself may introduce a bias. Since the embedding procedure used for the 2011 and 2012 dataset are slightly different, as described in chapter 7.1, the evaluation of systematic uncertainties differs as well.
For the 2011 data, three different, independent variations are applied. First, the fraction of energy deposited in the calorimeters that is attributed to the original muon and subtracted in the inner cone with $R < 0.1$ is varied by a factor of 2 to 0.5 to account for the possibility of pile-up related activity in this cone and some uncertainty about the amount of energy deposited by the muon. In a second and third variation, this factor is set to 1 but the inner cone size is changed to 0.05 and calorimeter cells outside a cone of $R = 0.1$ are not added to study a potential bias of the embedding settings.
Due to the different embedding procedure applied to 2012 data, the only systematic

uncertainty pertaining to the embedding procedure is the one concerning the amount of energy that is subtracted in calorimeter cells attributed to the muon. Following updated recommendations, it is varied by ±20% [157].

Effect of all Systematic Uncertainties on the Embedded Sample The effects of systematic uncertainties on the yield in the embedded samples is summarized in table 7.5. Some systematic uncertainties are combined here, e.g. all embedding procedure-related ones, all trigger-related uncertainties in the 2012 embedded samples and uncertainties related to the muon reconstruction and trigger corrections. Although numbers are given in this table, the full shape information is used for the statistical analysis presented in chapter 9. Dominant systematic uncertainties are due to uncertainties on the $\tau_{\text{had-vis}}$+$E_{\text{T}}^{\text{miss}}$ trigger efficiencies, on the identification (ID) efficiency and energy scale (ES) of the simulated $\tau_{\text{had-vis}}$ and the embedding procedure itself. In figure 7.24 and 7.25, the variations in the m_{T} shape and different yields after applying the full signal selection due to the individual systematic uncertainties are shown for the 2012 data.

Uncertainty	H^+ search 2011	low-mass H^+ search 2012	high-mass H^+ search 2012
τ ID	±5	±2.6	±2.7
τ ES	+4.8, −7.8	+4.8, −4.4	±4.7
Embedding parameters	±4.5	+3.5, −2.9	+2.0, −2.3
Muon isolation	±0.8	±0.8	±3.2
$\tau + E_{\text{T}}^{\text{miss}}$ trigger	+20.5, −18.3	+13.3, −13.2	+9.5, −9.1
μ ID, trigger	+3.3, −3.0	+1.3, −1.2	$\pm < 1$

Table 7.5. Systematic uncertainties on the embedded data samples. All variations given are percentages on the yield of the true τ background only. Full shape information of the m_{T} distributions is used for the statistical analysis in chapter 9 instead of the numbers given here.

7.4.4. Embedded Simulation

Embedded simulation is compared to default simulation samples as shown in figure 7.26 to validate the embedding procedure and compare events with embedded $\tau_{\text{had-vis}}$ candidates to nominal simulation events with $\tau_{\text{had-vis}}$ candidates. Embedding-related systematic uncertainties are included, but no other systematic uncertainties are shown. The distributions mostly agree within the uncertainties. However, the limited number of events available for embedding leads to significant statistical fluctuations.

7.4.5. Embedded Data

All distributions used as inputs for the m_{T} calculation, i.e. p_{T}^{τ}, $E_{\text{T}}^{\text{miss}}$ and $\Delta\phi(\tau, E_{\text{T}}^{\text{miss}})$ are shown in figure 7.27 for 2012 data and compared to simulation. For simulation, all trigger- and detector-related uncertainties are shown. Some of these are updated

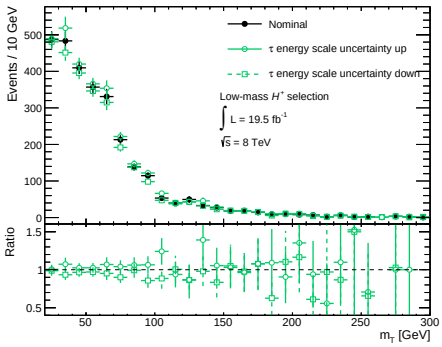

(a) Low-mass H^+ selection, τ ID uncertainty

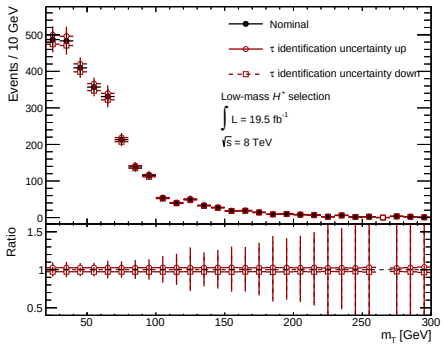

(b) Low-mass H^+ selection, τ ES uncertainty

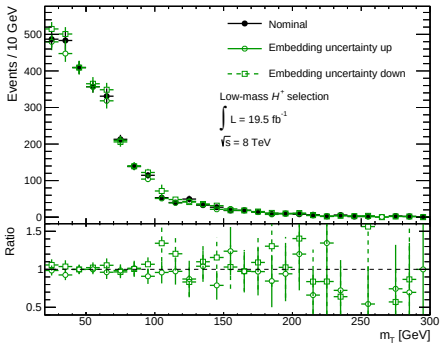

(c) Low-mass H^+ selection, embedding uncertainty

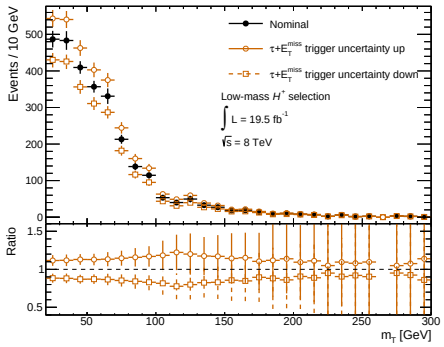

(d) Low-mass H^+ selection, $\tau + E_{\mathrm{T}}^{\mathrm{miss}}$ trigger uncertainty

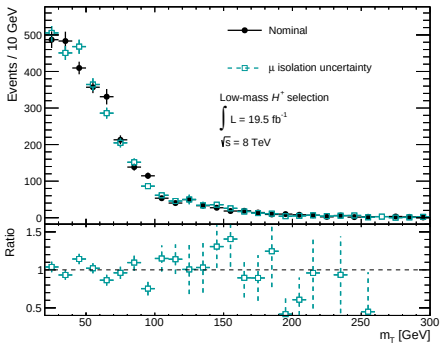

(e) Low-mass H^+ selection, μ isolation uncertainty

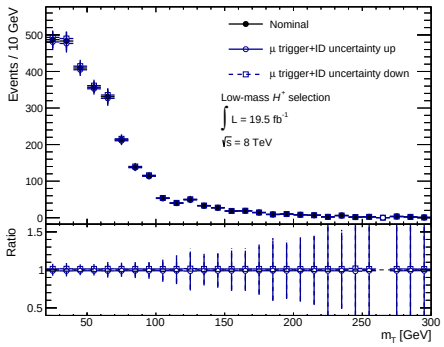

(f) Low-mass H^+ selection, μ reconstruction+trigger uncertainty

Figure 7.24. Effects of the (a) τ identification, (b) τ energy scale, (c) embedding, (d) $\tau + E_{\mathrm{T}}^{\mathrm{miss}}$ trigger, (e) muon isolation and (f) muon reconstruction and trigger uncertainties on the shape of the m_{T} distribution and yield after applying the low-mass H^+ selection for 2012. The uncertainty due to the muon isolation is shown as one-sided here but is symmetrized for the statistical analysis presented in chapter 9.

compared to those shown in figure 7.29 and thus slightly smaller. However, these differences only concern the distributions shown here and do not affect any results. Systematic uncertainties due to the $t\bar{t}$ production cross section, choice of generator model

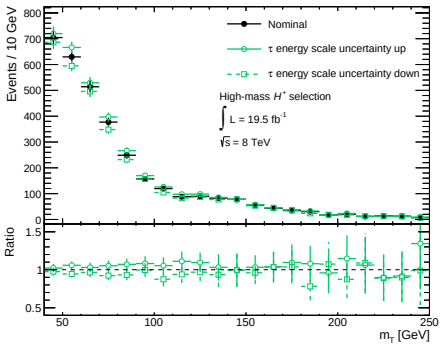

(a) High-mass H^+ selection, τ ID uncertainty

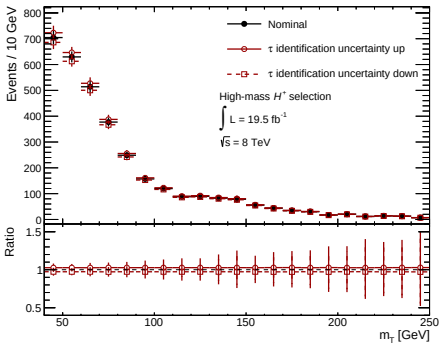

(b) High-mass H^+ selection, τ ES uncertainty

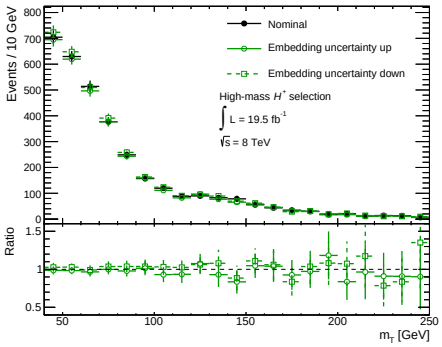

(c) High-mass H^+ selection, embedding uncertainty

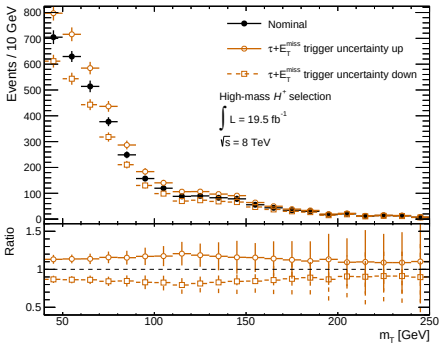

(d) High-mass H^+ selection, $\tau + E_{\mathrm{T}}^{\mathrm{miss}}$ trigger uncertainty

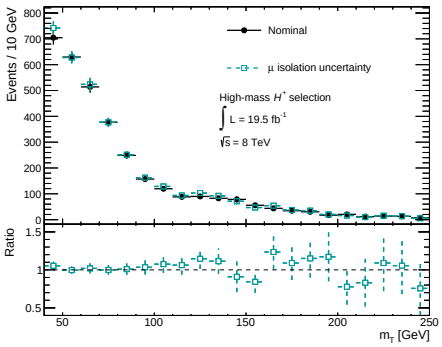

(e) High-mass H^+ selection, μ isolation uncertainty

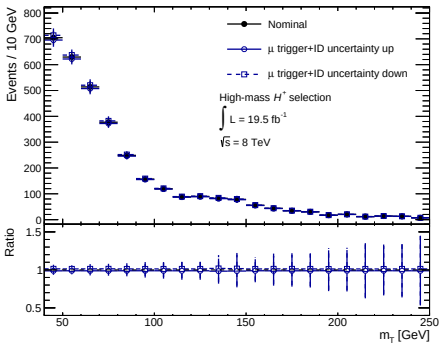

(f) High-mass H^+ selection, μ reconstruction+trigger uncertainty

Figure 7.25. Effects of the (a) τ identification, (b) τ energy scale, (c) embedding, (d) $\tau + E_{\mathrm{T}}^{\mathrm{miss}}$ trigger, (e) muon isolation and (f) muon reconstruction and trigger uncertainties on the shape of the m_{T} distribution and yield after applying the high-mass H^+ selection for 2012. The uncertainty due to the muon isolation is shown as one-sided here but is symmetrized for the statistical analysis presented in chapter 9.

and jet production rate, each causing a difference of about 10% on the event yield, are not included. The distributions agree well within systematic uncertainties.

The final m_{T} distributions of embedded data compared to default simulation after

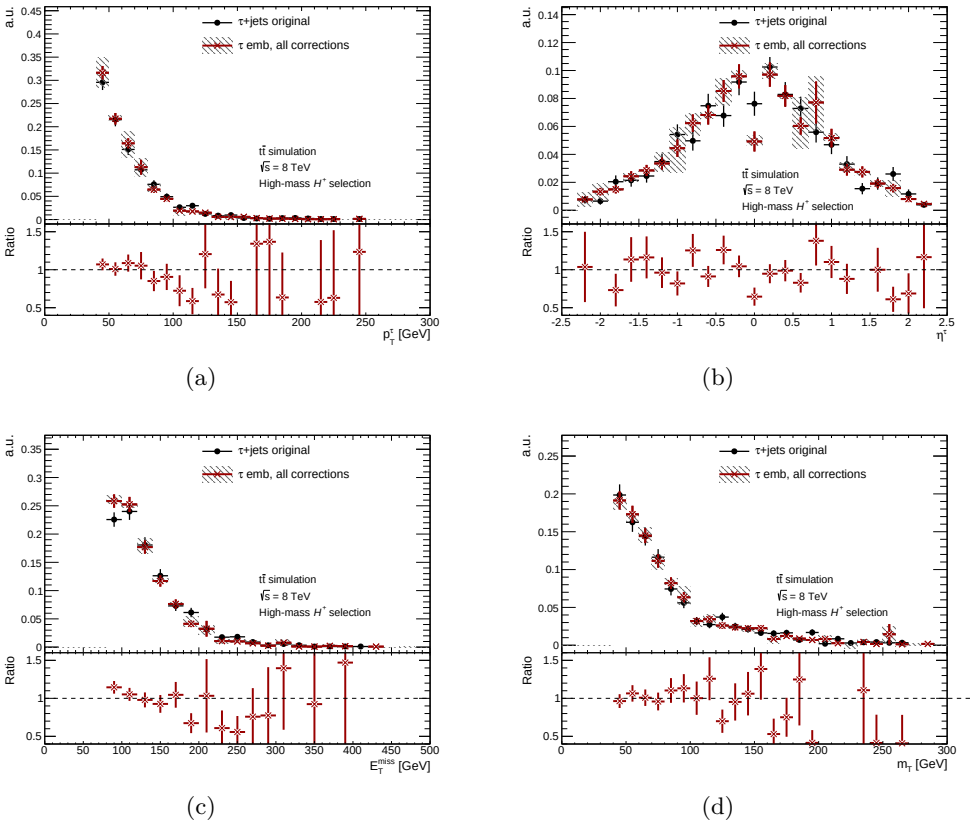

Figure 7.26. Comparisons of (a) p_{T}^{τ}, (b) η^{τ}, (c) $E_{\mathrm{T}}^{\mathrm{miss}}$ and (c) m_{T} of default and $\mu \to \tau$ embedded $t\bar{t}$ simulation after applying all corrections. The hatched gray areas indicate the embedding-related systematic uncertainties. The high-mass H^+ selection is applied.

applying the H^+ selection described in chapter 6.1 and all corrections described above are shown in figure 7.28 for the 2011 data. All systematic uncertainties pertaining to the embedded data are shown. For simulation, only trigger- and detector-related uncertainties are shown as explained above. Corresponding figures for the low-mass and high-mass H^+ searches in 2012 data are shown in figure 7.29.

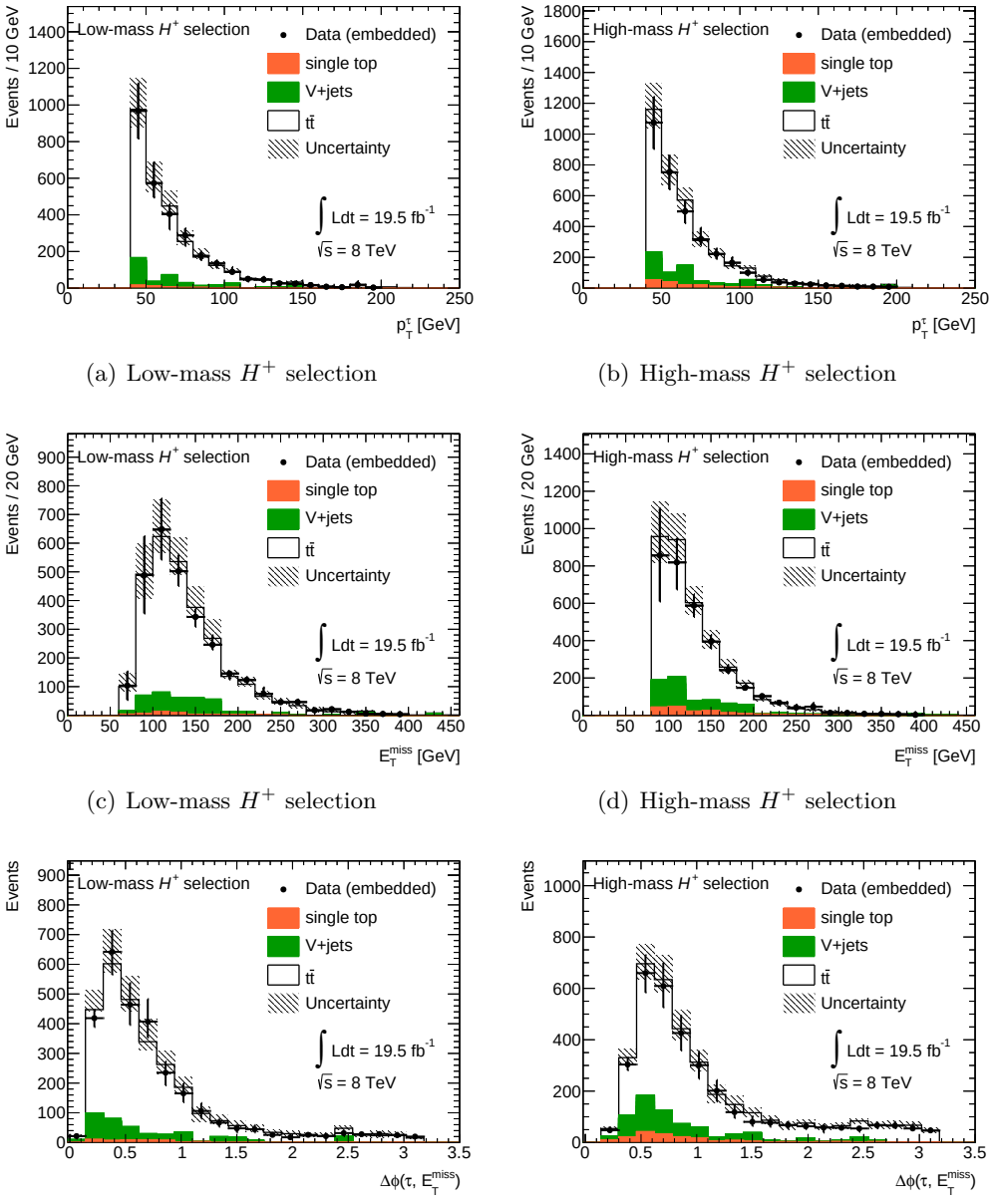

(a) Low-mass H^+ selection

(b) High-mass H^+ selection

(c) Low-mass H^+ selection

(d) High-mass H^+ selection

(e) Low-mass H^+ selection

(f) High-mass H^+ selection

Figure 7.27. Comparisons of (a, b) p_{T}^{τ}, (c, d) $E_{\mathrm{T}}^{\mathrm{miss}}$ and (e, f) $\Delta\phi$ of default simulation and $\mu \to \tau$ embedded data after applying all corrections and the low-mass (high-mass) H^+ selection in the left (right) column. Statistical and systematic uncertainties are shown for both simulation and embedded data.

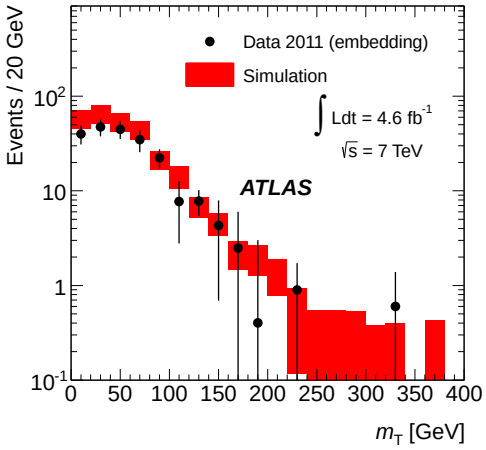

Figure 7.28. Transverse mass distribution comparing fully normalized and corrected embedded data using the 2011 data sample to simulation after applying the signal selection. Statistical and systematic uncertainties are shown for embedded data and simulation [1].

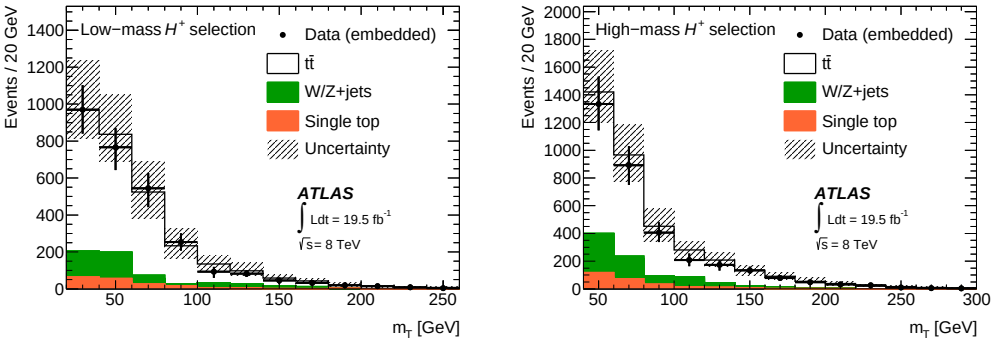

(a) Low-mass H^+ selection

(b) High-mass H^+ selection

Figure 7.29. Transverse mass distribution of the $\mu \to \tau$ embedded 2012 data sample of events with a true $\tau_{\text{had-vis}}$ compared to default simulation for the (a) low-mass and (b) high-mass H^+ search. Systematic uncertainties are shown for embedded data and simulation in error bars and hatched bands, respectively [2].

8 Estimation of Other Background Contributions and Systematic Uncertainties on the Signal Predictions

The background estimates described in this chapter were carried out by other people involved in the analyses described in this thesis. Since they are essential for the final results, however, a brief overview is given based on references [1, 2, 154, 155, 161].
The background estimates for processes where jets, electrons or muons are misidentified as $\tau_{\text{had-vis}}$ candidates are described below, separately for the 2011 and 2012 analyses. Additionally, systematic uncertainties concerning the signal predictions are described for the 2011 and 2012 analyses.

8.1. Other Background Contributions in the 7 TeV Analysis

8.1.1. Multi-jet Background

Multi-jet events can pass the signal selection through misidentification of final state objects. Since the uncertainties in simulating these events are large, a data-driven method is used to estimate the multi-jet background contribution. A template for the shape of the $E_{\text{T}}^{\text{miss}}$ distribution in multi-jet events is derived from data. This is done in a control sample (also called 'inverted sample') with events fulfilling the following requirements:

- The $\tau_{\text{had-vis}}$ candidate in the event passes 'loose' but not 'tight' identification criteria.
- No b-tagged jet is found, using the same b-tagging criterion as in the signal selection.
- The requirement on the m_{jjb} mass used in the signal selection is omitted.

The contributions of $t\bar{t}$, single top quark, W+jets and diboson events, amounting to less than 1% of the events observed in this control region, are subtracted from the control sample. The $E_{\text{T}}^{\text{miss}}$ distributions in the control region and after applying the requirements up to the lepton vetoes as described in chapter 6.1 and after subtracting expectations from $t\bar{t}$, W+jets and single top quark events are shown in figure 8.1. The assumption is that after the full event selection is applied, the agreement between the shapes is sufficiently good, within statistical uncertainties, for them to be used for the estimate. However, the disagreement between the shapes seen in figure 8.1 is taken into account as a source of a systematic uncertainty.
The $E_{\text{T}}^{\text{miss}}$ distribution of the control sample, $t\bar{t}$, single top quark, W+jets and diboson

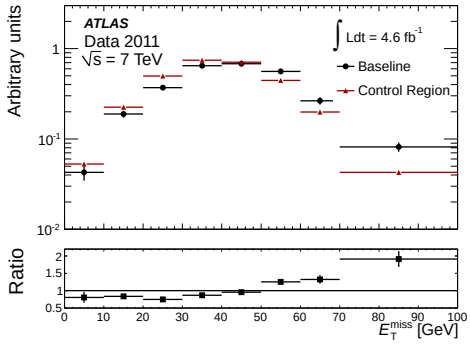

Figure 8.1. Shapes of the $E_{\mathrm{T}}^{\mathrm{miss}}$ distribution in the control region and after applying the baseline selection described in chapter 6.1 until just before the $E_{\mathrm{T}}^{\mathrm{miss}}$ requirement. In the control region, the $\tau_{\text{had-vis}}$ and b-tagging selection are modified compared to the baseline selection [162].

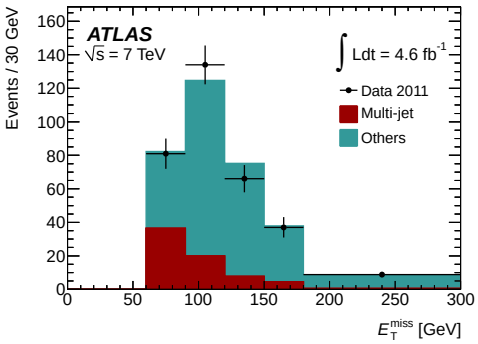

Figure 8.2. Fit of the $E_{\mathrm{T}}^{\mathrm{miss}}$ template to data in the signal region, including statistical uncertainties only [1].

events normalized to luminosity are then fit to the $E_{\mathrm{T}}^{\mathrm{miss}}$ distribution in data to which the full signal selection is applied. Only the overall normalization and fraction of multi-jet events are free fit parameters, but not the relative normalization of the template. The fit of the $E_{\mathrm{T}}^{\mathrm{miss}}$ template to data in the signal region is shown in figure 8.2.

The shape of the m_{T} distribution of the multi-jet background contribution is extracted from the inverted sample. This shape and the amount of multi-jet events determined through the $E_{\mathrm{T}}^{\mathrm{miss}}$ template fit are used to fit the m_{T} distribution in the signal region. The result is shown in figure 8.3 together with expectations from other background processes and compared to data.

Systematic Uncertainties The uncertainty on the theoretical $t\bar{t}$ cross section, $\sigma_{t\bar{t}} = 164.57^{+4.30}_{-9.27}\,\mathrm{pb}^{-1}$, the relative normalization of $t\bar{t}$ and W+jets events and the shapes of the $E_{\mathrm{T}}^{\mathrm{miss}}$ distribution in these events impact the template. The total uncertainty on the multi-jet background estimate due to these is $^{+0.03}_{-0.02}\%$. The template is fit in a limited $E_{\mathrm{T}}^{\mathrm{miss}}$ range, $E_{\mathrm{T}}^{\mathrm{miss}} < 300\,\mathrm{GeV}$. The uncertainty due to limiting this range is evaluated by varying the fit range by $\pm 50\,\mathrm{GeV}$, leading to an uncertainty of $^{+0.7}_{-0.0}\%$ in the estimated amount of multi-jet events. The bin width leads to variations in the shape of the $E_{\mathrm{T}}^{\mathrm{miss}}$

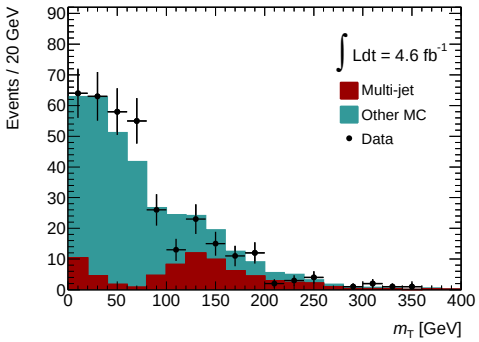

Figure 8.3. Estimated contribution of multi-jet events to the final m_{T} distribution after applying the full signal selection [154].

distribution, causing a systematic uncertainty of $^{+6.7}_{-0.9}\%$. It is evaluated by varying the bin widths. The shape differences between the $E_{\mathrm{T}}^{\mathrm{miss}}$ distribution shown in figure 8.1 leads to an uncertainty of $^{+4.6}_{-1.2}\%$. It is assessed by rescaling the number of entries per bin in the inverted sample to match that of the bins in the baseline sample and repeating the fit.
The total normalization uncertainty related to the estimation of multi-jet background events is 32% due to fit-related uncertainties and 16% due to the $E_{\mathrm{T}}^{\mathrm{miss}}$ shape in the control region.

8.1.2. Events with Jets Misidentified as Hadronically Decaying τ Leptons

Probabilities for jets misidentified as $\tau_{\text{had-vis}}$ candidates are determined in a control region enriched in W+jets events. Only events where the jet is not due to multi-jet production are assessed by this method. To pass the selection for the control sample, events have to meet the following requirements in addition to data quality cuts as used in the signal selection:

- The event is triggered by a single lepton trigger, with thresholds of 20 GeV or 22 GeV for electron triggers and 18 GeV for muon triggers.
- The event contains an electron or muon matching selection criteria described in chapter 6.1 and with $E_{\mathrm{T}} > 20\,\mathrm{GeV}$ in the case of an electron or $p_{\mathrm{T}} > 25\,\mathrm{GeV}$ in the case of a muon.
- A $\tau_{\text{had-vis}}$ candidate with $p_{\mathrm{T}} > 20\,\mathrm{GeV}$ is found.
- The event does not contain a jet that is b-tagged.

The misidentification probability p^j_{mID} is defined by

$$p^j_{mID} = \frac{\text{no. of } \tau_{\text{had-vis}} \text{ candidates passing object selection \& } \tau_{\text{had-vis}} \text{ ID}}{\text{no. of } \tau_{\text{had-vis}} \text{ candidates passing object selection}}$$

The misidentification probability is measured as a function of number of charged-particle tracks associated with the $\tau_{\text{had-vis}}$ candidate as well as p_{T} and $|\eta|$ of the $\tau_{\text{had-vis}}$ candidate

and shown in figure 8.4. It is applied to $t\bar{t}$, W+jets, single top quark, Z+jets and

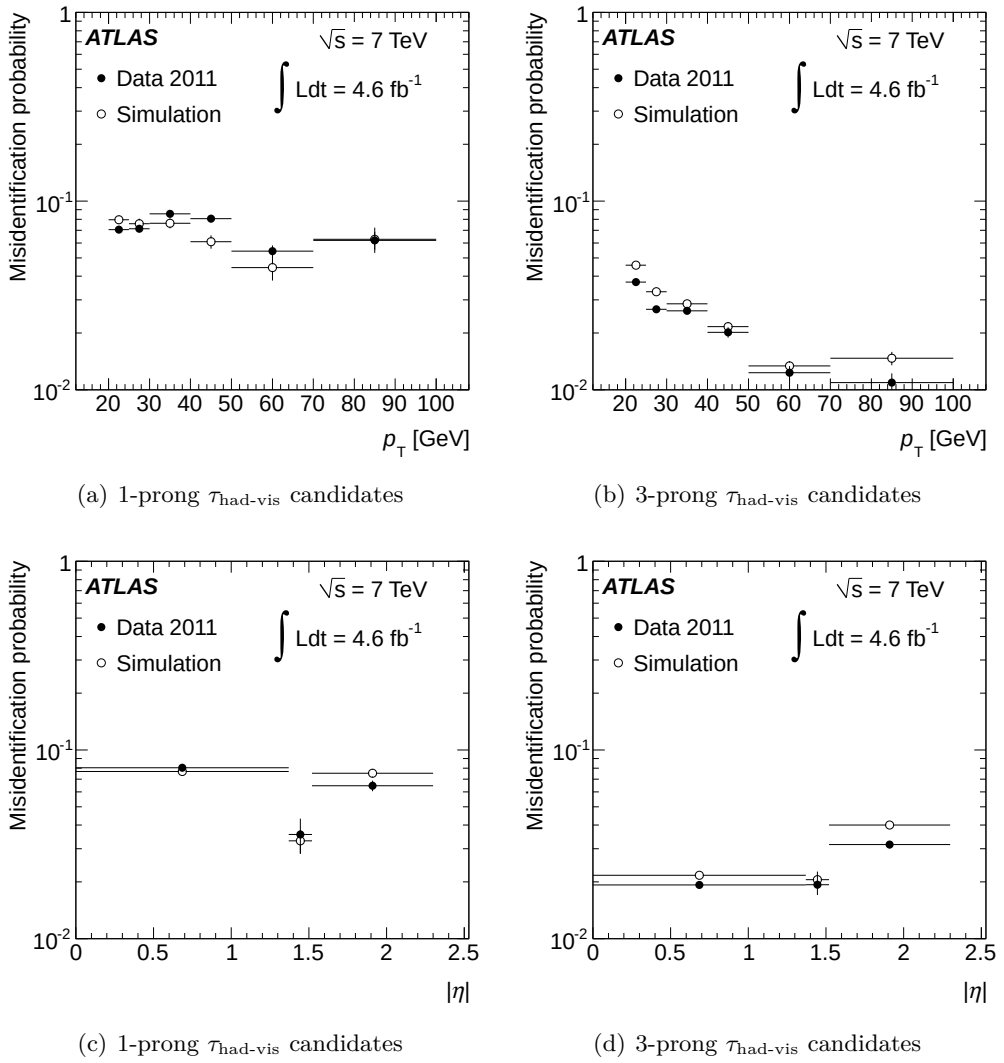

(a) 1-prong $\tau_{\text{had-vis}}$ candidates

(b) 3-prong $\tau_{\text{had-vis}}$ candidates

(c) 1-prong $\tau_{\text{had-vis}}$ candidates

(d) 3-prong $\tau_{\text{had-vis}}$ candidates

Figure 8.4. Probabilities for jets to be misidentified as $\tau_{\text{had-vis}}$ candidates, p^j_{mID}, separately for 1-prong (3-prong) $\tau_{\text{had-vis}}$ candidates in the left (right) column. Probabilities are binned in p^τ_{T} and $|\eta|^\tau$ and shown for data and simulation [162].

diboson events passing the nominal signal selection except for the $\tau_{\text{had-vis}}$ identification (ID) criteria and normalized to luminosity to estimate the number of events with jets misidentified as $\tau_{\text{had-vis}}$ candidates and not originating from multi-jet events.

Systematic Uncertainties The major systematic uncertainty is due to differences in jet composition (i.e. if jets are quark- or gluon-initiated) of $\tau_{\text{had-vis}}$ candidates between events in the control region where p^j_{mID} is measured and background events in the signal region. About 3% (20%) of the jets misidentified as $\tau_{\text{had-vis}}$ candidates in the control region are due to Z+jets (multi-jet) events. The difference in jet composition between all of these events is compared to that of another control region, consisting mostly of

$t\bar{t}$ events, using simulation. The systematic uncertainty due to the jet composition is estimated to be about 12%. The systematic uncertainty due to a contamination with $\tau_{\text{had-vis}}$ candidates not originating from jets in the W+jets control region is assessed based on simulation and estimated to be about 6%. The statistical uncertainty in the control region leads to a systematic uncertainty of 2%. Object-related systematic uncertainties result in a total uncertainty of about 21%. All of these numbers are given as uncertainties on the normalization.

8.1.3. Events with Electrons Misidentified as Hadronically Decaying τ Leptons

The measurement of the probability for electrons misidentified as $\tau_{\text{had-vis}}$ is based on a tag-and-probe method in $Z \to ee$ events. The background contribution of events with electrons misidentified as $\tau_{\text{had-vis}}$ candidates is small due to the very efficient electron veto applied, rejecting events with electrons misidentified as $\tau_{\text{had-vis}}$ candidates. Events have to pass the following selection criteria:

- The tag electron fulfills the selection criteria detailed in chapter 6.1, has $E_{\text{T}} > 25\,\text{GeV}$ and overlaps geometrically ($\Delta R < 0.1$) with the electron trigger object. The requirement on the electron trigger object is $E_{\text{T}} > 20$ or $> 22\,\text{GeV}$, depending on the data taking period.
- The probe electron is considered as a $\tau_{\text{had-vis}}$ candidate with $p_{\text{T}} > 20\,\text{GeV}$, $|\eta| < 2.5$ and exactly one associated charged-particle track.
- The tag and probe electrons have opposite charges.
- The missing transverse momentum is less than 20 GeV.
- If multiple electron-$\tau_{\text{had-vis}}$ pairs pass these requirements, the pair with the highest scalar sum of transverse energies that is also separated by $\Delta R > 0.4$, is chosen. The invariant mass m_{ll} of the chosen pair must also satisfy $80\,\text{GeV} < m_{ll} < 100\,\text{GeV}$.

The selected sample consists of about 99% $Z \to ee$ events, estimated from simulation. The impurity arises from events due to multi-jet processes, which are assessed based on a two-dimensional sideband subtraction method [163] and events due to $W \to e\nu$ or $Z/\gamma^* \to \tau\tau$ processes, which are estimated based on simulation. Multi-jet events and events due to electroweak processes are subtracted from the control sample.
The misidentification probability p^e_{mID} for electrons matching all selection criteria and being misidentified as $\tau_{\text{had-vis}}$ candidates is defined by

$$p^e_{mID} = \frac{\text{no. of } \tau_{\text{had-vis}} \text{ candidates passing object selection, } \tau_{\text{had-vis}} \text{ ID \& } e \text{ veto}}{\text{no. of } \tau_{\text{had-vis}} \text{ candidates passing object selection}}$$

The misidentification probability is determined in data and simulation and a scale factor is derived from the ratio of these. The scale factor, depending on $|\eta|$ and given in table 8.1 is applied to simulated events where the selected $\tau_{\text{had-vis}}$ candidate originates from a true electron.

$\lvert\eta^\tau\rvert$	Scale factor
≤ 1.37	1.28 ± 0.52
$1.37 - 1.52$	1.0 ± 1.0
$1.52 - 2.00$	0.54 ± 0.36
≥ 2.00	2.76 ± 1.29

Table 8.1. Scale factors applied to events in which electrons are misidentified as $\tau_{\text{had-vis}}$ and pass requirements as described in the text. Statistical and systematic uncertainties are combined [154].

Systematic Uncertainties The most important systematic uncertainty is due to the subtraction of events from multi-jet and electroweak processes. Another major systematic uncertainty arises from the selection criteria of the tag electron. It is assessed by requiring the tag electron to pass 'medium' instead of 'tight' identification criteria. The total systematic uncertainty on the normalization of this background contribution is about 22%.

8.2. H^+ Signal in the 7 TeV Analysis

The full event selection described in chapter 6.1 is applied to signal samples in a mass range $90\,\text{GeV} \leq m_{H^+} \leq 160\,\text{GeV}$.

Systematic Uncertainties All simulation-related uncertainties are taken into account. This encompasses uncertainties on $\tau_{\text{had-vis}}$ identification and energy scale, jet energy scale and resolution, b-tagging efficiency and $E_{\text{T}}^{\text{miss}}$ calculation. A systematic uncertainty associated with the trigger scale factors is considered. Additionally, generator-related systematic uncertainties are considered by comparing the default signal samples to samples produced with other generators and hadronization models as described in chapter 4.2.4. The systematic uncertainty on the theoretical $t\bar{t}$ cross section is considered. Effects of these systematic uncertainties are summarized in table 8.2.

For the interpretation in the $m_{\text{h}}^{\text{max}}$ scenario of the MSSM, the following uncertainties affecting $\sigma_{t\bar{t}} \times B(t \to H^+b) \times B(t \to Wb)$ are taken into account: a 5% uncertainty is considered for missing one-loop electroweak corrections, a 2% uncertainty for missing two-loop QCD corrections and an uncertainty of about 1% that depends on $\tan\beta$ to account for uncertainties caused by the running b quark mass [65, 164–166]. As recommended by the LHC Higgs cross section working group, these uncertainties are added linearly [166].

Source of uncertainty	Normalization uncertainty in %
$\tau_{\text{had-vis}}$ identification	4-7
$\tau_{\text{had-vis}}$ energy scale	2.5-5.0
Jet energy resolution	10-30
Jet energy scale (JES)	2.5-14 + pile-up term of 2-7
b-tagging efficiency	5-17
b-tagging mistag rate	12-21
b-tagged JES uncertainty	< 2.5
$E_{\text{T}}^{\text{miss}}$ uncertainty	object-related uncertainties are propagated to $E_{\text{T}}^{\text{miss}}$ calculation + additional CellOut and SoftJet terms + 10% uncertainty due to pile-up contribution
Generator and parton shower	5
Initial and final state radiation	19
$t\bar{t}$ cross section	10-11

Table 8.2. Detector- and simulation-related systematic uncertainties taken into account for signal processes in the 2011 analysis [1, 154].

8.3. Other Background Contributions in the 8 TeV Analyses

8.3.1. Events with Jets Misidentified as Hadronically Decaying τ Leptons

A matrix method is used to estimate the background contribution with jets misidentified as $\tau_{\text{had-vis}}$ candidates. Two data samples are defined that differ in the $\tau_{\text{had-vis}}$ identification criteria. Events in the tight sample are required to pass the same $\tau_{\text{had-vis}}$ identification as described in chapter 6.2 while this does not hold for events in the loose sample. Thus the tight sample contains a larger fraction of real $\tau_{\text{had-vis}}$ than the loose sample, which is enriched with misidentified $\tau_{\text{had-vis}}$ candidates.
The loose sample contains N_L events passing loose but not tight identification and N_T events passing tight identification. The loose sample also consists of N_r events with real and N_m events with misidentified $\tau_{\text{had-vis}}$ candidates. Thus $N_T = N_{T,r} + N_{T,m}$ and $N_L = N_{L,r} + N_{L,m}$. With the efficiencies p_r and p_m for a real or misidentified loose $\tau_{\text{had-vis}}$ candidates to pass the tight selection, i.e.

$$p_m = \frac{N_{T,m}}{N_{L,m}} \quad \text{and} \quad p_r = \frac{N_{T,r}}{N_{L,r}}, \tag{8.1}$$

the following relation holds:

$$N_{T,m} = \frac{p_m p_r}{p_r - p_m} N_L + \frac{p_m(p_r - 1)}{p_r - p_m} N_T \tag{8.2}$$

A weight is calculated for each event in the loose sample to compute the number of events with misidentified $\tau_{\text{had-vis}}$ candidates in the tight sample. For events passing loose

but not tight $\tau_{\text{had-vis}}$ identification, the weight is given by

$$w_L = \frac{p_m p_r}{p_r - p_m} \tag{8.3}$$

and for events also passing tight $\tau_{\text{had-vis}}$ identification it is given by

$$w_T = \frac{p_m(p_r - 1)}{p_r - p_m} \tag{8.4}$$

If there is more than one $\tau_{\text{had-vis}}$ candidate passing loose requirements in an event, which happens very rarely, each candidate is assigned a separate weight as if they were from individual events.
The probability p_r is determined using true $\tau_{\text{had-vis}}$ in simulated $t\bar{t}$ events after the full signal selection. The measurement is parameterized in p_{T}^{τ}, $|\eta^{\tau}|$ and $N_{\text{track}}^{\text{iso}}$, i.e. the number of tracks in a hollow isolation cone with $0.2 < \Delta R < 0.4$ around the $\tau_{\text{had-vis}}$ axis, and shown in figure 8.5. Scale factors to correct efficiencies in simulation to data are applied.
The probability p_m is measured in a W+jets control region in data. This control region is defined by

- a combined trigger on an electron with $E_{\text{T}} > 18\,\text{GeV}$ or muon with $p_{\text{T}} > 15\,\text{GeV}$ in addition to the $\tau_{\text{had-vis}}$ with $p_{\text{T}} > 20\,\text{GeV}$
- exactly one trigger-matched electron or muon in addition to a trigger-matched $\tau_{\text{had-vis}}$ candidate passing loose identification criteria
- no b-tagged jets
- a transverse mass $m_T^{\ell} = \sqrt{2p_{\text{T}}^{\ell} E_{\text{T}}^{\text{miss}}(1 - \cos\Delta\phi)} > 50\,\text{GeV}$, where ℓ refers to the muon or electron and $\Delta\phi$ is measured between the light lepton and $E_{\text{T}}^{\text{miss}}$.

The number of signal events in this region is negligible ($< 0.1\%$) and the amount of events with true $\tau_{\text{had-vis}}$ (7%) or electrons/muons mis-identified as $\tau_{\text{had-vis}}$ candidates (5%) is estimated based on simulation and subtracted. The probability p_m is parameterized in the same variables as p_r, i.e in p_{T} and $|\eta|$ of the $\tau_{\text{had-vis}}$, the number of charged-particle tracks in a cone with $R < 0.2$ around the $\tau_{\text{had-vis}}$ and the number of charged-particle tracks in an annulus with $0.2 < R < 0.4$ around the $\tau_{\text{had-vis}}$, $N_{\text{track}}^{\text{iso}}$. Correlations between these variables are investigated and found to be negligible. In figure 8.6, p_m is shown parameterized in the three variables mentioned above, separately for 1-prong and 3-prong $\tau_{\text{had-vis}}$ candidates.
The background contribution with jets misidentified as $\tau_{\text{had-vis}}$ candidates is especially important at high values of m_{T}. Because of the limited amount of events in this region, the m_{T} distribution is fit using a power-log function

$$f(x) = x^{a+b\ln(x)}, \tag{8.5}$$

where a and b are fitted constants, in the m_{T} mass range $200 - 800\,\text{GeV}$, shown in figure 8.7. The distribution is fit separately after considering each systematic uncertainty.

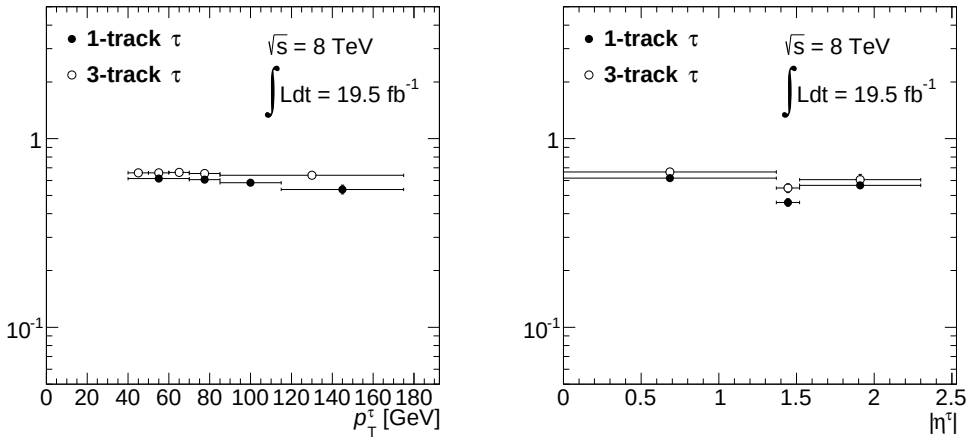

(a) p_r vs. p_{T}^{τ}

(b) p_r vs. $|\eta^{\tau}|$

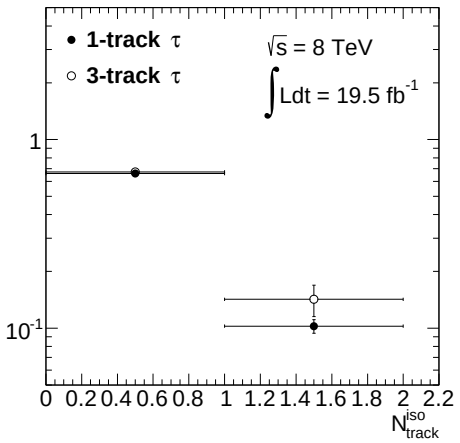

(c) p_r vs. $N_{\mathrm{track}}^{\mathrm{iso}}$

Figure 8.5. p_r measured in $t\bar{t}$ simulation, separately for 1-prong and 3-prong $\tau_{\text{had-vis}}$ candidates depending on (a) p_{T}^{τ}, (b) $|\eta^{\tau}|$ and (c) number of charged-particle tracks in an annulus with $0.2 < R < 0.4$ around the $\tau_{\text{had-vis}}$ candidate,$N_{\mathrm{track}}^{\mathrm{iso}}$ [155].

Systematic Uncertainties The most important systematic uncertainties are the statistical uncertainties on the probabilities p_m (14.3-15.9%) and p_r (2.5-3.9%) due to the limited size of the control samples and an uncertainty on p_m caused by differences in jet composition between the control sample and the signal region (8.1-9.2%). The latter is evaluated by measuring p_m in another control region that is enriched in gluon-initiated jets instead of quark-initiated jets in the W+jets control region. An additional systematic uncertainty is added for the choice of fit function in the high-m_{T} region. The fit is repeated with an alternative fit using an exponential function. The difference between the baseline and alternative fit is symmetrized and used as systematic uncertainty. Less important systematic uncertainties are simulation-related uncertainties on the $\tau_{\text{had-vis}}$ identification when measuring p_r and p_m (2.7-5.9%) and on the electron veto efficiency

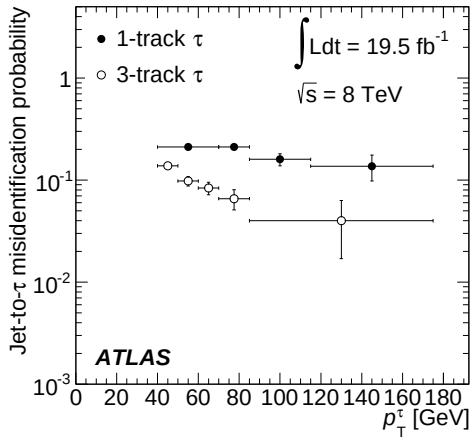

(a) p_m vs. p_{T}^{τ}

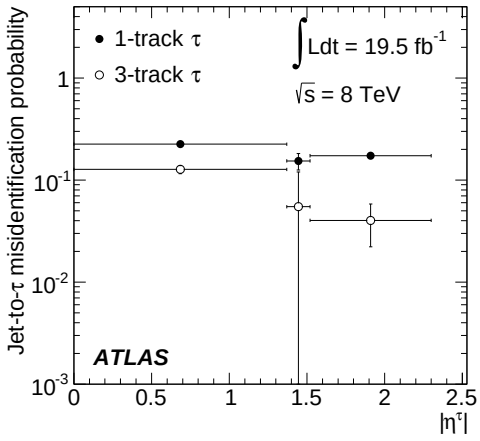

(b) p_m vs. $|\eta|^{\tau}$

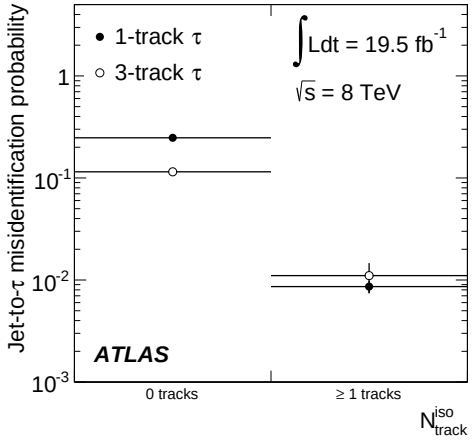

(c) p_m vs. $N_{\mathrm{track}}^{\mathrm{iso}}$

Figure 8.6. p_m measured in a W+jets control region, separately for 1-prong and 3-prong $\tau_{\text{had-vis}}$ candidates depending on (a) p_{T}^{τ}, (b) $|\eta^{\tau}|$ and (c) number of charged-particle tracks in an annulus with $0.2 < R < 0.4$ around the $\tau_{\text{had-vis}}$ candidate, $N_{\mathrm{track}}^{\mathrm{iso}}$ [156].

when measuring p_m (3.5-3.8%). All uncertainties are given as normalization uncertainties on the yield of this background estimate but full shape information, including the high-m_{T} fit uncertainties, is considered for the statistical analysis presented in chapter 9.

8.3.2. Events with Electrons or Muons Misidentified as Hadronically Decaying τ Leptons

The very small background contribution with electrons or muons that are misidentified as $\tau_{\text{had-vis}}$ candidates is estimated based on simulation. Scale factors [160] are applied to correct for differences in simulation and data. This background contribution comprises

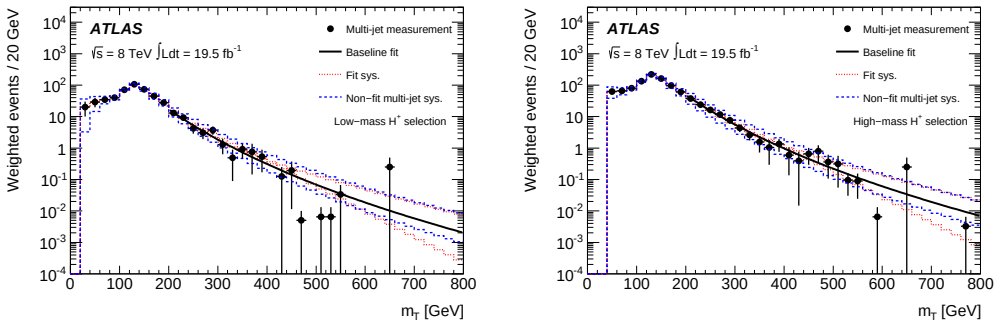

(a) Low-mass H^+ selection

(b) High-mass H^+ selection

Figure 8.7. The prediction for multi-jet background events estimated using the matrix method for the (a) low-mass and (b) high-mass H^+ selection for the analyses based on 2012 data. The solid line shows the nominal prediction resulting from the fit with a power-log function while the dotted lines show the systematic uncertainty due to the choice of the fit function for the high m_{T} region. The dashed lines indicate the total combined fits from all systematic uncertainties relevant for this background [2].

about 1-2% of the total background and consists of events from $t\bar{t}$, W+jets, single top quark, Z+jets and diboson processes.

Systematic Uncertainties Since this background contribution is estimated based on simulation, all detector-related and event generation-related systematic uncertainties have to be taken into account. The uncertainty due to the choice of generator and parton shower is 8-9%, while initial and final state radiation cause an uncertainty of 11%. The theoretical uncertainty on the $t\bar{t}$ cross section is considered, since the cross section is needed for normalizing the background contributions, $\sigma_{t\bar{t}} = 253^{+13}_{-15}$ pb. Since all objects are simulated, uncertainties on the jet energy scale for light and b-tagged jets, $\tau_{\text{had-vis}}$ electron veto, jet energy resolution, $E_{\mathrm{T}}^{\text{miss}}$ terms and b-tagging efficiency are considered. Trigger-related systematic uncertainties due to the choice of the fit function, varying efficiencies in the different data taking periods, muon isolation and p_{T} requirements, misidentified $\tau_{\text{had-vis}}$ candidates in the $\mu + \tau_{\text{had-vis}}$ sample and limited sample size are all taken into account.

8.4. H^+ Signal in the 8 TeV Analyses

The full event selections described in chapter 6.2 are applied to the signal samples detailed in chapter 4.2.3. For the low-mass (high-mass) H^+ search, a mass range 80 GeV $\leq m_{H^+} \leq$ 160 GeV (180 GeV $\leq m_{H^+} \leq$ 1000 GeV) is probed.

Systematic Uncertainties All systematic uncertainties described in chapter 4.2.4 are taken into account. Additionally, detector-related uncertainties are considered. These encompass uncertainties on the $\tau_{\text{had-vis}}$ identification and energy scale, on the energy

Source of uncertainty	Normalization uncertainty in %
Jet energy scale	2.2-14.2
Jet vertex fraction	1.9-2.7
$E_{\mathrm{T}}^{\mathrm{miss}}$	0.006-2.6
τ e-veto	0-0.04
$\tau_{\text{had-vis}}$ identification	3.2-3.3
τ energy scale	0.4-4.7
b-tagging	1.0-2.2
Trigger	6.3-7.0
Generator model (low-mass H^+)	9
Generator model (high-mass H^+)	2-9
Initial/final state radiation (low-mass H^+)	11
Initial/final state radiation (high-mass H^+)	1-2
H^+ production (4FS vs. 5FS)	3-5
$t\bar{t}$ cross section (low-mass H^+)	6

Table 8.3. Summary of generator-, detector- and trigger-related systematic uncertainties taken into account for the low-mass and high-mass signal samples in the 2012 analyses and effects on the final yields [2, 155].

scale of b-tagged and light jets, on the b-tagging efficiency, jet energy resolution and $E_{\mathrm{T}}^{\mathrm{miss}}$ terms. Trigger-related uncertainties due to residual correlations between the $\tau_{\text{had-vis}}$ and $E_{\mathrm{T}}^{\mathrm{miss}}$ legs of the trigger, varying efficiencies in different data taking periods, the amount of misidentified $\tau_{\text{had-vis}}$ candidates in the $\mu + \tau_{\text{had-vis}}$ sample, isolation and p_{T} requirements of the muon, the fit function used and the statistical uncertainty in the measurement are considered. The uncertainty due to the choice of pdf is evaluated and found to be negligible for the high-mass H^+ search. Effects of the uncertainties on the final yields are summarized in table 8.3. For the low-mass H^+ search, the uncertainty on the theoretical $t\bar{t}$ cross section is taken into account, causing a shift in the event yield of about 6%.

For the interpretation in different scenarios of the MSSM, presented in chapter 10.3, the following uncertainties are taken into account for the high-mass H^+ search, separately for the 4FS and 5FS calculations [33]. For the 4FS, only a scale uncertainty of about 30% is considered. For the 5FS, scale uncertainties of $10 - 20\%$ varying with m_{H^+}, are taken into account together with the combined uncertainty on the b-quark mass, parton distribution function and strong coupling constant of approximately $10 - 15\%$. These uncertainties are combined to uncertainties on the matched cross sections as described in chapter 2.3.4. For the low-mass H^+ search, the same uncertainties as for the signal in the 7 TeV analysis are considered, described in chapter 8.2.

9 Statistical Analysis

All statistical evaluation was carried out by other people involved in the analyses but is explained here in some detail for completeness. All embedded inputs and everything embedding-related was provided by the author of this thesis, who was also involved in the discussion and evaluation of the results. The descriptions given in chapters 9.1 and 9.2 are based on references [167–170].

9.1. The Likelihood Function and Test Statistic

The compatibility of the data with predictions from background and signal estimates is evaluated based on hypothesis tests. For setting upper limits, as is done in the searches presented in this thesis, the data is tested against the signal+background hypothesis. These tests are based on a ratio of profiled log-likelihoods using m_{T} as discriminating variable. The binned likelihood function is given by the Poisson probabilities of all N bins of the histogram of the discriminating variable [167]

$$L(\mu, \boldsymbol{\theta}) = \prod_{j=1}^{N} \frac{(\mu s_j + b_j)^{n_j}}{n_j!} \, \mathrm{e}^{-(\mu s_j + b_j)} \, . \tag{9.1}$$

The expected number of signal events given a signal-strength parameter μ is denoted by μs_j, assuming a certain signal cross section σ_s, and b_j denotes the number of expected background events in bin j, respectively. Setting $\mu = 0$ results in the background-only hypothesis.
In the low-mass H^+ searches presented here, the signal-strength parameter μ refers to the branching ratio $B(t \to H^+b)$ for the search using the 2011 data, where $B(H^+ \to \tau\nu) = 1$ is assumed and to $B(t \to H^+b) \times B(H^+ \to \tau\nu)$ for the search based on the 2012 data. Thus limits are set on $B(t \to H^+b)$ and $B(t \to H^+b) \times B(H^+ \to \tau\nu)$ in the low-mass H^+ search based on 2011 and 2012 data, respectively.
For the high-mass H^+ search, μ corresponds to the signal cross section compared to some reference cross section, here taken to be 1 pb. Limits are set on $\sigma(pp \to \bar{t}H^+ + X) \times B(H^+ \to \tau\nu)$.
Systematic uncertainties are incorporated into the likelihood via a vector of so-called nuisance parameters, denoted $\boldsymbol{\theta}$. Usually, both the signal and background contributions will depend on $\boldsymbol{\theta}$. Nuisance parameters that affect multiple background contributions and the signal are fully correlated.
The ratio of profiled log-likelihoods to test a hypothesized signal strength μ is defined as

$$\lambda(\mu) = \frac{L(\mu, \hat{\hat{\boldsymbol{\theta}}})}{L(\hat{\mu}, \hat{\boldsymbol{\theta}})}. \tag{9.2}$$

Here, $\hat{\hat{\boldsymbol{\theta}}}$ represents the conditional maximum-likelihood estimator of $\boldsymbol{\theta}$, i.e. the value of $\boldsymbol{\theta}$ that maximizes L for a specific signal-strength parameter μ. In the denominator, $\hat{\mu}$ and $\hat{\boldsymbol{\theta}}$ denote the likelihood estimators for the maximized unconditional likelihood function. The test statistic $\tilde{q}_\mu$ is used. It is given by

$$\tilde{q}_\mu \quad = \quad \begin{cases} -2 \ln \frac{L(\mu, \hat{\hat{\boldsymbol{\theta}}}(\mu))}{L(\hat{\mu}, \hat{\boldsymbol{\theta}})} & \hat{\mu} \leq \mu \\ 0 & \hat{\mu} > \mu \end{cases} \tag{9.3}$$

Data where $\hat{\mu} > \mu$ is not regarded as less compatible with μ than the data obtained. Hence it is not included in the rejection region of the test. The greater the value of $\tilde{q_\mu}$, the greater is the incompatibility of data and hypothesized value of μ. The agreement of data and presumed signal-strength parameter μ is quantified by a p-value given by

$$p_\mu = \int_{\tilde{q}_{\mu,obs}}^{\infty} f(\tilde{q}_\mu|\mu) \mathrm{d}q_\mu, \tag{9.4}$$

where $f(\tilde{q}_\mu|\mu)$ denotes the probability density function (pdf) of $\tilde{q}_\mu$ assuming μ. Usually, a threshold for the p value of 0.05 is used to exclude a signal hypothesis, i.e. a signal strength parameter μ is then excluded at a 95% confidence level (CL).
The pdf of data distributed with a strength parameter μ' can be found using a result of Wald [171]

$$-2 \ln \lambda(\mu) = \frac{(\mu - \mu')^2}{\sigma^2} + \mathcal{O}(1/\sqrt{N}) \tag{9.5}$$

in the case of a single parameter of interest. Here, $\hat{\mu}$ follows a Gaussian distribution with mean μ' and standard deviation σ. The sample size of the data is given by N. It can be shown that the test statistic $-2 \ln \lambda(\mu)$ follows a non-central chi-square distribution for one degree of freedom when neglecting the $\mathcal{O}(1/\sqrt{N})$ term in eq. 9.5. If the non-centrality parameter $(\mu - \mu')^2/\sigma^2 = 0$, the test statistic approaches a chi-square distribution [172]. An asymptotic approximation is used to derive expected limits [167]. An artificial data set is defined, referred to as 'Asimov data set'. It is defined such that using the Asimov data set to evaluate estimators for all parameters yields the best estimates of these parameters. The Asimov likelihood is given by

$$\lambda_\mathrm{A}(\mu) = \frac{L_\mathrm{A}(\mu, \hat{\hat{\boldsymbol{\theta}}})}{L_\mathrm{A}(\hat{\mu}, \hat{\boldsymbol{\theta}})} = \frac{L_\mathrm{A}(\mu, \hat{\hat{\boldsymbol{\theta}}})}{L_\mathrm{A}(\mu', \hat{\boldsymbol{\theta}})}, \tag{9.6}$$

where μ' is again the mean of $\hat{\mu}$, which follows a Gaussian distribution. For the Asimov data set it holds

$$-2 \ln \lambda_\mathrm{A}(\mu) \approx \frac{(\mu - \mu')^2}{\sigma^2}, \tag{9.7}$$

where $\mu' = \hat{\mu}$, which then may be used to derive the standard deviation σ of the expected upper limit:

$$\sigma^2 = \frac{(\mu - \mu')^2}{-2 \ln \lambda_{\mathrm{A}}(\mu)}. \tag{9.8}$$

For the median exclusion significance of a hypothesis μ assuming no signal this results in

$$\sigma^2 = \frac{\mu^2}{-2 \ln \lambda_{\mathrm{A}}(\mu)} \tag{9.9}$$

since then $\mu' = 0$.
Expected limits are used to assess the sensitivity of an experiment. They are given by the median limits assuming the background-only hypothesis. The 1σ and 2σ uncertainty bands are derived using the asymptotic approximation as described above.
A smoothing procedure is applied to nuisance parameters affecting the shape of the m_{T} distribution to avoid systematic uncertainties due to statistical fluctuations. Only nuisance parameters that remove (add) events from (to) the final m_{T} distributions are smoothed. First, the histogram with ratios of up and down variations of a nuisance parameter to the nominal m_{T} shape is rebinned, such that the relative error in the individual bins is less than a certain threshold. Then, this rebinned histogram is smoothed using a pre-defined smoothing function. For the background with true hadronically decaying τ leptons, only the $\tau_{\text{had-vis}}$ energy scale uncertainty is smoothed.
Systematic uncertainties that have negligible effects are not taken into account for the final results. If the up/down variation due to a normalization uncertainty is less than 0.5%, it is neglected. For shape uncertainties, the threshold for neglecting a nuisance parameter is 0.5% (after smoothing) for the maximal bin difference from the nominal m_{T} distribution. Nuisance parameters may be neglected for one background contribution but not another. For the background with true $\tau_{\text{had-vis}}$ candidates in the 2012 analyses, the shape variations due to the TES uncertainty propagated to the trigger scale factors and efficiencies and uncertainties related to the muon reconstruction and trigger efficiencies are thus neglected. For signal, some of the jet energy scale, b-tagging related and trigger-related systematic uncertainties are neglected both in shape and/or normalization.
Unless a systematic uncertainty is explicitly asymmetric its effect on the normalization and shape of the m_{T} distribution is symmetrized.

9.2. The CL$_s$ Method

The CL$_s$ procedure [168] is used to derive exclusion limits, i.e. reject signal+background hypotheses at a 95% confidence level.
The CL$_s$ value is defined as

$$\mathrm{CL}_s = \frac{p_{s+b}}{1 - p_b}, \tag{9.10}$$

where p_{s+b} is the probability of finding a value of $\tilde{q}$ that is equally or less compatible with the signal+background hypothesis than the observed value $\tilde{q}_{obs}$. It is given by eqn. 9.4.

The p-value of the background-only hypothesis is given by

$$p_b = \int_0^{\tilde{q}_{\mu,obs}} f(\tilde{q}_\mu|b)\mathrm{d}\tilde{q}_\mu \tag{9.11}$$

where $f(\tilde{q}_\mu|b)$ is the pdf of the test-statistic for the background-only hypothesis. Using CL_s, a signal is excluded at the confidence level CL, usually taken to be 95%, if

$$1 - \mathrm{CL}_s \leq 0.05. \tag{9.12}$$

Using the CL_s method ensures that signal strengths are not spuriously excluded based on fluctuations in the observed data. This is a potential problem for searches with low sensitivity. For such searches, the value of p_{s+b} decreases together with $1 - p_b$ and thus the exclusion condition $\mathrm{CL}_s < 0.05$ is prevented from being met. The coverage probability is thus larger than 95% and in this sense the method is conservative.
Exclusion intervals resulting from the CL_s method are consistent with those obtained using Bayesian methods for the mean values of measurements distributed following Poisson or Gauss distributions with a constant prior for μ.

9.3. Comparison of Expected Limits using Embedded Data and Simulation Samples

The expected improvement due to using embedded data compared to simulation for the estimate of the background contribution with true hadronically decaying τ leptons is evaluated by comparing expected limits in both cases. The expected limits using the 2012 data are summarized in tables 9.1 and 9.2 and shown in figure 9.1 for both the low-mass and high-mass H^+ search. Since the background contribution with true τ_{had} is dominant for the low-mass search and the systematic uncertainties on embedded data are smaller than those on simulation, the expected limits using embedded data are more stringent than those using simulation, as expected. For high H^+ masses, the contribution of background events with jets misidentified as $\tau_{\text{had-vis}}$ candidates becomes more important. Thus only very little or no improvement is achieved in the limits using embedded data compared to simulation for the high-mass H^+ search.

9.4. Effect of the m_{T} Requirement on Expected Limits

The effect of the m_{T} requirement, described in section 7.4.1, on the sensitivity of the searches is evaluated by calculating expected limits with and without this additional selection requirement. Only simulation is used for these comparisons. As can be seen in figure 9.2, the effect is negligible over the full investigated H^+ mass range.

	expected limit	
m_{H^+} [GeV]	simulation	embedded data
80	0.0175	0.0156
90	0.0174	0.0140
100	0.0133	0.0099
110	0.0072	0.0055
120	0.0056	0.0044
130	0.0048	0.0036
140	0.0042	0.0032
150	0.0041	0.0030
160	0.0036	0.0029

Table 9.1. Comparison of expected limits on $B(t \to H^+b) \times B(H^+ \to \tau\nu)$ for the 2012 low-mass H^+ search using simulation and embedded data for the estimate of the background contribution with true hadronically decaying τ leptons [173].

	expected limit [pb]	
m_{H^+} [GeV]	simulation	embedded data
180	0.660	0.552
190	0.578	0.502
200	0.527	0.468
225	0.396	0.366
250	0.313	0.304
275	0.235	0.232
300	0.177	0.171
350	0.102	0.095
400	0.059	0.060
450	0.040	0.042
500	0.030	0.031
550	0.022	0.023
600	0.017	0.017
750	0.010	0.010
1000	0.007	0.007

Table 9.2. Comparison of expected limits on $\sigma(pp \to \bar{t}H^+ + X) \times B(H^+ \to \tau\nu)$ for the 2012 high-mass H^+ search using simulation and embedded data for the estimate of the background contribution with true hadronically decaying τ leptons [173].

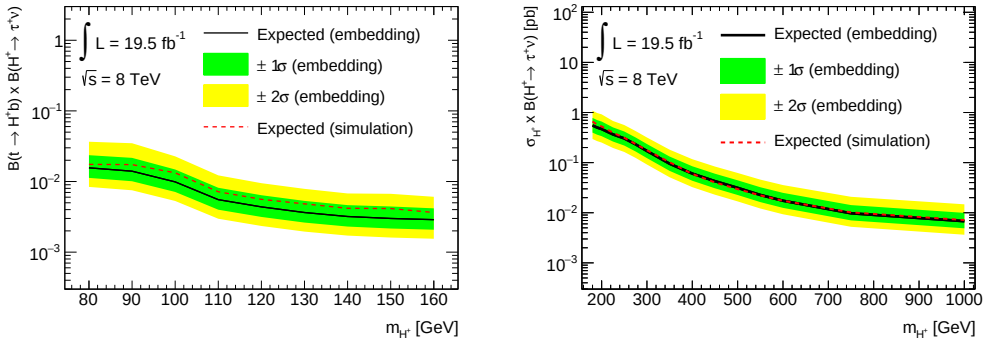

(a) low-mass H^+ search (b) high-mass H^+ search

Figure 9.1. Expected limits for the 2012 data using embedding (solid black line) or simulation (dashed red line) for the background contribution with true τ_{had} for the (a) low-mass and (b) high-mass H^+ search [173].

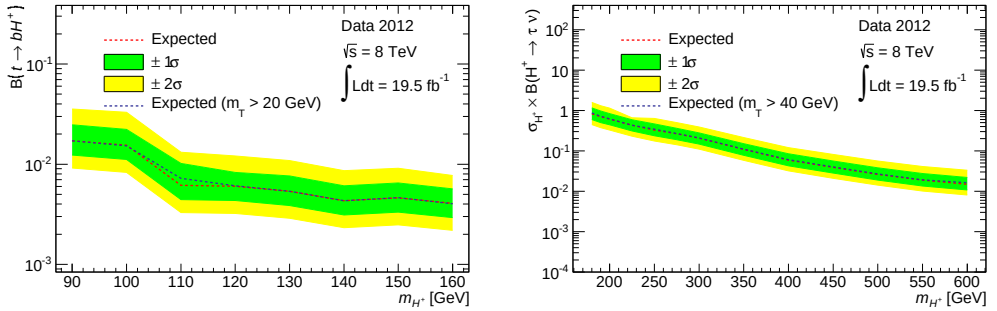

(a) low-mass H^+ search (b) high-mass H^+ search

Figure 9.2. Expected limits for the (a) low-mass and (b) high-mass H^+ search without (red dotted line) and with (blue dotted line) requiring $m_{\text{T}} > 20\,\text{GeV}$ (40 GeV) for the low-mass (high-mass) H^+ search [155].

9.5. Signal Contamination

A possible signal contamination in the embedded data sample due to events decaying via $H^+ \to \tau\nu_\tau \to \mu\nu_\mu\nu_\tau\nu_\tau$ is evaluated.
On average, the transverse momentum of the muon increases with the mass of the charged Higgs boson. Thus especially for high-mass H^+ signal events, τ leptons decaying via $\tau \to \mu\nu$ may pass the muon+jets selection, hence be included in the embedded sample and bias the background estimate. The background contribution with true hadronically decaying τ leptons would then be overestimated, resulting in limits that are too stringent. To evaluate this possible bias, the muon+jets selection is applied to signal events with leptonically decaying τ leptons for $m_{H^+} = 200$, 400 and 600 GeV. All selected events are then embedded and the full signal selection as described in chapter 6.2 is applied to these embedded signal events. The transverse mass distributions are shown in figure 9.3, comparing embedded signal and nominal signal after applying the full signal selection

on each sample. The transverse mass distributions are shifted to lower m_{T} values in embedded signal compared to nominal signal. The embedded τ leptons from original muons resulting from leptonic τ decays tend to have lower transverse momenta than the τ leptons, where the original muons come from W decays. This results in by trend lower m_{T} values.
Only statistical uncertainties are shown. The large uncertainties in the embedded samples are caused by the limited sample size available for embedding.
The maximal possible contamination of signal events through $H^+ \to \tau\nu_\tau \to \mu\nu_\mu\nu_\tau\nu_\tau$

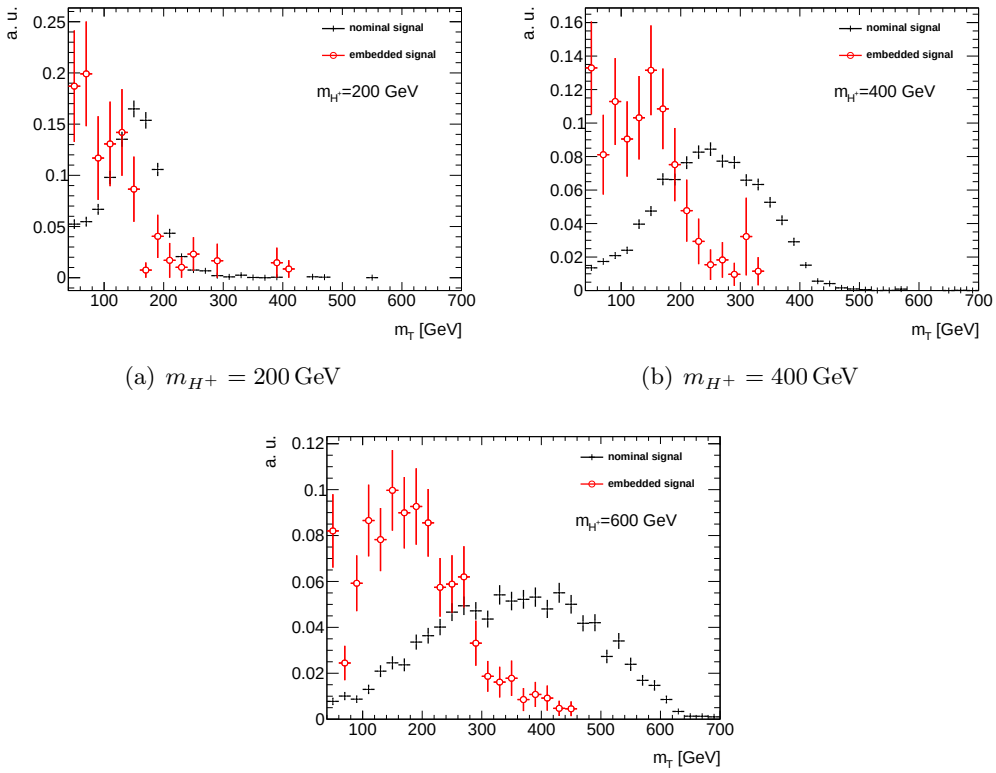

(a) $m_{H^+} = 200\,\mathrm{GeV}$ (b) $m_{H^+} = 400\,\mathrm{GeV}$

(c) $m_{H^+} = 600\,\mathrm{GeV}$

Figure 9.3. Transverse mass distributions of embedded signal compared to nominal signal after applying the full $\tau_{\text{had-vis}}$+jets selection for (a) $m_{H^+} = 200\,\mathrm{GeV}$, (b) $m_{H^+} = 400\,\mathrm{GeV}$ and (c) $m_{H^+} = 600\,\mathrm{GeV}$. All distributions are normalized arbitrarily for shape comparison.

decays in the embedded background estimate is evaluated statistically based on preliminary results presented in ref. [174]. There, the background contribution with true hadronically decaying τ leptons is estimated based on simulation only. The maximal contamination, i.e. the ratio of signal events in the embedded sample to nominal signal events expressed in terms of % is extracted from this number and shown in table 9.3, along with the effect on the expected upper limits. Three separate fits are performed as tests: fitting μ with injected signal and no signal contamination in the background, fitting μ with signal injection and signal contamination and fitting μ with signal injection and signal contamination simultaneously. For this simultaneous fit, the possible signal contamination is corrected for by treating it as a background component whose

m_{H^+} [GeV]	previous obs. limit [pb]	Max. contamination [%]	Expected limit [pb] contamination	Expected limit [pb] no contamination
200	0.688	4.9	0.647	0.646
400	0.075	5.4	0.054	0.054
600	0.0186	8.6	0.015	0.015

Table 9.3. Maximal signal contamination in the embedded sample based on [174] and the effect on expected limits for 3 signal mass points [155].

normalization scales negatively with μ. The total background will then be reduced in a proportionate amount to a signal that may be observed. The results of the three different tests are shown in table 9.4. Since the results are quite comparable among the three different fits and the impact on the expected limits is negligible, as shown in table 9.3, the effect of a possible signal contamination in the embedded sample is neglected for the final fit.

m_{H^+} [GeV]	Injected μ [pb]	Fitted $\hat{\mu}$ [pb] cont.	no cont.	cont., simultaneous fit
200	0.670	0.7	0.7	0.7
400	0.075	0.07	0.08	0.08
600	0.019	0.020	0.020	0.020

Table 9.4. Comparison of fit results for $\hat{\mu}$ when considering a contamination in the embedded sample, not considering it or considering it and fitting it and the signal simultaneously [155].

9.6. Effect of Systematic Uncertainties

The nuisance parameters that have the largest impact on the fitted signal-strength parameter $\hat{\mu}$ are investigated in detail in the searches for low-mass and high-mass charged Higgs bosons in the 2012 dataset and are shown in figure 9.4. They are ordered by decreasing impact on $\hat{\mu}$ from top to bottom.
The hatched blue areas, referring to the top horizontal axis, indicate how the fitted signal-strength parameter deviates after one specific nuisance parameter is changed up- or downwards by its post-fit uncertainty as a fraction of the total uncertainty of the fitted signal-strength parameter. The black dots and bars, referring to the bottom horizontal axis, show that none of the nuisance parameters deviates by more than one standard deviation and that none of the uncertainties are underestimated. The black dots indicate the deviation of each fitted nuisance parameter $\hat{\theta}$ from its nominal value θ_0 in terms of standard deviations with respect to its pre-fit uncertainty $\Delta\theta$. The black lines show the post-fit uncertainties of each nuisance parameter relative to their pre-fit values.
The most important uncertainties include uncertainties relating to the background with true τ_{had} for the low-mass H^+ search and the background with jets misidentified as $\tau_{\text{had-vis}}$ candidates for the high-mass H^+ search, respectively. This is expected since the

background contribution with true τ_{had} is more important for lower charged Higgs boson masses while the background contribution with jets misidentified as $\tau_{\text{had-vis}}$ candidates gains in importance for higher H^+ masses.

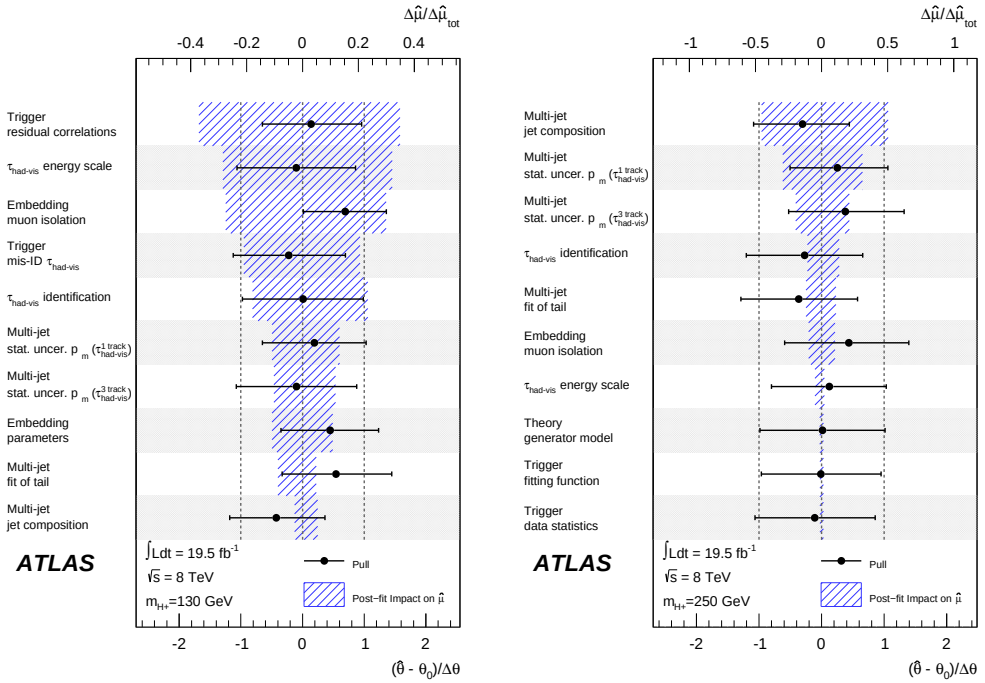

(a) Low-mass H^+ selection

(b) High-mass H^+ selection

Figure 9.4. Impact of the most important systematic uncertainties ordered by decreasing impact on the fitted signal-strength parameter $\hat{\mu}$ for charged Higgs boson masses of (a) $m_{H^+} = 130\,\text{GeV}$ and (b) $m_{H^+} = 250\,\text{GeV}$. The black dots indicate the deviation of each individual fitted nuisance parameter $\hat{\theta}$ from its nominal value θ_0 in terms of standard deviations with respect to the nominal uncertainty $\Delta\theta$. The black lines show the post-fit uncertainties of each nuisance parameter relative to their nominal values. Both black dots and lines refer to the bottom horizontal axis. The hatched blue areas, referring to the top horizontal axis, indicate the deviation of the fitted signal-strength parameter $\Delta\hat{\mu}$ after changing an individual nuisance parameter upwards or downwards by it post-fit uncertainty as a fraction of the total uncertainty of the fitted signal-strength parameter $\Delta\hat{\mu}_{tot}$ [2].

10 Results

10.1. Background Estimates and Final m_{T} Distributions

The final observed event yields are shown in tables 10.1, 10.2 and 10.3 for the low-mass H^+ search using 2011 and 2012 data and the high-mass H^+ search based on 2012 data and compared to the estimated background and possible signal contributions. The corresponding final m_{T} distributions are shown in figures 10.1 and 10.2.

The background contribution with true hadronically decaying τ leptons is dominant for

Sample	Low-mass H^+ search	% of total background
True τ_{had}	$210 \pm 10 \pm 44$	65.0
Misidentified jet $\rightarrow \tau_{\text{had-vis}}$	$36 \pm 6 \pm 10$	11.1
Misidentified $e \rightarrow \tau_{\text{had-vis}}$	$3 \pm 1 \pm 1$	1.0
Multi-jet processes	$74 \pm 3 \pm 47$	22.9
All SM backgrounds	$330 \pm 12 \pm 65$	
Data	355	
H^+ ($m_{H^+} = 130\,\mathrm{GeV}$)	$220 \pm 6 \pm 56$	

Table 10.1. Final event yields after the full event selection with statistical and systematic uncertainties shown in this order in $4.6\,\mathrm{fb}^{-1}$ of data taken at $\sqrt{s} = 7\,\mathrm{TeV}$ in 2011 and expected signal for $m_{H^+} = 130\,\mathrm{GeV}$ and $B(t \rightarrow H^+b) = 5\%$. For the background contributions, $B(H^+ \rightarrow \tau\nu) = 100\%$ is assumed [1].

both low-mass and the high-mass H^+ searches. For high-m_{T} regions, however, i.e. for high m_{H^+}, the background contribution with jets misidentified as $\tau_{\text{had-vis}}$ candidates gains in importance. The number of background events with electrons or muons misidentified as $\tau_{\text{had-vis}}$ candidates is small for the whole investigated mass range. For all background contributions, systematic uncertainties are larger than statistical ones.

For the low-mass H^+ search in 2011, a branching ratio of $B(H^+ \rightarrow \tau\nu) = 100\%$ is assumed. In figure 10.1, the background contributions with misidentified $\tau_{\text{had-vis}}$ are scaled down assuming $B(t \rightarrow H^+b) = 5\%$, i.e. $B(t \rightarrow W^+b) = 95\%$. Scaling down the background with true $\tau_{\text{had-vis}}$ candidates is not necessary. If charged Higgs bosons were produced in top quark decays, the branching ratio for $t \rightarrow Wb$ would be reduced with respect to the SM prediction. Thus the major fraction of the background contribution with true $\tau_{\text{had-vis}}$ candidates would also be reduced accordingly. The assumption that $B(H^+ \rightarrow \tau\nu) = 100\%$ is dropped in the 2012 analyses. In addition, based on preliminary results presented in ref. [174], the background contributions with misidentified $\tau_{\text{had-vis}}$

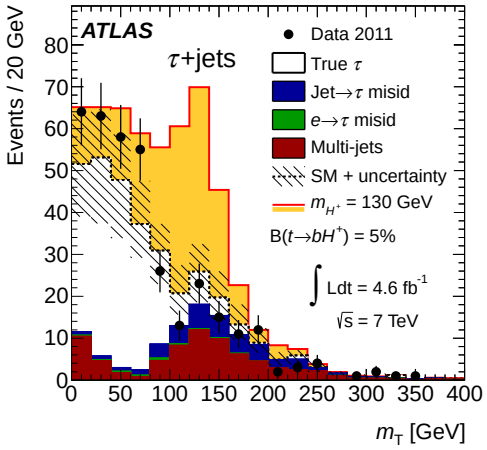

Figure 10.1. Final m_{T} distribution after all selection requirements for the 2011 data. The dashed line shows the SM-only expectation and the hatched areas show the total uncertainty for all SM backgrounds. The solid line incorporating also the yellow area shows the prediction for signal+background assuming $B(t \to H^+b) = 5\%$ for $m_{H^+} = 130\,\mathrm{GeV}$. The background contributions with misidentified $\tau_{\text{had-vis}}$ candidates are scaled down accordingly [1].

are not scaled down according to the assumed $B(t \to H^+b)$ shown in figure 10.2. The limit from ref. [174] is strong enough (between 2.1% and 0.24% in a mass range 90 GeV $\leq m_{H^+} \leq$ 160 GeV) so that the allowed branching ratio is too small to affect the background contributions or limits noticeably.

No significant excess of data over the background estimate is observed, in neither the

Sample	Low-mass H^+ search	% of total background
True τ_{had}	$2800 \pm 60 \pm 500$	85.6
Misidentified jet $\to \tau_{\text{had-vis}}$	$490 \pm 9 \pm 80$	13.5
Misidentified $e \to \tau_{\text{had-vis}}$	$15 \pm 3 \pm 6$	< 1
Misidentified $\mu \to \tau_{\text{had-vis}}$	$18 \pm 3 \pm 8$	< 1
All SM backgrounds	$3300 \pm 60 \pm 500$	
Data	3244	
H^+ ($m_{H^+} = 130\,\mathrm{GeV}$)	$230 \pm 10 \pm 40$	

Table 10.2. Final event yields after applying the full low-mass event selection with statistical and systematic uncertainties shown in this order for background contributions and 19.5 fb^{-1} of data taken at $\sqrt{s} = 8\,\mathrm{TeV}$ in 2012. The predicted signal contributions for $m_{H^+} = 130\,\mathrm{GeV}$ assuming $B(t \to H^+b) \times B(H^+ \to \tau\nu) = 0.9\%$ is shown as well [2].

low-mass nor the high-mass H^+ searches.

Sample	High-mass H^+ search	% of total background
True τ_{had}	$3400 \pm 60 \pm 400$	77.6
Misidentified jet $\rightarrow \tau_{\text{had-vis}}$	$990 \pm 15 \pm 160$	20.9
Misidentified $e \rightarrow \tau_{\text{had-vis}}$	$20 \pm 2 \pm 9$	< 1
Misidentified $\mu \rightarrow \tau_{\text{had-vis}}$	$37 \pm 5 \pm 8$	< 1
All SM backgrounds	$4400 \pm 70 \pm 500$	
Data	4474	
H^+ ($m_{H^+} = 250\,\text{GeV}$)	$58 \pm 1 \pm 9$	

Table 10.3. Final event yields after applying the full high-mass event selection with statistical and systematic uncertainties shown in this order for background contributions and $19.5\,\text{fb}^{-1}$ of data taken at $\sqrt{s} = 8\,\text{TeV}$ in 2012. The predicted signal contribution for $m_{H^+} = 250\,\text{GeV}$ for $\tan\beta = 50$ in the $m_{\text{h}}^{\text{max}}$ scenario of the MSSM ($\sigma = 0.1891\,\text{pb}$) is shown as well [2].

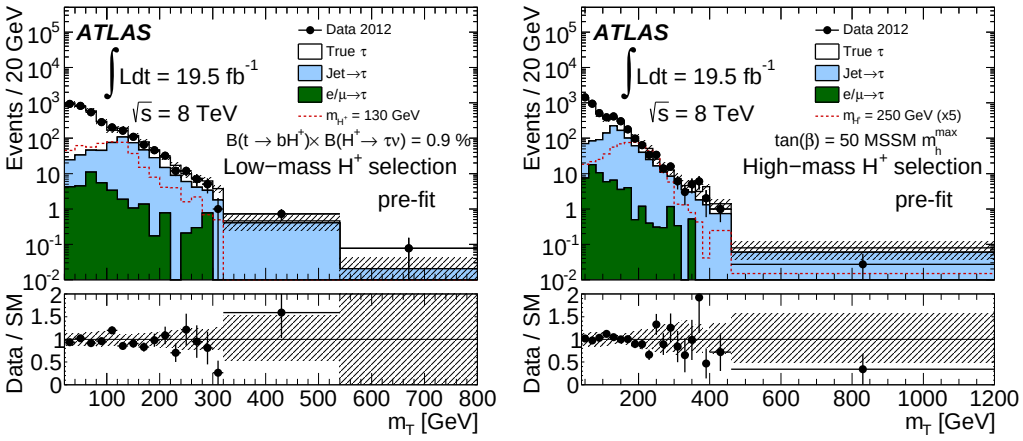

(a) low-mass H^+ selection

(b) high-mass H^+ selection

Figure 10.2. Final m_{T} distributions for the (a) low-mass and (b) high-mass H^+ searches in 2012 data. The hatched areas indicate the total uncertainty on the background estimates. Predicted signal contributions for $m_{H^+} = 130\,\text{GeV}$ assuming $B(t \rightarrow H^+b) \times B(H^+ \rightarrow \tau\nu) = 0.9\%$ in the low-mass H^+ search, based on results presented in ref. [1], and $m_{H^+} = 250\,\text{GeV}$ for $\tan\beta = 50$ in the $m_{\text{h}}^{\text{max}}$ scenario of the MSSM with the corresponding cross section scaled up by a factor of 5 in the high-mass H^+ search, are overlaid in the respective histograms. For the low-mass H^+ selection, bins are 20 GeV wide up to $m_{\text{T}} = 320\,\text{GeV}$, followed by bins from 320-540 GeV and $> 540\,\text{GeV}$. For the high-mass H^+ selection, bins are 20 GeV wide up to $m_{\text{T}} = 400\,\text{GeV}$, then 400-460 GeV and $> 460\,\text{GeV}$. All bins are normalized to a bin width of 20 GeV [156].

10.2. Model-independent Limits

Since background expectations and data agree well as shown in figures 10.1 and 10.2, in the search for low-mass H^+ at $\sqrt{s} = 7\,\text{TeV}$ as well as in the searches for low-mass

and high-mass H^+ at $\sqrt{s} = 8\,\text{TeV}$, limits are set on the branching ratio $B(t \to H^+b)$ for the low-mass H^+ searches and on $\sigma(pp \to \bar{t}H^+ + X) \times B(H^+ \to \tau\nu)$ for the high-mass H^+ search. In the low-mass H^+ search based on the 2012 dataset, the assumption that $B(H^+ \to \tau\nu) = 1$ used in the 2011 search is dropped, i.e. the limit is set on $B(t \to H^+b) \times B(H^+ \to \tau\nu)$ in the 2012 analysis. For the high-mass H^+ search, the limit is to be understood as a limit combined for H^+ and H^-.
All limits are set by rejecting the signal+background hypothesis at a 95% confidence level based on the CL_s procedure as described in chapter 9.2, based on the test statistic $\tilde{q}_\mu$ as detailed in chapter 9.1.
Observed and expected limits, shown in figures 10.3 and 10.4 agree well over the whole

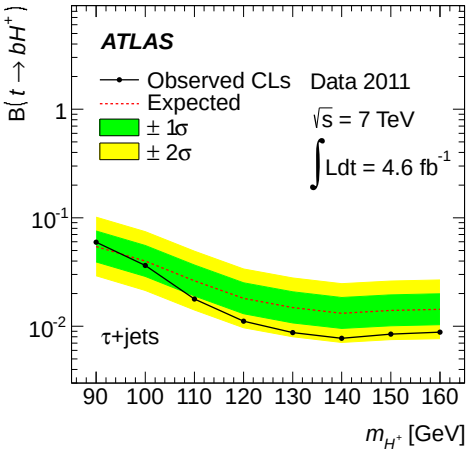

Figure 10.3. Observed and expected 95% CL exclusion limits on the branching ratio $\text{B}(t \to H^+b)$ for charged Higgs bosons decaying via $H^+ \to \tau\nu$ in a mass range $90\,\text{GeV} \leq m_{H^+} \leq 160\,\text{GeV}$ based on $4.6\,\text{fb}^{-1}$ of data taken at $\sqrt{s} = 7\,\text{TeV}$ [1].

investigated mass range.
The limits on $\text{B}(t \to H^+b)$ resulting from the low-mass H^+ search using $4.6\,\text{fb}^{-1}$ of data at $\sqrt{s} = 7\,\text{TeV}$, shown in figure 10.3, range from 6% at $m_{H^+} = 90\,\text{GeV}$ to 1% at $m_{H^+} = 160\,\text{GeV}$. The values of the expected and observed limits are summarized in table 10.4.

The limits on $B(t \to H^+b) \times B(H^+ \to \tau\nu)$ and $\sigma(pp \to \bar{t}H^+ + X) \times B(H^+ \to \tau\nu)$ resulting from the search for low-mass and high-mass H^+, respectively, based on $19.5\,\text{fb}^{-1}$ of data taken at $\sqrt{s} = 8\,\text{TeV}$ are shown in figure 10.4. For the low-mass H^+ search, they range from 1.3% at $m_{H^+} = 80\,\text{GeV}$ to 0.23% at $m_{H^+} = 160\,\text{GeV}$. For the high-mass H^+ search, they range from 0.76 pb to 4.5 fb in the mass range $180\,\text{GeV} \leq m_{H^+} \leq 1000\,\text{GeV}$. The results of the low-mass H^+ search constitute a significant improvement over those based on the 2011 data. The expected and observed limits are summarized in table 10.5.

Comparison to Limits by the CMS Collaboration The CMS collaboration at the LHC searched for charged Higgs bosons in the τ+jets and other final states. In the low-mass H^+ search and assuming $B(H^+ \to \tau\nu) = 1$, limits are set on the branching ratio $B(t \to H^+b)$ in a mass range $80\,\text{GeV} \leq m_{H^+} \leq 160\,\text{GeV}$. They range from

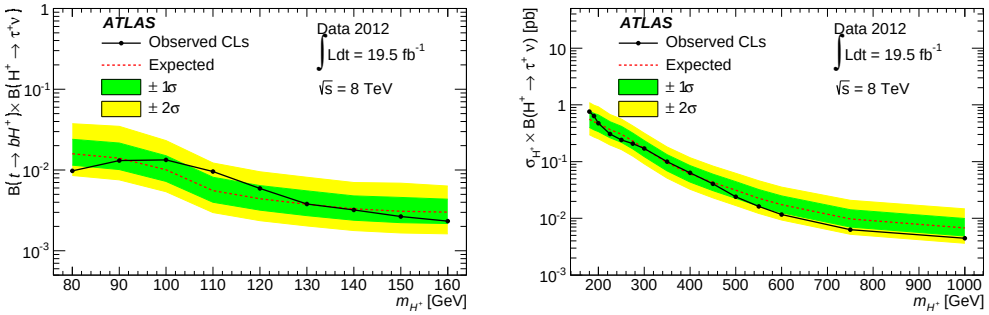

(a) Low-mass H^+ selection

(b) High-mass H^+ selection

Figure 10.4. Observed and expected 95% exclusion limits on the (a) branching ratio $B(t \to H^+b) \times B(H^+ \to \tau\nu)$ for low-mass charged Higgs bosons and (b) cross section $\sigma(pp \to \bar{t}H^+ + X) \times B(H^+ \to \tau\nu)$ for high-mass charged Higgs bosons in mass ranges $80\,\text{GeV} \leq m_{H^+} \leq 160\,\text{GeV}$ and $180\,\text{GeV} \leq m_{H^+} \leq 1000\,\text{GeV}$, respectively, based on $19.5\,\text{fb}^{-1}$ of data taken at $\sqrt{s} = 8\,\text{TeV}$. For the high-mass H^+ search, the limits are to be understood as applying to the total cross section times branching ratio for H^+ and H^- combined [2].

m_{H^+} [GeV]	observed limit in %	expected limit in %
90	5.953	5.438
100	3.636	3.990
110	1.784	2.629
120	1.114	1.808
130	0.876	1.490
140	0.775	1.318
150	0.846	1.401
160	0.882	1.431

Table 10.4. Observed and expected limits on $\text{B}(t \to H^+b)$ assuming $B(H^+ \to \tau\nu) = 1$ for the low-mass H^+ search using $4.6\,\text{fb}^{-1}$ of data taken at $\sqrt{s} = 7\,\text{TeV}$ in 2011 [175].

8.5% to 2% based on $2.27\,\text{fb}^{-1}$ of data taken at $\sqrt{s} = 7\,\text{TeV}$ [176]. These results are improved based on $19.7\,\text{fb}^{-1}$ of data taken at $\sqrt{s} = 8\,\text{TeV}$ and high-mass charged Higgs bosons are searched for based on this data as well [177]. The limits in the low-mass H^+ are set on $B(t \to H^+b) \times B(H^+ \to \tau\nu)$ and range from 1.2% to 0.15% in a mass range $80\,\text{GeV} \leq m_{H^+} \leq 160\,\text{GeV}$. For the high-mass search, limits are set on $\sigma(pp \to \bar{t}H^+ + X) \times B(H^+ \to \tau\nu)$ and range from 0.377 pb to 0.025 pb for charged Higgs boson masses between 180 GeV and 600 GeV. These limits are more stringent than those set by the ATLAS collaboration over most of the mass range except for very high H^+ masses and do not explore the region with $m_{H^+} > 600\,\text{GeV}$.

m_{H^+} [GeV]	observed limit in %	expected limit in %	m_{H^+} [GeV]	observed limit [pb]	expected limit [pb]
80	0.975	1.59	180	0.761	0.555
90	1.31	1.4	190	0.636	0.504
100	1.34	1.01	200	0.474	0.471
110	0.959	0.554	225	0.308	0.367
120	0.593	0.441	250	0.241	0.304
130	0.378	0.377	275	0.206	0.232
140	0.321	0.331	300	0.171	0.171
150	0.266	0.309	350	0.1	0.0952
160	0.234	0.301	400	0.0636	0.0604
			450	0.0407	0.0427
			500	0.0241	0.0314
			550	0.0162	0.0227
			600	0.0117	0.0174
			750	0.0063	0.0098
			1000	0.0045	0.0068

Table 10.5. Observed and expected limits on $B(t \to H^+b) \times B(H^+ \to \tau\nu)$ and $\sigma(pp \to \bar{t}H^+ + X) \times B(H^+ \to \tau\nu)$ for the low-mass and high-mass H^+ searches, respectively, using $19.5\,\text{fb}^{-1}$ of data taken at $\sqrt{s} = 8\,\text{TeV}$ in 2012 [155]..

10.3. Interpretation in Benchmark Scenarios of the MSSM

The model-independent limits are also interpreted in MSSM benchmark scenarios described in chapter 2.3.3. The limits on $B(t \to H^+b) \times B(H^+ \to \tau\nu)$ and $\sigma(pp \to \bar{t}H^+ + X) \times B(H^+ \to \tau\nu)$ for the low-mass and high-mass H^+ searches, respectively, are interpreted in the $\tan\beta - m_{H^+}$-plane. The assumption that $B(H^+ \to \tau\nu) = 1$ used for the model-independent limits in the low-mass H^+ search based on 2011 data is no longer held here. In the MSSM scenarios described, all but two parameters, which are $\tan\beta$ and m_{H^+}, are fixed.

The limits based on the 2011 dataset are only interpreted in the $m_{\text{h}}^{\text{max}}$ scenario, shown in figure 10.5. The structure with separate exclusion regions for large and small values of $\tan\beta$ is due to a minimum of the cross section at around $\tan\beta = 8$, as shown in chapter 2.3.4.

The limits of the low-mass and high-mass searches based on the 2012 dataset are interpreted in all 6 scenarios described in chapter 2.3.3. Due to interference with off-shell $t\bar{t}$ production in the mass range $180\,\text{GeV} < m_{H^+} < 200\,\text{GeV}$, results of the high-mass search are only shown for $m_{H^+} \geq 200\,\text{GeV}$.

The exclusion planes in the $m_{\text{h}}^{\text{max}}$, $m_{\text{h}}^{\text{mod+}}$, $m_{\text{h}}^{\text{mod}-}$, light stau, light stop and tauphobic scenarios for the low-mass H^+ search are shown in figure 10.6. Compared to the exclusion limits based on the 2011 data, the previously separate exclusion regions are now connected up to $m_{H^+} = 140\,\text{GeV}$. The achieved exclusion is similar in all 6 scenarios. In the tauphobic scenario, the exclusion for $m_{H^+} = 160\,\text{GeV}$ is slightly weaker than for the other scenarios due to different branching ratios.

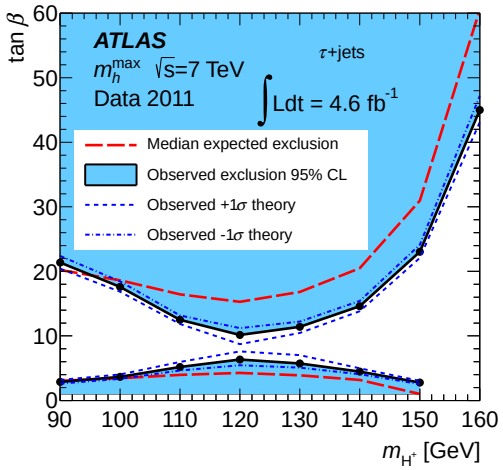

Figure 10.5. Interpretation of the 95% CL limits shown in figure 10.3 interpreted in the $m_{\mathrm{h}}^{\mathrm{max}}$ scenario, shown as limits on $\tan\beta$ vs. m_{H^+} [162].

For the high-mass H^+ search, limits interpreted in the $m_{\mathrm{h}}^{\mathrm{max}}$, $m_{\mathrm{h}}^{\mathrm{mod+}}$ and $m_{\mathrm{h}}^{\mathrm{mod-}}$ scenarios are shown in figure 10.7. While the exclusion is similar in the $m_{\mathrm{h}}^{\mathrm{max}}$ and $m_{\mathrm{h}}^{\mathrm{mod+}}$ scenarios, a slightly larger region is excluded in the $m_{\mathrm{h}}^{\mathrm{mod-}}$ scenario due to larger cross sections in this scenario. In all 3 scenarios, only regions of large $\tan\beta$ are excluded for $m_{H^+} \leq 250\,\mathrm{GeV}$. In the tauphobic, light stau and light stop scenarios no significant exclusion is achieved in the high-mass H^+ search.

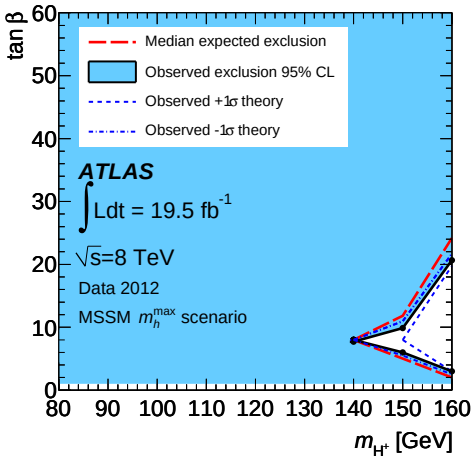

(a) Low-mass H^+ selection, $m_{\mathrm{h}}^{\mathrm{max}}$ scenario

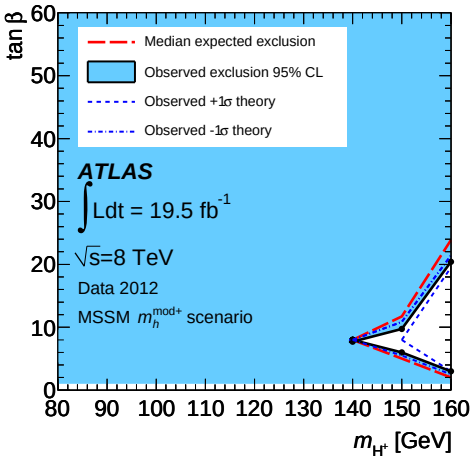

(b) Low-mass H^+ selection, $m_{\mathrm{h}}^{\mathrm{mod+}}$ scenario

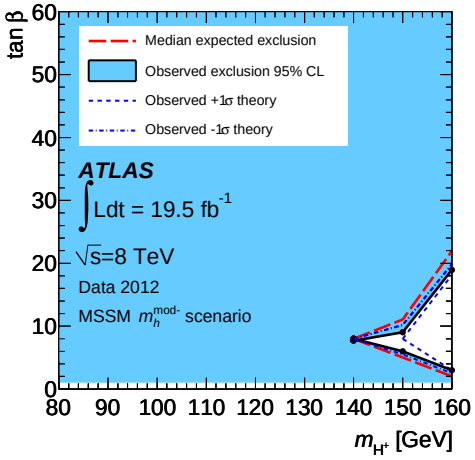

(c) Low-mass H^+ selection, $m_{\mathrm{h}}^{\mathrm{mod-}}$ scenario

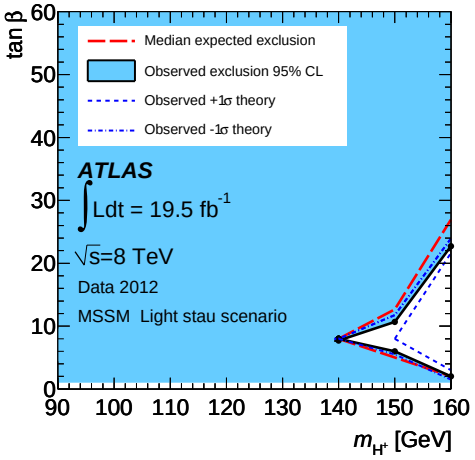

(d) Low-mass H^+ selection, light stau scenario

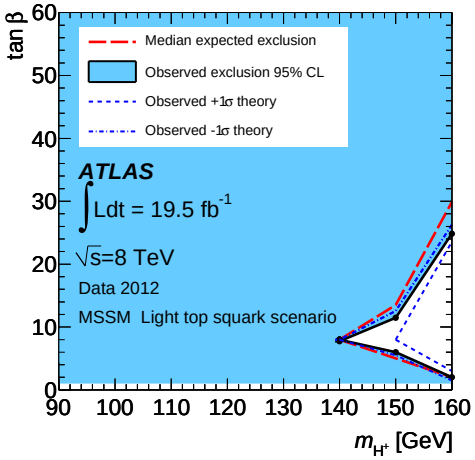

(e) Low-mass H^+ selection, light stop scenario

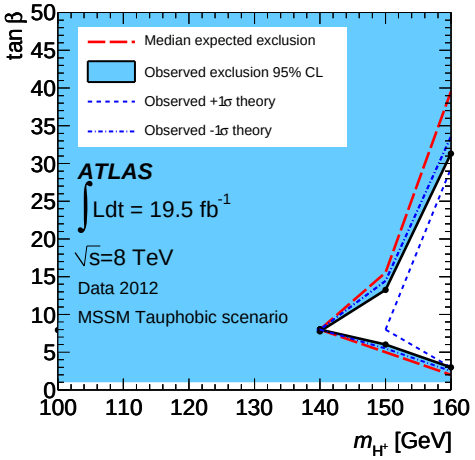

(f) Low-mass H^+ selection, tauphobic scenario

Figure 10.6. Interpretation of the 95% CL limits shown in figure 10.4 shown as limits on $\tan\beta$ vs. m_{H^+} in the (a) $m_{\mathrm{h}}^{\mathrm{max}}$, (b) $m_{\mathrm{h}}^{\mathrm{mod+}}$, (c) $m_{\mathrm{h}}^{\mathrm{mod-}}$, (d) light stau, (e) light stop and (f) tauphobic scenarios of the MSSM [2, 156].

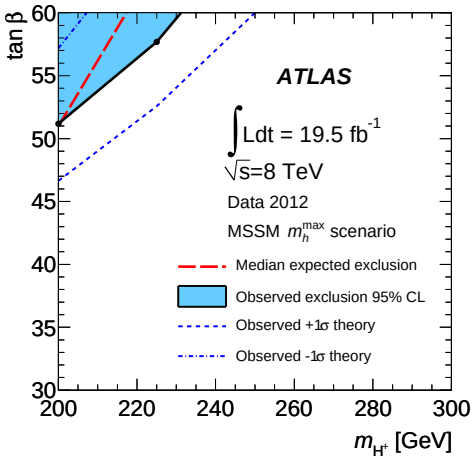

(a) High-mass H^+ selection, $m_{\mathrm{h}}^{\mathrm{max}}$ scenario

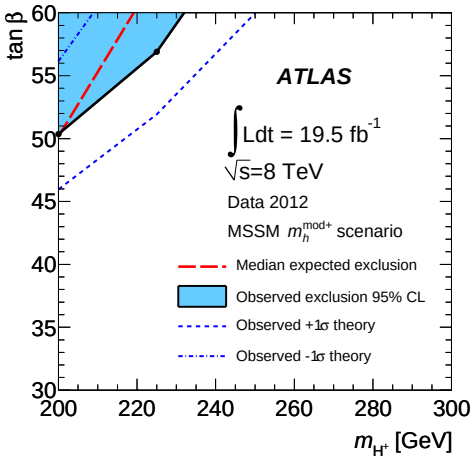

(b) High-mass H^+ selection, $m_{\mathrm{h}}^{\mathrm{mod+}}$ scenario

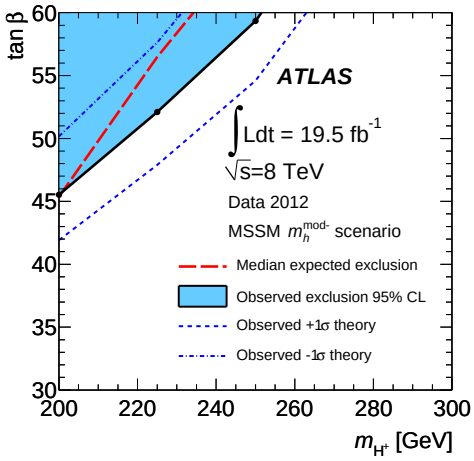

(c) High-mass H^+ selection, $m_{\mathrm{h}}^{\mathrm{mod-}}$ scenario

Figure 10.7. Interpretation of the 95% CL limits shown in figure 10.4 interpreted in various MSSM scenarios, shown as limits on $\tan\beta$ vs. m_{H^+}. Limits are shown in the (a) $m_{\mathrm{h}}^{\mathrm{max}}$, (b) $m_{\mathrm{h}}^{\mathrm{mod+}}$ and (c) $m_{\mathrm{h}}^{\mathrm{mod-}}$ scenarios for the high-mass H^+ search [2].

11 Summary

Searches for low-mass and high-mass charged Higgs bosons decaying via $H^+ \to \tau\nu$ have been presented in this thesis. They are based on $4.6\,\text{fb}^{-1}$ and $19.5\,\text{fb}^{-1}$ of data taken at $\sqrt{s} = 7\,\text{TeV}$ and $\sqrt{s} = 8\,\text{TeV}$ with the ATLAS detector in 2011 and 2012, respectively. The final states investigated include a hadronically decaying τ lepton, $E_{\text{T}}^{\text{miss}}$ due to neutrinos, jets and no electrons or muons. These final states arise from

$$t\bar{t} \to (W^-\bar{b})(bH^+) \to (q\bar{q}'\bar{b})(b\tau^+_{\text{had}}\nu)$$

for the low-mass H^+ search with charged Higgs boson masses less than the top quark mass and from

$$g\bar{b} \to \bar{t}H^+ \to (W^-\bar{b})H^+ \to (q\bar{q}'\bar{b})(\tau^+_{\text{had}}\nu) \text{ in the 5FS and}$$
$$gg \to \bar{t}bH^+ \to (W^-\bar{b})bH^+ \to (q\bar{q}'\bar{b})b(\tau^+_{\text{had}}\nu) \text{ in the 4FS,}$$

for the high-mass H^+ search with charged Higgs boson masses greater than the top quark mass. The event selections are optimized separately for the low-mass and high-mass H^+ searches and for data taken in 2011 and 2012.
The background contributions are divided according to the origin of the $\tau_{\text{had-vis}}$ candidate, resulting in events with true hadronically decaying τ leptons, jets misidentified as $\tau_{\text{had-vis}}$ candidates or light leptons misidentified as $\tau_{\text{had-vis}}$ candidates. In the low-mass H^+ search based on the 2011 data, all background contributions are estimated using data-driven methods. In the searches using the 2012 data, only the minor background where electrons or muons are misidentified as $\tau_{\text{had-vis}}$ candidates, accounting for 1-2% of the total background, are estimated based on simulation.
The major background contribution is due to events with true hadronically decaying τ leptons. It is assessed using a so-called embedding technique. This method relies on the assumption of lepton universality in W boson decays. A μ+jets sample is collected in data, the muon is extracted and removed from the data and subsequently used to simulate a hadronically decaying τ lepton. The decay products of the τ lepton are then merged with the original event except for the muon. This method has been used in all charged Higgs boson searches in this final state by ATLAS and is tested and validated extensively in both data and simulation samples. To test the technical aspects of removing the original muon and replacing it, $\mu \to \mu$ embedding is performed in simulation and data. The embedding of a hadronically decaying τ lepton into the original event in place of the muon is tested in simulation and this $\mu \to \tau$ embedded simulation is compared to default simulation with hadronically decaying τ leptons. All tests and validation are successful. Finally, $\mu \to \tau$ embedded data is compared to simulation and used for the statistical analysis of the searches.

A main advantage of the embedding method compared to using simulation samples is that it does not rely on the theoretical $t\bar{t}$ cross section and its uncertainties and is generally associated with fewer systematic uncertainties. Everything in the embedded data except for the decay products of the τ lepton is taken directly from collision data, thus many systematic uncertainties associated with simulation do not have to be considered. Hence the sensitivity of the H^+ searches is improved, particularly for the low-mass searches, when using embedded data instead of simulation to estimate the background contribution with true $\tau_{\text{had-vis}}$ candidates. Everything embedding-related in the searches presented here was provided by the author of this thesis.
In the 2011 search, the background contribution due to jets misidentified as $\tau_{\text{had-vis}}$ candidates from multi-jet production and W+jets events are estimated using a template method and misidentification probability, respectively. In the 2012 searches, a matrix method is used to assess all events where jets are misidentified as $\tau_{\text{had-vis}}$ candidates.
A transverse mass, built from the transverse momentum of the $\tau_{\text{had-vis}}$ candidate, the missing transverse momentum and the $\Delta\phi$ between the directions of the $\tau_{\text{had-vis}}$ candidate and the missing transverse momentum is used as final discriminant. Comparing the results of the background estimates to data, no significant deviation is observed and model-independent limits are set. They are set on the branching ratio $B(t \to H^+b)$ for the low-mass H^+ search in 2011, assuming $B(H^+ \to \tau\nu) = 1$ and range from 6% at $m_{H^+} = 90\,\text{GeV}$ to 1% at $m_{H^+} = 160\,\text{GeV}$. Using the 2012 data, the mass range is extended down to $m_{H^+} = 80\,\text{GeV}$. Limits are set on the branching ratio $B(t \to H^+b) \times B(H^+ \to \tau\nu)$ as the assumption that $B(H^+ \to \tau\nu) = 1$ is dropped. The limits range from 0.97% at 80 GeV to 0.23% at 160 GeV. These limits constitute a major improvement of a factor of 20 and more over previously published limits from the Tevatron collaborations.
In the high-mass H^+ search, based on data taken at $\sqrt{s} = 8\,\text{TeV}$, limits are set on the cross section $\sigma(pp \to \bar{t}H^+ + X) \times B(H^+ \to \tau\nu)$ in a mass range $180\,\text{GeV} \leq m_{H^+} \leq 1000\,\text{GeV}$. They range from 0.76 pb at 180 GeV to 0.0045 pb at 1000 GeV. The mass range around the top quark mass, $160\,\text{GeV} < m_{H^+} < 180\,\text{GeV}$ is not probed since no recommendations exist for the proper theoretical treatment of the interference between top quark and H^+ production processes. These results are the first published limits in a direct search for high-mass charged Higgs bosons.
The limits are interpreted as limits in the $\tan\beta - m_{H^+}$-plane in up to 6 benchmark scenarios of the MSSM. The limits derived from the low-mass H^+ search based on data taken in 2011 is interpreted in the $m_{\text{h}}^{\text{max}}$ scenario only. For the limits in the low-mass H^+ search based on data taken in 2012, interpretations in the $m_{\text{h}}^{\text{mod}-}$, $m_{\text{h}}^{\text{mod}+}$, light stop, light stau and tauphobic scenarios are added. In all of these scenarios the entire $\tan\beta - m_{H^+}$ plane is excluded except for a small area for $m_{H^+} > 140\,\text{GeV}$. In the high-mass H^+ search, only values for $\tan\beta > 45\,\text{GeV}$ are excluded for $m_{H^+} < 250\,\text{GeV}$ in the $m_{\text{h}}^{\text{max}}$, $m_{\text{h}}^{\text{mod}+}$ and $m_{\text{h}}^{\text{mod}-}$ scenarios, while no significant exclusion is achieved in the light stop, light stau and tauphobic scenarios.
With ATLAS now taking data at $\sqrt{s} = 13\,\text{TeV}$, new H^+ mass regions will be probed in the future. Searches for beyond the Standard Model Higgs bosons are continuing and the data taken in the next few years will hopefully shed light on the nature of the discovered Higgs boson and if it is the one of the SM or part of an extended Higgs sector. This key question in physics, if and how the SM needs to be extended, may be answered by discoveries made at the LHC experiments in the years to come.

Appendix

A $\mu \to \mu$ Embedding

A.1. Embedded Simulation

Default and $\mu \to \mu$ embedded $t\bar{t}$ simulation after applying the b-layer and muon reconstruction efficiency corrections and after applying the low-mass μ+jets selection are compared in figure A.1. As in chapter 7.3, the $E_{\mathrm{T}}^{\mathrm{miss}}$ distribution shown here is not exactly the same as the one used when selecting events, thus there are also entries for $E_{\mathrm{T}}^{\mathrm{miss}} < 20\,\mathrm{GeV}$. More distributions after applying the low-mass or high-mass μ+jets

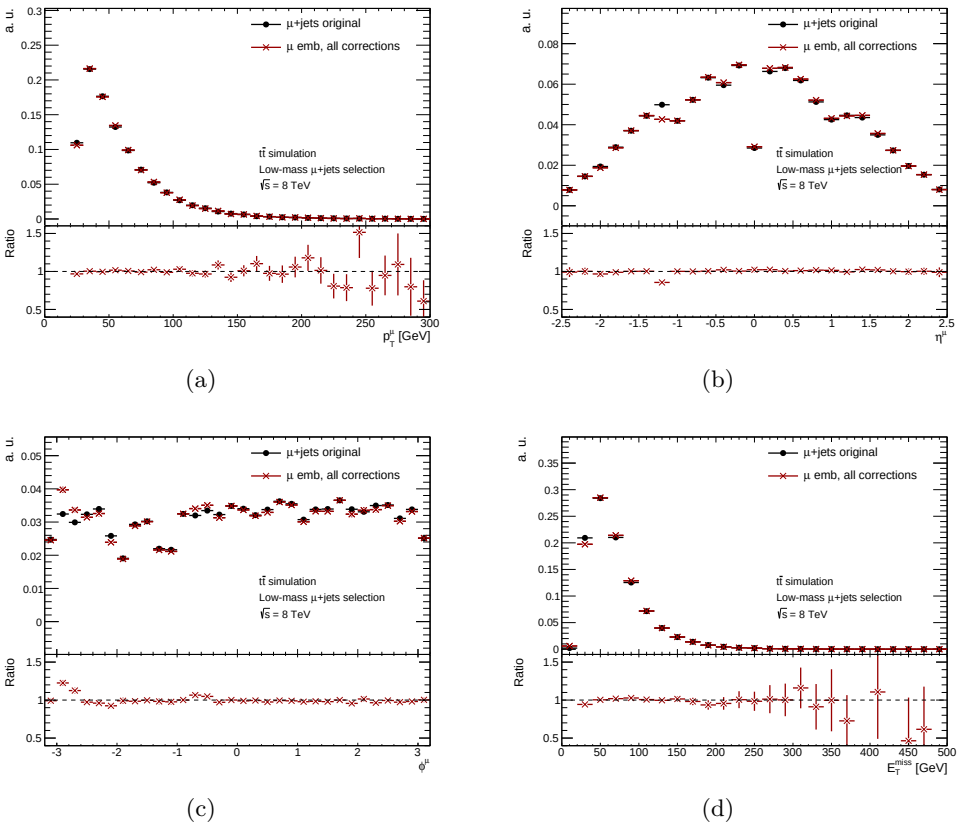

Figure A.1. Comparisons of (a) p_{T}^{μ}, (b) η^{μ}, (c) ϕ^{μ} and (d) $E_{\mathrm{T}}^{\mathrm{miss}}$ in default and $\mu \to \mu$ embedded $t\bar{t}$ simulation after applying all necessary corrections. The low-mass μ+jets selection is applied.

selection and all corrections to the $\mu \to \mu$ embedded simulation are compared to default

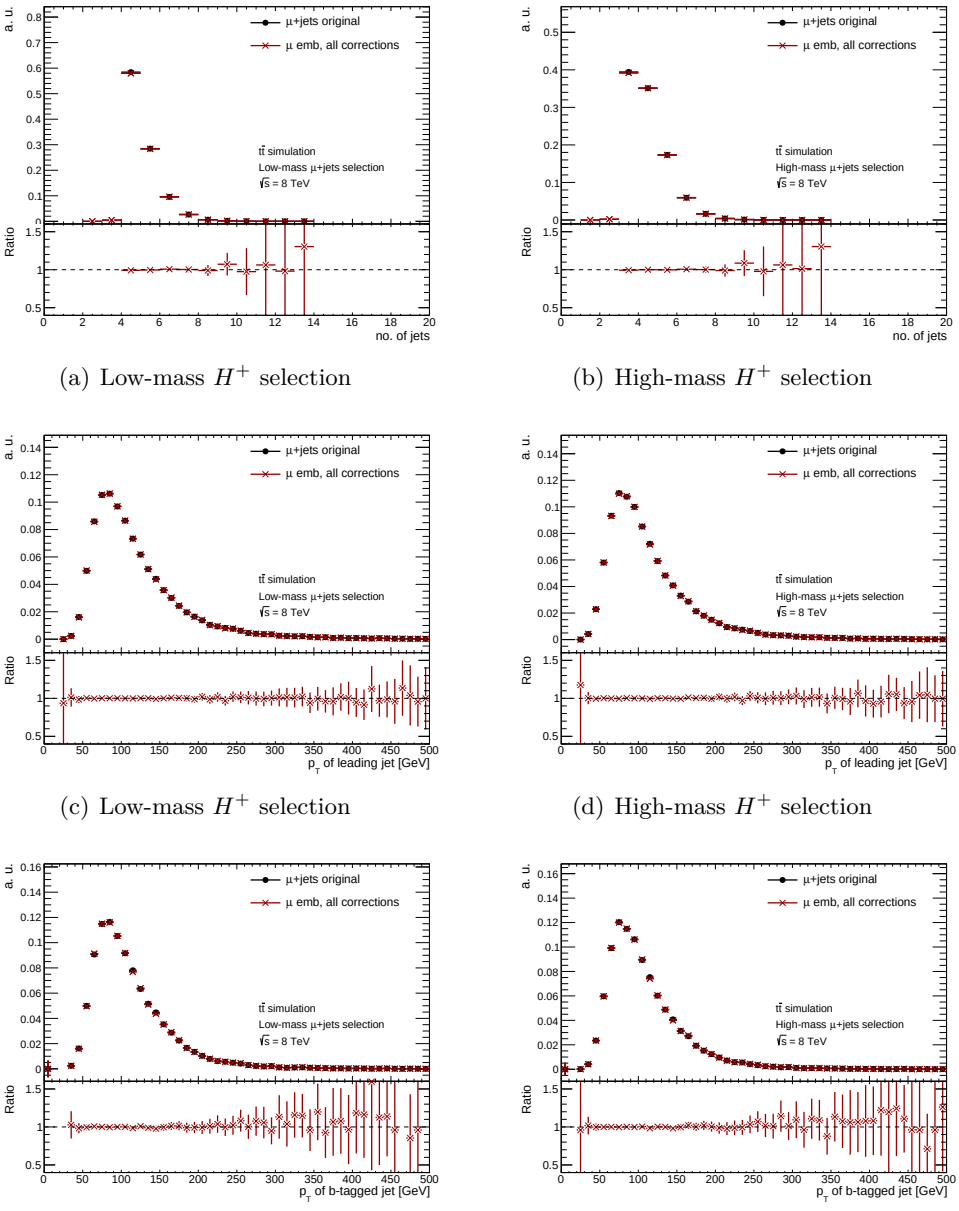

(a) Low-mass H^+ selection

(b) High-mass H^+ selection

(c) Low-mass H^+ selection

(d) High-mass H^+ selection

(e) Low-mass H^+ selection

(f) High-mass H^+ selection

Figure A.2. Comparisons of (a, b) number of jets passing all selection criteria, (c, d) p_{T} of the leading jet, (e, f) p_{T} of the b-tagged jet after applying the low-mass (high-mass) μ+jets selection in the left (right) column for default and $\mu \to \mu$ embedded $t\bar{t}$ simulation after applying all necessary corrections.

simulation in figure A.2. The distributions generally agree well. Discrepancies in the η^{μ} and ϕ^{μ} are due to the not-perfect b-layer correction, which was optimized for data and not simulation, and only affect $\mu \to \mu$ embedding.

A.2. Embedded Data

Default and $\mu \to \mu$ embedded data after applying the b-layer and muon reconstruction efficiency corrections and after applying the low-mass μ+jets selection are compared in figure A.3. As in chapter 7.3, the $E_{\mathrm{T}}^{\mathrm{miss}}$ distribution shown here is not exactly the same as the one used when selecting events, thus there are also entries for $E_{\mathrm{T}}^{\mathrm{miss}} < 20\,\mathrm{GeV}$. More distributions after applying the low-mass or high-mass μ+jets selection and all

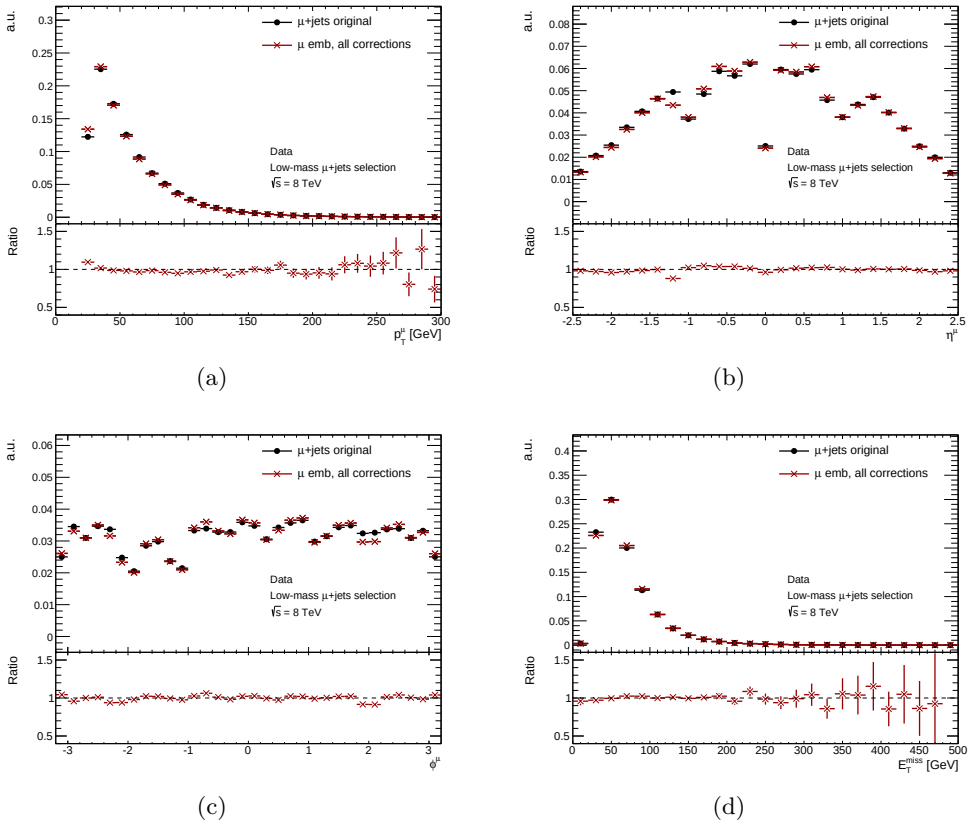

Figure A.3. Comparisons of (a) p_{T}^{μ}, (b) η^{μ}, (c) ϕ^{μ} and (d) $E_{\mathrm{T}}^{\mathrm{miss}}$ in collision data and $\mu \to \mu$ embedded data after applying all necessary corrections. The low-mass μ+jets selection is applied.

corrections to the $\mu \to \mu$ embedded data are compared to collision data in figure A.4. The distributions generally agree well.

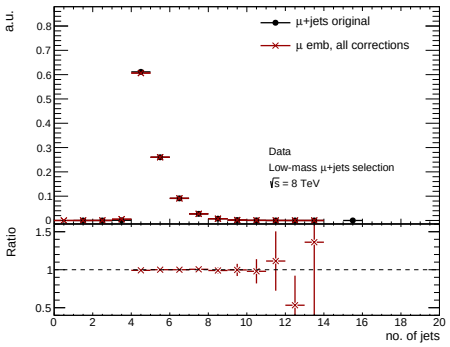

(a) Low-mass H^+ selection

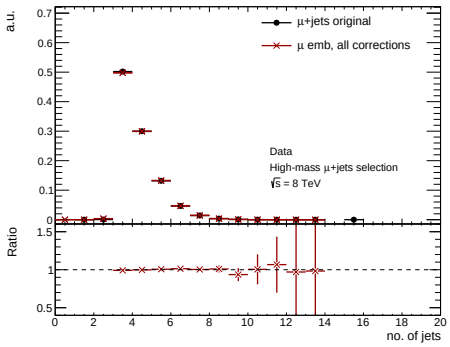

(b) High-mass H^+ selection

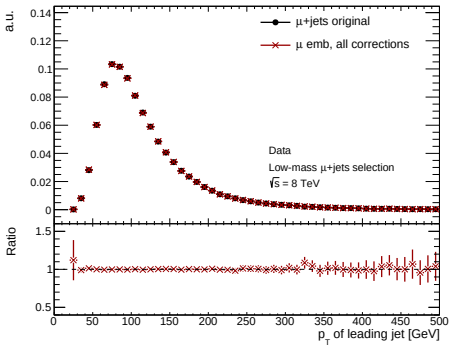

(c) Low-mass H^+ selection

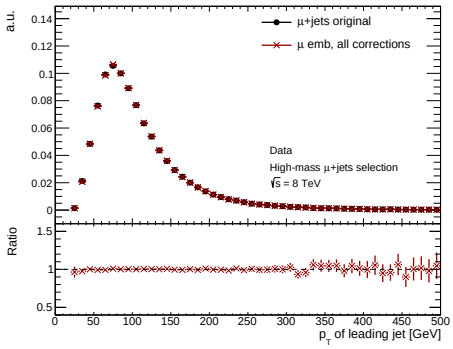

(d) High-mass H^+ selection

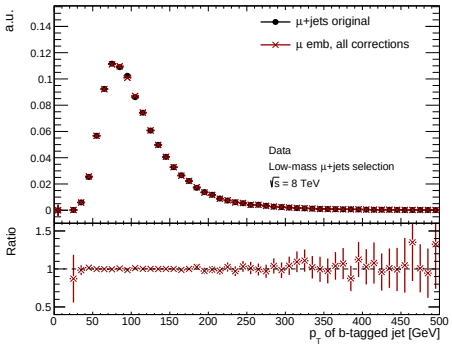

(e) Low-mass H^+ selection

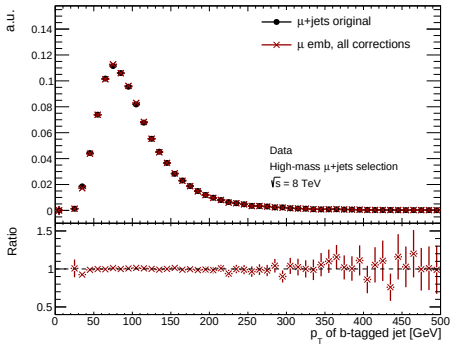

(f) High-mass H^+ selection

Figure A.4. Comparisons of (a, b) number of jets passing all selection criteria, (c, d) p_{T} of the leading jet, (e, f) p_{T} of the b-tagged jet after applying the low-mass (high-mass) μ+jets selection in the left (right) column for collision data and $\mu \to \mu$ embedded data after applying all necessary corrections.

B $\mu \rightarrow \tau$ Embedding

B.1. Embedded Simulation

In figure B.1, $\mu \rightarrow \tau$ embedded $t\bar{t}$ simulation is shown before and after applying the muon reconstruction and trigger efficiency corrections. All distributions are normalized arbitrarily to allow shape variations introduced by the correction to be seen. The low-mass H^+ selection is applied.

Distributions of more variables after applying either the low-mass or high-mass H^+

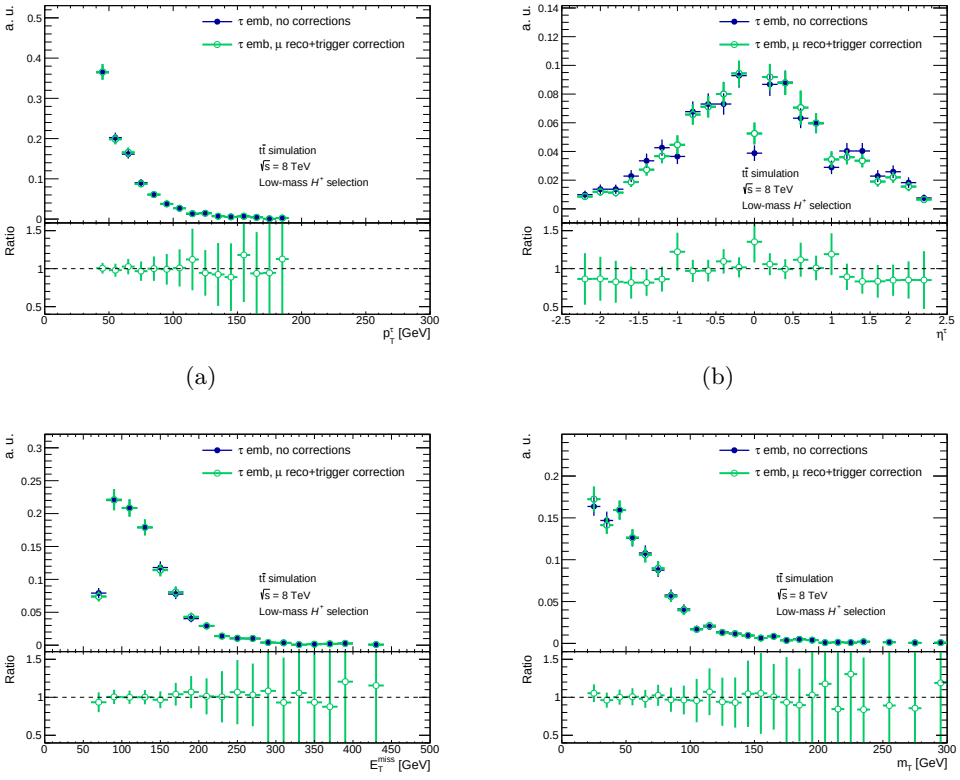

Figure B.1. Comparisons of (a) p_{T}^{τ}, (b) η^{τ}, (c) $E_{\mathrm{T}}^{\mathrm{miss}}$ and (d) m_{T} of $\mu \rightarrow \tau$ embedded $t\bar{t}$ simulation before and after applying the muon reconstruction and muon trigger efficiency corrections. The low-mass H^+ selection is applied.

selection are shown in figure B.2.

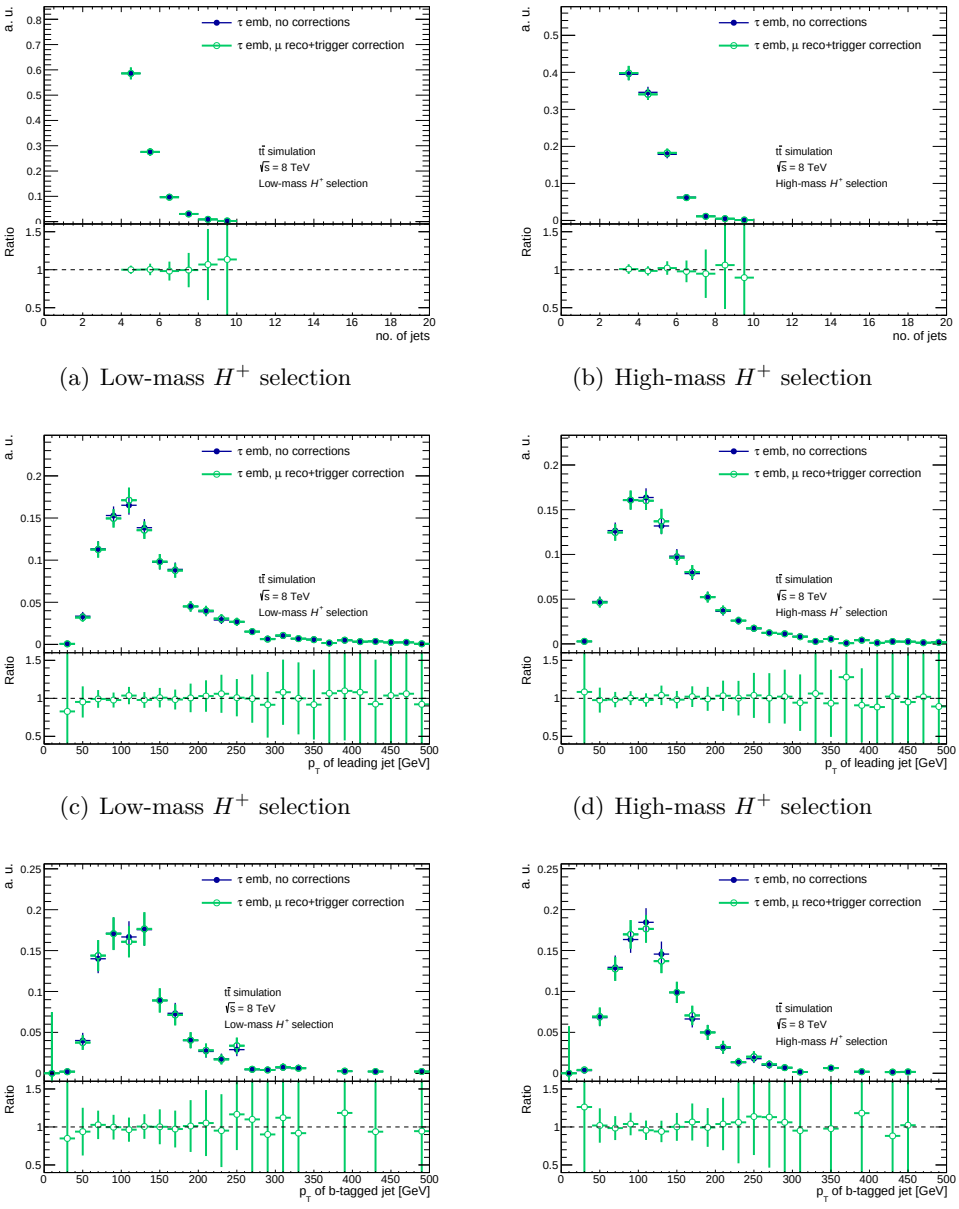

(a) Low-mass H^+ selection

(b) High-mass H^+ selection

(c) Low-mass H^+ selection

(d) High-mass H^+ selection

(e) Low-mass H^+ selection

(f) High-mass H^+ selection

Figure B.2. Comparisons of (a, b) number of jets passing all selection criteria, (c, d) p_{T} of the leading jet, (e, f) p_{T} of the b-tagged jet after applying the low-mass (high-mass) H^+ selection in the left (right) column for $\mu \to \tau$ embedded $t\bar{t}$ simulation before and after applying the muon reconstruction and muon trigger efficiency corrections.

Corresponding distributions, but after applying the $\tau_{\text{had-vis}} + E_{\text{T}}^{\text{miss}}$ trigger efficiency instead, are shown in figure B.3 after applying the low-mass H^+ selection. Distributions

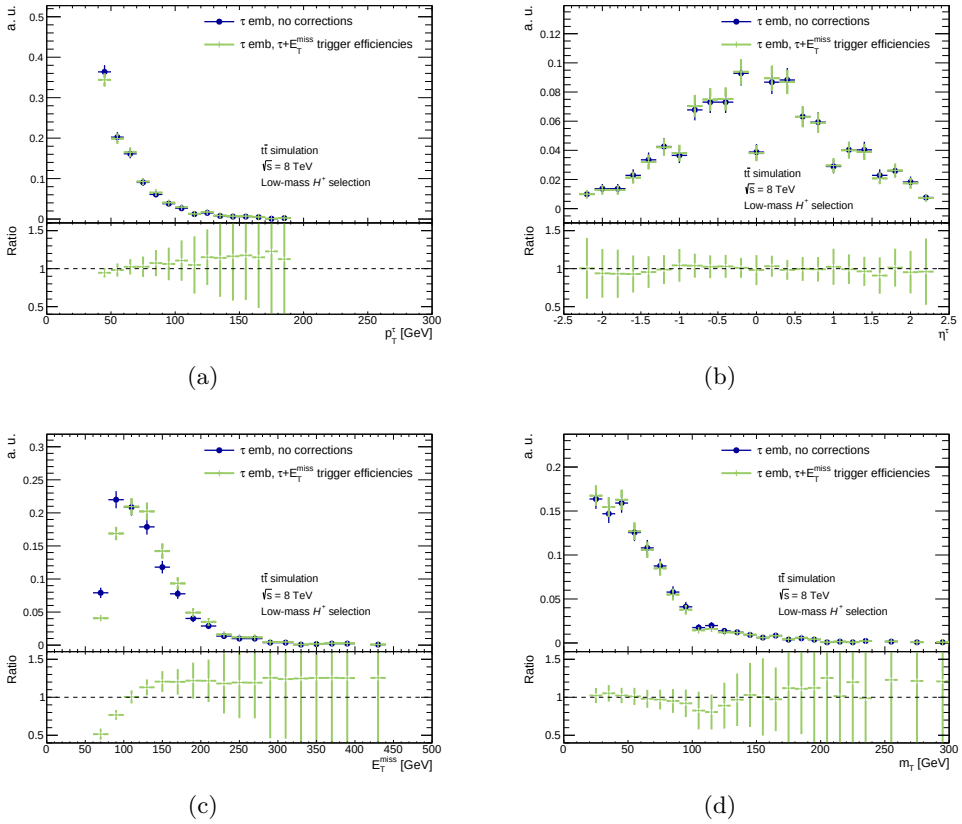

Figure B.3. Comparisons of (a) p_{T}^{τ}, (b) η^{τ}, (c) $E_{\text{T}}^{\text{miss}}$ and (d) m_{T} of $\mu \to \tau$ embedded $t\bar{t}$ simulation before and after applying the $\tau_{\text{had-vis}} + E_{\text{T}}^{\text{miss}}$ trigger efficiency correction. The low-mass H^+ selection is applied.

of more variables after applying either the low-mass or high-mass H^+ selection are shown in figure B.4.

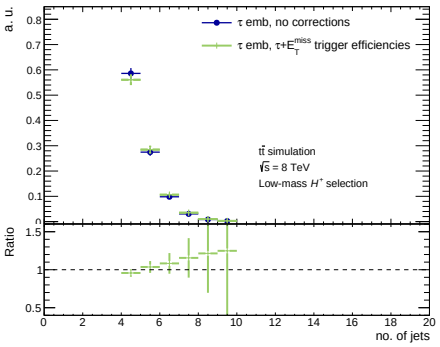

(a) Low-mass H^+ selection

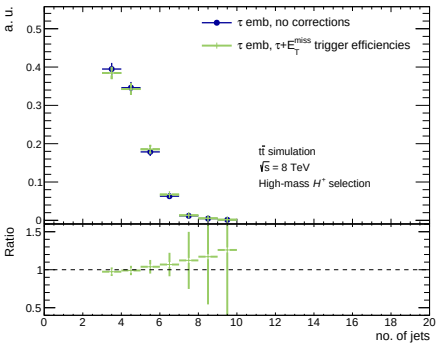

(b) High-mass H^+ selection

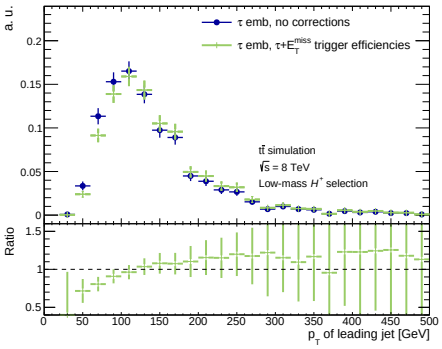

(c) Low-mass H^+ selection

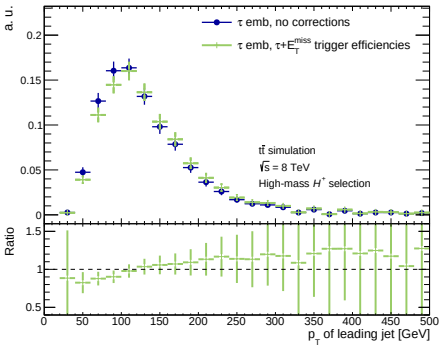

(d) High-mass H^+ selection

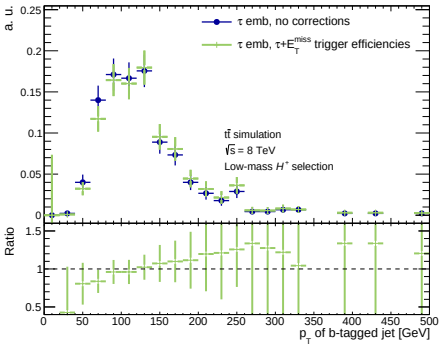

(e) Low-mass H^+ selection

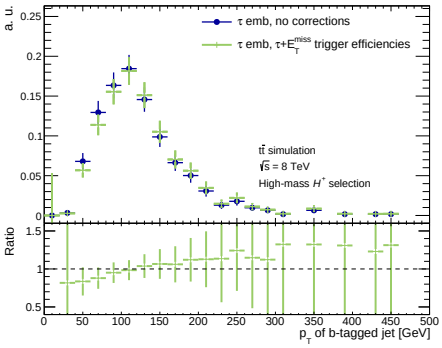

(f) High-mass H^+ selection

Figure B.4. Comparisons of (a, b) number of jets passing all selection criteria, (c, d) p_{T} of the leading jet, (e, f) p_{T} of the b-tagged jet after applying the low-mass (high-mass) H^+ selection in the left (right) column for $\mu \to \tau$ embedded $t\bar{t}$ simulation before and after applying the $\tau_{\text{had-vis}} + E_{\mathrm{T}}^{\mathrm{miss}}$ trigger efficiencies.

In figure B.5, $\mu \to \tau$ embedded $t\bar{t}$ simulation after applying the low-mass H^+ selection and all corrections is compared to default $t\bar{t}$ simulation. All distributions are normalized arbitrarily to allow shape comparisons. More distributions after applying either the low-mass or high-mass H^+ selection are shown in figure B.6. The statistical fluctuations are rather large due to the limited sample size available for embedding.

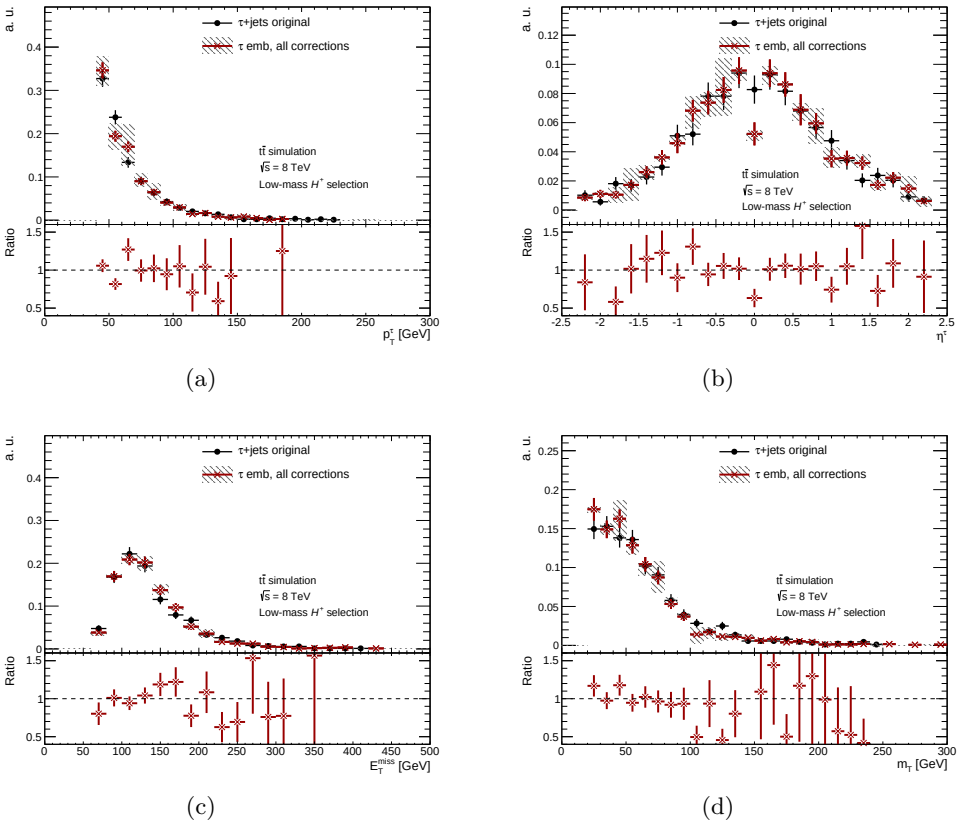

Figure B.5. Comparisons of (a) p_{T}^{τ}, (b) η^{τ}, (c) $E_{\mathrm{T}}^{\mathrm{miss}}$ and (d) m_{T} in default simulation and $\mu \to \tau$ embedded simulation after applying all necessary corrections. The low-mass H^+ selection is applied.

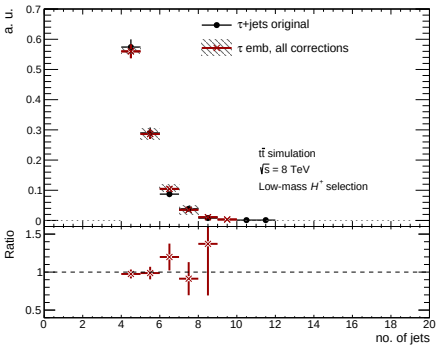

(a) Low-mass H^+ selection

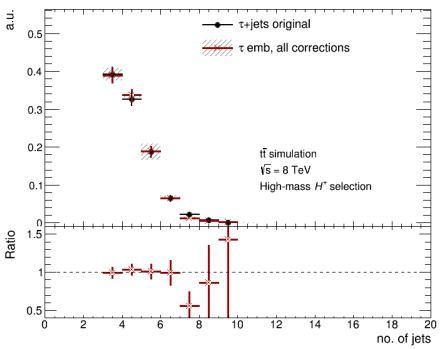

(b) High-mass H^+ selection

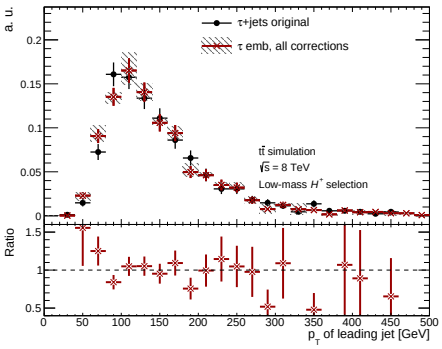

(c) Low-mass H^+ selection

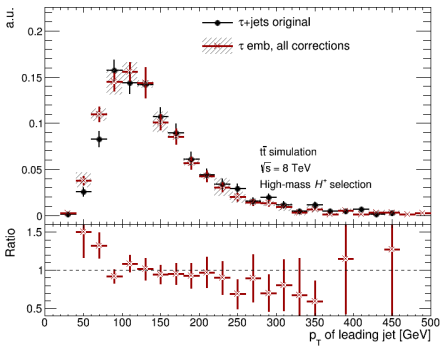

(d) High-mass H^+ selection

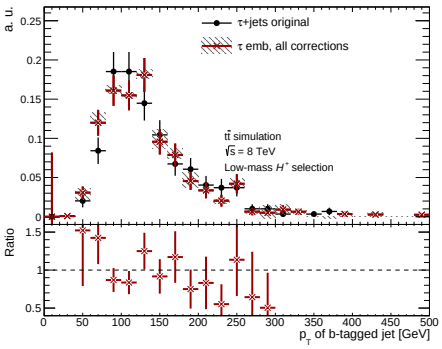

(e) Low-mass H^+ selection

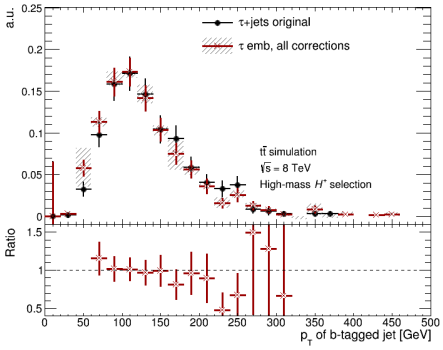

(f) High-mass H^+ selection

Figure B.6. Comparisons of (a, b) number of jets passing all selection criteria, (c, d) p_{T} of the leading jet, (e, f) p_{T} of the b-tagged jet after applying the low-mass (high-mass) H^+ selection in the left (right) column in default $t\bar{t}$ and $\mu \to \tau$ embedded $t\bar{t}$ simulation.

B.2. Embedded Data

In figure B.7, $\mu \to \tau$ embedded data after applying the low-mass H^+ selection is shown before and after applying the muon reconstruction and trigger efficiency corrections. All distributions are normalized to luminosity to allow both shape and normalization differences introduced by the corrections to be seen. More distributions after applying

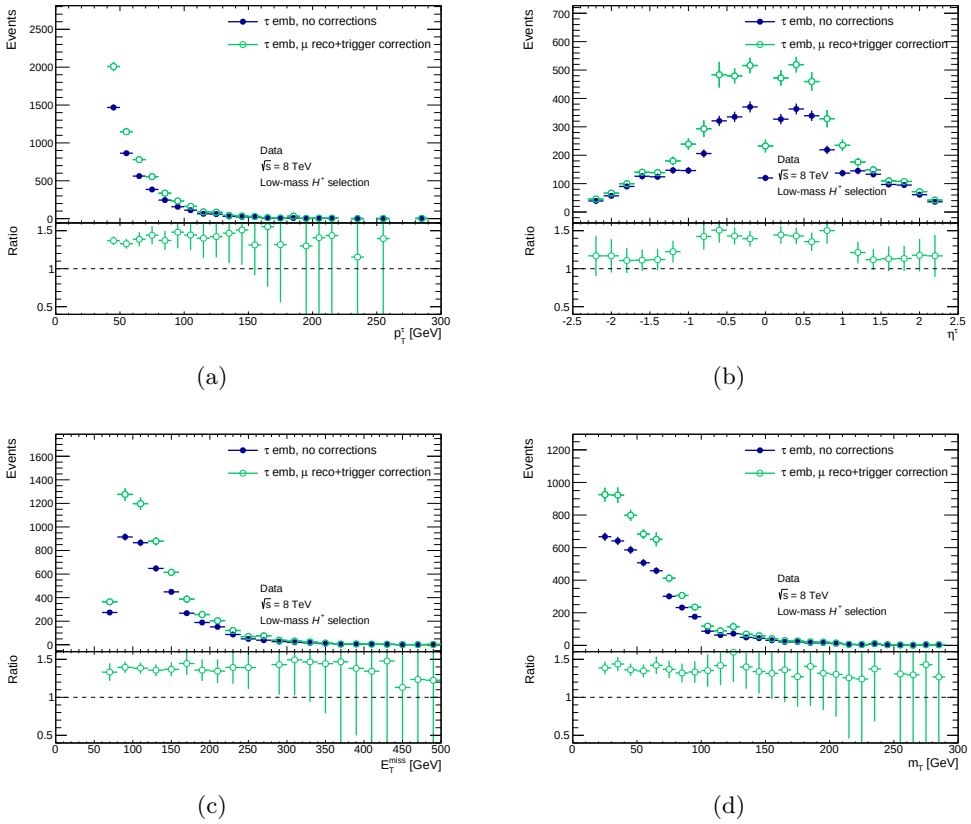

Figure B.7. Comparisons of (a) p_{T}^{τ}, (b) η^{τ}, (c) $E_{\mathrm{T}}^{\mathrm{miss}}$ and (d) m_{T} after applying the low-mass selection for default simulation and $\mu \to \tau$ embedded data after applying the muon trigger and reconstruction corrections.

either the low-mass or high-mass H^+ selection are shown in figure B.8.

In figure B.9, $\mu \to \tau$ embedded data after applying the low-mass H^+ selection is shown before and after applying the $\tau_{\text{had-vis}} + E_{\mathrm{T}}^{\mathrm{miss}}$ trigger efficiencies. All distributions are normalized to luminosity to allow both shape and normalization differences introduced by the corrections to be seen. More distributions after applying either the low-mass or high-mass H^+ selection are shown in figure B.10.

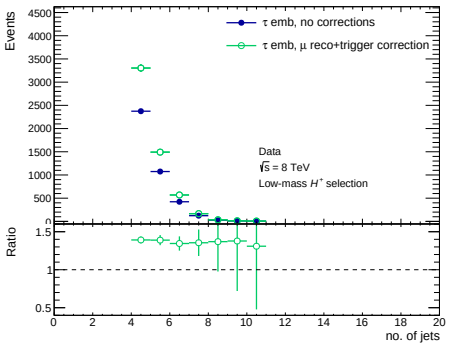

(a) Low-mass H^+ selection

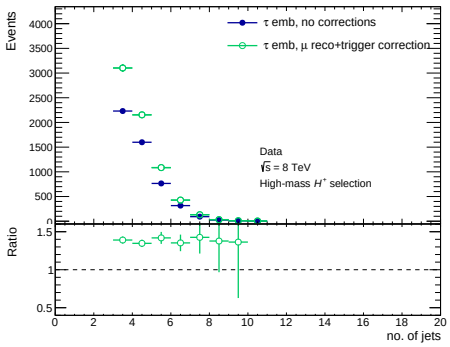

(b) High-mass H^+ selection

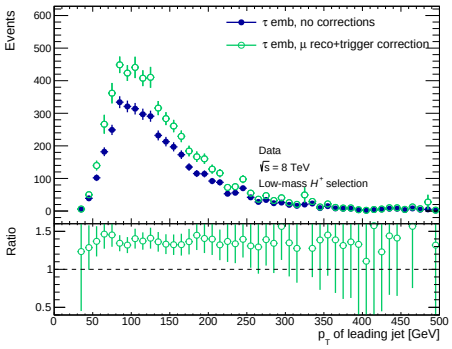

(c) Low-mass H^+ selection

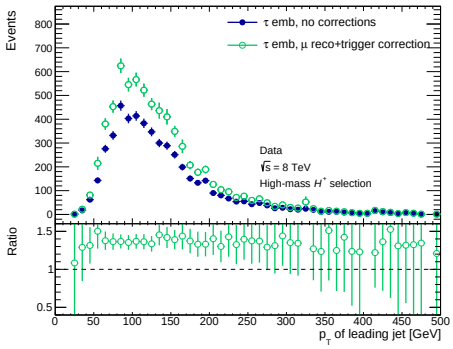

(d) High-mass H^+ selection

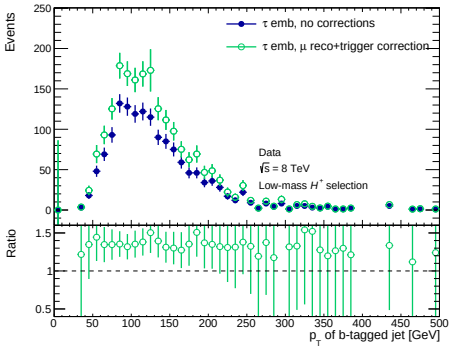

(e) Low-mass H^+ selection

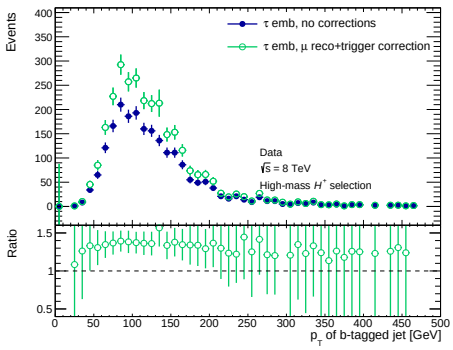

(f) High-mass H^+ selection

Figure B.8. Comparisons of (a, b) number of jets passing all selection criteria, (c, d) p_{T} of the leading jet, (e, f) p_{T} of the b-tagged jet after applying the low-mass (high-mass) H^+ selection in the left (right) column for default simulation and $\mu \to \tau$ embedded data after applying the muon trigger and reconstruction corrections.

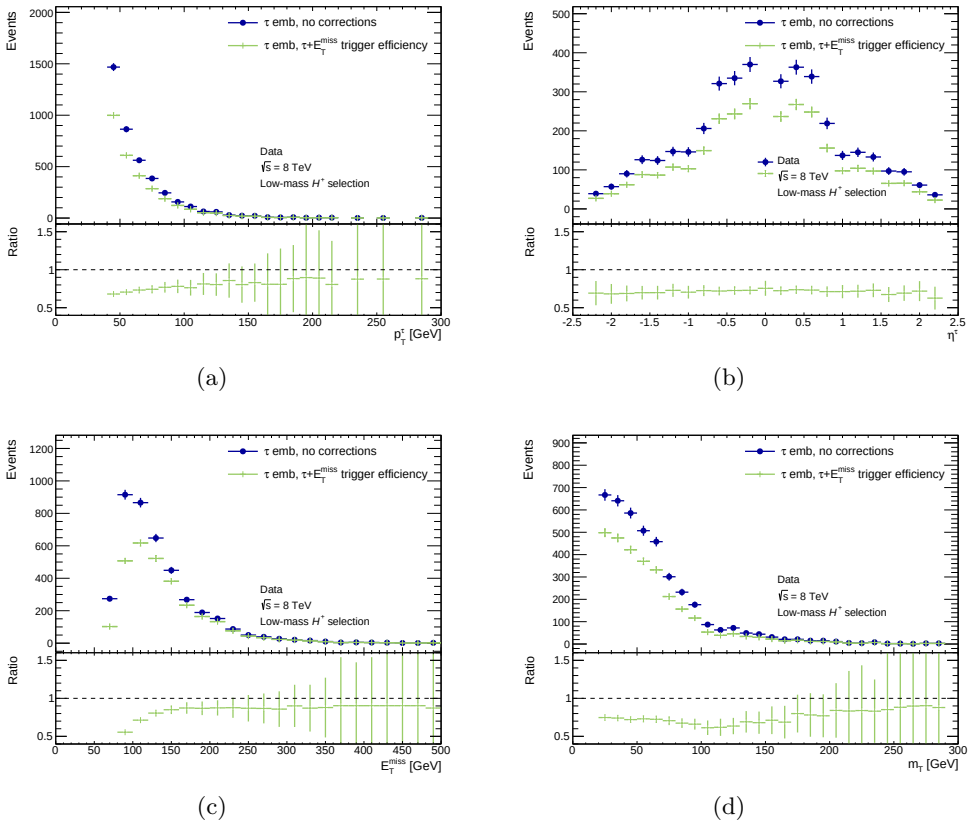

Figure B.9. Comparisons of (a) p_{T}^{τ}, (b) η^{τ}, (c) $E_{\mathrm{T}}^{\mathrm{miss}}$ and (d) m_{T} after applying the low-mass selection for default simulation and $\mu \to \tau$ embedded data after applying the $\tau_{\text{had-vis}} + E_{\mathrm{T}}^{\mathrm{miss}}$ trigger efficiencies.

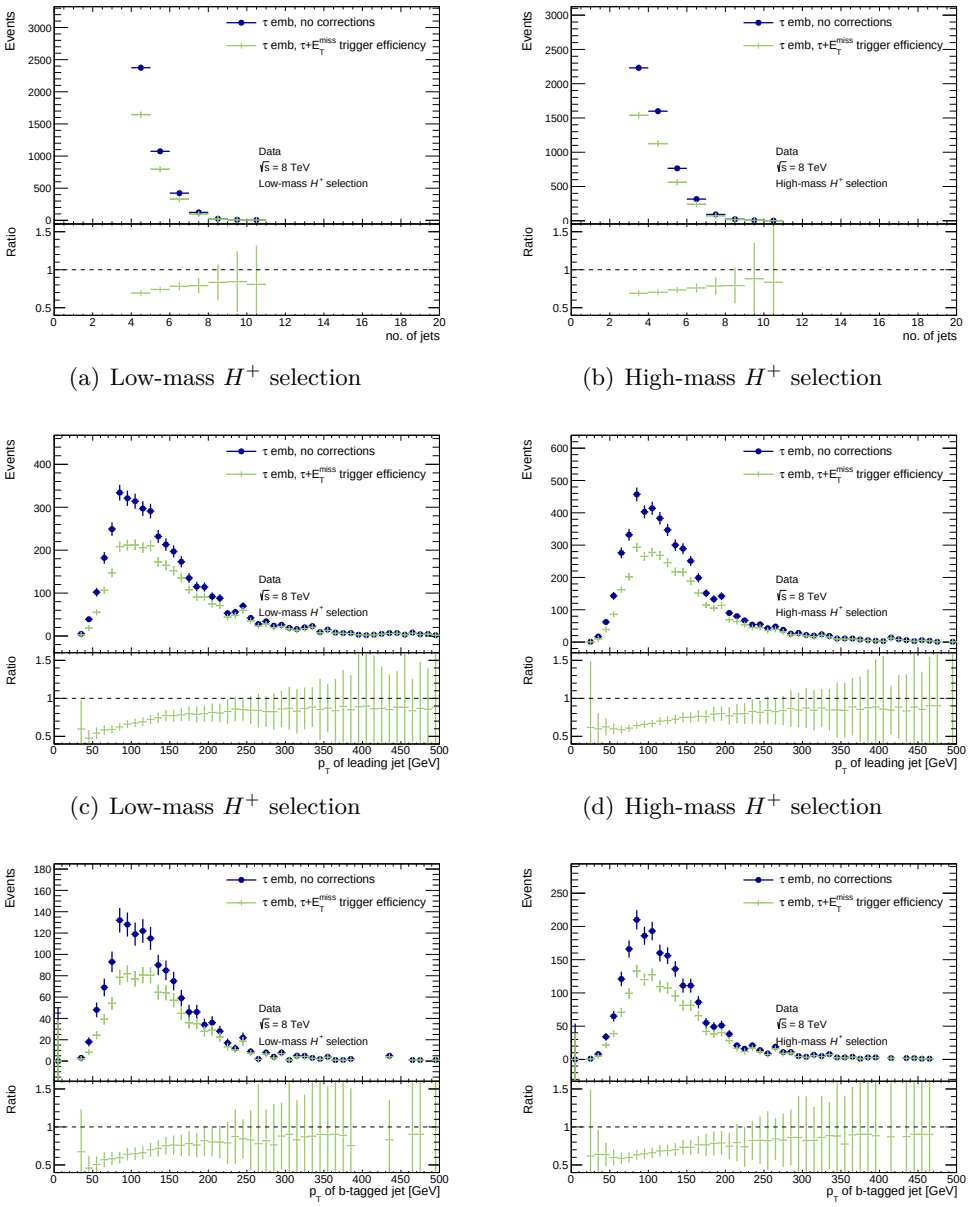

(a) Low-mass H^+ selection

(b) High-mass H^+ selection

(c) Low-mass H^+ selection

(d) High-mass H^+ selection

(e) Low-mass H^+ selection

(f) High-mass H^+ selection

Figure B.10. Comparisons of (a, b) number of jets passing all selection criteria, (c, d) p_{T} of the leading jet, (e, f) p_{T} of the b-tagged jet after applying the low-mass (high-mass) H^+ selection in the left (right) column for default simulation and $\mu \to \tau$ embedded data after applying the $\tau_{\text{had-vis}} + E_{\mathrm{T}}^{\mathrm{miss}}$ trigger efficiencies.

Bibliography

[1] ATLAS Collaboration, *Search for charged Higgs bosons decaying via $H^+ \to \tau\nu$ in top quark pair events using pp collision data at $\sqrt{s} = 7$ TeV with the ATLAS detector*, *JHEP* **1206** (2012) 039, [arXiv:1204.2760].

[2] ATLAS Collaboration, *Search for charged Higgs bosons decaying via $H^\pm \to \tau^\pm\nu$ in fully hadronic final states using pp collision data at $\sqrt{s} = 8$ TeV with the ATLAS detector*, *JHEP* **1503** (2015) 088, [arXiv:1412.6663].

[3] D. J. Gross and F. Wilczek, *Ultraviolet behavior of non-abelian gauge theories*, *Phys. Rev. Lett.* **30** (Jun, 1973) 1343–1346. http://link.aps.org/doi/10.1103/PhysRevLett.30.1343.

[4] H. D. Politzer, *Reliable perturbative results for strong interactions?*, *Phys. Rev. Lett.* **30** (Jun, 1973) 1346–1349. http://link.aps.org/doi/10.1103/PhysRevLett.30.1346.

[5] R. P. Feynman, *Relativistic cut-off for quantum electrodynamics*, *Phys. Rev.* **74** (Nov, 1948) 1430–1438. http://link.aps.org/doi/10.1103/PhysRev.74.1430.

[6] R. P. Feynman, *Space-time approach to quantum electrodynamics*, *Phys. Rev.* **76** (Sep, 1949) 769–789. http://link.aps.org/doi/10.1103/PhysRev.76.769.

[7] S. Tomonaga, *On a Relativistically Invariant Formulation of the Quantum Theory of Wave Fields*, *Progr. Theoret. Phys. (Kyoto)* **I** (1946) 27.

[8] J. Schwinger, *On Quantum-Electrodynamics and the Magnetic Moment of the Electron*, *Phys. Rev.* **73** (Feb, 1948) 416–417. http://link.aps.org/doi/10.1103/PhysRev.73.416.

[9] J. Schwinger, *Quantum Electrodynamics. I. A Covariant Formulation*, *Phys. Rev.* **74** (Nov, 1948) 1439–1461. http://link.aps.org/doi/10.1103/PhysRev.74.1439.

[10] J. Schwinger, *Quantum Electrodynamics. II. Vacuum Polarization and Self-Energy*, *Phys. Rev.* **75** (Feb, 1949) 651–679. http://link.aps.org/doi/10.1103/PhysRev.75.651.

[11] J. Schwinger, *Quantum Electrodynamics. III. The Electromagnetic Properties of the Electron Radiative Corrections to Scattering*, *Phys. Rev.* **76** (Sep, 1949) 790–817. http://link.aps.org/doi/10.1103/PhysRev.76.790.

[12] S. Glashow, *Partial-Symmetries of Weak Interactions*, *Nucl.Phys.* **22** (1961) 579–588.

[13] S. Weinberg, *A Model of Leptons*, *Phys.Rev.Lett.* **19** (1967) 1264–1266.

[14] A. Salam, *Weak and Electromagnetic Interactions*, *Conf.Proc.* **C680519** (1968) 367–377.

[15] P. W. Higgs, *Broken symmetries, massless particles and gauge fields*, *Phys.Lett.* **12** (1964) 132–133.

[16] F. Englert and R. Brout, *Broken symmetry and the mass of gauge vector mesons*, *Phys. Rev. Lett.* **13** (Aug, 1964) 321–323. http://link.aps.org/doi/10.1103/PhysRevLett.13.321.

[17] P. W. Higgs, *Broken Symmetries and the Masses of Gauge Bosons*, *Phys.Rev.Lett.* **13** (1964) 508–509.

[18] G. S. Guralnik, C. R. Hagen, and T. W. B. Kibble, *Global Conservation Laws and Massless Particles*, *Phys. Rev. Lett.* **13** (1964) 585–587.

[19] ATLAS Collaboration, *Observation of a new particle in the search for the Standard Model Higgs boson with the ATLAS detector at the LHC*, *Phys.Lett.* **B716** (2012) 1–29, [arXiv:1207.7214].

[20] CMS Collaboration, *Observation of a new boson at a mass of 125 GeV with the CMS experiment at the LHC*, *Phys.Lett.* **B716** (2012) 30–61, [arXiv:1207.7235].

[21] D. Griffiths, *Introduction to Elementary Particles*, Wiley-VCH, 2008.

[22] F. Halzen and A. D. Martin, *Quarks & Leptons: An Introductory Course in Modern Partile Physics*, Wiley, 1984.

[23] S. Dittmaier and M. Schumacher, *The Higgs Boson in the Standard Model - From LEP to LHC: Expectations, Searches, and Discovery of a Candidate*, *Prog.Part.Nucl.Phys.* **70** (2013) 1–54, [arXiv:1211.4828].

[24] S. P. Martin, *A Supersymmetry primer*, *Adv.Ser.Direct.High Energy Phys.* **21** (2010) 1–153, [hep-ph/9709356].

[25] A. Djouadi, *The Anatomy of electro-weak symmetry breaking. II. The Higgs bosons in the minimal supersymmetric model*, *Phys.Rept.* **459** (2008) 1–241, [hep-ph/0503173].

[26] J. F. Gunion, H. E. Haber, G. L. Kane, and S. Dawson, *The Higgs Hunter's Guide*, *Front.Phys.* **80** (2000) 1–448.

[27] The Super-Kamiokande Collaboration, Y. Fukuda et al., *Evidence for oscillation of atmospheric neutrinos*, *Phys.Rev.Lett.* **81** (1998) 1562–1567, [hep-ex/9807003].

[28] SNO Collaboration, *Direct evidence for neutrino flavor transformation from neutral current interactions in the Sudbury Neutrino Observatory*, *Phys.Rev.Lett.* **89** (2002) 011301, [nucl-ex/0204008].

[29] Particle Data Group, K. Olive et al., *Review of Particle Physics*, *Chin.Phys.* **C38** (2014) 090001.

[30] N. Cabibbo, *Unitary symmetry and leptonic decays*, *Phys. Rev. Lett.* **10** (Jun, 1963) 531–533. http://link.aps.org/doi/10.1103/PhysRevLett.10.531.

[31] M. Kobayashi and T. Maskawa, *CP Violation in the Renormalizable Theory of Weak Interaction*, *Prog.Theor.Phys.* **49** (1973) 652–657.

[32] M. Schumacher, *Suche nach neutralen Higgs Bosonen mit dem OPAL-Detektor bei LEP2*. PhD thesis, Bonn U., Bonn, 1999. BONN-IR-99-19.

[33] LHC Higgs Cross Section Working Group, S. Heinemeyer, C. Mariotti, G. Passarino, and R. Tanaka (Eds.), *Handbook of LHC Higgs Cross Sections: 3. Higgs Properties*, *CERN-2013-004* (CERN, Geneva, 2013) , [arXiv:1307.1347].

[34] ATLAS and CMS Collaborations, *Combined Measurement of the Higgs Boson Mass in pp Collisions at $\sqrt{s} = 7$ and 8 TeV with the ATLAS and CMS Experiments*, *Phys.Rev.Lett.* **114** (2015) 191803, [arXiv:1503.7589].

[35] ATLAS Collaboration, *Measurements of Higgs boson production and couplings in diboson final states with the ATLAS detector at the LHC*, *Phys.Lett.* **B726** (2013) 88–119, [arXiv:1307.1427].

[36] CMS Collaboration, *Observation of the diphoton decay of the Higgs boson and measurement of its properties*, *Eur. Phys. J.* **C74** (2014) no. 10 3076, [arXiv:1407.0558].

[37] CMS Collaboration, *Measurement of the properties of a Higgs boson in the four-lepton final state*, *Phys. Rev.* **D89** (2014) no. 9 092007, [arXiv:1312.5353].

[38] CMS Collaboration, *Measurement of Higgs boson production and properties in the WW decay channel with leptonic final states*, *JHEP* **01** (2014) 096, [arXiv:1312.1129].

[39] ATLAS Collaboration, *Evidence for the Higgs-boson Yukawa coupling to tau leptons with the ATLAS detector*, *JHEP* **04** (2015) 117, [arXiv:1501.4943].

[40] CMS Collaboration, *Evidence for the 125 GeV Higgs boson decaying to a pair of τ leptons*, *JHEP* **05** (2014) 104, [arXiv:1401.5041].

[41] ATLAS Collaboration, *Search for the $b\bar{b}$ decay of the Standard Model Higgs boson in associated $(W/Z)H$ production with the ATLAS detector*, *JHEP* **01** (2015) 069, [arXiv:1409.6212].

[42] CMS Collaboration, *Search for the standard model Higgs boson produced through vector boson fusion and decaying to $b\bar{b}$*, *Phys. Rev.* **D92** (2015) no. 3 032008, [arXiv:1506.0101].

[43] ATLAS Collaboration, *Study of the spin and parity of the Higgs boson in diboson decays with the ATLAS detector*, *submitted to EPJC* (2015) , [arXiv:1506.5669].

[44] CMS Collaboration, *Precise determination of the mass of the Higgs boson and tests of compatibility of its couplings with the standard model predictions using proton collisions at 7 and 8 TeV*, *Eur. Phys. J.* **C75** (2015) no. 5 212, [arXiv:1412.8662].

[45] ATLAS Collaboration, *Measurements of the Higgs boson production and decay rates and coupling strengths using pp collision data at $\sqrt{s} = 7$ and 8 TeV in the ATLAS experiment*, *submitted to EPJC* (2015) , [arXiv:1507.4548].

[46] F. Zwicky, *Die Rotverschiebung von extragalaktischen Nebeln*, *Helvetica Physica Acta* **6** (1933) 110–127.

[47] Supernova Cosmology Project, S. Perlmutter et al., *Measurements of Omega and Lambda from 42 high redshift supernovae*, *Astrophys. J.* **517** (1999) 565–586, [astro-ph/9812133].

[48] Supernova Search Team, A. G. Riess et al., *Observational evidence from supernovae for an accelerating universe and a cosmological constant*, *Astron. J.* **116** (1998) 1009–1038, [astro-ph/9805201].

[49] D. M. Wittman, J. A. Tyson, D. Kirkman, I. Dell'Antonio, and G. Bernstein, *Detection of weak gravitational lensing distortions of distant galaxies by cosmic dark matter at large scales*, *Nature* **405** (2000) 143–149, [astro-ph/0003014].

[50] W. de Boer and C. Sander, *Global electroweak fits and gauge coupling unification*, *Phys.Lett.* **B585** (2004) 276–286, [hep-ph/0307049].

[51] Yu. A. Golfand and E. P. Likhtman, *Extension of the Algebra of Poincare Group Generators and Violation of p Invariance*, [Pisma Zh. Eksp. Teor. Fiz.13,452(1971)], *JETP Lett.* **13** (1971) 323–326.

[52] D. V. Volkov and V. P. Akulov, *Is the Neutrino a Goldstone Particle?*, *Phys. Lett.* **B46** (1973) 109–110.

[53] J.-L. Gervais and B. Sakita, *Field Theory Interpretation of Supergauges in Dual Models*, *Nucl. Phys.* **B34** (1971) 632–639.

[54] S. Dimopoulos and H. Georgi, *Softly broken supersymmetry and SU(5)*, *Nuclear Physics B* **193** (Dec., 1981) 150–162.

[55] T.D. Lee, *A Theory of Spontaneous T Violation*, *Phys. Rev.* **D 8** (1973) 1226.

[56] G. C. Branco et al., *Theory and phenomenology of two-Higgs-doublet models*, *Phys. Rept.* **516** (2012) 1–102, [arXiv:1106.0034].

[57] P. Fayet, *Supersymmetry and Weak, Electromagnetic and Strong Interactions*, *Phys. Lett.* **B 64** (1976) 159.

[58] P. Fayet, *Spontaneously Broken Supersymmetric Theories of Weak, Electromagnetic and Strong Interactions*, *Phys. Lett.* **B 69** (1977) 489.

[59] G. R. Farrar and P. Fayet, *Phenomenology of the Production, Decay, and Detection of New Hadronic States Associated with Supersymmetry*, *Phys. Lett.* **B 76** (1978) 575.

[60] P. Fayet, *Relations Between the Masses of the Superpartners of Leptons and Quarks, the Goldstino Couplings and the Neutral Currents*, *Phys. Lett.* **B 84** (1979) 416.

[61] S. Dimopoulos and H. Georgi, *Softly Broken Supersymmetry and SU(5)*, *Nucl. Phys.* **B 193** (1981) 150.

[62] M. Carena et al., *MSSM Higgs Boson Searches at the LHC: Benchmark Scenarios after the Discovery of a Higgs-like Particle*, *Eur.Phys.J.* **C73** (2013) no. 9 2552, [arXiv:1302.7033].

[63] R. Harlander, M. Krämer and M. Schumacher, *Bottom-quark associated Higgs-boson production: reconciling the four- and five-flavour scheme approach*, arXiv:1112.3478.

[64] M. Flechl et al., *Improved cross-section predictions for heavy charged Higgs boson production at the LHC*, *Phys.Rev.* **D91** (2015) no. 7 075015, [arXiv:1409.5615].

[65] M. Carena, D. Garcia, U. Nierste, and C. E. M. Wagner, *Effective Lagrangian for the $\bar{t}bH^+$ interaction in the MSSM and charged Higgs phenomenology*, *Nucl. Phys.* **B577** (2000) 88–120, [hep-ph/9912516].

[66] LHC Higgs Cross Section Working Group, *MSSM Charged Higgs*, . https://twiki.cern.ch/twiki/bin/view/LHCPhysics/LHCHXSWGMSSMCharged.

[67] *LEP design report*, CERN, Geneva, 1984.

[68] M. Carena, S. Heinemeyer, C. Wagner, and G. Weiglein, *Suggestions for benchmark scenarios for MSSM Higgs boson searches at hadron colliders*, *Eur.Phys.J.* **C26** (2003) 601–607, [hep-ph/0202167].

[69] D0 Collaboration, V. Abazov et al., *Search for charged Higgs bosons in top quark decays*, *Phys.Lett.* **B682** (2009) 278–286, [arXiv:0908.1811].

[70] ALEPH, DELPHI, L3, OPAL Collaborations and the LEP working group for Higgs boson searches, *Search for Charged Higgs bosons: Combined Results Using LEP Data*, *Eur.Phys.J.* **C73** (2013) 2463, [arXiv:1301.6065].

[71] L. Evans and P. Bryant, *LHC Machine*, *JINST* **3** (2008) S08001.

[72] ALICE Collaboration, *The ALICE experiment at the CERN LHC*, *JINST* **3** (2008) S08002.

[73] ATLAS Collaboration, *The ATLAS Experiment at the CERN Large Hadron Collider*, *JINST* **3** (2008) S08003.

[74] CMS Collaboration, *The CMS experiment at the CERN LHC*, *JINST* **3** (2008) S08004.

[75] LHCb Collaboration, *The LHCb Detector at the LHC*, *JINST* **3** (2008) S08005.

[76] J. Haffner, *The CERN accelerator complex*, General Photo. https://cds.cern.ch/record/1621894.

[77] ATLAS Collaboration, *Performance of the ATLAS muon trigger in pp collisions at* $\sqrt{s} = 8$ *TeV*, *Eur.Phys.J.* **C75** (2015) no. 3 120, [arXiv:1408.3179].

[78] ATLAS Collaboration, *ATLAS twiki: Luminosity public results*, . https://twiki.cern.ch/twiki/bin/view/AtlasPublic/LuminosityPublicResults.

[79] P. Grafström and W. Kozanecki, *Luminosity determination at proton colliders*, *Progress in Particle and Nuclear Physics* **81** (2015) 97–148.

[80] ATLAS Collaboration, *Luminosity Determination in pp Collisions at* $\sqrt{s} = 7$ *TeV Using the ATLAS Detector at the LHC*, *Eur.Phys.J.* **C 71** (2011) 1630, [arXiv:1101.2185].

[81] ATLAS Collaboration, *Improved luminosity determination in pp collisions at* $\sqrt{s}$ *= 7 TeV using the ATLAS detector at the LHC*, *Eur. Phys. J.* **C 73** (2013) 2518, [arXiv:1302.4393].

[82] A. Buckley et al., *General-purpose event generators for LHC physics*, *Phys.Rept.* **504** (2011) 145–233, [arXiv:1101.2599].

[83] J. M. Campbell, J. W. Huston, and W. J. Stirling, *Hard Interactions of Quarks and Gluons: A Primer for LHC Physics*, *Rept. Prog. Phys.* **70** (2007) 89, [hep-ph/0611148].

[84] R. K. Ellis, W. J. Stirling and B. Webber, *QCD and Collider Physics*, Cambridge University Press, 1996.

[85] https://sherpa.hepforge.org/trac/wiki/MonteCarloGenerators.

[86] A. D. Martin, W. J. Stirling, R. S. Thorne, and G. Watt, *Parton distributions for the LHC*, *Eur. Phys. J.* **C63** (2009) 189–285, [arXiv:0901.0002].

[87] Y. L. Dokshitzer, *Calculation of the Structure Functions for Deep Inelastic Scattering and e+ e- Annihilation by Perturbation Theory in Quantum Chromodynamics.*, *Sov. Phys. JETP* **46** (1977) 641–653.

[88] V. Gribov and L. Lipatov, *Deep inelastic e p scattering in perturbation theory*, *Sov. J. Nucl. Phys.* **15** (1972) 438–450.

[89] G. Altarelli and G. Parisi, *Asymptotic Freedom in Parton Language*, *Nucl. Phys.* **B126** (1977) 298.

[90] R. D. Ball et al., *Parton distributions with LHC data*, *Nucl. Phys.* **B867** (2013) 244–289, [arXiv:1207.1303].

[91] J. Pumplin et al., *New generation of parton distributions with uncertainties from global QCD analysis*, *JHEP* **0207** (2002) 012, [hep-ph/0201195].

[92] W. Stirling, *private communication*, . http://www.hep.ph.ic.ac.uk/~wstirlin/plots/plots.html.

[93] S. Frixione and B. R. Webber, *Matching NLO QCD Computations and Parton Shower Simulations*, *JHEP* **06** (2002) 029, [hep-ph/0204244].

[94] B. Andersson, G. Gustafson, G. Ingelman, and T. Sjostrand, *Parton Fragmentation and String Dynamics*, *Phys. Rept.* **97** (1983) 31–145.

[95] B. Andersson, *The Lund model*, *Camb. Monogr. Part. Phys. Nucl. Phys. Cosmol.* **7** (1997) 1–471.

[96] D. Amati and G. Veneziano, *Preconfinement as a Property of Perturbative QCD*, *Phys. Lett.* **B83** (1979) 87.

[97] S. Wolfram, *Parton and Hadron Production in e^+e^- Annihilation*, *Largely based on a talk given at XV Rencontres de Moriond, March 1980* .

[98] G. C. Fox and S. Wolfram, *A Model for Parton Showers in QCD*, *Nuclear Physics B* **168** (1980) 285–295.

[99] R. D. Field and S. Wolfram, *A QCD Model for e^+e^- Annihilation*, *Nucl. Phys. B* **213** (1983) 65.

[100] GEANT4 Collaboration, S. Agostinelli et al., *GEANT4: A simulation toolkit*, *Nucl. Instrum. Meth.* **A 506** (2003) 250.

[101] ATLAS Collaboration, *The ATLAS Simulation Infrastructure*, *Eur. Phys. J.* **C 70** (2010) 823, [arXiv:1005.4568].

[102] T. Sjöstrand, S. Mrenna, and P. Z. Skands, *A Brief Introduction to PYTHIA 8.1*, *Comput. Phys. Commun.* **178** (2008) 852, [arXiv:0710.3820].

[103] ATLAS Collaboration, *ATLAS tunes of PYTHIA 6 and Pythia 8 for MC11*, *ATL-PHYS-PUB-2011-009* (2011) . https://cds.cern.ch/record/1363300.

[104] T. Sjöstrand, S. Mrenna, and P. Z. . Skands, *PYTHIA 6.4 Physics and Manual*, *JHEP* **05** (2006) 026, [hep-ph/0603175].

[105] B. P. Kersevan and E. Richter-Was, *The Monte Carlo event generator AcerMC versions 2.0 to 3.8 with interfaces to PYTHIA 6.4, HERWIG 6.5 and ARIADNE 4.1*, *Comput. Phys. Commun.* **184** (2013) 919, [hep-ph/0405247].

[106] G. Corcella et al., *HERWIG 6: An Event generator for hadron emission reactions with in terfering gluons (including supersymmetric processes)*, *JHEP* **01** (2001) 010, [hep-ph/0011363].

[107] ATLAS Collaboration, *New ATLAS event generator tunes to 2010 data*, *ATL-PHYS-PUB-2011-008* (2011) . https://cdsweb.cern.ch/record/1345343.

[108] S. Gieseke, C. Rohr, and A. Siodmok, *Colour reconnections in Herwig++*, *Eur. Phys. J.* **C72** (2012) 2225, [arXiv:1206.0041].

[109] P. Z. Skands, *Tuning Monte Carlo Generators: The Perugia Tunes*, *Phys. Rev.* **D 82** (2010) 074018, [arXiv:1005.3457].

[110] S. Frixione, P. Nason, and C. Oleari, *Matching NLO QCD computations with Parton Shower simulations: the POWHE G method*, *JHEP* **11** (2007) 070, [arXiv:0709.2092].

[111] ATLAS Collaboration, *Summary of ATLAS Pythia 8 tunes*, . http://cds.cern.ch/record/1474107.

[112] Z. Was and P. Golonka, *TAUOLA as tau Monte Carlo for future applications*, *Nucl. Phys. Proc. Suppl.* **144** (2005) 88, [hep-ph/0411377].

[113] E. Barberio, B. van Eijk, and Z. Was, *PHOTOS: A universal Monte Carlo for QED radiative corrections in decays*, *Comput. Phys. Commun.* **66** (1991) 115.

[114] S. Frixione, E. Laenen, P. Motylinski, and B. R. Webber, *Single-top production in MC@NLO*, *JHEP* **03** (2006) 092, [hep-ph/0512250].

[115] H.-L. Lai et al., *New parton distributions for collider physics*, *Phys. Rev.* **D 82** (2010) 074024, [arXiv:1007.2241].

[116] J. Butterworth, J. R. Forshaw, and M. Seymour, *Multiparton interactions in photoproduction at HERA*, *Z. Phys.* **C 72** (1996) 637, [hep-ph/9601371].

[117] M. Aliev et al., *HATHOR – HAdronic Top and Heavy quarks crOss section calculatoR*, *Comput. Phys. Commun.* **182** (2011) 1034, [arXiv:1007.1327].

[118] N. Kidonakis, *Next-to-next-to-leading-order collinear and soft gluon corrections for t-channel single top quark production*, *Phys. Rev.* **D 83** (2011) 091503, [arXiv:1103.2792].

[119] N. Kidonakis, *NNLL resummation for s-channel single top quark production*, *Phys. Rev.* **D 81** (2010) 054028, [arXiv:1001.5034].

[120] N. Kidonakis, *Two-loop soft anomalous dimensions for single top quark associated production with a W^- or H^-*, *Phys. Rev.* **D 82** (2010) 054018, [arXiv:1005.4451].

[121] M. L. Mangano et al., *ALPGEN, a generator for hard multiparton processes in hadronic collisions*, *JHEP* **07** (2003) 001, [hep-ph/0206293].

[122] P. M. Nadolsky et al., *Implications of CTEQ global analysis for collider observables*, *Phys. Rev.* **D 78** (2008) 013004, [arXiv:0802.0007].

[123] J. M. Campbell, R. Ellis, and C. Williams, *Vector boson pair production at the LHC*, *JHEP* **07** (2011) 018, [arXiv:1105.0020].

[124] R. Gavin, Y. Li, F. Petriello, and S. Quackenbush, *W Physics at the LHC with FEWZ 2.1*, *Comput. Phys. Commun.* **184** (2013) 208, [arXiv:1201.5896].

[125] R. Gavin, Y. Li, F. Petriello, and S. Quackenbush, *FEWZ 2.0: A code for hadronic Z production at next-to-next-to-leading order*, *Comput. Phys. Commun.* **182** (2011) 2388, [arXiv:1011.3540].

[126] M. Bahr et al, *Herwig++ physics and manual*, *Eur. Phys. J.* **C 58** (2008) 639, [arXiv:0803.0883].

[127] J. Alwall et al., *MadGraph 5 : Going Beyond*, *JHEP* **1106** (2011) 128, [arXiv:1106.0522].

[128] T. Cornelissen et al., *Concepts, Design and Implementation of the ATLAS New Tracking (NEWT)*, *ATL-SOFT-PUB-2007-007* . https://cds.cern.ch/record/1020106.

[129] ATLAS Collaboration, *Performance of the ATLAS Inner Detector Track and Vertex Reconstruction in the High Pile-Up LHC Environment*, *ATLAS-CONF-2012-042* . https://cds.cern.ch/record/1435196.

[130] ATLAS Collaboration, *Performance of primary vertex reconstruction in proton-proton collisions at $\sqrt{s}$ =7 TeV in the ATLAS experiment*, *ATLAS-CONF-2010-069* . https://cds.cern.ch/record/1281344.

[131] W. Lampl et al., *Calorimeter Clustering Algorithms: Description and Performance*, *ATL-LARG-PUB-2008-002* . https://cds.cern.ch/record/1099735.

[132] M. Cacciari, G. P. Salam, and G. Soyez, *The Anti-k_t jet clustering algorithm*, *JHEP* **0804** (2008) 063, [arXiv:0802.1189].

[133] M. Cacciari and G. P. Salam, *Dispelling the N^3 myth for the k_t jet-finder*, *Phys. Lett.* **B 641** (2006) 57, [hep-ph/0512210].

[134] M. Cacciari, G. P. Salam and G. Soyez. http:/fastjet.fr.

[135] M. Cacciari and G. P. Salam, *Pileup subtraction using jet areas*, *Phys.Lett.* **B659** (2008) 119–126, [arXiv:0707.1378].

[136] ATLAS Collaboration, *Pile-up subtraction and suppression for jets in ATLAS*, *ATLAS-CONF-2013-083* . https://cds.cern.ch/record/1570994.

[137] ATLAS Collaboration, *Jet energy measurement with the ATLAS detector in proton-proton collisions at $\sqrt{s} = 7$ TeV*, *Eur.Phys.J.* **C73** (2013) no. 3 2304, [arXiv:1112.6426].

[138] ATLAS Collaboration, *Data-driven determination of the energy scale and resolution of jets reconstructed in the ATLAS calorimeters using dijet and multijet events at $\sqrt{s} = 8$ TeV*, *ATLAS-CONF-2015-017* . https://cds.cern.ch/record/2008678.

[139] ATLAS Collaboration, *b-tagging in dense environments*, *ATL-PHYS-PUB-2014-014* . https://cds.cern.ch/record/1750682.

[140] ATLAS Collaboration, *Commissioning of the ATLAS high-performance b-tagging algorithms in the 7 TeV collision data*, *ATLAS-CONF-2011-102* . http://cds.cern.ch/record/1369219.

[141] ATLAS Collaboration, *Calibration of the performance of b-tagging for c and light-flavour jets in the 2012 ATLAS data*, *ATLAS-CONF-2014-046* . https://cds.cern.ch/record/1741020.

[142] ATLAS Collaboration, *Calibration of b-tagging using dileptonic top pair events in a combinatorial likelihood approach with the ATLAS experiment*, *ATLAS-CONF-2014-004* . http://cds.cern.ch/record/1664335.

[143] ATLAS Collaboration, *Identification and energy calibration of hadronically decaying tau leptons with the ATLAS experiment in pp collisions at* $\sqrt{s}$*=8 TeV*, *Eur. Phys. J.* **C75** (2015) no. 7 303, [arXiv:1412.7086].

[144] ATLAS Collaboration, *Performance of the Reconstruction and Identification of Hadronic Tau Decays with ATLAS*, *ATLAS-CONF-2011-152* . http://cds.cern.ch/record/1398195.

[145] ATLAS Collaboration, *Performance of the Reconstruction and Identification of Hadronic Tau Decays in ATLAS with 2011 Data*, *ATLAS-CONF-2012-142* . http://cds.cern.ch/record/1485531.

[146] L. Breiman, J. Friedman, C. J. Stone, and R. A. Olshen, *Classification and regression trees*, Chapman & Hall, New York, 1984.

[147] Y. Freund and R. E. Schapire, *A decision-theoretic generalization of on-line learning and an application to boosting*, *Journal of Computer and System Sciences* **55** (1997) no. 1 119.

[148] ATLAS Collaboration, *Measurement of the muon reconstruction performance of the ATLAS detector using 2011 and 2012 LHC proton-proton collision data*, *Eur.Phys.J.* **C74** (2014) no. 11 3130, [arXiv:1407.3935].

[149] ATLAS Collaboration, *Electron efficiency measurements with the ATLAS detector using the 2012 LHC proton-proton collision data*, *ATLAS-CONF-2014-032* . https://cds.cern.ch/record/1706245.

[150] ATLAS Collaboration, *Improved electron reconstruction in ATLAS using the Gaussian Sum Filter-based model for bremsstrahlung*, *ATLAS-CONF-2012-047* . https://cds.cern.ch/record/1449796.

[151] ATLAS Collaboration, *Electron reconstruction and identification efficiency measurements with the ATLAS detector using the 2011 LHC proton-proton collision data*, *Eur.Phys.J.* **C74** (2014) no. 7 2941, [arXiv:1404.2240].

[152] ATLAS Collaboration, *Electron performance measurements with the ATLAS detector using the 2010 LHC proton-proton collision data*, *Eur.Phys.J.* **C72** (2012) 1909, [arXiv:1110.3174].

[153] ATLAS Collaboration, *Performance of Missing Transverse Momentum Reconstruction in ATLAS studied in Proton-Proton Collisions recorded in 2012 at 8 TeV*, *ATLAS-CONF-2013-082* . https://cds.cern.ch/record/1570993/.

[154] ATLAS Collaboration, *Search for charged Higgs bosons in the τ+jets final state in $t\bar{t}$ decays with pp collision data recorded at $\sqrt{s}$ =7 TeV with the ATLAS experiment - Supporting note*, *ATL-PHYS-INT-2012-047* .

[155] ATLAS Collaboration, *Search for charged Higgs bosons in the τ+jets final state with pp collision data recorded at $\sqrt{s}$ =8 TeV with the ATLAS experiment*, *ATL-COM-PHYS-2014-211* .

[156] ATLAS Collaboration, *Search for charged Higgs bosons decaying via $H^{\pm} \to \tau^{\pm}\nu$ in fully hadronic final states using pp collision data at $\sqrt{s} = 8$ TeV with the ATLAS detector - Auxiliary Material*, . https://atlas.web.cern.ch/Atlas/GROUPS/PHYSICS/PAPERS/HIGG-2013-30/.

[157] ATLAS Collaboration, *Modelling $Z \to \tau\tau$ processes in ATLAS with τ-embedded $Z \to \mu\mu$ data*, *submitted to JINST* (2015) , [arXiv:1506.5623].

[158] ATLAS Collaboration, *Measurement of the Higgs boson couplings in the $\tau\tau$ final state with the ATLAS detector - Supporting Note*, *ATL-COM-PHYS-2014-170* .

[159] ATLAS Collaboration, *ATLAS twiki: TauSystematicsWinterConf2012*, . https://twiki.cern.ch/twiki/bin/view/AtlasProtected/TauSystematicsWinterConf2012.

[160] ATLAS Collaboration, *ATLAS twiki: TauRecommendationsWinterConf2013*, . https://twiki.cern.ch/twiki/bin/view/AtlasProtected/TauRecommendationsWinterConf2013.

[161] ATLAS Collaboration, *Search for a charged Higgs boson decaying via $H^+ \to \tau_{had}\nu$+lepton in $t\bar{t}$ events using 4.6 fb^{-1} of pp collision data recorded at $\sqrt{s} = 7$ TeV with the ATLAS detector - Supporting note*, *ATL-PHYS-INT-2012-046* .

[162] ATLAS Collaboration, *Search for charged Higgs bosons decaying via $H^+ \to \tau\nu$ in top quark pair events using pp collision data at $\sqrt{s} = 7$ TeV with the ATLAS detector - Auxiliary Material*, . https://atlas.web.cern.ch/Atlas/GROUPS/PHYSICS/PAPERS/HIGG-2012-09/.

[163] ATLAS Collaboration, *Measurement of the Mis-identification Probability of τ Leptons from Hadronic Jets and from Electrons*, *ATLAS-CONF-2011-113* . https://cds.cern.ch/record/1375550.

[164] S. Heinemeyer, W. Hollik, and G. Weiglein, *FeynHiggs: A program for the calculation of the masses of the neutral CP-even Higgs bosons in the MSSM*, *Comput. Phys. Commun.* **124** (2000) 76, [hep-ph/9812320].

[165] S. Dittmaier, M. Kramer, M. Spira, and M. Walser, *Charged-Higgs-boson production at the LHC: NLO supersymmetric QCD corrections*, *Phys.Rev.* **D83** (2011) 055005, [arXiv:0906.2648].

[166] LHC Higgs Cross Section Working Group, S. Dittmaier, C. Mariotti, G. Passarino, and R. Tanaka (Eds.), *Handbook of LHC Higgs Cross Sections: 2. Differential Distributions*, *CERN-2012-002* (CERN, Geneva, 2012) , [arXiv:1201.3084].

[167] G. Cowan, K. Cranmer, E. Gross, and O. Vitells, *Asymptotic formulae for likelihood-based tests of new physics*, *Eur. Phys. J.* **C 71** (2011) 1554, [arXiv:1007.1727].

[168] A. L. Read, *Presentation of search results: The CL(s) technique*, *J. Phys.* **G28** (2002) 2693–2704.

[169] Particle Data Group, J. Beringer et al., *Review of particle physics*, *Phys. Rev. D* **86** (Jul, 2012) 010001. http://link.aps.org/doi/10.1103/PhysRevD.86.010001.

[170] ATLAS Statistics Forum, *The CL_s method: information for conference speakers*, . https://twiki.cern.ch/twiki/pub/AtlasProtected/StatisticsTools/CLsInfo.pdf.

[171] A. Wald, *Sequential tests of statistical hypotheses*, *Ann. Math. Statist.* **16** (06, 1945) 117–186. http://dx.doi.org/10.1214/aoms/1177731118.

[172] S. S. Wilks, *The Large-Sample Distribution of the Likelihood Ratio for Testing Composite Hypotheses*, *Annals Math. Statist.* **9** (1938) no. 1 60–62.

[173] J. Griffiths, *private communication*, .

[174] ATLAS Collaboration, *Search for charged Higgs bosons in the τ+jets final state with pp collision data recorded at $\sqrt{s} = 8$ TeV with the ATLAS experiment*, *ATLAS-CONF-2013-090* . https://cds.cern.ch/record/1595533.

[175] M. Flechl, *private communication*, .

[176] CMS Collaboration, *Search for a light charged Higgs boson in top quark decays in pp collisions at $\sqrt{s} = 7$ TeV*, *JHEP* **07** (2012) 143, [arXiv:1205.5736].

[177] CMS Collaboration, *Search for a charged Higgs boson in pp collisions at sqrt(s) = 8 TeV*, submitted to JHEP, arXiv:1508.7774.

Danksagung/Acknowledgements

Throughout the last 4 years many people have helped and supported me in many different ways. Some of you are not mentioned here not because I forgot but rather because I want to keep this to the more directly work-related people.

Danke an Markus, für die Möglichkeit, in deiner Gruppe promovieren zu können, viel zu lernen, Unterstützung zu bekommen, wenn ich sie brauchte, aber dabei auch viele Freiheiten zu haben und eigenständig arbeiten zu können. Danke für die Möglichkeit des verlängerten und verlängerten etc. CERN-Aufenthalts.

Danke an Martin. Auch wenn du dich auf die dunkle Seite abgesetzt hast, habe ich in der Zeit davor doch viel von dir gelernt und du hast auch danach immer noch geholfen, wenn ich Hilfe benötigt habe. Danke, dass du mich viel hast selbstständig arbeiten lassen, aber zur Verfügung standest, wenn es nötig war. Thanks to Stan for help and support whenever I needed it, no matter where you were or what else you were busy with, even after you'd left. To both Martin and Stan also thanks for all kinds of τ-related help and support and for patiently answering many questions when I had to grade exercise sheets. Thanks to Elias. You always helped out when it was needed and helped me survive quite a few meetings. Danke an Michael, vor allem für Code- und Rechnerunterstützung aller Art zu jeder Zeit.

Danke an Christian. Egal ob als realer oder virtueller Büromitbewohner hast du immer bei allen Fragen und Problemen weitergeholfen, auch wenn du selbst meist reichlichst beschäftigt warst. Danke an den Rest der Gruppe. Ihr habt geholfen und wart da, egal ob's um Physik, Code, Unterkünfte, Kaffeetrinken, Pflanzengießen oder was auch immer ging. Danke an Chris, ohne dich hätte nichts so funktioniert, wie es funktioniert hat.

Thanks to the other charged Higgs people, especially those in 'τ+jets', including Allison, Justin and Steve. I enjoyed working with you all and the results presented here would not have been possible without you. Thanks also to Jianming for the Jianming Effect.